



UNIVERSITY OF  
BIRMINGHAM

THE DEVELOPMENT OF RADIOACTIVE GAS IMAGING FOR  
THE STUDY OF CHEMICAL FLOW PROCESSES

by

SARAH DAWN BELL

A thesis submitted to  
The University of Birmingham  
For the degree of  
DOCTOR OF PHILOSOPHY

School of Chemical Engineering  
College of Engineering and Physical  
Sciences

University of Birmingham

September 2015

UNIVERSITY OF  
BIRMINGHAM

**University of Birmingham Research Archive**

**e-theses repository**

This unpublished thesis/dissertation is copyright of the author and/or third parties. The intellectual property rights of the author or third parties in respect of this work are as defined by The Copyright Designs and Patents Act 1988 or as modified by any successor legislation.

Any use made of information contained in this thesis/dissertation must be in accordance with that legislation and must be properly acknowledged. Further distribution or reproduction in any format is prohibited without the permission of the copyright holder.

## **ABSTRACT**

The development and use of functional medical imaging has grown rapidly in importance over the last few decades. The field of medicine primarily uses nuclear imaging techniques for the non-invasive study of physiological processes within the human body. At the University of Birmingham a considerable research effort has been made into adapting these techniques for the study of flow and mixing in solid and liquid systems. However, despite capability, little work has been reported on imaging gases for industrial use. The emission tomography techniques available at Birmingham were adapted and utilised for the study of gaseous flow processes. The work presented in this thesis provides details of the development of a radioactive gas imaging technique capable of studying chemical flow processes. Feasibility studies were performed to compare the capabilities of Single Photon Emission Computed Tomography (SPECT) and Positron Emission Tomography (PET) for imaging dynamic gas flows in a gas fluidised bed, a bubble column and a low pressure adsorption column leading to a more detailed study of CO<sub>2</sub> adsorption at high pressure using PET. In order to verify the technique a comparison between breakthrough data obtained using a CO<sub>2</sub> analyser and the PET image data was made and a qualitative study of the adsorption kinetics inside the column is provided.

## **ACKNOWLEDGEMENTS**

There are many people who have provided valuable help and support that I would like to thank for their contribution to this project.

Firstly, I would like to express my great appreciation to my supervisors for their constant support and guidance through the entire project. Dr Andy Ingram and Dr Tom Leadbeater provided many hours of advice and encouragement and their doors were always open when I needed help, for which I am truly grateful.

I would like to say a special thank you to Prof David Parker and Mike Smith for making the radioactive gases, often on very short notice. I had difficulty in organising my experiments and their flexibility and help was greatly appreciated. I would also like to thank Simon Caldwell and Dr Bushra Al-Duri whose advice and experiences were vital to my experimental design and Prof Joe Wood for the use of his equipment. I would also like to acknowledge Dr James Bowen for performing the characterisation experiments.

Thank you to the Engineering and Physical Sciences Research Council (EPSRC) for providing financial support.

Thanks also to other staff and students at the University of Birmingham who made me feel welcome and became good friends over the years. A special thank you to the lunch group who never failed to meet every day for interesting and completely pointless conversation. In particular Helen Stone who was always good for a cup of tea and a moan.

I would like to say a special thank you to Tom Skuse for putting up with me and always knowing how to make me smile, even when it got tough. I'll never forget your patience.

Finally I would like to thank my family for their constant support and encouragement despite never fully understanding the work that I've done. I will always be grateful for the opportunities that I have been given and their help along the way.

# CONTENTS

ABSTRACT .....	i
ACKNOWLEDGEMENTS.....	ii
LIST OF FIGURES.....	vi
LIST OF TABLES .....	xxxv
NOMENCLATURE .....	xxxvii
General nomenclature .....	xxxvii
Imaging.....	xxxvii
Fluidised bed .....	xxxvii
Bubble column.....	xxxviii
Adsorption.....	xxxviii
ACRONYMS.....	xli
1 INTRODUCTION.....	1
1.1 Background.....	1
1.2 Aims and objectives .....	3
1.3 Layout of thesis .....	3
2 LITERATURE REVIEW.....	6
2.1 Introduction .....	6
2.2 Global considerations.....	6
2.3 Single Photon Emission Computed Tomography (SPECT).....	10
2.3.1 Introduction.....	10
2.3.2 Theory of SPECT.....	10
2.3.3 Applications of SPECT .....	22
2.4 Positron Emission Tomography (PET) .....	27
2.4.1 Introduction.....	27
2.4.2 Theory of PET.....	27
2.4.3 Applications of PET .....	39
2.5 Image reconstruction techniques .....	41
2.5.1 Introduction.....	41
2.5.2 Filtered Back Projection (FBP).....	42
2.5.3 Ordered Subset Expectation Maximization (OS-EM).....	49
2.6 Making radioactive tracers .....	51
2.6.1 Making $^{81}\text{Kr}^m$ .....	51
2.6.2 Making $^{11}\text{CO}_2$ .....	51
2.7 Fluidised bed.....	52
2.7.1 Introduction.....	52

2.7.2	Theory .....	52
2.7.3	Industrial applications .....	57
2.8	Bubble column .....	58
2.8.1	Introduction .....	58
2.8.2	Theory .....	58
2.8.3	Industrial applications .....	61
2.9	Adsorption .....	62
2.9.1	Introduction .....	62
2.9.2	Theory of adsorption .....	63
2.9.3	Capacity and breakthrough .....	68
2.9.4	Adsorption equilibria .....	78
2.9.5	Kinetics .....	82
2.9.6	Measurement techniques .....	84
2.10	Hardware .....	86
2.10.1	SPECT camera .....	86
2.10.2	PET camera .....	87
3	PRELIMINARY STUDIES .....	89
3.1	SPECT investigation .....	89
3.1.1	Fluidised bed study .....	89
3.1.2	Bubble column study .....	94
3.1.3	SPECT study conclusion .....	105
3.2	PET investigation .....	106
3.2.1	Steady state PET study .....	106
3.2.2	Preliminary dynamic PET study .....	113
3.2.3	PET study conclusions .....	119
3.3	SPECT vs. PET .....	120
4	MATERIALS AND METHODS .....	121
4.1	PET camera calibration .....	121
4.1.1	Sensitivity and resolution tests .....	121
4.2	Experimental procedure .....	146
4.2.1	Materials .....	147
4.2.2	Experimental method .....	151
5	RESULTS .....	154
5.1	CO <sub>2</sub> analyser results .....	154
5.1.1	Capacity and isotherms .....	154
5.1.2	Breakthrough .....	161

5.2	Image data results.....	168
5.2.1	Capacity and isotherms .....	168
5.2.2	Breakthrough .....	175
5.3	Detailed analysis of adsorption using the developed imaging technique....	196
5.3.1	Concentration profiles.....	196
5.3.2	Mass Transfer Wave velocity.....	204
5.3.3	CO <sub>2</sub> accumulation .....	212
5.3.4	Mass Transfer Zone.....	226
5.4	Discussions .....	247
6	CONCLUSIONS AND FUTURE WORK.....	250
6.1	Conclusions.....	250
6.2	Future work .....	254
7	REFERENCES.....	258
8	APPENDIX .....	265
8.1	APPENDIX A Risk Assessment .....	265
8.2	APPENDIX B CO <sub>2</sub> Mass Flow Controller Correction .....	271
8.3	APPENDIX C Concentration profiles.....	272
8.4	APPENDIX D Accumulation Profiles .....	278
9	Publications.....	284

## LIST OF FIGURES

Figure 2.1. (a) shows the projected intensity profiles of two point sources placed three times their FWHM apart. The bar underneath the profiles shows a visual representation of the point sources. (b) shows the sources placed one FWHM apart. The visual representation shows that it is possible to distinguish the two sources but there is an element of blurring in between them. (c) shows the two sources less than one FWHM apart. The two sources are now indistinguishable.....	7
Figure 2.2. This image <sup>1</sup> defines the terms used when discussing image planes.....	9
Figure 2.3. Configuration of a gamma-ray detector system.....	11
Figure 2.4. (a) shows a diagram of gamma-rays being emitted from a uniform source and hitting the detector at all angles. Without a means of correlating the emissions to a point of origin the image produced would fill the FoV of the detector with a maximum intensity in the centre with reducing intensity following the inverse square law towards the edge of the FoV.....	13
Figure 2.5. Cross-sectional view of a collimator placed between the gamma-source and detector. The black arrows at the bottom of the figure show the range of rays within the acceptance angle that reach the detector and the red arrows indicate examples of rays that approach at an angle greater than the acceptance angle so are absorbed by the septa.....	14
Figure 2.6. Photograph of a parallel-hole collimator <sup>1</sup> . Collimators are made of lead and contain thousand of small holes a few centimetres long and define the emission trajectory of a detected photon. ....	15
Figure 2.7. Diagram <sup>1</sup> showing the structure of parallel hole, pinhole, converging and diverging collimators and their corresponding mapping ratio. Parallel hole collimators provide a direct one-to-one mapping of the radioactive distribution. Pinhole collimators	

magnify and invert the image of the object, converging collimators magnify the image and diverging collimations minify the image. .... 16

Figure 2.8. (a) Shows a point source located at distance  $d$  from the collimator.  $P$  indicated the projected diameter of the point source as detected by the crystal. (b) Shows increased collimator hole diameter which increase the size of  $P$  and results in a larger spatial resolution. (c) Shows the point source located twice the distance from the collimator, which also results in larger  $P$  and degraded spatial resolution. Finally (d) shows a decreased  $P$  with an increased collimator hole length. This results in improved spatial resolution..... 18

Figure 2.9. Diagram depicting how the Point Spread Function (PSF) of the projected image of a point source is formed. (a) Shows that if the source is placed close to the detector the LSF shows a higher intensity peak and less spreading compared to (b) where the source distance from the detector is doubled. .... 19

Figure 2.10. (a) shows a point source emitting gamma-rays radially. In this example only the ray parallel to the collimator septa reaches the detector. (b) shows the same point source moved closer to the collimator where a higher proportion of gamma-rays reach the detector. .... 20

Figure 2.11. An example of image data gained from a gated myocardial perfusion study<sup>1</sup>. .... 23

Figure 2.12. Array of cross-sectional images of a bubble column at different heights produced by de Mesquita et al. (2012). The images on the left highlight the low density gaseous areas in red (labelled gas holdup) and the images on the right show higher density liquid regions in red. The blue area is a void of liquid (labelled liquid holdup) and is indicated by the white arrow. .... 26

Figure 2.13. (a) shows a positron ( $\beta^+$ ) moving towards an electron at rest ( $e^-$ ) and (b) shows the results annihilation and release of two back-to-back gamma-rays ( $\gamma$ ) which are detected in coincidence.....29

Figure 2.14. Different types of events that can be detected in PET imaging. (a) Shows a true coincidence event, which is the coincident detection of two annihilation photon originating from the same point. (b) Shows a single detection where only one photon is detected within the timing window due to the other photon passing through the detector or leaving the FoV. (c) Shows a random event where an LOR is created between two single detections that are not connected and finally (d) shows a scatter event where one of the annihilation photons is scattered resulting in a LOR that does not represent the actual event. ....30

Figure 2.15. Definition of detector pair location in Cartesian co-ordinates of a coincident detection which is recorded as an LOR in polar co-ordinates. The perpendicular distance of the LOR from the origin is denoted by  $r$  and the angle is denoted by  $\theta$ ...32

Figure 2.16. A set of parallel LORs at angle  $\theta$  and the resulting projection of line integrals, which is a simple line of the sinogram corresponding to angle  $\theta$ .  $P_\theta$  displays a distribution of LOR counts. ....32

Figure 2.17. Figure<sup>1</sup> showing the formation of a sinogram. (A) shows four different LORs, for one point of annihilation, labelled A to D, the point of origin has been labelled with an x. (B) shows how the LORs A to D would be stored as angle ( $\theta$ ) vs. displacement ( $r$ ) in a sinogram. (C) is an example of a more complex sinogram obtained from a brain scan and (D) is the resulting image. ....33

Figure 2.18. Photo of a detector block coupled with four PMTs .....35

Figure 2.19. Photo of a bucket which consists of 2 x 4 blocks of detectors.....35

Figure 2.20. Definition of opposing detectors for a full ring of detectors. For detector block A a pairing can be made with a detector between B and C (shaded in red).....36

Figure 2.21. The left hand diagram shows that direct planes are defined as a coincidence event detected in the same detector ring. By placing septa between the detectors the amount of randoms and scatter detected is reduced. The middle diagram shows a cross plane span of three and the right hand diagram shows a cross plane span of seven. ....37

Figure 2.22. The relative axial sensitivity map for direct planes, cross plane span of three and cross plane span of seven.....38

Figure 2.23. For 3D data acquisition the septa are retracted allowing the full range of detector pairings. The diagram on the right shows the resulting relative axial sensitivity map. ....39

Figure 2.24. Diagram showing how projection profiles are made from parallel line integrals for a specific angle  $\theta$ . The resulting projection is a function of  $r$ , perpendicular distance from origin, and  $\theta$ , angle of LOR. The object is in Cartesian co-ordinates so in a function of  $x$  and  $y$ ,  $f(x, y)$ .....43

Figure 2.25. Projection profiles for three angles and object profile  $f(r)$  .....44

Figure 2.26. Backprojection with no filter results in  $1/r$  blurring at the edges due to low frequency overlapping of backprojections .....44

Figure 2.27. Backprojection (as Figure 2.26) with ramp filter. (a) Shows the object projection with the ramp filter applied and the result of three filtered backprojections. (b) Shows the resulting image after many filtered back projections. There is blurring in the background of the image but the object is more defined. ....47

Figure 2.28. Object projection with ramp and Gaussian filter applied.....48

Figure 2.29. Image model grid of  $N$  pixels.  $H_{ij}$ , highlighted as the bold black ray element, is the probability that the activity in pixel  $f_j$ , shown as a blue pixel, will be detected by projection  $P_i$ .....50

Figure 2.30. Schematic of a fluidised bed. The top of the bed is open and the solid particles are supported by a distributor which uniformly distributes the fluid, in this case air, as it flows up through the bed. The length of the bed before fluidisation is  $L_0$ . ....53

Figure 2.31. Different fluidisation regimes. The fixed bed is the state before fluidisation. The superficial velocity is below the minimum fluidisation velocity and the solid particles do not move so the bed length is  $L_0$ . At minimum fluidisation the length of the bed,  $L_f$ , increases as the upward friction of the gas flow is equal to the gravitational force meaning the particles begin to move. In particulate fluidisation the bed length increases as the particles move more with increasing superficial velocity. The particle distribution is uniform and the gas-solid mixture behaves as a fluid. At high superficial velocities most of the air passes through the bed as bubbles and is called bubbling or aggregative fluidisation. With a bed with smaller diameter the bubbles can grow to be as large as the cross section of the bed and is called slugging. ....55

Figure 2.32. Schematic of a bubble column. Gas is introduced to the liquid of liquid-solid phase through a distributor in the form of bubbles which pass upwards through the bed. ....59

Figure 2.33. Figure showing the three different flow regimes of bubble column reactors. Bubbly flow occurs at low superficial velocities and the bubbles formed are small and uniformly distributed. By increasing the superficial velocity churn-turbulent flow is observed. With this regime bubbles coalesce and break apart causing unsteady flow

through the column. At high velocities and small enough column diameter slug flow occurs. This is when the bubble diameter is comparable to that of the column.....60

Figure 2.34. The top plot shows the attractive and repulsive energy,  $E_A$  and  $E_R$  respectively, acting on an approaching molecule and resulting total energy,  $E$ . The bottom plot shows the attractive and repulsive forces,  $F_A$  and  $F_R$  respectively, as a function of interatomic separation,  $x$ , and resulting net force,  $F$ . The equilibrium separation is the point at which the net force is zero and corresponds to a minimum energy,  $E_0$ .....65

Figure 2.35. Diagram demonstrating preferential attraction of adsorbate gas molecules to the surface of the adsorbent.....66

Figure 2.36. Diagram showing the progression of the MTZ along the column as time passes.....68

Figure 2.37. The plots on the left show adsorbate loading,  $X$ , along the length,  $L$ , of the column and the plots on the right show corresponding exit adsorbate concentration,  $C$ , against time,  $t$ .....70

Figure 2.38. Two fixed bed adsorbers operating in parallel. (a) shows the “dirty” exhaust gas entering Adsorber A where the  $\text{CO}_2$  is adsorbed and “clean” gas exits the bed. Simultaneously Adsorber B is being regenerated, whereby the adsorber is heated providing the adsorbate molecules with enough energy to be released and passed on to a condensing and storage process. (b) shows that when breakthrough occurs for Adsorber A the active adsorber is switched to Adsorber B and Adsorber A is regenerated.....71

Figure 2.39. Figure showing<sup>1</sup> the tetrahedral structure of silica and alumina that make up Zeolite 13X. This structure contains consistent pore diameters of 0.1 nm. ....73

Figure 2.40. Diagram showing how the critical diameter, $d_c$ , is defined for CO <sub>2</sub> . .....	74
Figure 2.41. Diagram showing the structure of macropores, mesopores and micropores.....	74
Figure 2.42. Example of Langmuir isotherms. ....	81
Figure 3.1. Experimental set up of the fluidised bed study. The pseudo 2D fluidised bed was placed in between the two gamma camera heads and compressed air was used to fluidise the solid particles.....	90
Figure 3.2. Image data acquired for a bed height of 30 cm and feed flow rate of 2 l min <sup>-1</sup> . Each image from (a) to (d) shows a consecutive 1 second image frame from the initial introduction of <sup>81</sup> Kr <sup>m</sup> to 4 seconds into the run. ....	92
Figure 3.3. The bubble column was placed vertically between the two gamma camera heads .....	95
Figure 3.4. These images all show the same data but with different acquisition rates. (a) is 1 fps, (b) is 10 fps, (c) is 100 fps and (d) is 200 fps.....	99
Figure 3.5. Plot of counts detected against time. The peaks in event rate indicate the presence of a bubble in the FoV.....	100
Figure 3.6. (a) shows bubble 1 at y = 718 in frame 77 and (b) shows bubble 1 at y = 472 in frame 100. ....	101
Figure 3.7. The black diamonds represent detected counts per second (cps) against time (sec) for experiment 12 and a peak in counts indicate a bubble of <sup>81</sup> Kr <sup>m</sup> passing through the FoV. The exponential decay of each bubble as it passes through the FoV of the camera is shown as the blue lines.....	102
Figure 3.8. (a) shows bubble 1 circled in yellow and (b) shows bubble 2 circled in yellow. (c) is the resulting bubble after coalescence. ....	104

Figure 3.9. Axial slice through the centre of spherical glass vessel. The point of intensity at the centre of the vessel is the gas inlet pipe. This image clearly shows the star artefact inherent with FBP techniques and there is blurring at the edges as expected. The high intensity vessel walls, however, have minimal noise and provide good comparable intensity values which would differ for materials of different densities.

..... 109

Figure 3.10. The plot at the bottom of this figure is the intensity profile of the row of pixels highlighted in red across the image at the top of the figure. There are clear peaks at the walls of the glass vessel and a peak in the centre which is the gas inlet pipe.

..... 110

Figure 3.11. The image at the top shows the plastic column filled with six steel spheres. The intensity profile shows that the dense spheres have minimum activity and the highest region of activity is at the boundary between the gas and the rubber bung.

..... 111

Figure 3.12. Experimental set up of mock adsorption study. .... 114

Figure 3.13. This series of images shows the bed packed with Zeolite 13X filling with  $^{11}\text{CO}_2$  over 14 image frames where each frame contains data acquired over 45 seconds. In these images the gas is flowing from right to left. .... 116

Figure 3.14. This series of intensity profiles shows the distribution of  $^{11}\text{CO}_2$  concentration along the length of the column for the first 14 image frames. .... 117

Figure 3.15. This breakthrough curve was obtained with experimental conditions 3 MPa system pressure and 27%  $\text{CO}_2$  feed concentration. The error in  $\text{CO}_2$  concentration is  $\pm 1\%$  and the error in time is  $\pm 2.25$  minutes. This curve was used to determine optimal imaging acquisition frame duration. .... 119

Figure 4.1. Single intensity profile along z direction for 2 mm spherical particle at 90 mm measured by the ruler and 88 mm in the image data with FWHM = 10 mm. .... 122

Figure 4.2. Super imposed single pixel intensity plots for each 10 mm position..... 122

Figure 4.3. Summed intensity plot for point source with peak at 80 mm. FWHM is 10 mm ..... 125

Figure 4.4. Superimposition of all point source locations. The maximum peak height is  $5.8 \times 10^5$  counts per 30 sec at 100 mm, the minimum peak height is  $5.20 \times 10^5$  counts per 30 sec at 140 mm and the average peak height is  $5.44 \times 10^5$  counts per 30 sec. .... 126

Figure 4.5. An image of the point source at 90 mm (plane 26). This is an example of how the blurring is observable in the images. The maximum point of intensity ( $2.56 \times 10^5$  counts per 30 sec) is indicated by the dark red pixel and the range of yellow to light blue pixels show the blurring..... 128

Figure 4.6. Photo of set up for resolution test 1. The orange marker indicates the position of source 5 and the yellow marker indicates the position of source 5 (a purple line is used in the image analysis for the location of this source). .... 130

Figure 4.7. Image of resolution test 1. The position of source 1 is 200 mm on the ruler which should correspond to 156 mm in the image. The position of source 5 is at 40 mm on the ruler and should correspond to 0 mm in the image; however the point of intensity is 3 pixels from the left which equates to 6.9 mm as pixel 1 = 0 mm. The maximum intensity of source 1 at the edge of the FoV is  $\sim 1/3$  of source 5 which leads to the assumption that source 1 is just outside the FoV of the camera. .... 131

Figure 4.8. Resolution test 1: Source 1 measured at the edge of or outside the FoV (156 mm) and source 5 measured at 6.9 mm (FWHM = 10 mm). See Table 9 for separation measurements. .... 131

Figure 4.9. Photo of set up for resolution test 2. The central yellow marker indicates the position of source 4. Source 4 is a spherical source and source 5, also identified by a yellow marker, is a pellet. .... 132

Figure 4.10. Image of resolution test 2. The position of sources 1 was the same as the previous test and source 5 was moved 10 mm to 50 mm on the ruler (10 mm in the image data). Source 4 was placed between the two at 120 mm on the ruler (80 mm in the image data). The observed location of source 4 was measured to be 78 mm and the observed location of source 5 was the same as the previous measurement of 6.9 mm. .... 133

Figure 4.11. Resolution test 2: Source 1 measured at 156 mm, source 4 measured at 78 mm (FWHM = 12 mm) and source 5 measured at 6.8 mm (FWHM = 10 mm) in the z direction. See Table 9 for separation measurements. .... 133

Figure 4.12. Photo of set up for resolution test 3. The blue marker indicates the location of source 3 and the green marker indicates the location of source 2. .... 134

Figure 4.13. Image of resolution test 3. Source 1 is still positioned at 200 mm (156 mm in the image data), source 2 was positioned at 160 mm (120 mm in the image data), source 4 was still positioned at 120 mm (80 mm in the image data), source 3 was positioned at 80 mm (40 mm in the image data) and source 5 was kept at 50 mm (10 mm in the image data)..... 135

Figure 4.14. Resolution test 3: Source 1 measured at 156 mm, source 2 measured at 115 mm (FWHM = 11 mm), source 4 measured at 76 mm (FWHM = 13 mm), source 3

measured at 37 mm (FWHM = 11 mm) and source 5 measured at 7 mm (FWHM = 10 mm). Sources are separated by 30 or 40 mm which is 3 – 4 times the observable spatial resolution of the camera. See Table 9 for separation measurements. .... 135

Figure 4.15. Photo of the set up for resolution test 4. The sources have been re-ordered to 5, 4, 2, 3 and 1 and moved closer to each other, separated by 20 mm with source 1 positioned 30 mm away..... 136

Figure 4.16. Image of resolution test 4. Source 1 was moved to 170 mm (130 mm in the image data), source 2 was positioned at 140 mm (100 mm in the image data), source 3 was positioned at 120 mm (80 mm in the image data), source 4 was positioned at 100 mm (60 mm in the image data) and source 5 was moved to 80 mm (40 mm in the image data)..... 137

Figure 4.17. Resolution test 4: Source 1 measured at 126 mm (FWHM = 11 mm), source 2 measured at 97 mm (FWHM = 11 mm), source 3 measured at 77 mm (FWHM = 9 mm), source 4 measured at 57 mm (FWHM = 11 mm) and source 5 measured at 38 mm (FWHM = 10 mm). Sources are separated by 2 or 3 cm which is which is 2 – 3 times the observable spatial resolution of the camera. See Table 9 for separation measurements. .... 137

Figure 4.18. Photo of set up for resolution test 5. Similar set up to test 4 but with source 5 placed 30 mm away from the rest of the sources which are separated by 20 mm. .... 139

Figure 4.19. Image of resolution test 5. Source 1 was kept at 170 mm (130 mm in the image data), source 2 was moved to 150 mm (110 mm in the image data), source 3 was positioned at 130 mm (90 mm in the image data), source 4 was positioned at

110 mm (70 mm in the image data) and source 5 was kept at 80 mm (40 mm in the image data). ..... 139

Figure 4.20. Resolution test 5: Source 1 measured at 126 mm (FWHM = 12 mm), source 2 measured at 105 mm (FWHM = 10 mm), source 3 measured at 87 mm (FWHM = 3 mm), source 4 measured at 67 mm (FWHM = 11 mm) and source 5 measured at 38 mm (FWHM = 11 mm). Sources are separated by 2 or 3 cm which is which is 2 – 3 times the observable spatial resolution of the camera. See Table 9 for separation distance measurements..... 140

Figure 4.21. Photo of set up for resolution test 6. All five sources are spaced 10 mm apart..... 141

Figure 4.22. Image of resolution test 6. The sources were all moved so that each was separated by 10 mm. Source 1 was moved to 130 mm (90 mm in the image data), source 2 was moved to 120 mm (80 mm in the image data), source 3 was positioned at 110 mm (70 mm in the image data), source 4 was positioned at 100 mm (60 mm in the image data) and source 5 was moved to 90 mm (50 mm in the image data). ... 141

Figure 4.23. Resolution test 6: Source 1 assumed to be 85 mm, source 2 measured at 75 mm, source 3 assumed to be 67 mm, source 4 measured at 58 mm and source 5 assumed to be 47 mm. Sources are separated by 10 mm which has been determined to be equal to the spatial resolution. There are no clear peaks so FWHM and location separation could not be determined. .... 142

Figure 4.24. An image of resolution test 5 with axial profiles of the regions of blurring above (profile 1) and below (profile 2) the point sources included..... 144

Figure 4.25. A close up image of point source 2 from resolution test 5 and the corresponding intensity profile in the *y*-direction across the centre of the source.... 145

Figure 4.26. Experimental set-up for the adsorption study. ....	146
Figure 4.27. (a) is a photograph of the stainless steel adsorption column with Swagelok fittings and (b) is a diagram displaying the dimensions of the column and the adsorbent region has been highlighted. ....	148
Figure 4.28. Photo of 3 mm Zeolite 13X beads. ....	149
Figure 4.29. Photo of the 3mm to 10 mm pellets of Activated Carbon. ....	149
Figure 5.1. An example of a breakthrough curve from experimental data. The solid line shows the CO <sub>2</sub> exit flow rate (mln min <sup>-1</sup> ), the bold dashed line shows the constant CO <sub>2</sub> feed rate (mln min <sup>-1</sup> ) and the dotted lines highlight the points considered to be breakthrough (5% of feed) and saturation (95% of feed). This curve was produced using Activated Carbon at a system pressure of 1.6 MPa and CO <sub>2</sub> concentration of 30%. ....	156
Figure 5.2. Plot showing the volume of CO <sub>2</sub> that exits the bed shaded in white under the curve (mln) and the volume of CO <sub>2</sub> captured by the column is shown by the grey region about the curve (mln). ....	156
Figure 5.3. Isotherm for Activated Carbon at 292K using CO <sub>2</sub> analyser data. The Toth model has been included for comparison using parameters from Table 11. ....	159
Figure 5.4. Isotherm for Zeolite 13X at 292K using CO <sub>2</sub> analyser data. The Toth model has been included for comparison using parameters from Table 11. ....	160
Figure 5.5. Isotherm for Activated Carbon and Zeolite 13X at 292K using CO <sub>2</sub> analyser data. The Toth model has been included for comparison. ....	160
Figure 5.6. Breakthrough plots of normalised exiting CO <sub>2</sub> concentration with respect to maximum CO <sub>2</sub> concentration ( $C/C_{max}$ ) against time for Activated Carbon at total system pressure of 2.6 MPa. ....	162

Figure 5.7. Breakthrough plots of normalised exiting CO <sub>2</sub> concentration with respect to maximum CO <sub>2</sub> concentration ( $C/C_{max}$ ) against time for Activated Carbon at total system pressure of 1.6 MPa. ....	162
Figure 5.8. Breakthrough plots of normalised exiting CO <sub>2</sub> concentration with respect to maximum CO <sub>2</sub> concentration ( $C/C_{max}$ ) against time for Zeolite 13X at total system pressure of 2.6 MPa (10% CO <sub>2</sub> concentration at 3.1 MPa) .....	163
Figure 5.9. Breakthrough plots of normalised exiting CO <sub>2</sub> concentration with respect to maximum CO <sub>2</sub> concentration ( $C/C_{max}$ ) against time for Zeolite 13X at total system pressure of 1.6 MPa. ....	163
Figure 5.10. Two runs at different pressure but the same CO <sub>2</sub> feed concentration of 10% for Activated Carbon. ....	166
Figure 5.11. Two runs at different pressure but the same CO <sub>2</sub> feed concentration of 10% for Zeolite 13X. ....	166
Figure 5.12. Two runs with similar CO <sub>2</sub> partial pressure (~0.8 MPa) but different CO <sub>2</sub> feed concentrations for Activated Carbon. ....	167
Figure 5.13. Two runs with similar CO <sub>2</sub> partial pressure (~0.8 MPa) but different CO <sub>2</sub> feed concentrations for Zeolite 13X. ....	167
Figure 5.14 The image at the top of this figure shows the position of the adsorption column in the FoV. The ends of the column are packed with glass beads and the middle section contains the adsorbent (Activated Carbon in this example). The red dashed line through the centre of the column defines the pixels used to make the intensity profile at the bottom of the figure. The intensity is measured in counts per minute (cpm) and is a direct indication of the concentration of <sup>11</sup> CO <sub>2</sub> . This image shows the column 20 minutes into the experiment at $P_{sys} = 1.6$ MPa and $C_{max} = 10\%$ . ....	169

Figure 5.15. The adsorption column at 100 minutes into the same experiment illustrated in Figure 5.14. By this point the column is at full saturation. The smearing at the ends of the column which are clearly seen in the intensity profile at the bottom of the figure is due to axial smoothing in the reconstruction technique (section 2.5.2 and 2.10.2). ..... 169

Figure 5.16 Figure showing how the breakthrough curves are created from the same image data as Figure 5.14. To make the curves comparable to the CO<sub>2</sub> analyser data information was taken from the outlet of the adsorbent region. The total cpm for each pixel in the transverse slice at plane 40 (z = 140 mm), indicated by the dashed red line, was summed for each time frame. The resulting breakthrough curve is shown in the plot at the bottom of this figure. .... 170

Figure 5.17. The original image data is subject to noise, particularly for long imaging sessions due to the decay of the radioisotope and hence a reduction in count rate, so a 10 point rolling ball average was applied to the breakthrough curves to smooth the data. This plot shows the same breakthrough data as Figure 5.16. The plot of residuals shows a relatively large difference between the original image data and smoothed data in the breakthrough region and a fairly even distribution at saturation. .... 172

Figure 5.18. The region highlighted in grey is the area within the standard deviation of the smoothed image data and shows the possible variation between maximum captured CO<sub>2</sub> volume and the minimum. .... 173

Figure 5.19. Isotherm created using image data and CO<sub>2</sub> analyser data for Activated Carbon at 292 K. .... 174

Figure 5.20. Isotherm created using image data and CO<sub>2</sub> analyser data for Zeolite 13X at 292 K. .... 174

Figure 5.21. Breakthrough plots of normalised exiting CO <sub>2</sub> concentration with respect to maximum CO <sub>2</sub> concentration ( $C/C_{max}$ ) against time for Activated Carbon at total system pressure of 2.6 MPa using smoothed image data. ....	176
Figure 5.22. Breakthrough plots of normalised exiting CO <sub>2</sub> concentration with respect to maximum CO <sub>2</sub> concentration ( $C/C_{max}$ ) against time for Activated Carbon at total system pressure of 1.6 MPa using smoothed image data. ....	177
Figure 5.23. A comparison between breakthrough curves for Activated Carbon produced using image data and CO <sub>2</sub> analyser data with corresponding calculated capacities. The experimental conditions were system pressure of 2.6 MPa and CO <sub>2</sub> concentration of 50%. ....	179
Figure 5.24. A comparison between breakthrough curves for Activated Carbon produced using image data and CO <sub>2</sub> analyser data with corresponding calculated capacities. The experimental conditions were system pressure of 2.6 MPa and CO <sub>2</sub> concentration of 30%. ....	180
Figure 5.25. A comparison between breakthrough curves for Activated Carbon produced using image data and CO <sub>2</sub> analyser data with corresponding calculated capacities. The experimental conditions were system pressure of 2.6 MPa and CO <sub>2</sub> concentration of 10%. ....	180
Figure 5.26. Times to breakthrough and saturation calculated from image data and CO <sub>2</sub> analyser data for system pressure of 2.6 MPa using Activated Carbon. The results have been plotted against each other to clarify similarities between the two measurement techniques and a linear LSF has been applied ( $m = 1.04$ , $\sigma_m = 0.09$ , $c = 0.47$ and $\sigma_c = 5.23$ ). ....	181

Figure 5.27. A comparison between breakthrough curves for Activated Carbon produced using image data and CO<sub>2</sub> analyser data with corresponding calculated capacities. The experimental conditions were system pressure of 1.6 MPa and CO<sub>2</sub> concentration of 50%..... 182

Figure 5.28. A comparison between breakthrough curves for Activated Carbon produced using image data and CO<sub>2</sub> analyser data with corresponding calculated capacities. The experimental conditions were system pressure of 1.6 MPa and CO<sub>2</sub> concentration of 30%..... 183

Figure 5.29. A comparison between breakthrough curves for Activated Carbon produced using image data and CO<sub>2</sub> analyser data with corresponding calculated capacities. The experimental conditions were system pressure of 1.6 MPa and CO<sub>2</sub> concentration of 10%..... 183

Figure 5.30. Times to breakthrough and saturation calculated from image data and CO<sub>2</sub> analyser data for system pressure of 1.6 MPa using Activated Carbon. The results have been plotted against each other to clarify similarities between the two measurement techniques and a linear LSF has been applied ( $m = 0.97$ ,  $\sigma_m = 0.1$ ,  $c = 2.25$  and  $\sigma_c = 4.16$ )..... 184

Figure 5.31. Breakthrough plots of normalised exiting CO<sub>2</sub> concentration (calculated using cpm) with respect to maximum CO<sub>2</sub> concentration ( $C/C_{max}$ ) against time for Zeolite 13X at total system pressure of 2.6 MPa using smoothed image data (10% CO<sub>2</sub> concentration at 3.1 MPa). ..... 186

Figure 5.32. Breakthrough plots of normalised exiting CO<sub>2</sub> concentration (calculated using cpm) with respect to maximum CO<sub>2</sub> concentration ( $C/C_{max}$ ) against time for Zeolite 13X at total system pressure of 1.6 MPa using smoothed image data. .... 186

Figure 5.33. A comparison between breakthrough curves produced for Zeolite 13X using image data and CO<sub>2</sub> analyser data with corresponding calculated capacities. The experimental conditions were system pressure of 2.6 MPa and CO<sub>2</sub> concentration of 50%. ..... 188

Figure 5.34. A comparison between breakthrough curves for Zeolite 13X produced using image data and CO<sub>2</sub> analyser data with corresponding calculated capacities. The experimental conditions were system pressure of 2.6 MPa and CO<sub>2</sub> concentration of 30%. ..... 188

Figure 5.35. A comparison between breakthrough curves for Zeolite 13X produced using image data and CO<sub>2</sub> analyser data with corresponding calculated capacities. The experimental conditions were system pressure of 3.1 MPa and CO<sub>2</sub> concentration of 10%. ..... 189

Figure 5.36. Times to breakthrough and saturation calculated from image data and CO<sub>2</sub> analyser data for system pressure of 2.6 MPa (10% CO<sub>2</sub> concentration at 3.1 MPa) using Zeolite 13X. The results have been plotted against each other to clarify similarities between the two measurement technique and a linear LSF has been applied ( $m = 1.28$ ,  $\sigma_m = 0.07$ ,  $c = -17.45$  and  $\sigma_c = 5.23$ ). ..... 190

Figure 5.37. A comparison between breakthrough curves for Zeolite 13X produced using image data and CO<sub>2</sub> analyser data with corresponding calculated capacities. The experimental conditions were system pressure of 1.6 MPa and CO<sub>2</sub> concentration of 50%. ..... 191

Figure 5.38. A comparison between breakthrough curves for Zeolite 13X produced using image data and CO<sub>2</sub> analyser data with corresponding calculated capacities. The

experimental conditions were system pressure of 1.6 MPa and CO<sub>2</sub> concentration of 30%. ..... 191

Figure 5.39. A comparison between breakthrough curves for Zeolite 13X produced using image data and CO<sub>2</sub> analyser data with corresponding calculated capacities. The experimental conditions were system pressure of 1.6 MPa and CO<sub>2</sub> concentration of 10%. ..... 192

Figure 5.40. Times to breakthrough and calculated from image data and CO<sub>2</sub> analyser data for system pressure of 1.6 MPa using Zeolite 13X. The results have been plotted against each other to clarify similarities between the two measurement techniques and a linear LSF has been applied ( $m = 1.23$ ,  $\sigma_m = 0.07$ ,  $c = -4.38$  and  $\sigma_c = 3.85$ ). ..... 192

Figure 5.41. 2D slice showing how the concentration profiles were created using the image data. The number of counts for each pixel across each plane for each time frame were summed to create an array of  $S_{n=1}$  to  $S_{n=47}$  where  $n$  is plane number. This example was created using data from experimental conditions 10% CO<sub>2</sub> at system pressure 1.6 MPa for adsorbent Activated Carbon at 20 minutes into the experiment. .... 197

Figure 5.42. Progressive intensity profiles along the adsorption column for each minute of the experiment. Data acquired for the first minute after the removal of noise is shown as dark blue and the final image frame is red. The dashed black lines indicate the location of the start and end of the adsorbent region ..... 199

Figure 5.43 Intensity profiles for Zeolite 13X at a system pressure of 1.6 MPa and CO<sub>2</sub> feed concentration of 10%. The lines ranging from blue to red are representative of concentration profiles from the first image frame to the last. The concentration profiles are close together which implies a slow progression of the MTZ through the bed. .202

Figure 5.44. Intensity profiles for Zeolite 13X at a system pressure of 2.6 MPa and CO<sub>2</sub> feed concentration of 50%. The lines ranging from blue to red are representative of concentration profiles from the first image frame to the last. These profiles are spaced apart indication a fast moving MTZ. ....202

Figure 5.45. Intensity profiles for Activated Carbon at 1.6 MPa and 30% feed concentration.....203

Figure 5.46. Figure showing how the velocity of the adsorption front was calculated for experimental conditions 10% CO<sub>2</sub> feed concentration and system pressure 1.6 MPa for Zeolite 13X. The time at which the intensity reaches a specified threshold (3/4, 1/2 and 1/3 of the maximum) has been marked by a \* and was recorded.....204

Figure 5.47. Distance against time to show the progression of the adsorption front along the bed using different intensities as the leading point of the front. The linear least squares fit has been included, the gradient of which is the apparent velocity. This plot shows data obtained for 1.6 MPa 10% CO<sub>2</sub> using Zeolite 13X.....205

Figure 5.48. Distance against time plots for Activated Carbon at 2.6 MPa for 50%, 30% and 10% CO<sub>2</sub> feed concentrations. The linear least squares fits used to calculate the velocity have been included to show linearity and the time scale has been kept consistent for all plots for easy comparison.....207

Figure 5.49. Distance against time plots for Activated Carbon at 1.6 MPa for 50%, 30% and 10% CO<sub>2</sub> feed concentrations. The linear least squares fits used to calculate the velocity have been included to show linearity.....208

Figure 5.50. Distance against time plots for Zeolite 13X at 2.6 MPa for 50%, 30% and 10% CO<sub>2</sub> feed concentrations. The linear least squares fits used to calculate the velocity have been included to show linearity.....208

Figure 5.51. Distance against time plots for Zeolite 13X at 1.6 MPa for 50%, 30% and 10% CO<sub>2</sub> feed concentrations. The linear least squares fits used to calculate the velocity have been included to show linearity.....209

Figure 5.52. Calculated velocity of the adsorption front against corresponding CO<sub>2</sub> feed concentration for system pressures 1.6 MPa and 2.6 MPa for Activated Carbon....211

Figure 5.53. Calculated velocity of the adsorption front against corresponding CO<sub>2</sub> feed concentration for system pressures 1.6 MPa and 2.6 MPa for Activated Carbon. The similarity between these plots implies very little effect of pressure .....212

Figure 5.54. Cross sectional slice at plane 35 for Zeolite 13X at  $P_{sys} = 1.6$  MPa and  $C_{max} = 10\%$  at nine minute intervals. Time = 1 min is the time at which <sup>11</sup>CO<sub>2</sub> is initially detected in the plane and the final image is a time at which the plane in question has reached its maximum intensity meaning it is saturated. ....213

Figure 5.55. The left hand side of this figure shows intensity profiles across the column at the central slice (plane 25) of the adsorbent region from and the right hand side shows the increasing intensity average against time. This figure is for Activated Carbon at 1.6 MPa with CO<sub>2</sub> feed concentration of 10%. ....215

Figure 5.56. The left hand side of this figure shows intensity profiles across the column at the central slice (plane 35) of the adsorbent region from and the right hand side shows the increasing intensity average against time. This figure is for Zeolite 13X at 1.6 MPa with CO<sub>2</sub> feed concentration of 10%. ....215

Figure 5.57. Plot of increasing amount of CO<sub>2</sub> accumulating in the central plane with time for Activated Carbon at 2.6 MPa for feed concentrations 50%, 30% and 10%. The calculated velocities of the adsorption front have been included in the legend to help

determine a relationship. These plots were produced normalising the average plane intensity with respect to equilibrium capacity of each run. ....	216
Figure 5.58. Plot of increasing amount of CO <sub>2</sub> accumulating in the central plane with time for Activated Carbon at 1.6 MPa for feed concentrations 50%, 30% and 10%. The calculated velocities of the adsorption front have been included in the legend to help determine a relationship. These plots were produced normalising the average plane intensity with respect to equilibrium capacity of each run. ....	216
Figure 5.59. Plot of increasing amount of CO <sub>2</sub> accumulating in the central plane with time for Zeolite 13X at 2.6 MPa for feed concentrations 50%, 30% and 10% (system pressure 3.1 MPa for 10% feed concentration). The calculated velocities of the adsorption front have been included in the legend to help determine a relationship. These plots were produced normalising the average plane intensity with respect to equilibrium capacity of each run. ....	217
Figure 5.60. Plot of increasing CO <sub>2</sub> concentration in the central plane with time for Zeolite 13X at 1.6 MPa for feed concentrations 50%, 30% and 10%. The calculated velocities of the adsorption front have been included in the legend to help determine a relationship. These plots were produced normalising the average plane intensity with respect to equilibrium capacity of each run. ....	217
Figure 5.61. Rate of increasing CO <sub>2</sub> loading for the central slice (plane 25) of Activated Carbon at 2.6 MPa. ....	218
Figure 5.62. Rate of increasing CO <sub>2</sub> loading for the central slice (plane 25) of Activated Carbon at 1.6 MPa. ....	219
Figure 5.63. Rate of increasing CO <sub>2</sub> loading for the central slice (plane 25) of Zeolite 13X at 2.6 MPa (10% feed concentration at 3.1 MPa). ....	219

Figure 5.64. Rate of increasing CO <sub>2</sub> loading for the central slice (plane 25) of Zeolite 13X at 1.6 MPa.....	220
Figure 5.65. Plot of rate of increasing CO <sub>2</sub> capacity against the velocity of the adsorption front for Activated Carbon and Zeolite 13X. A linear LSF has been included to show the relationship between the two rates.....	222
Figure 5.66. Plot of normalised concentration against time for the non linear region of the CO <sub>2</sub> accumulation at a specific point for Activated Carbon at 2.6 MPa. ....	223
Figure 5.67. Plot of normalised concentration against time for the non linear region of the CO <sub>2</sub> accumulation at a specific point for Activated Carbon at 1.6 MPa. ....	224
Figure 5.68. Plot of normalised concentration against time for the non linear region of the CO <sub>2</sub> accumulation at a specific point for Zeolite 13X at 2.6 MPa (3.1 MPa for 10% feed concentration).....	224
Figure 5.69. Plot of normalised concentration against time for the non linear region of the CO <sub>2</sub> accumulation at a specific point for Zeolite 13X at 1.6 MPa. ....	225
Figure 5.70. Percent saturation of Activated Carbon at 2.6 MPa for feed concentrations 50%, 30% and 10% from top to bottom at 20 minutes into the experiment. The plot at the bottom of the figure shows a percent saturation profile along the column. The distributions for $C_{max} = 50%$ and 30% show a minimum of 40% saturation for the length of the adsorbent region implying a MTZ that is longer than the bed. The distribution for $C_{max} = 10%$ shows low saturation percentage at the exit of the bed implying a smaller MTZ.....	227
Figure 5.71. Percent saturation of Activated Carbon at 1.6 MPa for feed concentrations 50%, 30% and 10% from top to bottom at 20 minutes into the experiment. The plot at the bottom of the figure shows a percent saturation profile along the column. The	

distributions for  $C_{max} = 50\%$  and  $30\%$  show a minimum saturation of about  $35\%$  at the exit of the adsorbent region implying a MTZ that is longer than the bed. The distribution for  $C_{max} = 10\%$  shows low saturation percentage at the exit of the bed implying a smaller MTZ. The saturation percentage at the inlet of the column is high at  $95\%$ . 228

Figure 5.72. Percent saturation of Zeolite 13X at 2.6 MPa for feed concentrations 50%, 30% and 10% ( $P_{sys} = 3.1$  MPa for  $C_{max} = 10\%$ ) from top to bottom at 20 minutes into the experiment. The plot at the bottom of the figure shows a percent saturation profile along the column. All of the distributions plateau at a maximum of  $75\%$  saturation and each distribution shows a clear step down from  $75\%$  saturation to background level indicating a clear and relatively small MTZ.....229

Figure 5.73. Percent saturation of Zeolite 13X at 1.6 MPa for feed concentrations 50%, 30% and 10% from top to bottom at 20 minutes into the experiment. The plot at the bottom of the figure shows a percent saturation profile along the column. The profiles for 10% and 50% feed concentration have a maximum of  $80\%$  saturation at the inlet of the column. Unusually the profile for 30% feed concentration shows a higher percentage saturation of about  $90\%$  at the inlet which is expected to be due to considerable dead time correction for this data set. ....230

Figure 5.74. Occupancy plots with superimposed calculated MTZ for Activated Carbon at 2.6 MPa for 50% feed concentration. The calculated MTZ length is 104 mm (30 planes) which is 25 mm longer than the length of the adsorbent region and the adsorption front velocity is  $5.78 \text{ mm min}^{-1}$ . ....234

Figure 5.75. Occupancy plots with superimposed calculated MTZ for Activated Carbon at 2.6 MPa for 30% feed concentration. The calculated MTZ length is 78 mm (23

planes) which is about the same length as the adsorbent region and the adsorption front velocity is 4.90 mm min <sup>-1</sup> .....	235
Figure 5.76. Occupancy plots with superimposed calculated MTZ for Activated Carbon at 2.6 MPa for 10% feed concentration. The calculated MTZ length is 39 mm (11 planes) which is about half the length of the adsorbent region and the adsorption front velocity is 2.62 mm min <sup>-1</sup> .....	236
Figure 5.77. Occupancy plots with superimposed calculated MTZ for Activated Carbon at 1.6 MPa for 50% feed concentration. The calculated MTZ length is 92 mm (27 planes) which is 13 mm longer than the adsorbent region and the adsorption front velocity is 5.40 mm min <sup>-1</sup> .....	237
Figure 5.78. Occupancy plots with superimposed calculated MTZ for Activated Carbon at 1.6 MPa for 30% feed concentration. The calculated MTZ length is 74 mm (22 planes) which is 4 mm longer than the adsorbent region and the adsorption front velocity is 4.14 mm min <sup>-1</sup> .....	238
Figure 5.79. Occupancy plots with superimposed calculated MTZ for Activated Carbon at 1.6 MPa for 10% feed concentration. The calculated MTZ length is 58 mm (14 planes) which is about 83% of the length of the adsorbent region and the adsorption front velocity is 3.05 mm min <sup>-1</sup> .....	239
Figure 5.80. Occupancy plots with superimposed calculated MTZ for Zeolite 13X at 2.6 MPa for 50% feed concentration. The calculated MTZ length is 40 mm (11 planes) which is about 57% of the adsorption region and the adsorbent front velocity is 3.05 mm min <sup>-1</sup> .....	240
Figure 5.81. Occupancy plots with superimposed calculated MTZ for Zeolite 13X at 2.6 MPa for 30% feed concentration. The calculated MTZ length is 26 mm (7 planes) which	

is about 37% of the adsorbent region and the adsorption front velocity is 2.32 mm min <sup>-1</sup> . .....	241
Figure 5.82. Occupancy plots with superimposed calculated MTZ for Zeolite 13X at 3.1 MPa for 10% feed concentration. The calculated MTZ length is 16 mm (5 planes) which is about 23% of the adsorbent region and the adsorption front velocity is 0.78 mm min <sup>-1</sup> . .....	242
Figure 5.83. Occupancy plots with superimposed calculated MTZ for Zeolite 13X at 1.6 MPa for 50% feed concentration. The calculated MTZ length is 68 mm (20 planes) which is about the same length of the adsorbent region (70 mm) and the adsorption front velocity is 5.95 mm min <sup>-1</sup> . .....	243
Figure 5.84. Occupancy plots with superimposed calculated MTZ for Zeolite 13X at 1.6 MPa for 30% feed concentration. The calculated MTZ length is 35 mm (10 planes) which is half the length of the adsorbent region and the adsorption front velocity is 2.07 mm min <sup>-1</sup> . .....	244
Figure 5.85. Occupancy plots with superimposed calculated MTZ for Zeolite 13X at 1.6 MPa for 30% feed concentration. The calculated MTZ length is 27 mm (9 planes) which is about 39% of the adsorbent region and the adsorption front velocity is 0.71 mm min <sup>-1</sup> . .....	245
Figure 8.1. Intensity profiles along the adsorption column for Activated Carbon at 2.6 MPa and 50% CO <sub>2</sub> feed concentration.....	272
Figure 8.2. Intensity profiles along the adsorption column for Activated Carbon at 2.6 MPa and 30% CO <sub>2</sub> feed concentration.....	272
Figure 8.3. Intensity profiles along the adsorption column for Activated Carbon at 2.6 MPa and 10% CO <sub>2</sub> feed concentration.....	273

Figure 8.4. Intensity profiles along the adsorption column for Activated Carbon at 1.6 MPa and 50% CO <sub>2</sub> feed concentration. ....	273
Figure 8.5. Intensity profiles along the adsorption column for Activated Carbon at 1.6 MPa and 30% CO <sub>2</sub> feed concentration. ....	274
Figure 8.6. Intensity profiles along the adsorption column for Activated Carbon at 1.6 MPa and 10% CO <sub>2</sub> feed concentration. ....	274
Figure 8.7. Intensity profiles along the adsorption column for Zeolite 13X at 2.6 MPa and 50% CO <sub>2</sub> feed concentration. ....	275
Figure 8.8. Intensity profiles along the adsorption column for Zeolite 13X at 2.6 MPa and 30% CO <sub>2</sub> feed concentration. ....	275
Figure 8.9. Intensity profiles along the adsorption column for Zeolite 13X at 3.1 MPa and 10% CO <sub>2</sub> feed concentration. ....	276
Figure 8.10. Intensity profiles along the adsorption column for Zeolite 13X at 1.6 MPa and 50% CO <sub>2</sub> feed concentration. ....	276
Figure 8.11. Intensity profiles along the adsorption column for Zeolite 13X at 1.6 MPa and 30% CO <sub>2</sub> feed concentration. ....	277
Figure 8.12. Intensity profiles along the adsorption column for Zeolite 13X at 1.6 MPa and 10% CO <sub>2</sub> feed concentration. ....	277
Figure 8.13. Intensity profiles across the adsorption column at plane 25 for Activated Carbon at 2.6 MPa and 50% CO <sub>2</sub> feed concentration and corresponding plot of average intensity per minute. ....	278
Figure 8.14. Intensity profiles across the adsorption column at plane 25 for Activated Carbon at 2.6 MPa and 30% CO <sub>2</sub> feed concentration and corresponding plot of average intensity per minute. ....	278

Figure 8.15. Intensity profiles across the adsorption column at plane 25 for Activated Carbon at 2.6 MPa and 10% CO <sub>2</sub> feed concentration and corresponding plot of average intensity per minute. ....	279
Figure 8.16. Intensity profiles across the adsorption column at plane 25 for Activated Carbon at 1.6 MPa and 50% CO <sub>2</sub> feed concentration and corresponding plot of average intensity per minute. ....	279
Figure 8.17. Intensity profiles across the adsorption column at plane 25 for Activated Carbon at 1.6 MPa and 30% CO <sub>2</sub> feed concentration and corresponding plot of average intensity per minute. ....	280
Figure 8.18. Intensity profiles across the adsorption column at plane 25 for Activated Carbon at 1.6 MPa and 10% CO <sub>2</sub> feed concentration and corresponding plot of average intensity per minute. ....	280
Figure 8.19. Intensity profiles across the adsorption column at plane 35 for Zeolite 13X at 2.6 MPa and 50% CO <sub>2</sub> feed concentration and corresponding plot of average intensity per minute. ....	281
Figure 8.20. Intensity profiles across the adsorption column at plane 35 for Zeolite 13X at 2.6 MPa and 30% CO <sub>2</sub> feed concentration and corresponding plot of average intensity per minute. ....	281
Figure 8.21. Intensity profiles across the adsorption column at plane 35 for Zeolite 13X at 3.1 MPa and 10% CO <sub>2</sub> feed concentration and corresponding plot of average intensity per minute. ....	282
Figure 8.22. Intensity profiles across the adsorption column at plane 35 for Zeolite 13X at 1.6 MPa and 50% CO <sub>2</sub> feed concentration and corresponding plot of average intensity per minute. ....	282

Figure 8.23. Intensity profiles across the adsorption column at plane 35 for Zeolite 13X at 1.6 MPa and 30% CO<sub>2</sub> feed concentration and corresponding plot of average intensity per minute. ....283

Figure 8.24. Intensity profiles across the adsorption column at plane 35 for Zeolite 13X at 1.6 MPa and 10% CO<sub>2</sub> feed concentration and corresponding plot of average intensity per minute. ....283

## LIST OF TABLES

Table 1. Experimental conditions of the bubble column study including initial generator activity, generator age, generator activity at time of use and feed flow rate. ....	97
Table 2. Table containing the relative difference in pixel intensity, mean pixel density and total intensity of the image frame for 1, 10, 100 and 200 fps. ....	98
Table 3. This table shows relative cross-sectional area, pixel intensity, pixel density and velocity of bubble 1, 2 and the resulting combined bubble. ....	105
Table 4. The object combinations that were imaged for the steady state PET study are defined here. ....	107
Table 5. A comparison between the actual dimensions of the vessels and media and the measurements obtained from the image data. Also included is the relative intensity of events detected and gas-solid interfaces and the densities of the solids. ....	112
Table 6. Maximum peak height and FWHM for the irradiated particle for 10 mm increments along the FoV for the single pixel intensity profiles across the particle. ....	123
Table 7. Maximum peak height and FWHM for the irradiated particle for 10 mm increments along the FoV for the cross-sectional summation intensity profiles across the particle. ....	127
Table 8. Point source specifications for resolution test. ....	130
Table 9. Set and measured separation distances between point sources. ....	143
Table 10. Table describing the desired experimental conditions used for each adsorption run. ....	152
Table 11. Parameters of the Toth equation for Activated Carbon and Zeolite 13X. ....	158
Table 12. Calculated time to breakthrough, $t_{bt}$ , and saturation, $t_{sat}$ , for experimental data measured using the CO <sub>2</sub> analyser. The capacity of the column at $t_{bt}$ , $q_{bt}$ , and at $t_{sat}$ , $q_{sat}$	

has been included and the percentage of saturation capacity at breakthrough is given.

..... 164

Table 13. Calculated time to breakthrough,  $t_{bt}$ , and saturation,  $t_{sat}$ , for image data. The capacity of the column at  $t_{bt}$ ,  $q_{bt}$ , and at  $t_{sat}$ ,  $q_{sat}$  has been included and the percentage of saturation capacity at breakthrough is given. .... 193

Table 14. Comparison between CO<sub>2</sub> analyser data and image data for time to breakthrough, time to saturation and percentage of total saturated capacity adsorbed at breakthrough. .... 195

Table 15. Comparison of calculated adsorption front velocities using 3/4 max, 1/2 max and 1/3 max as points of reference ..... 206

Table 16. Calculated adsorption front velocities ..... 210

Table 17. Calculated linear rate of CO<sub>2</sub> loading at the central slice of each adsorbent. The calculated adsorption front velocities have been included for comparison. .... 220

Table 18. Table showing calculated length of MTZ from the duration of linear accumulation and adsorption front velocity. .... 222

Table 19. Correction factors for CO<sub>2</sub> Mass Flow Controller..... 271

# NOMENCLATURE

## GENERAL NOMENCLATURE

$A$	Activity	Bq
$A_0$	initial activity	Bq
$d$	Distance	m
$R$	Universal gas constant (8.314 JK <sup>-1</sup> mol <sup>-1</sup> )	J K <sup>-1</sup> mol <sup>-1</sup>
$T$	Temperature	K
$t$	Time	min
$t_{1/2}$	Half-life	s
$V$	Volume	m <sup>3</sup>
$\lambda$	Decay constant	
$\rho$	Density	kg m <sup>-3</sup>

## IMAGING

$B$	Butterworth filter	Hz
$f_m$	Cut-off frequency	Hz
$G$	Gaussian filter	Hz
$H$	Hanning filter	Hz
$H_R$	Ramp filter	Hz
$n$	Order parameter for Butterworth filter	-
$P_\theta$	Projection for angle $\theta$	°
$r$	Perpendicular distance between LOR and origin	m
$\theta$	Angle of LOR	°
$\sigma$	Standard deviation of Gaussian distribution	-

## FLUIDISED BED

$A$	Cross sectional area of bed	m <sup>2</sup>
$D_p$	Diameter of solid particles	m
$f_p$	Friction factor of solid particles	-
$L$	Bed length	m

$L_0$	Length of bed before fluidisation	m
$L_f$	Length of bed at minimum fluidisation	m
$Q$	Volumetric flow rate	ml min <sup>-1</sup>
$Re$	Reynolds number	-
$V_s$	Superficial velocity	m s <sup>-1</sup>
$\Delta p$	Pressure drop	Pa
$\varepsilon$	Void fraction of bed	-

## BUBBLE COLUMN

$d_b$	Bubble diameter	m
$D_C$	Column diameter	m
$g$	Gravitational constant (9.81 m s <sup>-2</sup> )	m s <sup>-2</sup>
$\nu_L$	Liquid viscosity	m <sup>2</sup> s <sup>-1</sup>
$V_{sg}$	Superficial gas velocity	m s <sup>-1</sup>
$\rho_L$	Liquid density	kg m <sup>-3</sup>
$\sigma$	Surface tension	N m <sup>-1</sup>

## ADSORPTION

$A_i$	Toth parameter relating to thermal variation	-
$b$	Affinity constant	kPa
$B_i$	Toth parameter relating to thermal variation	K <sup>-1</sup>
$C_{max}$	Equilibrium/feed concentration of CO <sub>2</sub>	%
$C_t$	Concentration at time t	%
$C_{T0}$	Heterogeneity parameter	-
$d_c$	critical diameter of a molecule	m
$D_e$	intraparticle diffusion coefficient	m <sup>2</sup> s <sup>-1</sup>
$d_p$	adsorbate particle diameter	m
$E$	Potential energy	eV
$E_0$	minimum potential energy	eV
$E_a$	Attractive energy when describing Van der Waals interaction, Activation energy when discussing desorption	eV
$EF_{CO_2}$	Exit fraction of CO <sub>2</sub>	-
$E_k$	Kinetic energy	eV
$E_R$	Repulsive energy	eV

$F$	net force	N
$F_A$	Attractive Force	N
$FF_{CO_2}$	Feed fraction of CO <sub>2</sub>	-
$F_R$	Repulsive force	N
$k_B$	Boltzmann's constant	J K <sup>-1</sup>
$K_d$	Desorption rate constant	mol m <sup>-2</sup> s <sup>-1</sup>
$K_{d^\infty}$	Desorption rate constant at infinite temperature	mol m <sup>-2</sup> s <sup>-1</sup>
$k_{eff}$	intraparticle mass transfer coefficient	m s <sup>-1</sup>
$k_{ext}$	external mass transfer coefficient	m s <sup>-1</sup>
$K_i$	Adsorption constant for component $i$	Pa <sup>-1</sup>
$K_i^0$	Infinite adsorption constant	Pa <sup>-1</sup>
$k_{int}$	internal mass transfer coefficient	m s <sup>-1</sup>
$M$	Molar mass of substance	g mol <sup>-1</sup>
$\dot{m}$	Mass flow rate	kg s <sup>-1</sup>
$m_{ad}$	Mass of adsorbent	kg
$M_{CO_2}$	Molar mass of CO <sub>2</sub> (44.01 g mol <sup>-1</sup> )	g mol <sup>-1</sup>
$m_{CO_2ad}$	Mass of adsorbed CO <sub>2</sub>	kg
$M_{N_2}$	Molar mass of N <sub>2</sub>	g mol <sup>-1</sup>
$n$	molecular density	m <sup>-3</sup>
$n_{ad}$	Amount of CO <sub>2</sub> adsorbed	mol
$n_{CO_2}$	Amount of CO <sub>2</sub>	mol
$n_{N_2}$	Amount of N <sub>2</sub>	mol
$n_{tot}$	Total amount of a substance	mol
$P'$	Pressure of 'normal' conditions (101, 325 Pa)	Pa
$P_{CO_2}$	Partial pressure of CO <sub>2</sub>	Pa
$P_{N_2}$	Partial pressure of N <sub>2</sub>	Pa
$P_{sys}$	System pressure	Pa
$Q$	Volumetric flow rate	m <sup>3</sup> s <sup>-1</sup>
$Q'_{CO_2}$	Normal feed flow rate of CO <sub>2</sub> (at 1 atm and 0° C)	mln min <sup>-1</sup>
$Q'_{CO_2exit}$	Normal exit flow rate of CO <sub>2</sub> (at 1 atm and 0° C)	mln min <sup>-1</sup>
$Q'_{N_2}$	Normal flow rate of N <sub>2</sub> (at 1 atm and 0° C)	mln min <sup>-1</sup>
$Q'_{N_2exit}$	Normal exit rate of N <sub>2</sub> (at 1 atm and 0° C)	mln min <sup>-1</sup>
$q_0$	initial capacity	mol kg <sup>-1</sup>
$q_{bt}$	Capacity at breakthrough	mol kg <sup>-1</sup>
$Q_{CO_2exit}$	Exit volumetric flow rate of CO <sub>2</sub>	m <sup>3</sup> s <sup>-1</sup>

$q_i$	Capacity of component $i$	$\text{mol kg}^{-1}$
$q_m$	equilibrium capacity	$\text{mol kg}^{-1}$
$q_{sat}$	Capacity at saturation	$\text{mol kg}^{-1}$
$r$	radius of adsorbent bead	m
$R_a$	Rate of adsorption	$\text{mol m}^{-2} \text{s}^{-1}$
$R_d$	Rate of desorption	$\text{mol m}^{-2} \text{s}^{-1}$
$T'$	Temperature of 'normal' conditions (273.15 K)	K
$t_0$	Start time	min
$t_{bt}$	Time to breakthrough	min
$t_{max}$	End time	min
$t_{sat}$	Time to saturation	min
$V$	Total volume of gas	$\text{m}^3$
$\bar{v}$	average molecular velocity	$\text{m s}^{-1}$
$V_{CO2ad}$	Volume of adsorbed $\text{CO}_2$	$\text{m}^3$
$V_{CO2out}$	Volume of non-adsorbed $\text{CO}_2$	$\text{m}^3$
$V_{N2}$	Partial volume of $\text{CO}_2$	$\text{m}^3$
$V_{N2}$	Partial volume of $\text{N}_2$	$\text{m}^3$
$\bar{V}_{N2}$	Partial normal volume of $\text{CO}_2$ (at 1 atm and $0^\circ \text{C}$ )	$\text{m}^3$
$\bar{V}_{N2}$	Partial normal volume of $\text{N}_2$ (at 1 atm and $0^\circ \text{C}$ )	$\text{m}^3$
$x$	interatomic separation	m
$x_0$	equilibrium interatomic separation	m
$\alpha$	sticking coefficient	-
$\theta$	Fractional surface coverage	-
$\theta$	fractional surface coverage	-
$\sigma_q$	Capacity uncertainty	$\text{mol kg}^{-1}$
$\sigma_t$	Time uncertainty	min
$T_a$	Residence time of adsorption	s
$T_{d\infty}$	Adatom period of thermal vibration	s
$\Phi$	Impingement rate	$\text{m}^{-2} \text{s}^{-1}$

## ACRONYMS

CCS	Carbon Capture and Storage
CDR	Collimator-Detector Response
CFD	Computational Fluid Dynamics
CMC	Carboxymethyl Cellulose
ECG	Electrocardiogram
ECT	Electrical Capacitance Tomography
FBP	Filtered Backprojection
FoV	Field of View
FWHM	Full-Width at Half Maximum
LDF	Linear Driving Force
LLD	Lower Limit of Detection
LOR	Line of Response
LSF	Least-Squares Fit
ML-EM	Maximum-Likelihood Expectation-Maximization
MTZ	Mass Transfer Zone
OS-EM	Ordered Subset Expectation Maximization
PEPT	Positron Emission Particle Tracking
PET	Positron Emission Tomography
PMT	Photo-Multiplier Tube
PSA	Pressure Swing Adsorption
PSF	Point Spread Function
SOP	Standard Operating Procedure
SPECT	Single Photon Emission Computed Tomography
TSA	Temperature Swing Adsorption
ULD	Upper Limit of Detection

# 1 INTRODUCTION

## 1.1 BACKGROUND

The development and use of functional medical imaging has grown rapidly in importance over the last few decades. The field of medicine relies on imaging to aid the diagnosis and treatment of many diseases and ailments. As the technology behind medical imaging is improved the number of applications it can be used for increases. As it stands nuclear imaging is primarily used for the non-invasive study of physiological processes within the human body but these techniques designed for clinical applications have been developed and adapted for industrial use. At the University of Birmingham the Positron Imaging Centre has the equivalent of four Positron Emission Tomography (PET) cameras and one Single Photon Emission Computed Tomography (SPECT) camera which has been adapted for Positron Emission Particle Tracking (PEPT) (Parker et al. 2008). Over the last twenty years a considerable research effort had been made into the study of flow and mixing in solid and liquid systems using nuclear imaging techniques at the University of Birmingham and the development of PEPT has made it possible to study multi-phase flow within industrial processes. However, despite capability, little work has been reported on producing and imaging gases for industrial use. It was decided to adapt and utilise the functional medical imaging techniques available at Birmingham for the study of chemical flow processes. It has been proposed that a technique capable of observing a process within a system with no external interference would provide a deeper understanding of the process allowing improvements to be developed for the system and a greater theoretical understanding of such gas transport processes.

Nuclear imaging techniques have been developed to evaluate chemical processes within multiphase systems, such as fluidised beds and bubble column reactors. SPECT has been proven to be a promising means of exploring the structure and distributions of solid and liquid phases within these multiphase systems (Mesquita et al. 2012; Barth et al. 2013). Likewise, a limited number of studies have utilised PET for the study of fluidised beds (Dechsiri et al. 2005) and fluid flow within porous rock samples (Ferno et al. 2015) but it has not been possible to discover published work using a radioactive gas as a tracer for industrial processes. The work presented in this thesis provides an initial feasibility study which compares the capabilities of SPECT and PET for imaging dynamic gas flows in a gas fluidised bed, a bubble column and a low pressure adsorption column leading to a more detailed study of CO<sub>2</sub> adsorption in a high pressure adsorption column.

Gas fluidised beds are a result of passing a gas through a bed of solid particles and are used as multiphase reactors (McCabe et al. 1993a). At sufficient gas velocity known as the minimum fluidisation velocity,  $u_{mf}$ , the particles become suspended in the gas phase resulting in fluid-like behaviour. Bubble column reactors are also multiphase reactors, but unlike gas fluidised beds the gas is passed through a liquid instead of a bed of solid particles. A bubble column reactor is typically a vertical cylindrical vessel containing a liquid or liquid-solid suspension (Kantarci et al. 2005). Gas is introduced to the bottom of the column forming bubbles which pass up through the liquid.

Gas adsorption is a technique that can separate specific gas molecules from a mixture via preferential attraction to the surface of a solid (McCabe et al. 1993b). Gas molecules diffuse to the surface of the solid where they are held by weak inter-

molecular forces and the magnitude of the attractive force for different molecules dictates the degree and efficiency of the separation process.

For these gaseous systems the aim of this thesis is investigating measurement techniques which can be used to better quantify system behaviour and lead to improved theoretical understanding.

## **1.2 AIMS AND OBJECTIVES**

The overall aim of the work presented here was to develop a radioactive gas imaging technique capable of studying chemical flow processes. By imaging a well known chemical process and comparing the obtained image data to results obtained using a commonly used measurement technique the capabilities of the imaging technique can be well defined. This would verify the practicality of the imaging technique and lead to a standard imaging and data analysis protocol to be implemented for the study of processes that are less well understood. The steps followed to achieve this aim were: 1). Preliminary studies to test the temporal and spatial resolutions of the SPECT and PET cameras available at the University of Birmingham and to determine the practicality of adapting these techniques for industrial use, 2). The development of a Standard Operating Procedure (SOP) for the dynamic imaging of a gaseous flow process and for image results analysis, 3). The calibration of the imaging technique to be used, and 4). The application of the developed imaging technique to the study of a well known chemical process for verification and discussion.

## **1.3 LAYOUT OF THESIS**

This thesis is comprised of six chapters. The first chapter provides an outline of the background of the project and describes the main aims and objectives of the work.

The second chapter is a critical review of the literature relevant to the theory of the imaging techniques used, SPECT and PET and the processes imaged. The history and physics of the imaging techniques are explained and the common applications in medicine are discussed. The review of theory is followed by a general description of current applications of the imaging techniques in industry and their potential indicated by existing studies. The general theory of the multiphase processes which are studied through the course of the project is also explained in the literature review including a description of their applications in industry.

The third chapter presents the preliminary studies performed to investigate SPECT and PET for applicability in flow process imaging. The spatial and temporal resolutions of both techniques have been investigated and the practicality of experimental design and radioactive gas availability is discussed. A comparison between the two techniques is made and a conclusion to utilise PET for the study of CO<sub>2</sub> adsorption in a pressurised adsorption column is drawn.

The materials and methods chapter is fourth. The initial sensitivity and spatial resolution calibration tests are presented in this chapter and the experimental method is explained including a description of the equipment used.

The fifth chapter contains the results of the adsorption column study and has been split into two main sections. The first section is a comparison between breakthrough data obtained using a CO<sub>2</sub> analyser and the PET image data for verification of the imaging technique. The second section describes the detailed information about the process within the column that is provided by PET and a qualitative study of the adsorption kinetics inside the column is provided.

The final chapter summarises the main finding of each section and draws a final conclusion with respect to the aims and objectives of the project. The potential of the imaging technique for future studies is discussed and recommendations in experimental design and imaging protocol are made.

## **2 LITERATURE REVIEW**

### **2.1 INTRODUCTION**

This literature review explains and summarises the imaging techniques used for this project, Single Photon Emission Computed Tomography (SPECT) and Positron Emission Tomography (PET). The common applications of these techniques and their potential for industrial studies have been discussed and the availability and production of various radiotracers is included.

These imaging techniques were used to perform brief feasibility measurements on a fluidised bed and a bubble column, therefore a review of the theory of these multiphase flow processes has been provided to give the reader sound understanding of the resulting image data. Also included in the literature review is a more in depth explanation of adsorption as this is the chemical flow process that has been studied to test the capabilities of using gas imaging systems as a practical measurement technique.

### **2.2 GLOBAL CONSIDERATIONS**

A number of terms which will be referred to throughout the thesis are defined here.

When imaging techniques are discussed an important factor to consider is the spatial resolution of the system. The spatial resolution of an imaging system is defined by the minimum separation distance between two point sources required to identify them as two individual points (Prekeges 2011d). The resolution is generally expressed as the full width at half maximum (FWHM) of the peak intensity of a point source, therefore it

is necessary to separate two points by at least one FWHM otherwise they will appear as one, somewhat blurred, point as depicted in Figure 2.1.

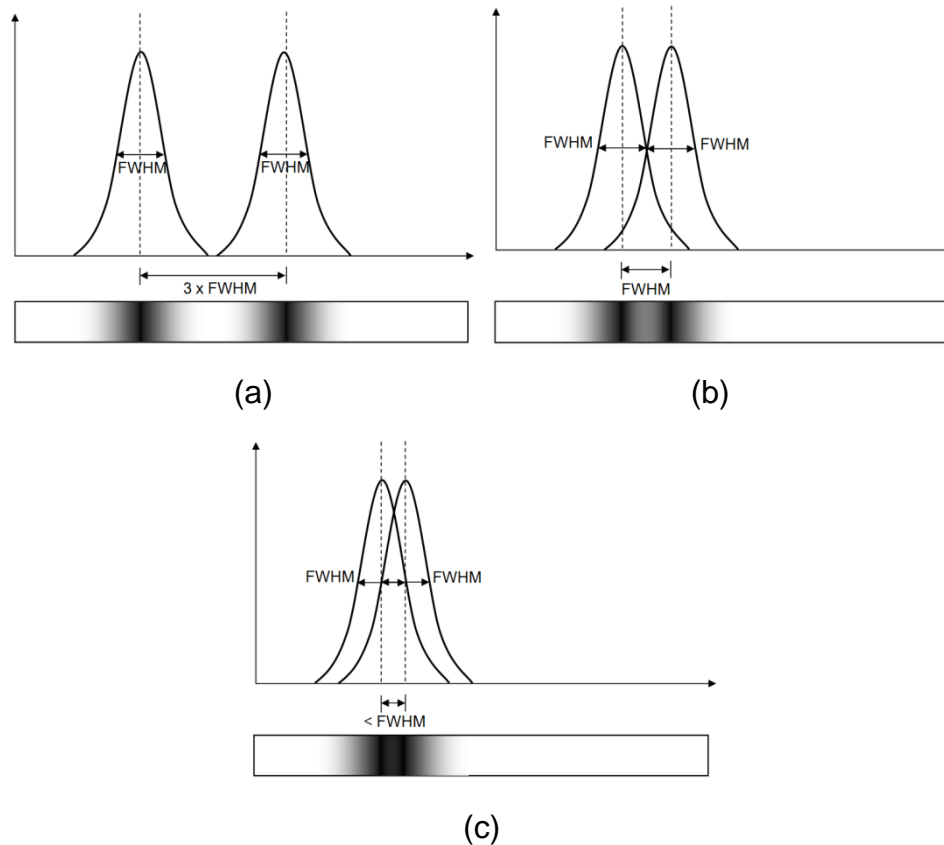


**Figure 2.1. (a) Shows the projected intensity profiles of two point sources placed three times their FWHM apart. The bar underneath the profiles shows a visual representation of the point sources. (b) Shows the sources placed one FWHM apart. The visual representation shows that it is possible to distinguish the two sources but there is an element of blurring in between them. (c) Shows the two sources less than one FWHM apart. The two sources are now indistinguishable.**

Two more terms used to describe the performance of an imaging system are sensitivity and efficiency. The term sensitivity refers to the ratio of the source activity and the number of emissions detected by the imaging system (Biersack & Freeman 2007).

Efficiency defines the proportion of emissions that are detected and converted into useful signals.

Temporal resolution is a term used to describe the length of time required to acquire enough emission information to produce a statistically meaningful observation, thus there is a trade off between spatial and temporal resolution (Rahmim & Zaidi 2008). For dynamic systems an optimal ratio between having an acquisition frame long enough to gain sufficient information and short enough to have the sample rate of the process being imaged as high as practicably possible must be determined.

The dead time of an imaging system is defined as the minimum amount of time required between two detection events to distinguish them as separate events (Gupta 2013). For scintillation crystals, the material used in detectors for SPECT and PET, the dead time is primarily dependent on the decay time of the scintillation crystal. A detection occurs when a gamma ray hits a scintillation crystal and deposits its kinetic energy into an electron which then scintillates, meaning it re-emits the deposited energy in the form of light. The decay time of a scintillation crystal is defined as the length of time it takes for the energy of the emission to drop to  $e^{-1}$  of its maximum. The dead time of the scintillation crystal is dominated by a 'pile-up' within the crystal, which is to say the background level of light from too great a number of scintillations becomes too high to distinguish separate flashes of light. This results in some events not being processed by the detector system when the activity of the radioactive source is too high (Mazoyer et al. 1985).

Finally, when discussing image planes the standard terms used for medical imaging have generally been used in this thesis as these are the definitions provided by the

imaging equipment manufacturers. Figure 2.2 shows the plane definitions used for clinical purposes and these terms have been adopted for discussing the imaging results presented in this work. The transverse plane is a cross-sectional slice through the narrowest part of the object, the sagittal plane is a slice through the length of the object that splits left from right and is referred to as the axial plane in this thesis and finally the coronal plane is also a slice through the length of the object but this plane splits front from back.

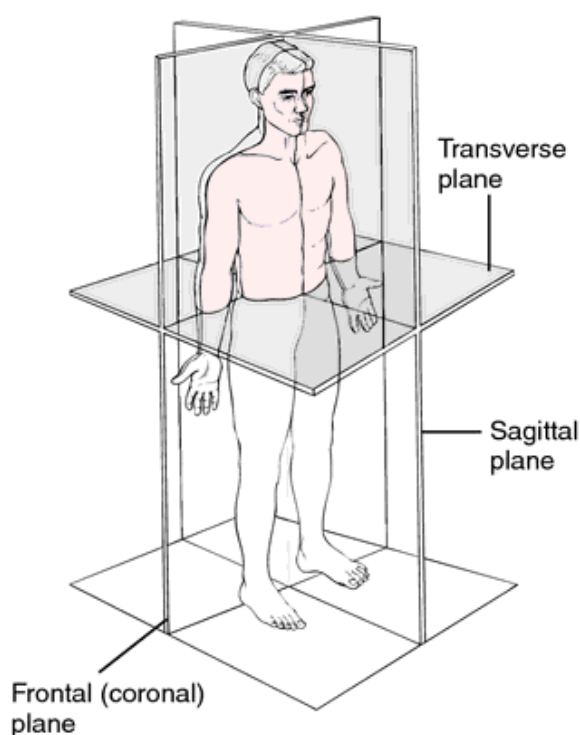


**Figure 2.2. This image<sup>1</sup> defines the terms used when discussing image planes.**

---

<sup>1</sup> <http://medical-dictionary.thefreedictionary.com/plane> (accessed: Aug 2015)

## **2.3 SINGLE PHOTON EMISSION COMPUTED TOMOGRAPHY (SPECT)**

### **2.3.1 Introduction**

Single Photon Emission Computed Tomography (SPECT) is a nuclear imaging technique that was originally developed over 50 years ago by Kuhl & Edwards (1963). The progression of the SPECT technique has been propelled by the medical field as a relatively simple and fast technique for diagnostic imaging and is able to provide 3D images of the internal structure and processes of a patient in a non-invasive manner (Jaszczak 2006). The following sections explain the theory of SPECT and the equipment available for gamma imaging at the University of Birmingham.

### **2.3.2 Theory of SPECT**

SPECT imaging is performed using a gamma camera to detect photons emitted by a radioactive isotope undergoing gamma decay. These detections provide a series of 2D images for multiple angles around the gamma source and a tomographic reconstruction algorithm may then be applied to produce a 3D image. Provided the angular sampling is sufficient slices of the 3D image in the axial, sagittal and coronal plane may be extracted and manipulated to gain information, however this is complex and requires high computational power so is it common for 2D images to be used for diagnosis (Lyra 2009).

The next section explains the theory of data acquisition and processing followed by a section discussing spatial resolution.

#### ***2.3.2.1 Data acquisition and processing***

A gamma camera generally comprises two detectors mounted onto a gantry. The detectors are often set to be parallel or at 90° to each other and are able to rotate

around the object to be imaged. A diagram showing the configuration of a gamma-ray detector system is shown in Figure 2.3. The gamma-ray detector is made of a single flat plane scintillation crystal or multiple smaller scintillation crystals. The type of crystal most commonly used is thallium doped sodium iodide (NaI (TI)) because it has very high light output (Prekeges 2011c). When a gamma ray enters the scintillation crystal it will interact with the molecules via either photo-electric absorption or Compton scattering if it has energy below 1 MeV. These interactions create fast electrons which travel through the crystal and excite a large number of electrons from the valence to the conduction band. The de-excitation via activator sites leads to visible photons which can be detected via a Photo- Multiplier Tubes (PMTs) (Anger 1958). The light pulse location circuit determines the co-ordinates of the location of the gamma-ray

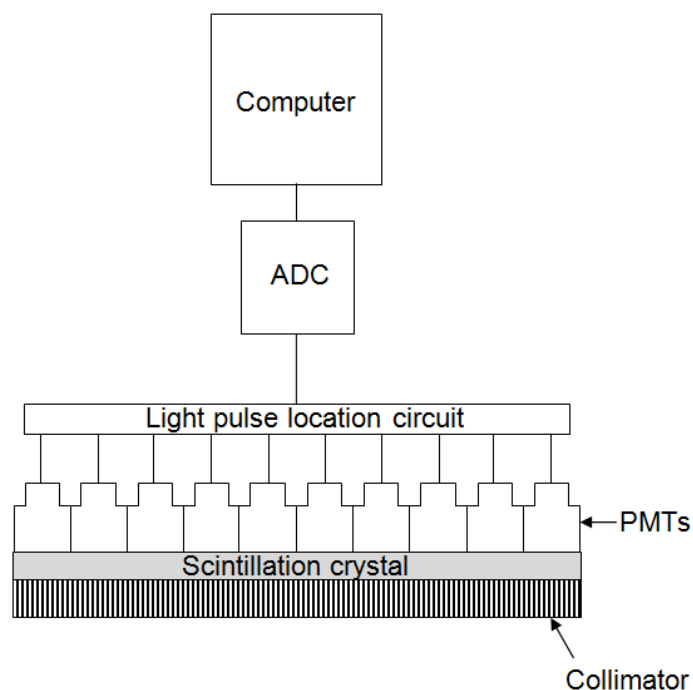


**Figure 2.3. Configuration of a gamma-ray detector system.**

detection from the scintillation crystal because each PMT will have detected varying intensity of light depending on the proximity. The closer the PMT is to the gamma ray detection the larger the resulting current is that is produced by the PMT. The PMT intensity distribution is determined in  $x$  and  $y$  co-ordinates for the crystal plane for each gamma-ray detection and the centroid, i.e. the location of the detection, is determined to within the intrinsic spatial resolution of the detector and PMT system. Each PMT is connected to an analogue to digital converter so that a computer can record the image data.

The system or object to be imaged is placed in between the two gamma camera heads with collimators attached. Collimators provide a means of obtaining spatial information about the gamma emissions from the gamma emission source (Prekeges 2011a) and are explained in more detail in the following section.

### ***2.3.2.2 Collimators and spatial resolution***

If a uniform gamma source, which is emitting gamma-rays at all angles, was placed next to a gamma-ray detector then the entire detector will detect emissions with no useful spatial information about the source. This allows a highly sensitive measurement of total radioisotope concentration in the FoV of the gamma camera as a large proportion of emissions will be detected, which may be useful for investigations such as kidney function where the only information needed is the efficiency of flushing the radioisotope through the system. Figure 2.4 (a) shows a uniform gamma source smaller than the dimensions of the detector. If this source is placed in the centre of the detectors' Field of View (FoV) then the resulting image would have high intensity in the centre which decreases towards the edge following the inverse square law as shown

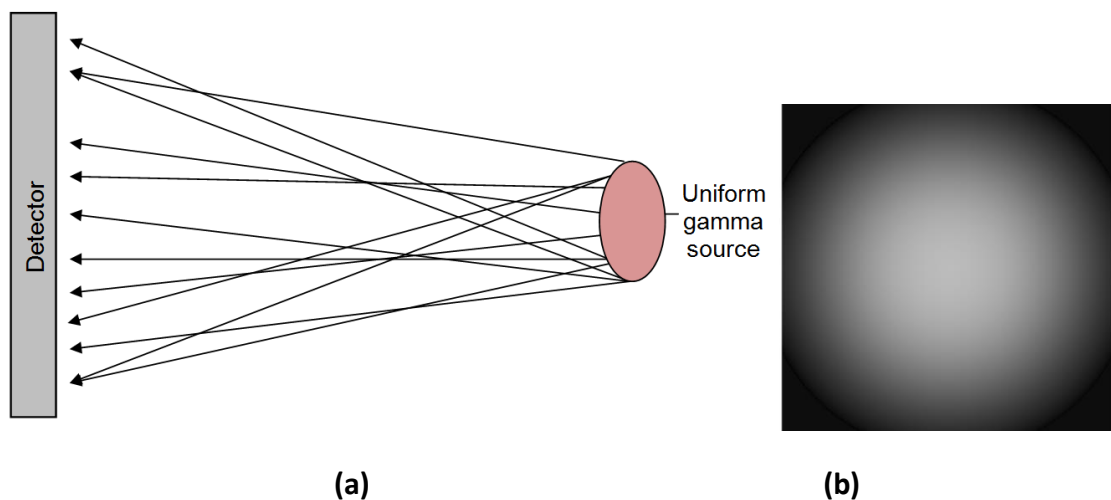


**Figure 2.4. (a) Shows a diagram of gamma-rays being emitted from a uniform source and hitting the detector at all angles. Without a means of correlating the emissions to a point of origin the image produced would fill the FoV of the detector with a maximum intensity in the centre with reducing intensity following the inverse square law towards the edge of the FoV as shown in (b).**

in Figure 2.4 (b). It is not possible to distinguish from the resulting image any spatial information about the object and there is effectively no spatial resolution, so in order to form a useful image of the distribution of a gamma emitting isotope a method to correlate the detected emissions to their point of origin is required. This section explains how spatial information is gained from a radioactive distribution and how the resolution is defined.

In order to link a gamma-ray detection to its point of emission a collimator is required. The function of a collimator is to restrict the gamma-rays which are absorbed by the scintillation crystal so that each detection can be correlated to a specific location of emission. A typical collimator is a lead sheet a few centimetres thick with a regular pattern of thousands of precisely aligned holes through it.

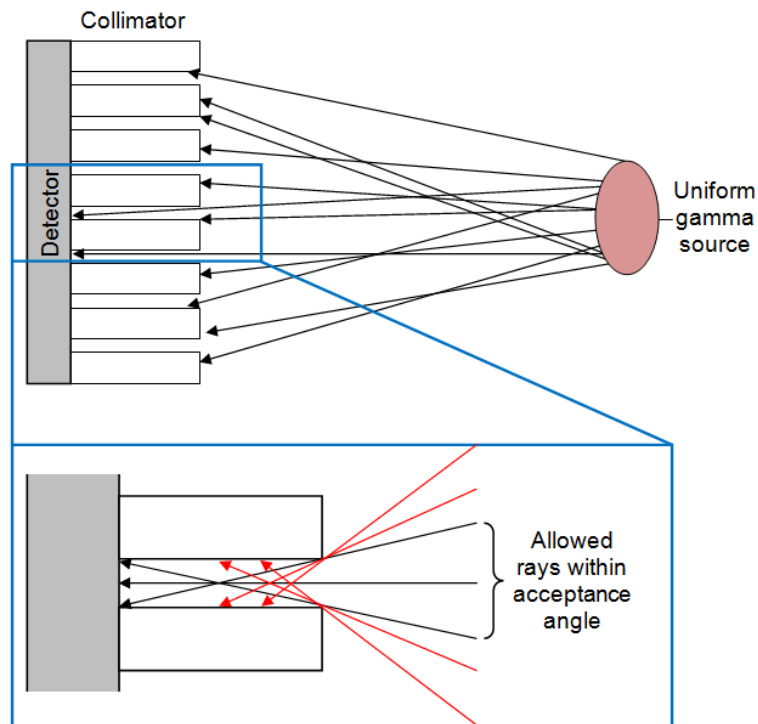


**Figure 2.5. Cross-sectional view of a collimator placed between the gamma-source and detector. The black arrows at the bottom of the figure show the range of rays within the acceptance angle that reach the detector and the red arrows indicate examples of rays that approach at an angle greater than the acceptance angle so are absorbed by the septa.**

Although a gamma source emits photons at all angles only the photons with a trajectory parallel to the alignment of the collimator holes will reach the detector. Lead is used to make the collimators because it has a high atomic number ( $Z = 82$ ) and density ( $11.3 \text{ g cm}^{-3}$ ) meaning that any photons that hit the walls (septa) between the collimator holes will be absorbed (Kahlil 2011), as shown in Figure 2.5. The close-up diagram at the bottom of the figure shows the range of emitted rays that pass through the collimator unimpeded as black arrows. The parameter that limits this range is the acceptance angle and is dependent on collimator thickness and hole diameter. These factors influence the spatial resolution and are explained in more detail later on. Some

examples of rays that approach the detector at an angle greater than the acceptance angle are indicated by red arrows and it is shown that ideally they are absorbed before reaching the detector. This means that the line of trajectory of each detected photon is known (within an error given by the acceptance angle). There are a number of different types of collimators that are used in clinical applications, most commonly parallel-hole, pin-hole, diverging and converging (Prekeges 2011a). Figure 2.6 is a photograph of a parallel-hole collimator commonly used for clinical purposes. It is about 2 – 3 cm thick and the diameter of the holes is in the order of 1 – 2 millimetres. The parallel-hole collimator allows only photons that are emitted perpendicular to the

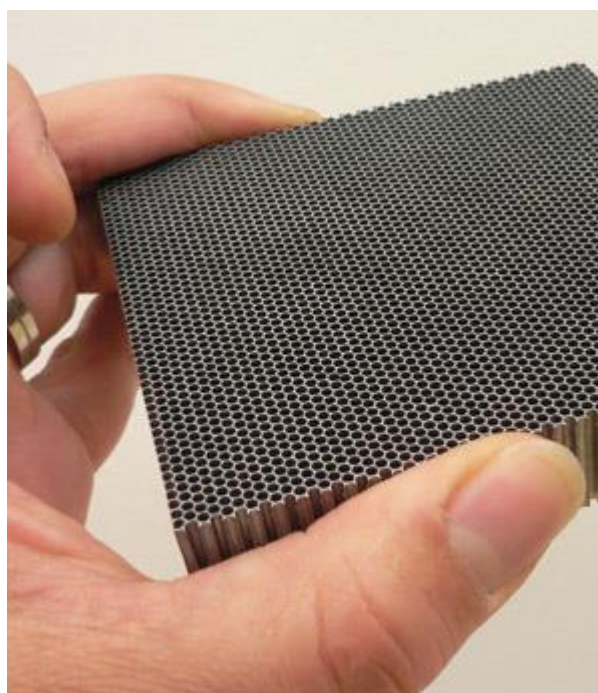


**Figure 2.6. Photograph of a parallel-hole collimator<sup>1</sup>. Collimators are made of lead and contain thousands of small holes a few centimetres long and define the emission trajectory of a detected photon.**

---

<sup>1</sup> <http://www.nuclearfields.com/collimators-nuclear-medicine.htm> (accessed: Aug 2015)

detector to be absorbed providing a one-to-one geometric mapping of the gamma source distribution. Figure 2.7 shows how the different types of collimators are used to provide useful spatial information. A pinhole collimator consists of a large hollow lead cone with a small hole a few millimetres in diameter (3-7 mm) at the narrow end. This collimator is used to magnify the object by a factor dependent on the distance between the cone hole and detector and the distance between the object and the hole. The resulting magnified image is inverted and must be corrected or accounted for in image analysis. The converging collimator also magnifies the image as the diameters of the

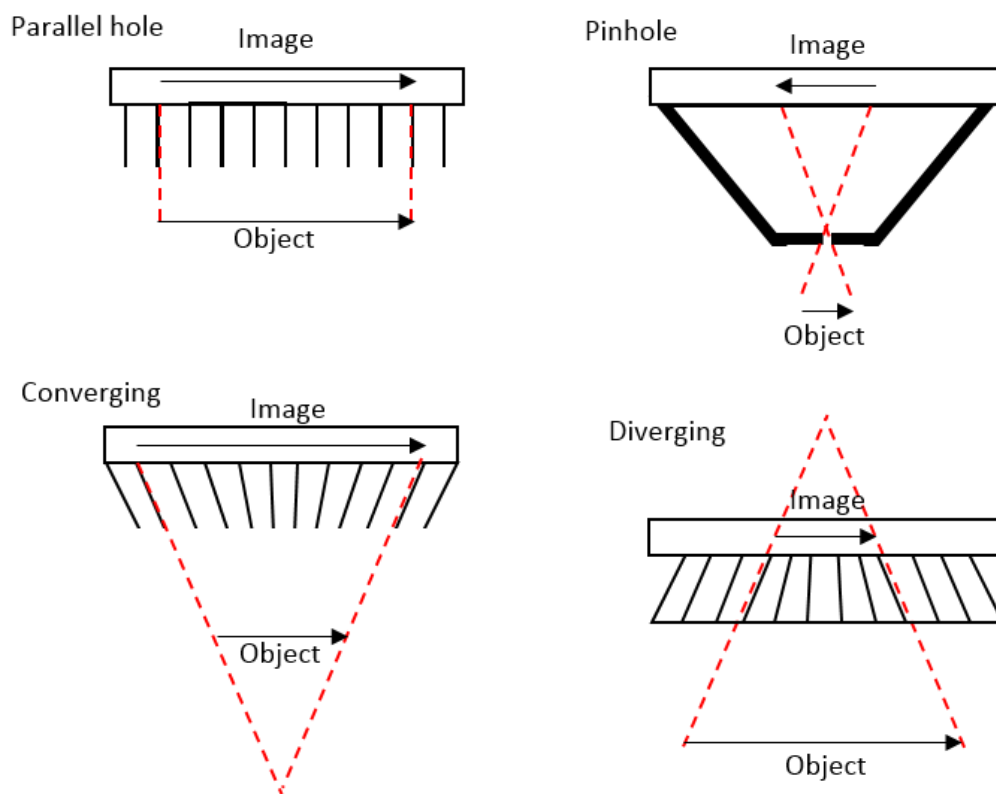


**Figure 2.7. Diagram showing the structure of parallel hole, pinhole, converging and diverging collimators and their corresponding mapping ratio. Parallel hole collimators provide a direct one-to-one mapping of the radioactive distribution. Pinhole collimators magnify and invert the image of the object, converging collimators magnify the image and diverging collimations minify the image.**

collimator holes on the side closest to the object are smaller than the side closest to the detector. One main difference between the pinhole and converging collimator for practical use is that the FoV of the detector increases as the object is moved away with the pinhole but decreases with the converging collimator. Finally the diverging collimator minifies the image of the object as the holes of the collimator are narrower at the side closest to the detector. This allows imaging of objects that are larger than the detector as the diverging collimator provides an increased FoV.

As mentioned previously a number of factors affect the ability of the collimators to provide useful spatial information about the object. For simplicity the parallel hole collimator will be discussed here as an example of the limiting parameters of the collimators. Figure 2.8 shows an array of diagrams depicting how the collimator hole diameter, hole length and distance between the object and detector affects the spatial resolution of the detector system for a point source. Figure 2.8 (a) shows the distance between the object and collimator denoted by  $d$  and the projected image diameter of the point source is shown as  $P$ . Figure 2.8 (b) shows that if the collimator hole diameters are increased then the  $P$  is also increased, indicating larger spatial resolution, thus a degraded image. Figure 2.8 (c) shows the point source located at twice the distance from the collimator. Again, this results in a larger  $P$ , thus degraded spatial resolution compared to that of (a). Figure 2.8 (d) shows longer collimator hole length. This decreases the angle of acceptance producing a smaller projected image diameter which indicates an improved spatial resolution.

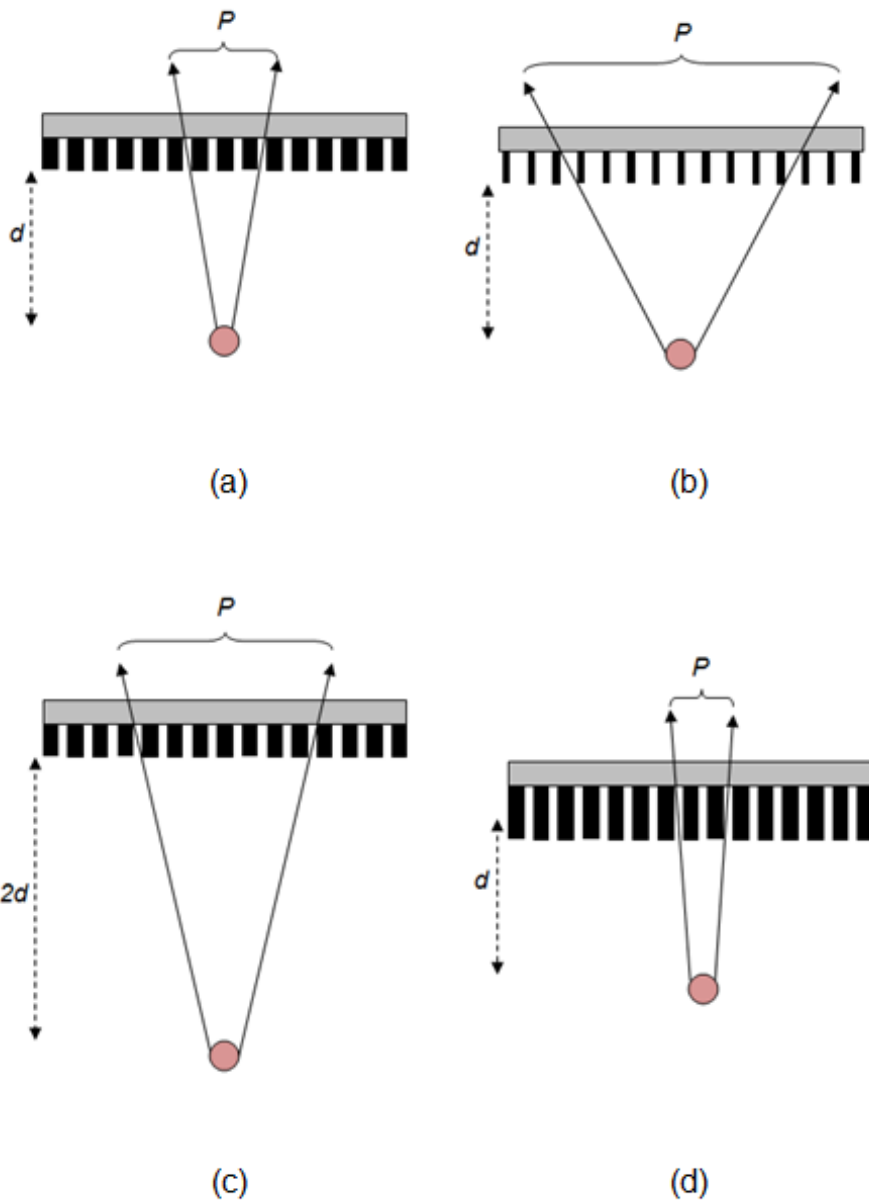
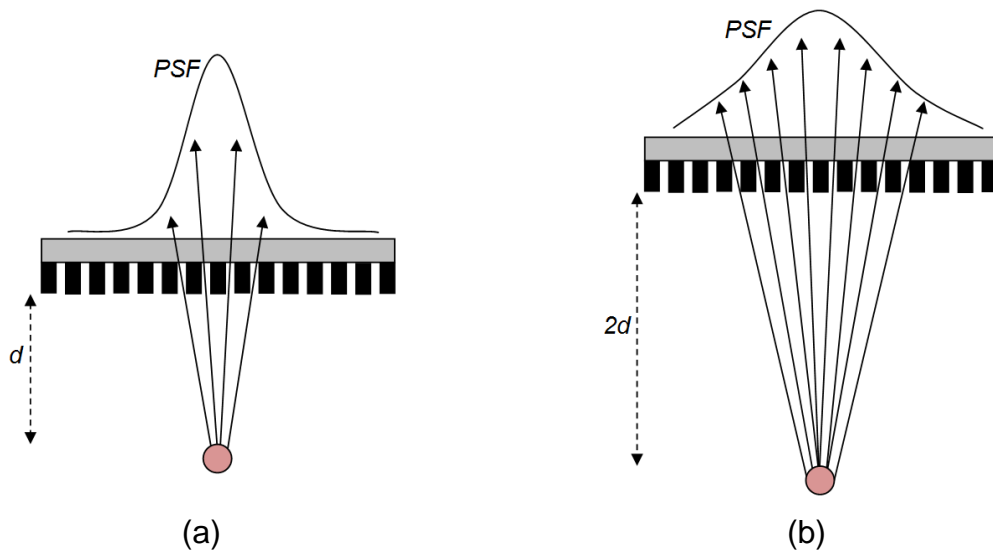


Figure 2.8. (a) Shows a point source located at distance  $d$  from the collimator.  $P$  indicated the projected diameter of the point source as detected by the crystal. (b) Shows increased collimator hole diameter which increase the size of  $P$  and results in a larger spatial resolution. (c) Shows the point source located twice the distance from the collimator, which also results in larger  $P$  and degraded spatial resolution. Finally (d) shows a decreased  $P$  with an increased collimator hole length. This results in improved spatial resolution.



**Figure 2.9. Diagram depicting how the Point Spread Function (PSF) of the projected image of a point source is formed. (a) Shows that if the source is placed close to the detector the LSF shows a higher intensity peak and less spreading compared to (b) where the source distance from the detector is doubled.**

Now it is understood how the projected image diameter is affected by the design parameters of a collimator and the placement of the object in the FoV the intensity profile of the projection will be discussed. The Intensity profile is a product of the Collimator-Detector Response (CDR) which is dependent on the geometry of the object-detector set up and the septal penetration and scatter of the collimator (Liu & Farncombe 2007). For high energy emitted gamma rays the thickness of the septa will not be adequate to absorb all rays that approach at an angle greater than the acceptance angle. A fraction of the rays will be able to penetrate the septa, and this loss of intensity is dependent on the distance travelled through the lead septa. There will also be some scatter as photons hit the septa and reflect back with reduced energy. Some of the scattered photons will reach the detector.

Figure 2.9 demonstrates the effect of the distance between the point source and the collimator combined with the penetration and scatter of the septa. The result is a point spread function (PSF) which approximately follows a Gaussian distribution with maximum intensity in the centre where photons hit the detector without being attenuated and decreasing intensity to the diameter of the projected image (Sorenson & Phelps 1977). From Figure 2.9 it is observed that by placing the point source close to the camera the intensity peak is large and the spread is reasonably small. This is due to approaching photon trajectories greater than the acceptance angle needing to penetrate a reasonably large total lead thickness to reach the camera. This results in a large proportion of photons being absorbed by the septa. By moving the source further away from the detector a large projected diameter as shown in Figure 2.8 (c) is obtained. The intensity of the PSF is reduced as a smaller proportion of photons will reach the detector as shown in Figure 2.10.

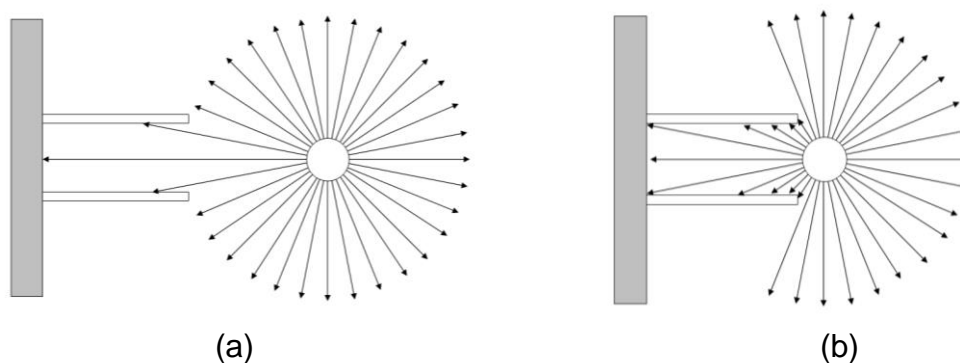


**Figure 2.10. (a) Shows a point source emitting gamma-rays radially. In this example only the ray parallel to the collimator septa reaches the detector. (b) Shows the same point source moved closer to the collimator where a higher proportion of gamma-rays reach the detector.**

The resulting combination of the CDR and intrinsic detector system resolution determines the absolute spatial resolution of the system. The full width at half maximum (FWHM) of the resulting Gaussian distribution is the spatial resolution and as explained in section 2.2 this is the minimum separation between two points for them to be distinguishable.

From the theory presented here it is observed that by reducing the diameter of the collimator holes the location of the emission source can be determined more accurately as the acceptance angle is smaller, decreasing  $P$  and improving the spatial resolution. However this introduces the concept of decreased sensitivity with improved spatial resolution as the number of photons able to reach the detector is decreased. This results in a trade-off between acquiring enough information to make a statistically meaningful observation and having spatial resolution small enough to create a useful image within the resolution limits of the detector (Rahmim & Zaidi 2008). If a collimator were to have infinite collimation, meaning only the gamma-rays that were emitted in parallel to the collimation would reach the detector, then this would mean that the exact location of the emission, and therefore the source, would be known. However, the number of emissions that would be parallel to the collimation would be incredibly small and as the collimation  $\rightarrow \infty$  the length of time required to make a statistically meaningful observation  $\rightarrow \infty$ . Realistically, of course, it is not possible to have a collimator with infinite collimation and the improved spatial resolution will be limited by the intrinsic resolution of the detector system rendering infinite collimation ineffective. An optimal ratio between resolution and sensitivity which is determined by the particular requirements of a detector system must be decided. A spatial resolution of 1 cm is sufficient for most clinical SPECT studies as the distribution of the radioactive tracer is

of interest, i.e. for organ functionality studies, rather than the internal structure of objects.

### **2.3.3 Applications of SPECT**

The functional imaging technique of SPECT has many applications, primarily in the medical field. The following sections provide insight into the capabilities of this non-invasive nuclear imaging technique.

#### **2.3.3.1 Medical applications**

SPECT is primarily used in the field of medicine and most developments in technology and technique are for use in this area. By labelling pharmaceuticals with a gamma-emitting radioisotope a tracer is produced which may be used to observe localised function of organs in vivo. A common radioactive tracer is technetium-99m which emits 140 keV gamma rays and has a half-life of about 6 hours (Webb 1988a). By administering the tracer, also known as a radiopharmaceutical, to a patient information about biochemical processes within the body may be gained. Depending on the pharmaceutical that has been labelled the tracer will be distributed in the body according to the organ or tissue that takes up that particular pharmaceutical.

This technique can be used to perform myocardial perfusion studies, for example, where the tracer is introduced to the blood stream and taken up by healthy heart muscle tissue (Rory et al. 1996). Figure 2.11 is an example of the images obtained from a gated myocardial perfusion study. Where the radioactive tracer has not been absorbed by the heart indicates unhealthy muscle tissue as there is a decreased blood flow and is shown as the dark blue/black regions in Figure 2.11. By guiding the image acquisition using an Electrocardiogram (ECG) it is possible to perform gated SPECT

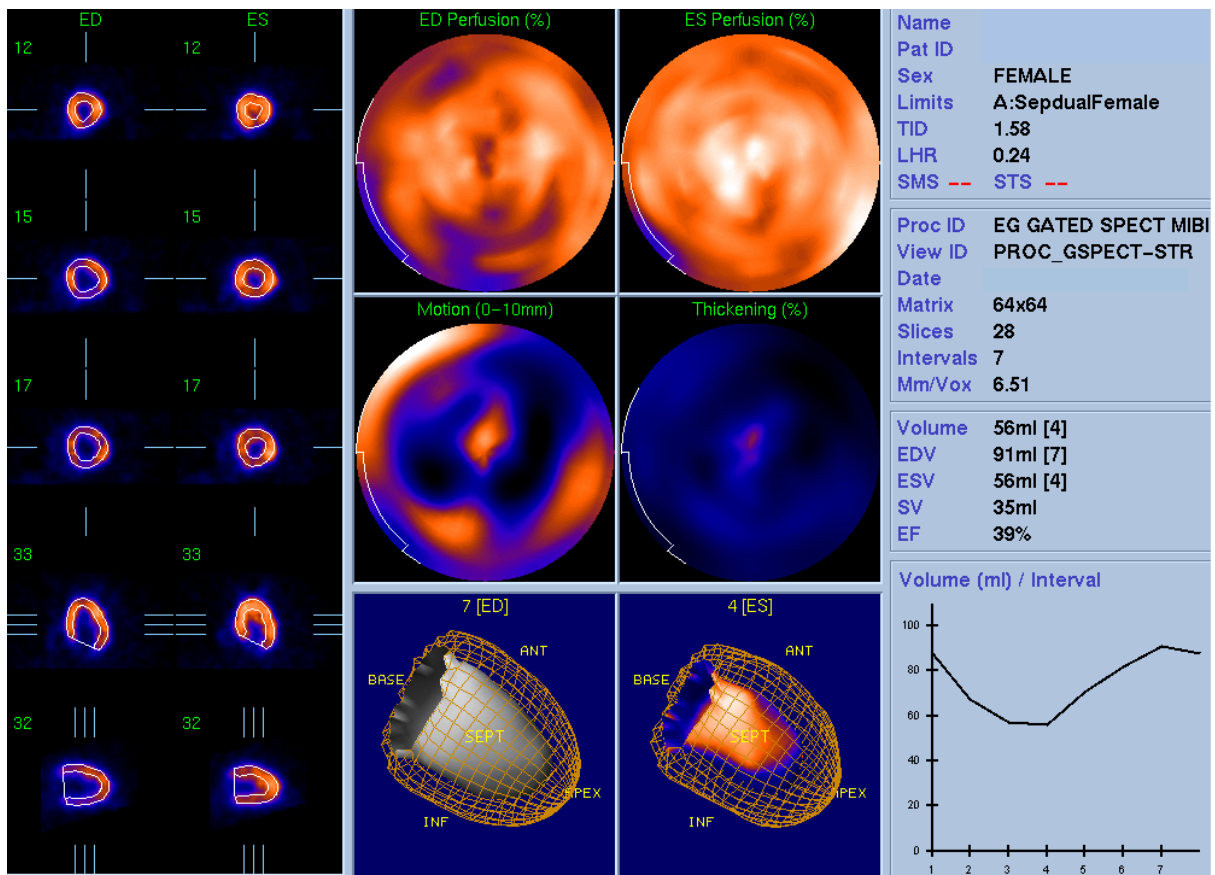


**Figure 2.11.** An example of image data gained from a gated myocardial perfusion study<sup>1</sup>.

as it selects images at the time frames at which the heart is fully contracted or relaxed. This allows the user to observe heart motion and determine whether the contractions are normal or if the heart is not able to contract as expected. SPECT may be used to study a number of different processes in the body in a similar manner including brain function, tumours and lung scintigraphy (Webb 1988b). The MC40 cyclotron at the University of Birmingham supplies krypton generators to around 50 hospitals in the UK

<sup>1</sup> <http://gamma.wustl.edu/mi033mi356.gif>

each week for lung function studies and pulmonary embolism diagnosis. The generators contain Rubidium 81 ( $^{81}\text{Rb}$ ) which decays to Krypton-81m ( $^{81}\text{Kr}^m$ ) with a half-life of about 4.5 hours. Krypton-81m is an unstable isotope that emits 190 keV gamma-rays and has a 13.1 second half life. By passing air through the generator  $^{81}\text{Kr}^m$  is eluted and inhaled by the patient to provide non-invasive information about how air is dispersed in the lungs (Hartmann et al. 2001).

### **2.3.3.2 Industrial applications**

Although SPECT is primarily used for medical purposes studies have been made to determine the feasibility of using SPECT to investigate industrial processes. The ability to non-invasively study opaque systems and processes gives nuclear imaging techniques a unique advantage over more traditional measurement techniques. In the Republic of Korea a group have been using SPECT to study chemical reactors and have provided a performance evaluation of their SPECT system under static and dynamic flow conditions (Park et al. 2014). In this study SPECT was used as a measurement technique of the dispersion of a radiotracer in a chemical reactor and was compared to the use of a high-speed camera to image the dispersion of a coloured tracer. An array of 12 detectors with diverging collimators was positioned in a ring with a diameter of 84 cm. The collimators were 22 cm wide, 9 cm deep and had a height of 6 cm. The use of diverging collimators resulted in an increased imaging FoV, although the spatial resolution of this set-up was not stated by the authors. It was concluded that the developed SPECT system was suitable for the visualization and investigation of flows using 3 s imaging frames and it was stated that it shows “fairly good agreement” with the video frames obtained using the high-speed camera. Although this statement does not provide any quantifiable information and the authors do not

state the limitations of “fairly good agreement” it does offer an introduction to the feasibility of utilising SPECT for industrial studies. Ideally the use of SPECT as a quantifiable measurement technique would be verified more conclusively against results obtained simultaneously using a known and well established technique. The use of the Maximum-Likelihood Expectation-Maximization (ML-EM) iterative reconstruction technique was claimed by the author to preserve the number of photons detected through the calculation, however this was not expanded upon to draw conclusions.

Qualitative studies of bubble column reactors have been performed using SPECT by a number of institutes including the Nuclear Energy Research Institute at the University of Sao Paulo (Mesquita et al. 2012). By positioning a gamma emitting  $^{137}\text{Cs}$  source opposite an arc of gamma detectors and placing a lab-scale bubble column in the centre the level of attenuation of the gamma rays as they pass through the column provide information about the properties of the fluid phase within the column. A high level of attenuation would indicate higher density, therefore the liquid phase, and lower attenuation would indicate the low density gas phase. The source – detector apparatus rotates around the column providing 360° angular sampling range and parallel-hole collimators were utilised to gain spatial information. The acquired attenuation information for full angular sampling has been used to produce 2D cross-sectional images of the bubble column allowing the flow regimes of bubbles may be observed and analysed. Characteristics such as bubble volume, velocity and coalescence can be made clear from image data, as shown in Figure 2.12. For more information about bubble columns please refer to section 2.8. As these studies have shown the potential

of using SPECT as a technique to study industrial processes an initial investigation into the use of SPECT was performed for this project and discussed in section 3.1.

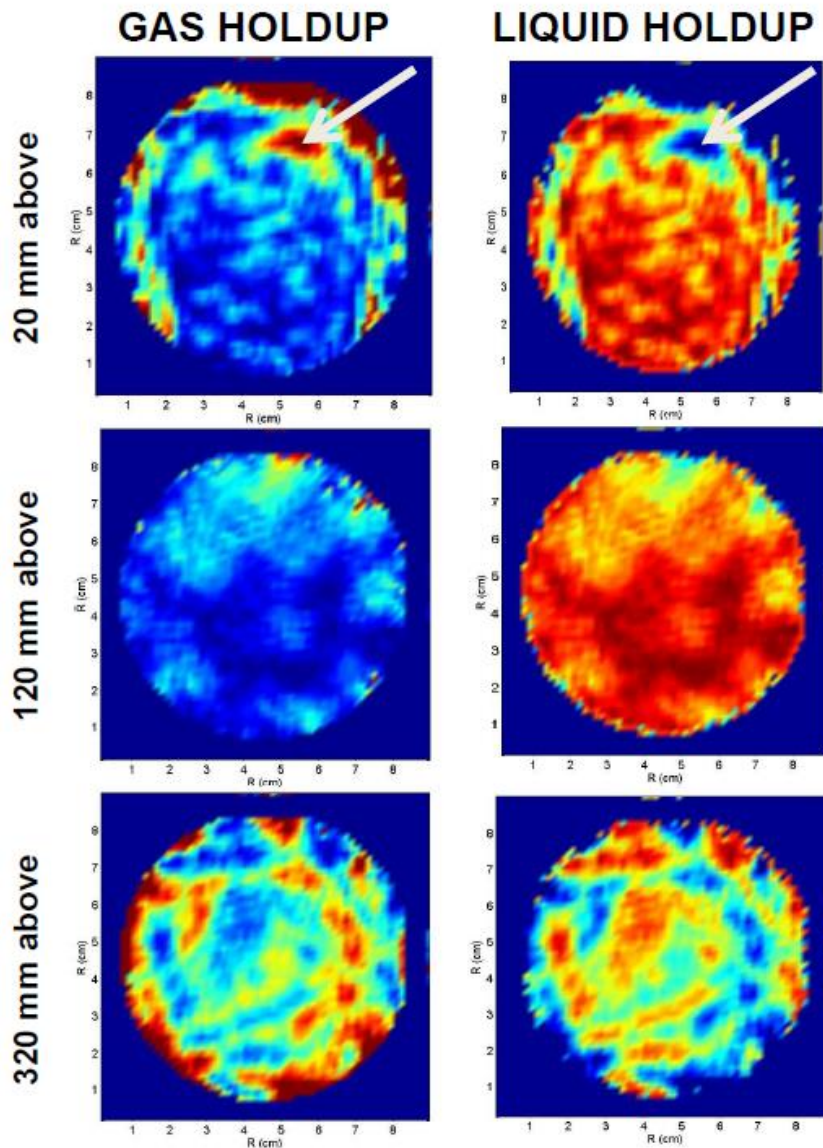


Figure 2.12. Array of cross-sectional images of a bubble column at different heights produced by de Mesquita et al. (2012). The images on the left highlight the low density gaseous areas in red (labelled gas holdup) and the images on the right show higher density liquid regions in red. The blue area is a void of liquid (labelled liquid holdup) and is indicated by the white arrow.

## **2.4 POSITRON EMISSION TOMOGRAPHY (PET)**

### **2.4.1 Introduction**

Coincidence imaging has taken a relatively long time to be developed for medical use. Positron Emission Tomography (PET) was first commercially available in 1974, but was initially used for research purposes rather than for clinical diagnosis due to the need to develop radiopharmaceuticals (Nutt 2002). For a long time PET was used primarily in universities with a cyclotron so radioactive tracers could be made on site. With the development of radiopharmaceuticals in the 80s and 90s PET has become a powerful functional imaging technique capable of performing non-invasive investigations of physiological processes. As positron emitting radioactive isotopes  $^{11}\text{C}$ ,  $^{13}\text{N}$ , and  $^{15}\text{O}$  are isotopes of commonly occurring atoms in biological molecules and because the radioactive isotopes behave in the same way as their stable counterparts they are ideal for making radioactive tracers (Schlyer 2004). For example, glucose can be labelled with  $^{11}\text{C}$  for investigations involving glucose metabolism or  $^{11}\text{C}$ -methionine, a labelled amino acid, is used for protein synthesis studies.

In order to understand how this powerful clinical imaging technique can be adapted for the study of industrial flow processes a description of the theory of PET and its practical applications in industry have been provided.

### **2.4.2 Theory of PET**

#### **2.4.2.1 Coincidence detection**

Unlike SPECT, which directly detects gamma emissions from the radioactive source, PET cameras detect pairs of annihilation photons in coincidence (Ziegler 2005). The positrons emitted by the radioactive source collide with local electrons within a few

millimetres of the source resulting in an annihilation which releases two back to back gamma photons as shown in Figure 2.13. For positron-electron annihilation the positron must lose its kinetic energy through collisions with other atoms meaning that the distance a positron can travel from the source depends on its emission energy and the average range of a positron is of the order of millimetres (Prekeges 2011b). If a positron does not lose all of its kinetic energy before annihilation then the resulting gamma photons will not be at exactly  $180^\circ$  due to conservation of momentum. This introduces an uncertainty of  $\pm 5^\circ$  to the angle between the emitted annihilation photons. The simultaneous detection, within a short timing window of about 12 ns, of the two released gamma rays by opposing detectors allows a Line of Response (LOR) to be created between the two detection locations. This LOR defines the line along which the positron-electron annihilation occurred. This means that the event being imaged is not a direct emission of the source, rather a point of annihilation. This introduces an uncertainty in the location of the radioactive tracer which combined with the uncertainty of the collinearity of the annihilation photons is a major factor in determining the spatial resolution of the PET system. Unlike SPECT, where the spatial resolution is an effect of the point spread function due to the attenuation of the collimator, the spatial resolution of PET is a product of the positron range and possible acollinearity of the annihilation photon pair. The spatial resolution is also dependent on the size of the detector elements, which is discussed in the next section (Saha 2010). As an LOR can be determined by the coincident detection of two approximately collinear gamma photons physical collimators are unnecessary to provide correlation between the detection and point of annihilation. With PET the coincident detection of two photons within the timing window is known as electronic collimation, which means PET cameras

are more sensitive than SPECT cameras as emissions are not absorbed by collimators.

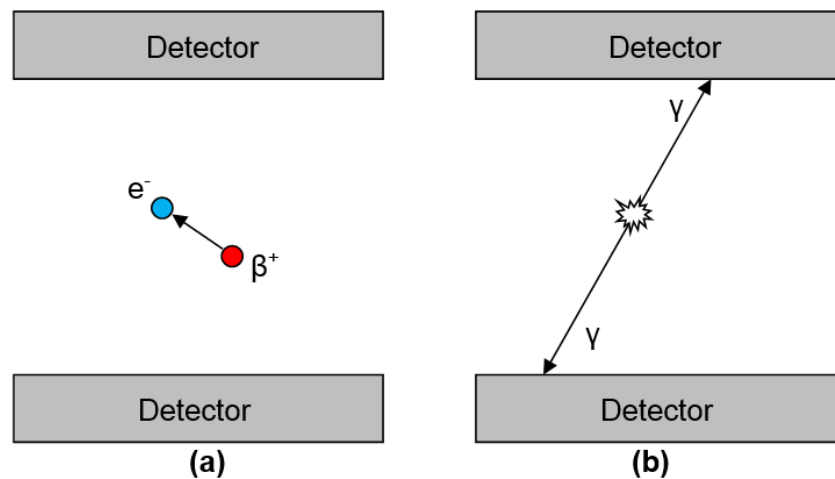


**Figure 2.13. (a) Shows a positron ( $\beta^+$ ) moving towards an electron at rest ( $e^-$ ) and (b) shows the results annihilation and release of two back-to-back gamma-rays ( $\gamma$ ) which are detected in coincidence.**

There are a number of different types of events that are detected in PET (Turkington 2001). The type of detection that has been discussed thus far is a true coincidence. A true coincidence is defined as the coincident detection of collinear annihilation photons that have not been scattered as shown in Figure 2.14 (a). Figure 2.14 (b) shows a single detection, which is when only one of the annihilation photon pairs is detected and the other photon passes through the camera without detection or leaves the FoV. Single events are not usually counted but the location of the single event is held for the duration of the timing window as the camera is waiting for an opposing detection to pair it with. If it so happens that another detection is made within the timing window

that is not connected to the original detection this is called a random coincidence and an LOR that connects the two detections is made as shown in (c). The resulting LORs contain no useful information and contribute to the background noise of the image. Scatter coincidences, shown in (d) are the coincident detection of an annihilation photon pair that have been scattered. Like with random coincidences, this results in a false LOR and does not provide useful information but contributes to the background. The ratio of detected events, or counts, is dependent on the detector configuration,

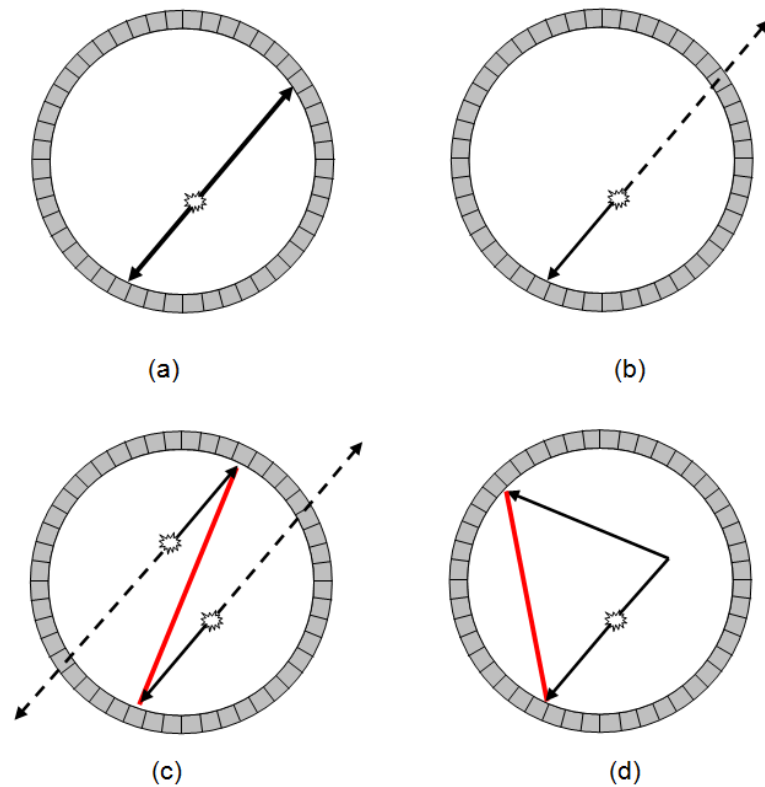


**Figure 2.14. Different types of events that can be detected in PET imaging. (a) Shows a true coincidence event, which is the coincident detection of two annihilation photon originating from the same point. (b) Shows a single detection where only one photon is detected within the timing window due to the other photon passing through the detector or leaving the FoV. (c) Shows a random event where an LOR is created between two single detections that are not connected and finally (d) shows a scatter event where one of the annihilation photons is scattered resulting in a LOR that does not represent the actual event.**

acquisition mode and the coincidence timing window. A large contributor to the number of scatter counts is the structure and density of the object being imaged. A general trend of detected count rate with increasing activity is an exponential increase in single counts as each annihilation event has potential to be detected as a single event. Random counts will also increase exponentially due to the increase in single counts, however the increase in random counts is limited by the dead time of the PET camera. The true events will increase with activity; however the count rate will also plateau due to dead time and the scatter also plateaus but at a lower rate. There are techniques available to correct for scatter and random events for quantitative measurements.

#### **2.4.2.2 Data acquisition and storage**

For the detection of coincident events the PET detectors need to be positioned in opposition. Two common configurations are an array of detectors in a complete ring around the FoV or two opposing banks of detectors which rotate around the FoV; this allows a complete 360° view of the object being imaged. As mentioned earlier, the detection of two back-to-back gamma-rays by two opposing detectors creates an LOR from the co-ordinates of the detector pair. The produced LOR defines the line along which the annihilation event is assumed to have occurred and the polar co-ordinates are stored in a sinogram (Fahey 2002). Figure 2.15 shows the annihilation photon pair in Cartesian co-ordinate space ( $x, y$ ) and the determination of the co-ordinates in polar space ( $r, \theta$ ). The perpendicular distance of the LOR from the point of origin is distance  $r$  in polar co-ordinates and the angle of the LOR is given by  $\theta$ . A sinogram is a matrix of each possible combination of  $r$  and  $\theta$  determined by the detector set up. Each row of the sinogram contains the total number of LORs detected for a single angle but

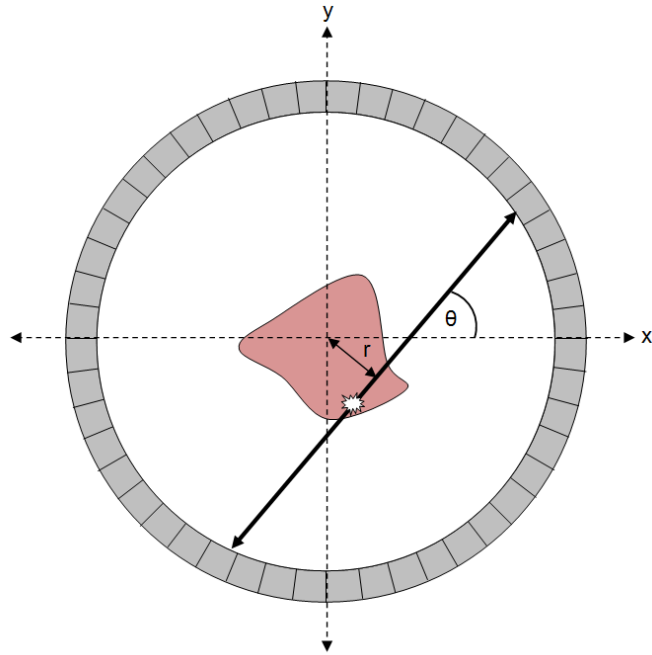


Figure 2.15. Definition of detector pair location in Cartesian co-ordinates of a coincident detection which is recorded as an LOR in polar co-ordinates. The perpendicular distance of the LOR from the origin is denoted by  $r$  and the angle is denoted by  $\theta$ .

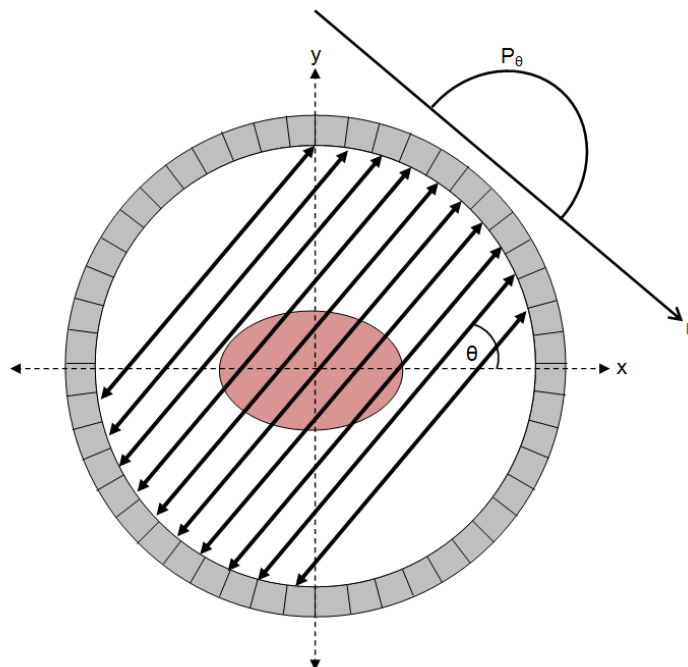
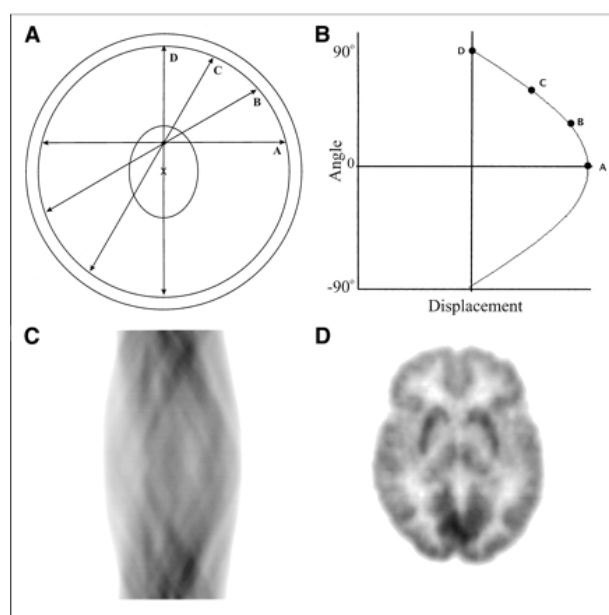


Figure 2.16. A set of parallel LORs at angle  $\theta$  and the resulting projection of line integrals, which is a simple line of the sinogram corresponding to angle  $\theta$ .  $P_\theta$  displays a distribution of LOR counts.

varying  $r$  and is called a projection. Each element of the projection is the number of LORs detected for the specific  $r, \theta$  combination, commonly called the line integral, and if the projection is plotted against  $r$  a distribution of LOR counts is observed. Figure 2.16 shows parallel LORs at angle  $\theta$  and the resulting projection,  $P_\theta$ .

Figure 2.17 is an example of how a sinogram would look for a range of angles. (A) Shows four different LORs labelled A to D for a single point of annihilation within an object. The origin is marked as  $x$  and the polar co-ordinates of each LOR are stored in a sinogram as displayed in (B). It is observed that the sinogram is a function of angle ( $\theta$ ) against displacement ( $r$ ). This is an example of a simple sinogram for a single point



**Figure 2.17. Figure<sup>1</sup> showing the formation of a sinogram. (A) Shows four different LORs, for one point of annihilation, labelled A to D, the point of origin has been labelled with an  $x$ . (B) Shows how the LORs A to D would be stored as angle ( $\theta$ ) vs. displacement ( $r$ ) in a sinogram. (C) Is an example of a more complex sinogram obtained from a brain scan and (D) is the resulting image.**

<sup>1</sup><http://tech.snmjournals.org/content/30/2/39/F1.expansion.html> (accessed: Aug 2015)

of annihilation and a sinusoidal trend can be observed, hence the name sinogram. (C) is a more complex sinogram obtained from a brain scan and is composed of many overlapping sine waves and on each horizontal line the greyscale represents the number of LORs detected at each  $r$  for a particular angle. Finally (D) is the resulting image corresponding to the reconstruction of the sinogram shown in (C). The reconstruction of images from sinograms is discussed in section 2.5.

As mentioned previously two common detector configurations are one or more rings of detector blocks or two opposing banks of detector blocks that rotate around the FoV. A detector block commonly consists of one scintillation crystal that has been scored to create individual detectors. Figure 2.18 is a photo of a PET detector block coupled with four PMTs. It can be seen that the scintillation crystal has been scored to produce an array of 64 individual detectors. As with SPECT the PMTs detect electron scintillation as a flash of light and a comparison of light intensities from the PMTs allows the specific detector element that absorbed the photon to be identified. The size of the detector element is the dominant contributor to determining the spatial resolution of the detector system. The dimensions of the detector elements are usually  $\sim 4\text{-}6$  mm square which is added to the average positron range and acollinearity uncertainty to give a total spatial resolution of about 6 mm for a conventional medical PET camera. A complete circle of these blocks around the FoV is known as a ring. The detector blocks can be further arranged into buckets, as shown in Figure 2.19. This photo shows an example of eight detector blocks in a bucket. This bucket is from a PET camera that had two complete rings of detector blocks. Coincidence counts would only be recorded if the photon pair was detected in opposing buckets, that is to say in



**Figure 2.18. Photo of a detector block coupled with four PMTs.**



**Figure 2.19. Photo of a bucket which consists of 2 x 4 blocks of detectors.**

Figure 2.20 block A could only be paired with blocks between B and C. The range of blocks allowed to be in coincidence with a specific block defines the size of the FoV. However, with a detector set up of two opposing banks of detectors that rotate around a FoV, detections are only in coincidence if measured by detector elements in opposing blocks but as the detectors rotate the FoV is not limited to an angular range.

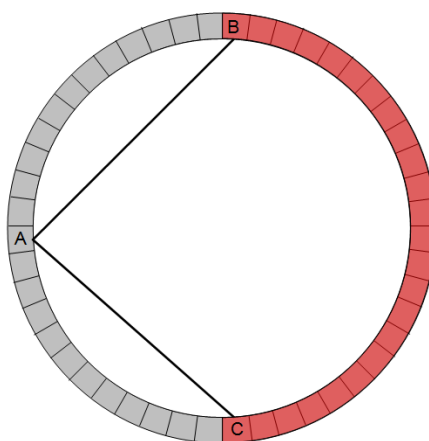


**Figure 2.20. Definition of opposing detectors for a full ring of detectors. For detector block A a pairing can be made with a detector between B and C (shaded in red).**

### **2.4.2.3 2D and 3D data acquisition**

By referring back to section 2.3.2.2 the function of septa can be recalled. As with SPECT septa are used in PET to limit the acceptance angles of photon trajectories (Fahey 2002). For 2D data acquisition septa are placed between the detector rings as shown in Figure 2.21. The left most diagram shows direct plane coincidences. This means that only LORs detected in the same ring are recorded, improving the ratio of true events to randoms and scatters as these will be blocked by the septa. It is important to recall that the coincident nature of PET allows electronic collimation so the septa are not being used to define the point of annihilation but to reduce scatter.

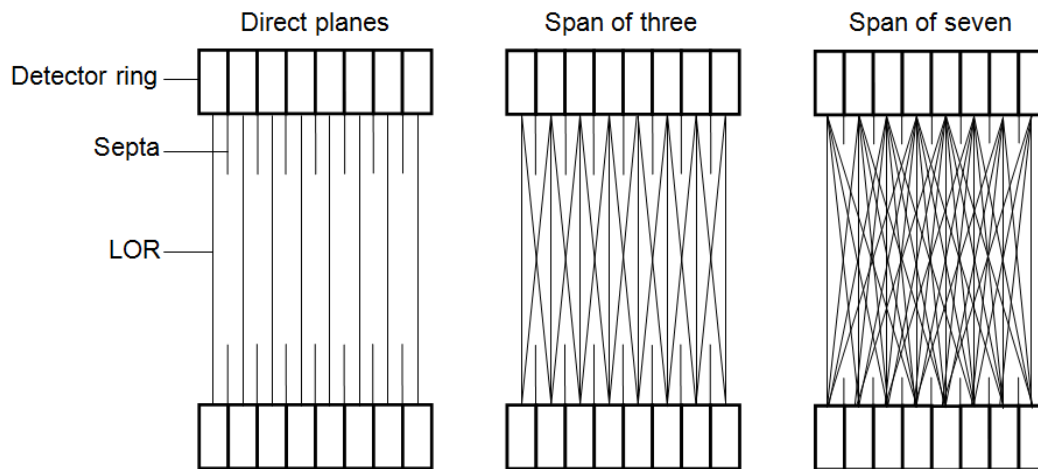


**Figure 2.21.** The left hand diagram shows that direct planes are defined as a coincidence event detected in the same detector ring. By placing septa between the detectors the amount of randoms and scatter detected is reduced. The middle diagram shows a cross plane span of three and the right hand diagram shows a cross plane span of seven.

Using the septa does not limit the detections to direct planes only, cross planes can be defined, as shown in the central diagram, and this allows virtual planes in between the direct planes to be created (Christian & Waterstram-Rich 2012). With a span of three the virtual planes have double the sensitivity of the direct planes as they are the result of two cross planes as opposed to one direct plane. By increasing the span of the cross planes being detected the overall sensitivity of the acquisition is increased as a larger proportion of total emitted annihilation photons will be detected. The diagram on the right in Figure 2.21 shows a span of seven cross planes and Figure 2.22 shows how the relative axial sensitivity increases with increasing span number. For a plane span of seven the maximum sensitivity is a result of four cross plane LORs for the virtual planes compared to one direct and two cross planes for the actual planes. As the edge of the detectors rings is approached the sensitivity reduces.

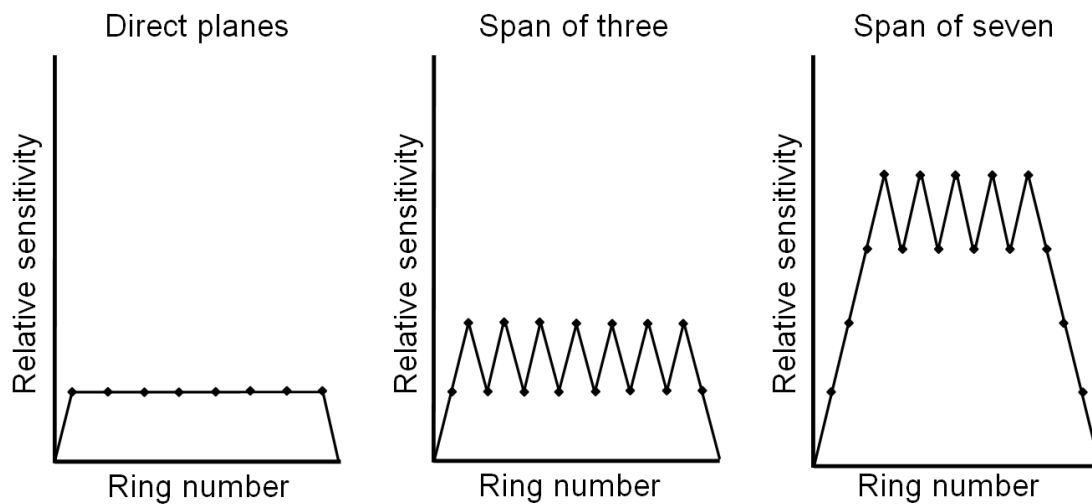


**Figure 2.22. The relative axial sensitivity map for direct planes, cross plane span of three and cross plane span of seven.**

For 3D data acquisition the septa are retracted allowing the full range of detector pairs to record data as shown in the left diagram of Figure 2.23. Although this greatly increases the number of true events that are detected by removing the septa the number of randoms and scatters are also greatly increased. The significant increase in total number of LORs detected results in high computational cost for reconstruction (Christian & Waterstram-Rich 2012). The resulting axial sensitivity map shows maximum sensitivity in the centre of the FoV and a linear decrease to the edges.

### 3D acquisition

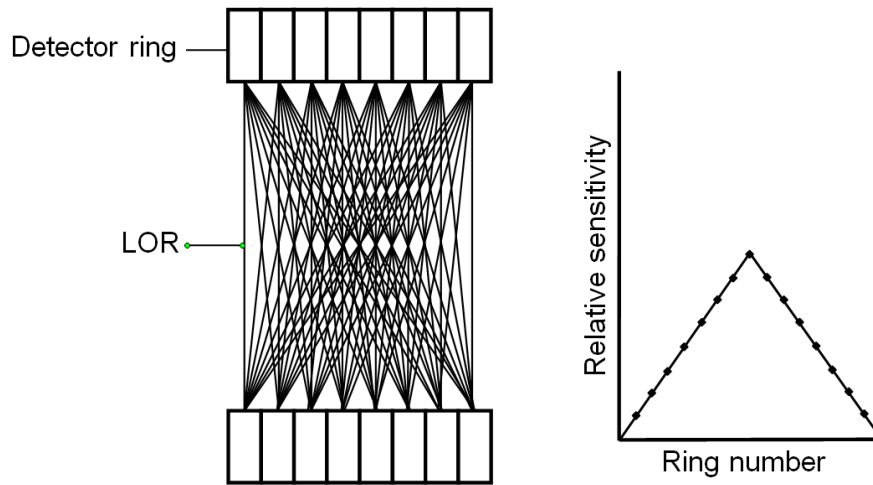


**Figure 2.23.** For 3D data acquisition the septa are retracted allowing the full range of detector pairings. The diagram on the right shows the resulting relative axial sensitivity map.

#### 2.4.3 Applications of PET

PET is considered to be one of the most powerful functional imaging techniques but due to the high cost, which stems not only from the installation and upkeep of the PET camera itself but the necessity of a local cyclotron to produce the short half-life radiopharmaceuticals, it is not a technique many hospitals can support. This also results in little industrial research as only a few universities own or have access to a particle accelerator. The University of Birmingham has acquired the equivalent of four PET scanners which have been adapted and utilised over the past 20 years for studying flow processes in engineering equipment. The following subsection provides a brief overview of previously performed studies from the University of Birmingham and other institutions.

### **2.4.3.1 Industrial applications**

For many years at the University of Birmingham Positron Emission Particle Tracking (PEPT) has been the technique of choice for studying flow processes in engineering. PEPT is an adaptation of PET where a single particle is labelled with a positron emitting isotope and can be accurately tracked in a fluid flow through triangulation of detected LORs. This technique has allowed detailed studies of flow processes such as mixing (Barigou 2004), particle grinding (Conway-Baker et al. 2002) and convection in granular flows (Wildman et al. 2001). Recently, however there has been increased interest in the use of conventional PET for process applications. In 2008, Parker et al. reported a study using an Ecat951 PET camera to image powder mixing in a laboratory-scale pharmaceutical blender. An initial attenuation scan was performed with the blender filled with an unlabelled powder in order to correct for attenuation in post processing. Then a small amount of powder labelled with an unspecified radioisotope was added to the top of the blender and imaged. Then a process of tumbling the blender for 5 revolutions followed by a 20 minute PET scan was repeated 12 times in total. The resulting images provided an insight into how different regions within the blender mix over time. An analysis of radioactive tracer concentration within the blender was also performed to determine quantitatively the uniformity of the labelled powder distribution within the bulk unlabelled powder. It was concluded from this study that PET has proved to provide practical and detailed study of pharmaceutical mixing, and the potential for using this technique for alternative process studies was realised.

Dechsiri et al. (2005) reported a study using a clinically active ECAT EXACT HR+ PET camera at the University Hospital in Gronigen, the Netherlands, to track labelled

particles in a fluidised bed. A macroporous anion-exchange resin, 470  $\mu\text{m}$  in diameter, and an FCC catalyst powder, 79.5  $\mu\text{m}$  in diameter, were immersed in a fluoride containing positron emitting  $^{18}\text{F}$  ions to create labelled particles, and the particle transport of a fluidised bed could be studied. The FCC catalyst particles were tracked as a pulse and the resin particle could be tracked as a single particle. The position of the radioactive tracer as a function of time could be measured to within two particle diameters once per millisecond allowing the particle velocity in different sections of the bed to be calculated. With the ability to make a particle location measurement every ms to within two particle diameters it was concluded that PET provided a practical means of studying a fast flow process with reasonable accuracy. A stochastic particle transport model was presented and the two results showed good agreement.

The studies referred to in this section give an idea of the detailed insight PET can provide into industrial flow processes. However, after extensive research it was not possible to discover published work using a radioactive gas as a radioactive tracer for industrial processes.

## **2.5 IMAGE RECONSTRUCTION TECHNIQUES**

### **2.5.1 Introduction**

The process of reconstructing raw acquisition data stored in sinogram form into a series of images for PET may be done using analytical or iterative methods (Alessio & Kinahan 2006). The two options available using the PET imaging system at the Positron Imaging Centre are Filtered Backprojection (FBP) method and Ordered Subset Expectation Maximization (OS-EM) method, analytical and iterative methods respectively. Each method is quite different in its approach to image reconstruction and

the pros and cons of each are briefly discussed in the following sections with a final conclusion of the optimal technique for the purposes of this study.

### **2.5.2 Filtered Back Projection (FBP)**

FBP is a commonly used analytical image reconstruction technique for clinical purposes. It is a relatively fast technique and may be easily implemented in a clinical setting. There are two primary steps in the process of FBP: filtering the raw acquisition data and backprojecting this filtered data. As explained in section 2.4.2 the information recorded by the scanner are the polar coordinates of the LOR of each emission/annihilation and these coordinates are stored in a sinogram. The information from the sinogram is used to create a series of projection profiles. A projection is a series of line integrals, or summed counts, for parallel LORs as described in section 2.4.2.2 and shown in Figure 2.24. For each acquisition time frame a series of projections for all angles are produced as demonstrated in Figure 2.25. If these projections are backprojected without performing any filtering or smoothing then the result would be a diffusely blurred image of the object being scanned (Bushberg et al. 2012). Figure 2.25 is a diagram showing 3 projections of a small circle in the corner of a reconstruction image array, at the bottom of the figure is the profile through the object  $f(r)$ , where  $r$  is the radial direction from the centre of the object. Figure 2.26 shows the result of backprojecting without any filter. The total summation of counts would be distributed evenly back along the same path of the original line integral resulting in a star artefact for a finite number of projection angles.

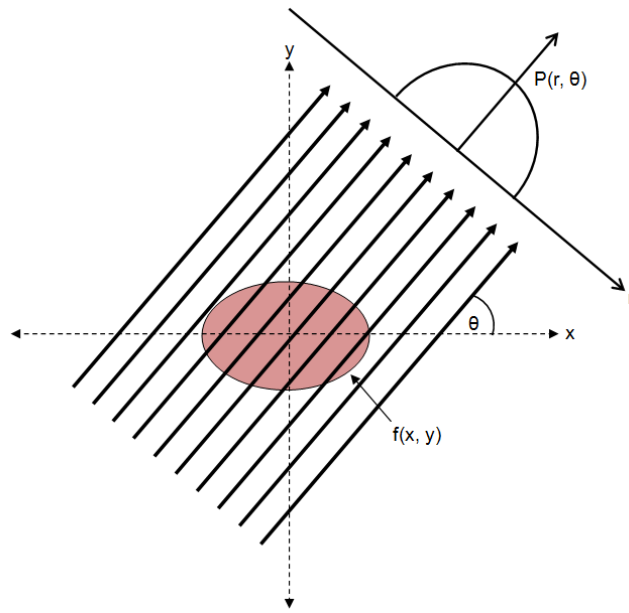


**Figure 2.24.** Diagram showing how projection profiles are made from parallel line integrals for a specific angle  $\theta$ . The resulting projection is a function of  $r$ , perpendicular distance from origin, and  $\theta$ , angle of LOR. The object is in Cartesian co-ordinates so in a function of  $x$  and  $y$ ,  $f(x, y)$ .

This results in blurring at the edges of the object. This blurring appears to have convoluted the original object profile with a convolution kernel that has a  $1/r$  shape (Cherry et al. 2012). This means that the number of counts that a pixel originally had has been spread around neighbouring pixels resulting in a backprojected array of pixels with original counts multiplied by  $1/r$ . A filter is required to reduce noise and minimise  $1/r$  blurring which must be applied to the projections in the frequency domain before backprojection.

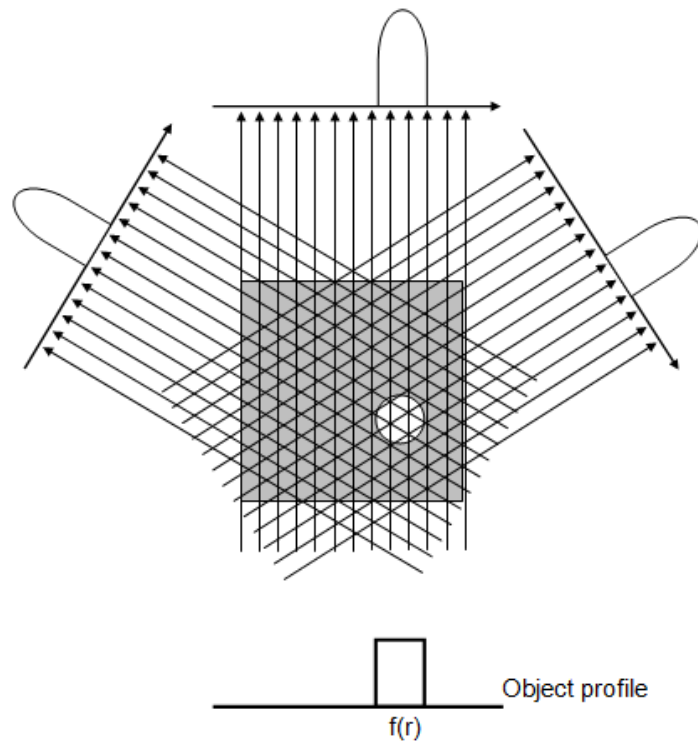


Figure 2.25. Projection profiles for three angles and object profile  $f(r)$ .

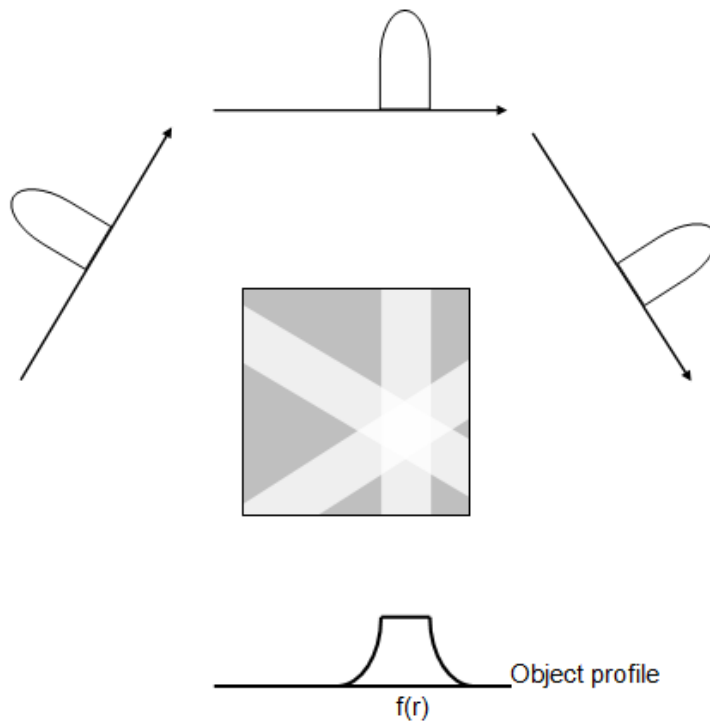


Figure 2.26. Backprojection with no filter results in  $1/r$  blurring at the edges due to low frequency overlapping of backprojections.

Before being able to perform the first step of FBP, filtering, the emission data acquired by the PET camera must be transformed from polar coordinates into the frequency domain. The equation of an LOR contributing to the projection profile is

$$x \cos (\theta) + y \sin (\theta) = r, \quad 2.1$$

where  $\theta$  is the angle between the ray and the  $x$  axis. The line integral can then be defined as

$$P_{\theta}(x) = \int_{-\infty}^{\infty} f(x, y) dy, \quad 2.2$$

where  $f(x, y)$  is the object function in Cartesian co-ordinates. From the Fourier Slice theorem (Kak & Slaney 1988) it is known that the 1-D Fourier transform of an object projection is equal to a slice of the 2-D Fourier transform of that object. By acquiring the 1-D Fourier transformations of the object projections for all angles they can be interpolated to reconstruct a full 2-D Fourier transform of the object. The 2-D Fourier transform of an object can be defined as

$$F(u, v) = \int_{-\infty}^{\infty} \int_{-\infty}^{\infty} f(x, y) e^{-j2\pi(ux+vy)} dx dy, \quad 2.3$$

where  $u$  and  $v$  are spatial frequencies. This may be simplified by considering a projection at  $\theta = 0$  to prove the Fourier Slice theorem. This would mean  $v = 0$  in the frequency domain giving a simplified 2-D Fourier transform:

$$F(u, 0) = \int_{-\infty}^{\infty} \int_{-\infty}^{\infty} f(x, y) e^{-j2\pi ux} dx dy, \quad 2.4$$

which is no longer dependent on  $y$ . This allows the integral to be separated

$$F(u, 0) = \int_{-\infty}^{\infty} \left[ \int_{-\infty}^{\infty} f(x, y) dy \right] e^{-j2\pi ux} dx. \quad 2.5$$

The term inside the square brackets is the same as equation 2.2, the line integral of the object function. By substituting equation 2.2 into equation 2.5 we get

$$F(u,0) = \int_{-\infty}^{\infty} P_{\theta=0}(x) e^{-j2\pi ux} dx, \quad 2.6$$

and the 1-D Fourier transform of the line integral for one slice is

$$S_{\theta}(u) = \int_{-\infty}^{\infty} P_{\theta}(x) e^{-j2\pi ur} dr. \quad 2.7$$

This proves the Fourier Slice theorem as the 1-D Fourier transform of the object is equal to a slice of the 2-D Fourier transform of the object (equation 2.6 for one slice is equal to equation 2.7).

Once the emission acquisition data has been transformed into the frequency domain a filter may be applied to reduce noise and  $1/r$  blurring which occurs in the transaxial plane. There are several different types of filters that may be used in FBP that serve different purposes but the two main groups are high pass and smoothing filters. Lyra & Ploussi (2011) published a review detailing the commonly used filters for medical imaging and this section discusses some comparative characteristics. The high pass filters, such as the ramp filter, do not permit low frequencies to appear in the image. Equation 2.8 is the mathematical expression for the ramp filter,  $H_R$ , in the frequency domain.

$$H_R(u,v) = (u^2+v^2)^{1/2} \quad 2.8$$

The ramp filter adds a weighting factor that increases linearly with frequency, directly correcting for the  $1/r$  blurring. As the  $1/r$  blurring is a low frequency artefact a high pass filter would greatly minimise this blurring and enhance object edge information as this is high frequency information (Figure 2.27).

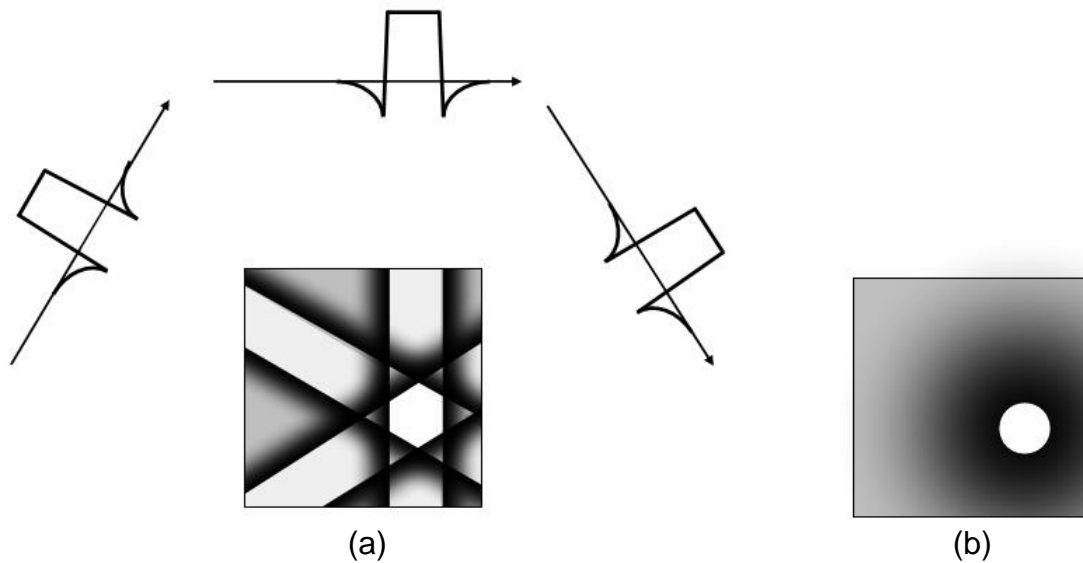


**Figure 2.27. Backprojection (as Figure 2.26) with ramp filter. (a) Shows the object projection with the ramp filter applied and the result of three filtered backprojections. (b) Shows the resulting image after many filtered backprojections. There is blurring in the background of the image but the object is more defined.**

Unfortunately this type of filter would severely amplify statistical noise, which is high frequency information. This may be reduced somewhat by combining the high pass filter with a low pass filter such as the Hanning filter, equation 2.9.

$$H(f) = \begin{cases} 0.5 + 0.5 \cos\left(\frac{\pi f}{f_m}\right), & 0 \leq |f| \leq f_m, \\ 0, & \text{otherwise,} \end{cases} \quad 2.9$$

where  $f$  is the spatial frequency domain and  $f_m$  is the cut-off frequency of the filter. The low pass filters are smoothing filters and allow low frequencies to remain unaltered but the higher frequencies are not permitted above a maximum cut-off frequency. Equation 2.10 is the mathematical expression of the Gaussian smoothing (low pass) filter in 2-D, which is the default filter combined with the ramp filter for the PET imaging system used for this project and is dependent on the standard deviation of the Gaussian distribution,  $\sigma$  which sets the width of the filter and is predefined.

$$G(x,y) = \frac{1}{2\pi\sigma^2} e^{-\frac{x^2+y^2}{2\sigma^2}} \quad 2.10$$

The resulting projection profile with a Gaussian and ramp filter applied is shown in Figure 2.28.

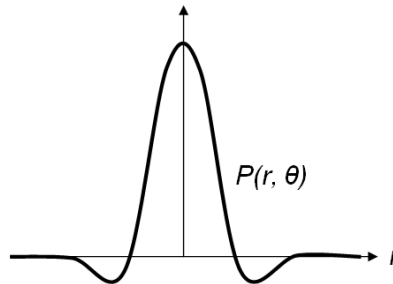


**Figure 2.28. Object projection with ramp and Gaussian filter applied.**

One advantage of the Gaussian filter is that the shape of the filter is the same in the frequency and spatial domain so unwanted effects are not backprojected into the spatial domain. Using this low pass smoothing filter is good for reducing statistical noise but has the trade-off that resolution is greatly compromised as the  $1/r$  blurring in the transaxial plane is exaggerated. For more information regarding the limitations see (Narayanan & Perkins 2013). A commonly used filter in nuclear medicine is the Butterworth filter as it offers noise reduction with a variable cut-off frequency and maintains reasonable resolution as it utilises the Order parameter. The Order parameter,  $n$ , controls the slope of the filter function which is used to try to minimise  $1/r$  blurring.

$$B(f) = \frac{1}{[1+(f/f_m)^{2n}]} \quad 2.11$$

The Butterworth filter shows a similar result to the Gaussian filter in the spatial domain but at a higher computational cost.

Once a filter has been applied to the image data in the frequency domain the projections need to be backprojected back into the spatial domain. To do this the Inverse Fourier transform is required:

$$F(x) = \int_{-\infty}^{\infty} P_{\theta}(u) e^{-j2\pi xt} dt. \quad 2.12$$

This results in a reconstructed image that may be analysed for spatial information about the distribution of activity in an object.

### 2.5.3 Ordered Subset Expectation Maximization (OS-EM)

Ordered-Subset Expectation-Maximization (OS-EM) is an iterative reconstructive technique that is used for emission tomography (Alessio & Kinahan 2006). Iterative reconstruction algorithms are a variation of algebraic reconstruction algorithms. Each of the variations of iterative algorithms begins with a 'grid' of the same dimensions as that of the object to be imaged called an image model. Figure 2.29 shows the image model with  $N$  distinct pixels. The system model starts out as a representation of the probability that the activity in a pixel from the image model,  $f_j$ , is detected in a specific projection,  $P_i$  where  $j$  denotes pixel number from 1 to  $N$  and  $i$  denotes projection number from 1 to  $M$ . The system model consists of elements  $H_{ij}$  as shown in Figure 2.29 and the mean of the  $i$ -th projection,  $\bar{P}_i$  is given by

$$\bar{P}_i = \sum_{j=1}^N H_{ij} f_j \quad 2.13$$

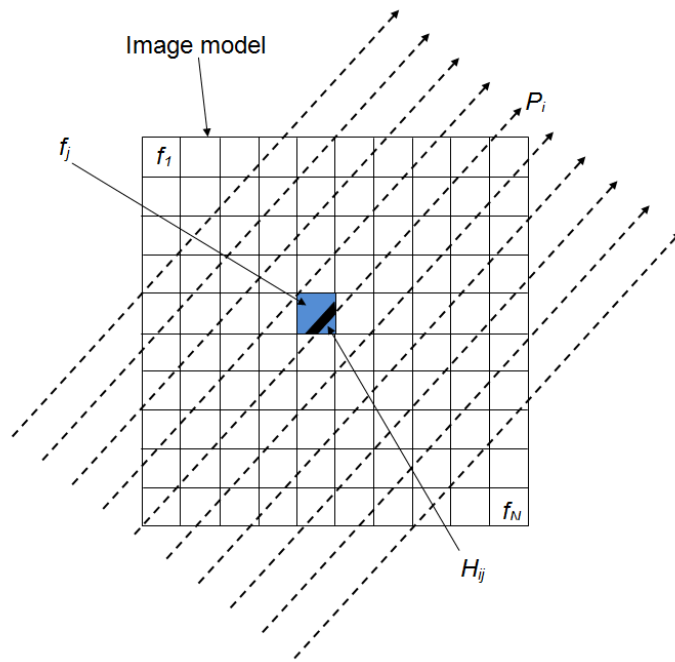


**Figure 2.29. Image model grid of  $N$  pixels.  $H_{ij}$ , highlighted as the bold black ray element, is the probability that the activity in pixel  $f_j$ , shown as a blue pixel, will be detected by projection  $P_i$ .**

A data model which is a model that describes the statistical relationship between the value of the actual projection data,  $P$ , and the expected value of the data  $\bar{P}$  is the third component of an iterative technique. Iterative algorithms approach the reconstruction of an image by using multiple iterative steps to apply a governing principle to update the system model with an estimate of the object that a statistical distribution of counts equals the true counts. This allows an increase in the quality of the image which has been reconstructed but this comes at the cost of increased computational time.

OS-EM is an adaptation of the Maximum-Likelihood Expectation Maximization (ML-EM) algorithm that was developed to decrease the reconstruction time. The adaptation introduced the use of subsets of the entire data set for updating the image.

A full description of ML-EM is given by Shepp & Vardi (1982) and the algorithm for OS-EM is given in equation 2.14.

$$\hat{f}_j^{n+1} = \frac{\hat{f}_j^n}{\sum_{i' \in S_b} H_{ij'}} \sum_{i \in S_b} H_{ij} \frac{P_i}{\sum_k H_{ik} \hat{f}_k^n} \quad 2.14$$

Here,  $\hat{f}_j^{n+1}$  is the next estimate of pixel  $j$  for the current estimate  $\hat{f}^n$  and  $S_b$  is the subset for  $b = 1$  to  $B$ . This means that one image iteration will have  $B$  updates.

## 2.6 MAKING RADIOACTIVE TRACERS

### 2.6.1 Making $^{81}\text{Kr}^m$

The gas used for the SPECT studies was Krypton-81m which was produced by a  $^{81}\text{Rb}/^{81}\text{Kr}^m$  generator. Rubidium-81 is produced by the University of Birmingham's MC40 cyclotron via the bombardment of Krypton-82 gas with protons according to the  $^{82}\text{Kr}(p,2n)^{81}\text{Rb}$  reaction. The  $^{81}\text{Rb}$  is trapped in an ion exchange column of zirconium phosphate and decays to  $^{81}\text{Kr}^m$  gas (Brits & Haasbroek 1987). The  $^{81}\text{Kr}^m$  gas is extracted by blowing air through the ion exchange column. Krypton-81m undergoes isomeric decay to  $^{81}\text{Kr}^m$ , has a half-life of 13.1 seconds and the main emission is via 191 keV gamma rays.

### 2.6.2 Making $^{11}\text{CO}_2$

Carbon-11 is a positron ( $\beta^+$ ) emitting isotope with a half-life of 20.5 minutes which can be used for PET studies. One method used to produce this isotope is to bombard a Nitrogen-14 target with protons using a cyclotron (Vandewalle & Vandecasteele 1983). The energy of the proton colliding with a nitrogen atom can cause an alpha particle to be released producing a  $^{11}\text{C}$  atom (this is the  $^{14}\text{N}(p,\alpha)^{11}\text{C}$  reaction). Other methods may be used to create  $^{11}\text{C}$ , such as  $^{10}\text{B}(d,n)^{11}\text{C}$  and  $^{11}\text{B}(p,n)^{11}\text{C}$  reactions, both of

which require a boron target, however, the method used for the purposes of the work presented in this thesis is the  $^{14}\text{N}(p,\alpha)^{11}\text{C}$  reaction. When traces of oxygen are mixed in with the nitrogen gas target it allows the production of  $^{11}\text{CO}_2$ , which is chemically indistinguishable from  $\text{CO}_2$ . This results in a gas which is predominantly nitrogen containing traces of radioactive carbon dioxide (parts-per-billion).

## **2.7 FLUIDISED BED**

### **2.7.1 Introduction**

For the initial feasibility study a fluidised bed was imaged using SPECT with  $^{81}\text{Kr}^m$  as the radioactive tracer. This section provides an overview of the theory of fluidisation and the applications of fluidised beds in industry.

### **2.7.2 Theory**

Fluidisation is the process of applying the necessary conditions to cause a solid-fluid mixture to behave as a fluid (McCabe et al. 1993a). To cause fluidisation a bed of solid particles must have a flow of gas or liquid to pass through, and at high enough gas/fluid superficial velocities,  $V_s$ , the pressure drop,  $\Delta p$ , and drag on the solid particle becomes sufficient to cause the particles to become suspended in the fluid phase. The resulting solid-fluid mixture behaves as a dense fluid and one property is the ability for free-flow allowing the solid-fluid mixture to flow through pipes and valves as a liquid. Figure 2.30 shows a schematic of a fluidised bed. The bed is open at the top and a distributor plate is used to support the solid particles and to uniformly distribute the fluid flow. In this example air is pumped into the bottom of the bed and flows upwards through the bed. At low velocity the solid particles will not move and the initial unfluidised bed length,

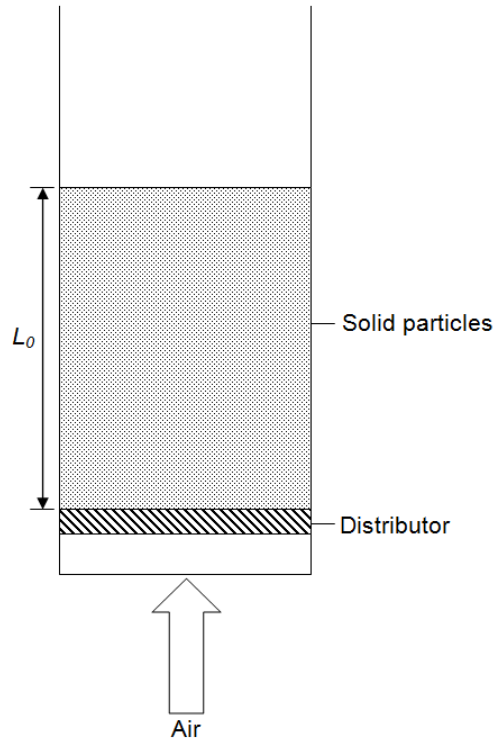


**Figure 2.30. Schematic of a fluidised bed. The top of the bed is open and the solid particles are supported by a distributor which uniformly distributes the fluid, in this case air, as it flows up through the bed. The length of the bed before fluidisation is  $L_0$ .**

$L_0$ , will not change and the pressure drop across the bed will be proportional to the fluid velocity for turbulent flow. Ergun's equation (equation 2.32) can be used to calculate the pressure drop, a full description of which is given by Ergun (1952).

$$f_p = \frac{150}{Re} + 1.75, \quad 2.15$$

where the Reynolds number,  $Re$ , is given by

$$Re = \frac{D_p v_s \rho}{(1-\varepsilon)\mu}. \quad 2.16$$

and the friction factor of the solid particles,  $f_p$ , is given by

$$f_p = \frac{\Delta\rho D_p}{L \rho V_s^2} \left( \frac{\varepsilon^3}{1-\varepsilon} \right) \quad 2.17$$

Here,  $L$  is bed length,  $D_p$  is the diameter of the solid particles,  $\rho$  is the fluid density,  $\mu$  is the dynamic fluid viscosity and  $\varepsilon$  is the void fraction of the bed. The superficial velocity,  $V_s$ , is defined as the velocity of the fluid if the solid particles are ignored and is determined using equation 2.18 where  $Q$  is the volumetric flow rate and  $A$  is the cross-sectional area of the bed.

$$V_s = \frac{Q}{A} \quad 2.18$$

At a certain threshold the increasing pressure drop caused by the increasing velocity will counterbalance the force of gravity on the particles as the friction from the upward moving fluid phase acts in opposition. This causes the particles to move more and results in an expanded bed where  $L$  increases. Up to this point the bed state is known as a fixed bed as there is no particle movement and  $L$  is equal to  $L_0$ . After reaching a minimum fluidisation threshold velocity,  $v_{OM}$ , the bed is fluidised and the type of fluidisation can vary depending on the superficial velocity and Reynolds number. Figure 2.31 contains a series of diagrams showing the different fluidisation regimes. The formation of a minimum fluidisation state has already been discussed. By increasing the superficial velocity of the gas flow the movement of the particles increases creating an expanded bed and resulting in particulate fluidisation, generally most common in liquid-solid fluidised beds. Beds of solid particles fluidised by a gas usually result in a bubbling fluidisation regime at high superficial velocities. This is caused by the majority of the gas entering the bed forming bubbles or voids

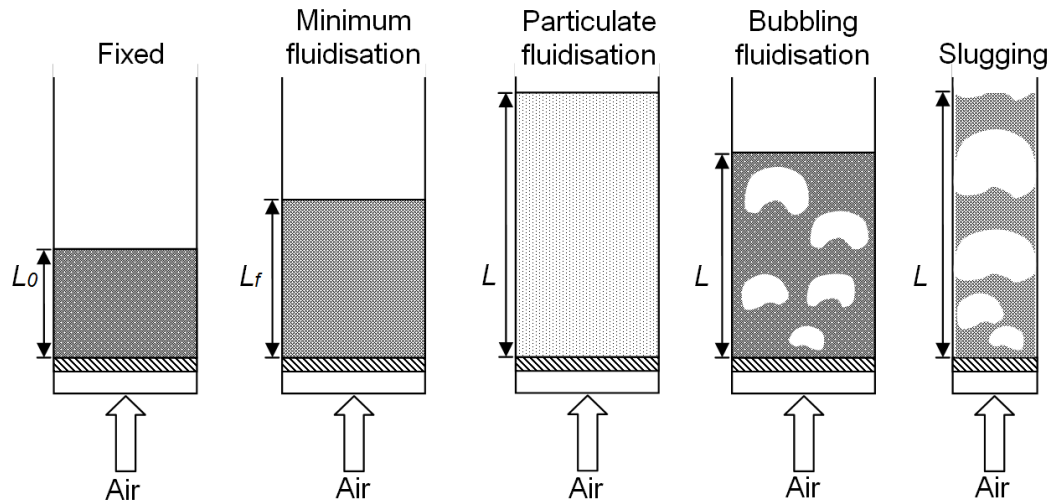


**Figure 2.31. Different fluidisation regimes. The fixed bed is the state before fluidisation. The superficial velocity is below the minimum fluidisation velocity and the solid particles do not move so the bed length is  $L_0$ . At minimum fluidisation the length of the bed,  $L_f$ , increases as the upward friction of the gas flow is equal to the gravitational force meaning the particles begin to move. In particulate fluidisation the bed length increases as the particles move more with increasing superficial velocity. The particle distribution is uniform and the gas-solid mixture behaves as a fluid. At high superficial velocities most of the air passes through the bed as bubbles and is called bubbling or aggregative fluidisation. With a bed with smaller diameter the bubbles can grow to be as large as the cross section of the bed and is called slugging.**

which are mostly free of solid particles. Only a small fraction of the gas passes through between the particles. The bubble sizes formed in this regime vary according to superficial velocity, particle size and density and bed geometry. As the bubbles move up the bed they will join each other and coalesce creating larger bubbles. In a deep bed with relatively small diameter the coalesced bubble diameter can be equal to the cross sectional area of the bed creating slugging which causes pressure fluctuations in the bed.

As mentioned previously the specifications of the solid particles used can determine the fluidisation of the bed. Geldart (1973) proposed four different groups of solid

particles based on their size and solid-fluid density difference which show distinct differences in behaviour when fluidised. The four groups are defined as follows:

- *Group A* – particles in group A have low particle density of about  $1.4 \text{ g m}^{-3}$  or less and small average particle diameters of between 20 and 100  $\mu\text{m}$ . Upon minimum fluidisation the bed will expand considerably before the transition to bubbling fluidisation. Once the bed begins bubbling rapid mixing occurs as the particles in the bed begin to circulate, similar to convection currents in liquids.
- *Group B* – particles in group B are within the density range of 1.4 to  $4 \text{ g m}^{-3}$  and particle size range of 40 to 500  $\mu\text{m}$ . Upon minimum fluidisation bubbling occurs almost instantly resulting in small bed expansion
- *Group C* – particles in group C have mean particle sizes in the range 20 to 30  $\mu\text{m}$  and are defined as cohesive as they stick to each other to form aggregates. This makes group C particles very difficult to fluidise as the interparticle forces are greater than the friction exerted by the fluid. Fluidisation can be achieved by exerting external mechanical force such as a vibrator or stirrer but the particle mixing is poor with group C particles.
- *Group D* – the particles in group D are relatively large and/or dense with particle sizes greater than 600  $\mu\text{m}$ . In this group bubbling fluidisation bubbles move slowly and coalesce readily. Fluidisation requires a large fluid energy input and with high enough superficial velocity spouting occurs which is where a jet is formed in the bed which can blow material out of the top of bed.

Fluidised beds are used for a number of purposes including fluidised bed reactors, heat or mass transfer applications and fluid catalytic cracking. The practical applications of fluidised beds are discussed in the following section.

### **2.7.3 Industrial applications**

With fluidised bed reactors the solid particles in a fluidised bed are often a catalyst and the fluid pumped into the bed is a reactant. Generally if the reactant is a liquid the resulting state of fluidisation is homogeneous particulate fluidisation. With a gas reactant the regime will be aggregative with the majority of the reactant forming gas bubbles. This type of mixing results in uniform bed temperature which increases the mass-transfer and reaction rates. The good mass transfer rates of fluidised beds due to constant temperature and high surface area contact between the fluid and solid (Dwivedi & Upadhyay 1977) have led to the development of using fluidised beds for coating particles, absorbing liquid vapours from gas streams and drying. This has led to the development of processes such as water treatment (Heijnen et al. 1989) and for making polymers (Fernandes & Lona 2001). Another application of a fluidised bed reactor is for fluid catalytic cracking (Elnashaie & El-Hennawi 1979). In this process the catalyst particles are used to break apart hydrocarbons in petroleum crude oils to make petrol and distillate fuels.

The capability of SPECT to non-invasively image the internal dynamics of an opaque system has proven to be a practical means of studying bubble velocity, size and coalescence in a fluidised bed for bubbling fluidisation regimes and a measurement of fluid distribution in particulate fluidised regimes. A full description of the SPECT imaging feasibility study can be found in section 3.1.1.

## **2.8 BUBBLE COLUMN**

### **2.8.1 Introduction**

As a continuation of the SPECT feasibility study a bubble column was imaged and analysed. There are similarities in the basic principles behind fluidised beds and bubble columns but, as will be made clear in this section, the bubble column allows more control over the velocity of the radioactive gas tracer therefore the temporal resolution of the SPECT camera could be more clearly defined.

### **2.8.2 Theory**

Bubble column reactors are widely used as multiphase reactors in industry. A basic description of a bubble column reactor is a vertical cylindrical vessel filled with liquid or a liquid-solid suspension and a gas distributor at the bottom. The gas is introduced to the system in the form of bubbles which pass up through the bed. A schematic of a bubble column is shown in Figure 2.32. With a bubble column the gas flow may be controlled to a certain degree by altering the viscosity of the fluid within the column and the rate of flow at which the gas is introduced to the column. As the bubbles pass through the liquid the edge of the bubble creates a phase boundary between the gas and liquid phase where reactions between the two phases. Bubble columns are particularly useful for slow reaction rates as the bubbles have relatively long residence times in the reactor compared to fluidised beds.

There are three common regimes of bubble flow observed in bubble column reactors (Kantarci et al. 2005): bubbly flow, churn-turbulent flow and slug flow. Bubbly flow is a homogeneous flow regime. As with fluidised beds the superficial velocity of the gas flowing through the system affects the observed regime and bubbly flow is seen at low

superficial velocities. The bubbles rising through the liquid are reasonably small in size and uniformly distributed with a good level of mixing across the whole cross section of the column. With this regime there is a good liquid-gas contact and reasonably high liquid-gas mass transfer rate.

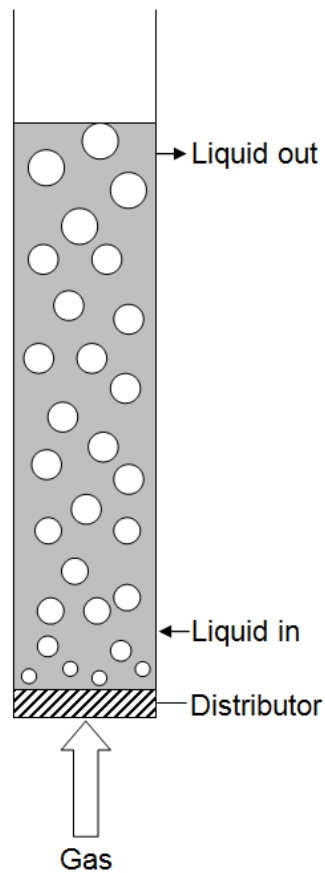


**Figure 2.32. Schematic of a bubble column. Gas is introduced to the liquid of liquid-solid phase through a distributor in the form of bubbles which pass upwards through the bed.**

The churn-turbulent flow is a heterogeneous regime and is caused by increasing the superficial velocity. Bubbles in this regime show unsteady flow patterns and are not uniformly sized due to coalescence and break-up caused by high gas flow rates. There is vigorous mixing with this regime but liquid-gas transfer rates are decreased.

Finally a slug flow regime, as described in section 2.7, occurs when the diameter of the reactor is sufficiently small enough for bubbles to be formed of comparable size.

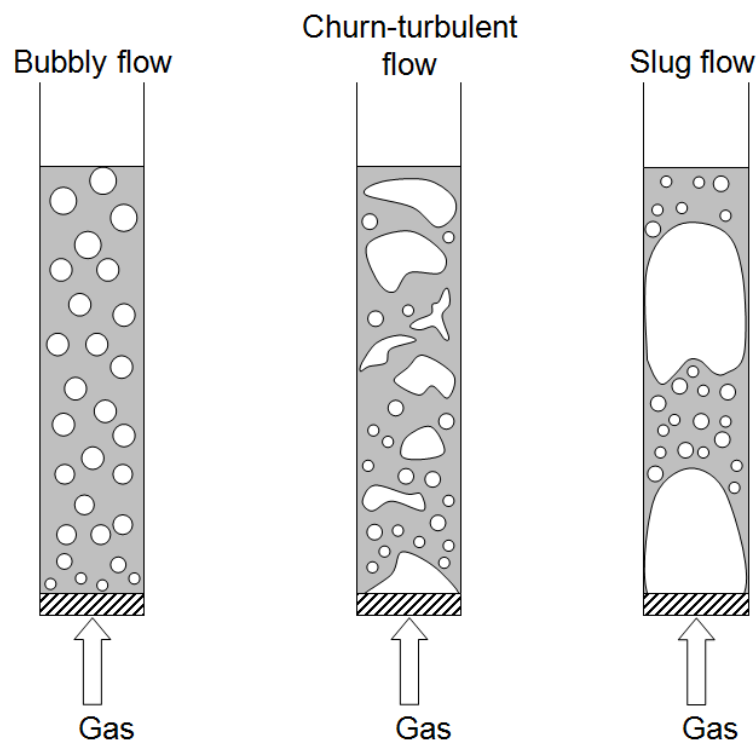


**Figure 2.33. Figure showing the three different flow regimes of bubble column reactors. Bubbly flow occurs at low superficial velocities and the bubbles formed are small and uniformly distributed. By increasing the superficial velocity churn-turbulent flow is observed. With this regime bubbles coalesce and break apart causing unsteady flow through the column. At high velocities and small enough column diameter slug flow occurs. This is when the bubble diameter is comparable to that of the column.**

Equation 2.19 describes the relationship between bubble diameter,  $d_b$ , liquid viscosity,  $\nu_L$ , superficial gas velocity,  $V_{sg}$  and column diameter,  $D_C$ , as proposed by Akita & Yoshida (1974).

$$d_b = 26 D_C \left( \frac{D_C^2 g \rho_L}{\sigma} \right)^{-0.5} \left( \frac{g D_C^3}{\nu_L^2} \right)^{-0.12} \left( \frac{V_{sg}}{\sqrt{g D_C}} \right)^{-0.12}, \quad 2.19$$

where  $g$  is the gravitational constant,  $\rho_L$  is the liquid density and  $\sigma$  is the surface tension.

The following section discusses a few applications of bubble columns in industry.

### 2.8.3 Industrial applications

Bubble columns are widely used as multiphase reactors in chemical industries. The high heat and mass transfer coefficients available using this type of reactor makes the bubble column particularly efficient for chemical processes which involve oxidation, hydrogenation and polymerization. A particularly well known application of the bubble column reactor is the Fischer-Tropsch process (Dry 2002). This process converts syngas, a mixture of hydrogen and carbon monoxide, into liquid hydrocarbons in a slurry bubble column. Slurry is the term used to describe a solid-liquid suspension where solid catalyst particles such as cobalt are mixed into the liquid phase.

For the secondary stage of the SPECT feasibility study it was expected that bubble velocity, size and coalescence in a bubble column could be studied by varying the viscosity of the liquid phase. A full description of the SPECT imaging feasibility study can be found in section 3.1.2.

## **2.9 ADSORPTION**

Adsorption is a gaseous chemical flow process that was chosen for the final radioactive gas imaging study. The reasons for choosing this process to study will be made clear over the following section as the theory is explained and applications discussed. The initial reasons, however, for choosing this process is that gas adsorption is a relatively slow process with a progression rate in the order of  $\text{mm min}^{-1}$  (Caldwell 2014), meaning that it is a dynamic process within the temporal and spatial resolution of the PET camera. Radioactive carbon dioxide,  $^{11}\text{CO}_2$ , can be produced on site using the University's MC40 cyclotron and this radioactive isotope is chemically indistinguishable from stable  $\text{CO}_2$ . As discussed in section 2.6.2 the majority of gas produced when making  $^{11}\text{CO}_2$  is  $\text{N}_2$  which is commonly used as a carrier gas for  $\text{CO}_2$  adsorption studies as it is inert, meaning that the  $^{11}\text{CO}_2$  gas cylinder produced by the cyclotron can act as an  $\text{N}_2$  feed and a controlled amount of  $\text{CO}_2$  can be mixed in for studying.

### **2.9.1 Introduction**

Gas adsorption is a technique that can separate specific gas molecules from a mixture and selectively capture them, which means that  $\text{CO}_2$  can be captured and stored instead of being released into the atmosphere (Yu et al. 2012). Adsorption is also used for drying, gas purification and the sorption of pollutants or poisonous gases, such as in a gas mask. In recent years  $\text{CO}_2$  capture has been of great interest to researchers as there is an increasing need to actively reduce the release of greenhouse gases. One method of reducing  $\text{CO}_2$  levels in industrial exhaust gases, particularly applicable to power stations, is to capture the  $\text{CO}_2$  before it leaves the flue and enters the atmosphere. For the purposes of this project the use of adsorption for capturing  $\text{CO}_2$

will be considered for the reasons described previously with the hope of furthering the understanding of adsorption.

This section provides a description of the theory of gas adsorption and is followed by commonly used measurement techniques.

### **2.9.2 Theory of adsorption**

Adsorption is used for separating specific gas molecules from a mixture through preferential attraction to the surface of a solid. Adsorption is usually classified as either physisorption or chemisorption and depends on the gas selected for capture, the adsorbate, and the material used to capture the gas, the adsorbent. For both types of adsorption the process begins with an initial attraction of the gas molecule to the surface of the adsorbent due to weak van der Waals' interactions. At the surface of a material there are atoms with incomplete bonds as they are surrounded on only one side by the bulk material, this results in an excess energy at the surface. As a gas molecule approaches the surface of the adsorbent there are both repulsive and attractive forces acting between the two and the magnitude of the forces is dependent on the interatomic separation of the gas molecule and surface,  $x$  (Padmavathi 2011). The resulting potential energy curve at the surface of a solid is a combination of the longer range attractive van der Waals potential (of order  $x^{-6}$ ) with the short-range repulsive potential arising from electron orbital overlap (of order  $x^{-12}$ ), described by the Pauli exclusion principle (Stadie 2013). The attractive forces are specific to the interaction between the gas molecule and the surface atoms and the repulsive forces are a result of the Pauli principle. The top plot of Figure 2.34 shows a graphical representation of the attractive and repulsive potential energies,  $E_A$  and  $E_R$  respectively, at an atomic scale. The total energy,  $E$ , is shown as a blue curve and is

the summation of  $E_A$  and  $E_R$ . The equilibrium separation,  $x_0$ , is the point at which the net force acting on the gas molecule is zero, i.e. when the attractive force  $F_A$  is equal and opposite to the repulsive force,  $F_R$  as shown in the bottom plot of Figure 2.34. The red line shows the resulting force as a function of the interatomic separation. The energy and force for atomic systems are related by

$$E = \int F dx. \quad \mathbf{2.20}$$

When the net force acting on the molecule is zero there is a corresponding minimum potential energy,  $E_0$ , which acts as a potential well and is known as the binding energy. If a molecule approaches the surface of the adsorbent with kinetic energy,  $E_k$ , less than the binding energy of the surface the molecule becomes trapped in the potential well. This physical attraction between the molecule and surface is physisorption.

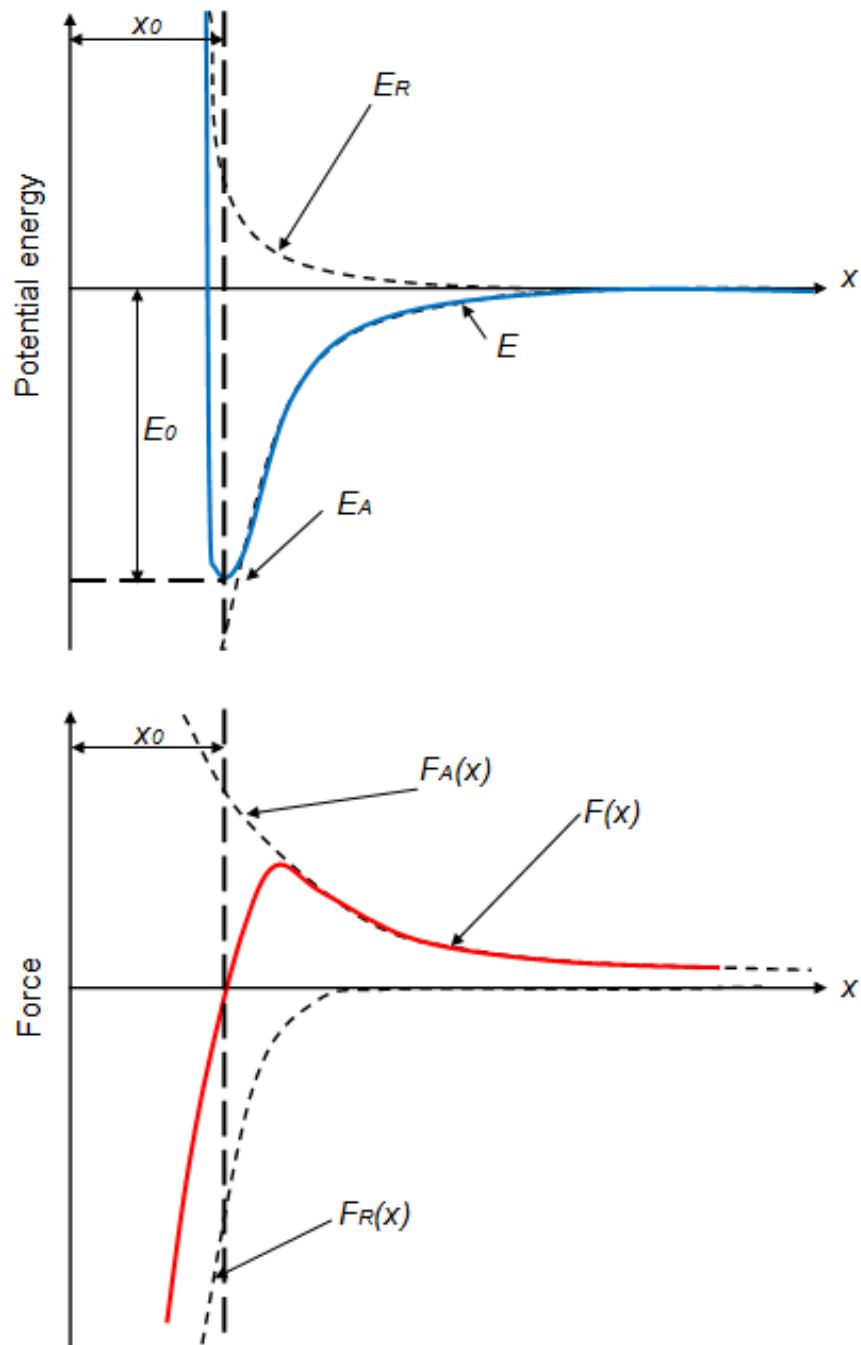
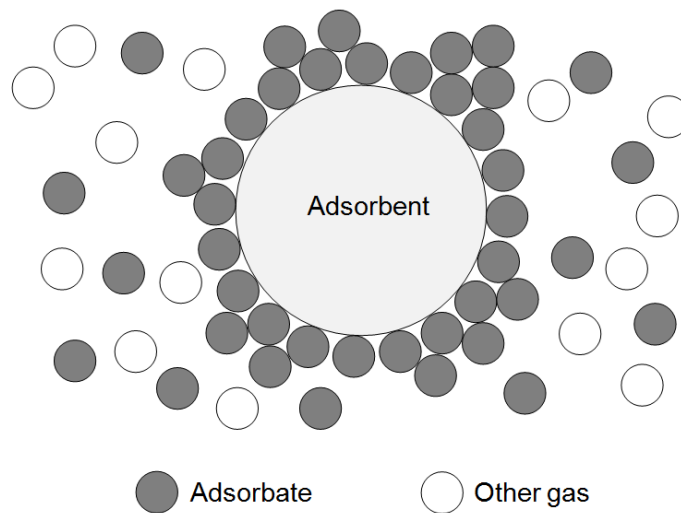


Figure 2.34. The top plot shows the attractive and repulsive energy,  $E_A$  and  $E_R$  respectively, acting on an approaching molecule and resulting total energy,  $E$ . The bottom plot shows the attractive and repulsive forces,  $F_A$  and  $F_R$  respectively, as a function of interatomic separation,  $x$ , and resulting net force,  $F$ . The equilibrium separation is the point at which the net force is zero and corresponds to a minimum energy,  $E_0$ .

Chemisorption involves a chemical reaction between the gas molecule and the adsorbent surface where a chemical bond is created (Webb 2003; Ho & McKay 1998). When the gas mixture is in contact with the surface of the adsorbent gas molecules will collide with the surface. If the gas molecule undergoes an inelastic collision with the surface it will lose energy and will not be able to escape the potential well of the surface. Once the molecule is trapped then it will react with the surface if the adsorbent and adsorbate are compatible forming a chemical bond.

The adsorption process that describes the attraction of CO<sub>2</sub> to the adsorbents chosen for this project, Activated Carbon and Zeolite 13X, is physisorption so chemisorption will not be discussed in more detail.



**Figure 2.35. Diagram demonstrating preferential attraction of adsorbate gas molecules to the surface of the adsorbent.**

An adsorption column is a tube packed with an adsorbent material, most commonly in bead, pellet or powder form, through which a gas mixture is passed (McCabe et al. 1993b). As the gas is passed through the column the adsorbate gas molecules that

come into contact with the surface of the adsorbent will be attracted to the surface displacing any molecules with a lower attractive force. One adsorbent bead will have a finite number of “vacancies” which may be filled with adsorbate gas molecules as shown in Figure 2.35. Once these vacancies are filled the adsorbent bead is saturated and the gas molecules in the gas mixture are no longer attracted to the surface meaning they pass over the saturated bead until they find a vacancy on a different bead. This means that there is a Mass Transfer Zone (MTZ) that progresses down the length of the column and in this zone are the adsorbent beads that are undergoing adsorption. Upstream of this MTZ is the saturated section of the bed, where all of the adsorption sites on the surface of the adsorbent are occupied. The rest of the bed downstream will theoretically be untouched by the adsorbate gas molecules; however the rest of the gas mixture which is not adsorbed will pass through the bed unimpeded resulting in “clean” effluent.

Figure 2.36 is a simple diagram showing how the MTZ progresses along the length of an adsorption column as time passes. Before the introduction of the gas mixture the adsorbent in the column will be fresh and untouched by the adsorbate. As the gas mixture is introduced to the system the specific adsorbate gas molecules will theoretically be attracted to the first vacancy they come into close proximity to, displacing the existing molecule occupying the site and removing the adsorbate gas molecule from the gas stream. The MTZ progresses in this manner until it reaches the end of the bed, at which point the whole adsorption column is completely saturated and cannot capture any more of the adsorbate. This means the adsorbate can flow directly through the column, rendering the column ineffective. Before this point the bed must be purged and regenerated so that it may be used again. The following sections

go into greater detail about the adsorption process, how it is measured and its uses in industry.

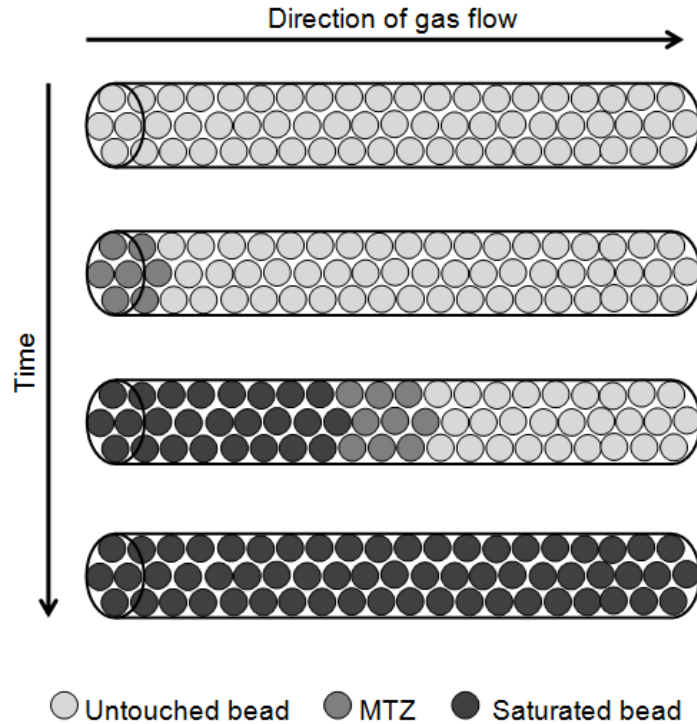


**Figure 2.36. Diagram showing the progression of the MTZ along the column as time passes.**

### 2.9.3 Capacity and breakthrough

The efficiency and effectiveness of an adsorption process can be determined by analysing the rate at which the adsorbent exits the column (McKetta 1993). Figure 2.37 shows the loading of adsorbate along the column with time and the resulting progression of the breakthrough curve. The plots on the left of the figure show the progression of the MTZ along the column with increasing time for each successive plot. The loading of adsorbate,  $q_i$ , refers to the quantity of adsorbate  $i$  captured by the adsorbent and is usually measured in  $\text{mol kg}^{-1}$ . The initial loading of a fresh bed,  $q_0$ , is

zero and  $q_m$  refers to the maximum loading at equilibrium indicating saturation. The plots on the right show the breakthrough curve at each time interval where the amount of adsorbate exiting the column is measured as a percentage of the total gas mixture at the outlet. The point at which the first molecules of the adsorbate exit the column because they did not make contact with an available vacancy is called breakthrough. As time passes and the vacancies in the column fill up the amount of adsorbate exiting the bed will increase until a point is reached where the amount of adsorbate exiting the bed is equal to the amount entering. This point is called equilibrium and occurs because the adsorbent is completely saturated. The resulting plot of amount of adsorbate exiting against time is known as a breakthrough curve and is generally S-shaped, as described in Figure 2.37. The breakthrough curve can be used to determine a number of adsorption characteristics such as efficiency, capacity and reusability. One clear indication of an efficient adsorption system is a steep breakthrough curve as this would imply a narrow MTZ meaning the uptake of adsorbate from the gas phase to the solid is rapid. The breakthrough curve allows a calculation of the quantity of adsorbate that is captured by the adsorbent at equilibrium and is known as the adsorbent capacity.

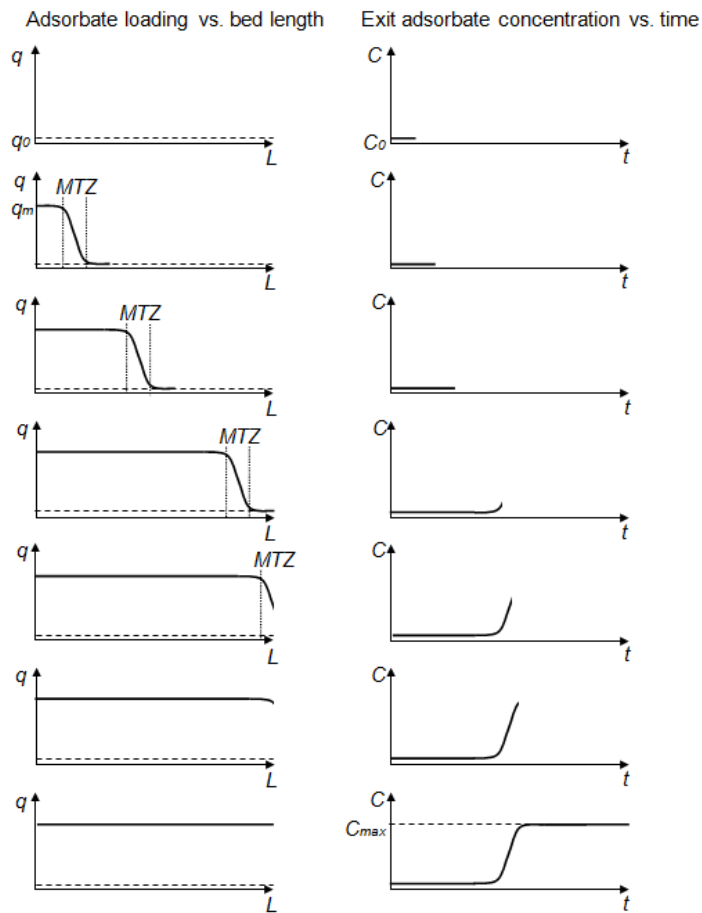


**Figure 2.37.** The plots on the left show adsorbate loading,  $q$ , along the length,  $L$ , of the column and the plots on the right show corresponding exit adsorbate concentration,  $C$ , against time,  $t$ .

The efficiency of the process is determined by the quantity of adsorbate captured before breakthrough. For the use of adsorption in industry for removing  $\text{CO}_2$  (or other unwanted gas molecules) from exhaust gas the adsorption column cannot operate beyond breakthrough if 100% capture is required. Once the amount of  $\text{CO}_2$  exiting the bed is greater than some breakthrough threshold (usually  $\sim 5\%$ ) the adsorbent is no longer considered to be effectively separating the  $\text{CO}_2$  from the gas mixture. At this point the column will need to be “cleaned”, or regenerated, and the captured  $\text{CO}_2$  will

need to be recovered and stored. Figure 2.38 shows a schematic of two adsorption columns operating in parallel for continual CO<sub>2</sub> removal from “dirty” exhaust gas (Ho et al. 2008). Figure 2.38 (a) shows the route of the gas flow in red. The “dirty” exhaust gas is flowed into Adsorber A where the CO<sub>2</sub> is adsorbed and the “clean” effluent exits at the bottom. The exhaust inlet and treated gas outlet for Adsorber B is closed during this stage of the process as it is regenerated. A common method of regeneration is to heat the adsorber (temperature swing adsorption) or reduce the pressure (pressure swing adsorption) which gives the captured adsorbate enough energy to escape from the surface of the adsorbent. The released adsorbate is then passed through to a condensing and storage process. Once CO<sub>2</sub> reaches the exit of Adsorber A the process is switched and Adsorber B becomes the active adsorber while Adsorber A is regenerated, as shown in Figure 2.38 (b).

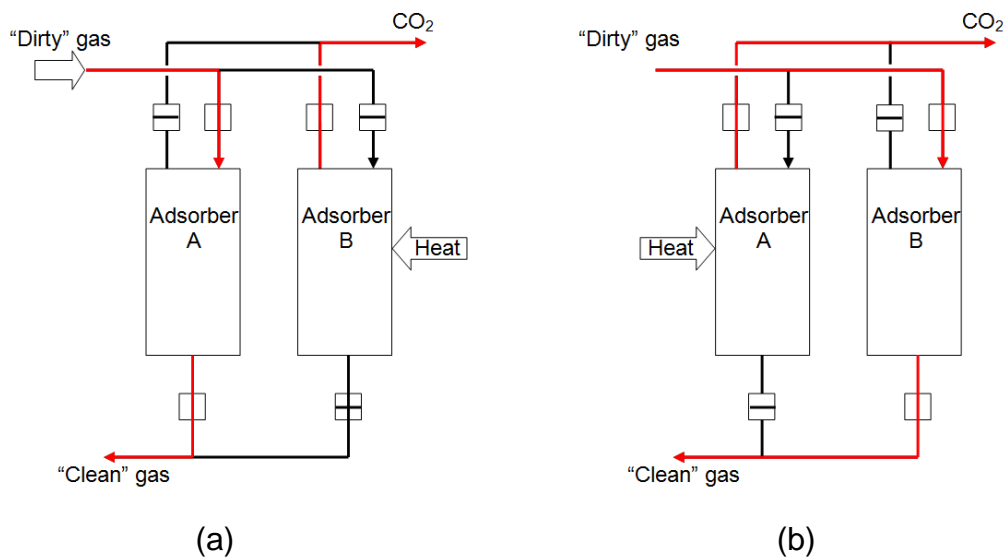


**Figure 2.38. Two fixed bed adsorbers operating in parallel. (a) Shows the “dirty” exhaust gas entering Adsorber A where the CO<sub>2</sub> is adsorbed and “clean” gas exits the bed. Simultaneously Adsorber B is being regenerated, whereby the adsorber is heated providing the adsorbate molecules with enough energy to be released and passed on to a condensing and storage process. (b) Shows that when breakthrough occurs for Adsorber A the active adsorber is switched to Adsorber B and Adsorber A is regenerated.**

A number of factors can affect the efficiency of the adsorption process and the capacity of the adsorbent, the most influential are: type of adsorbent used, the pressure of the system, the temperature of the system, the flow rate of the gas mixture entering the column and the concentration of adsorbate in the gas mixture.

There are different options available for adsorbent material depending on the specific gas that is to be captured. These options include zeolites and activated carbons, which have both been used in the course of this project. The main requirement of an adsorbent material is to have a very large surface area to mass ratio as this provides more sites to attract the adsorbate. For example activated carbons can have a surface area greater than 500 m<sup>2</sup> per gram of material (Dabrowski & Meurant 1999). For the purposes of discussing adsorption the surface area of an adsorbent is defined as the maximum monolayer coverage of an adsorbate on the surface. When selecting an adsorbent there are many things which need to be considered: capacity, selectivity, regenerability, kinetics, compatibility and cost (Choi et al. 2009). It is not very often that an adsorbent will be found to meet all of these requirements so it is also important to decide which factors are most desirable for a given purpose.

The capacity of an adsorbent, as mentioned earlier, is defined as the amount of adsorbate that can be captured by the adsorbent per unit mass of adsorbent. A number of factors can affect the capacity of an adsorbent, such as temperature and pressure. Generally speaking the capacity of an adsorbent decreases with increased temperature and increases with increasing pressure. Capacity data is generally presented as isotherms: plots of capacity at equilibrium against partial pressure of adsorbate at constant temperature. This allows a comparison between adsorbent materials. A major contributor to the difference between various adsorbents, aside

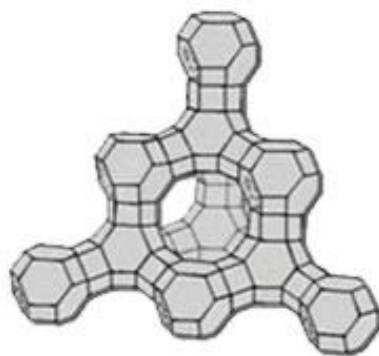


**Figure 2.39. Figure showing<sup>1</sup> the tetrahedral structure of silica and alumina that make up Zeolite 13X. This structure contains consistent pore diameters of 0.1 nm.**

from chemical structure, is the pore size distribution. The particular zeolite used in this project was 2-3 mm beads of Zeolite 13X from Sigma Aldrich (USA). The zeolite 13X beads are crystalline metal aluminosilicates with a network of silica and alumina tetrahedral as shown in Figure 2.39. To produce the uniform cavities required to selectively adsorb specific molecules smaller than a predefined critical diameter,  $d_c$ , the beads are heated to remove the natural water of hydration. The surface area of zeolite 13X is around  $750 \text{ m}^2 \text{ g}^{-1}$  (Vyas et al. 2004) and the pore diameters of zeolite 13X are a consistent 0.1 nm allowing adsorption of molecules with a critical diameter less than 0.1 nm. The critical diameter of a molecule is defined as the diameter of the smallest cross section of a molecule as show for  $\text{CO}_2$  in Figure 2.40 the critical diameter for  $\text{CO}_2$  is 0.028 nm and the critical diameter of  $\text{N}_2$  is 0.03 nm. Activated carbon, on the other hand, has a network of pores of a range of sizes which can be

---

<sup>1</sup> <http://molsieveabsorbent.com/choose-zeolite-molecular-sieve.html> (accessed: June 2015)

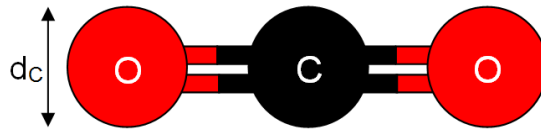


**Figure 2.40. Diagram showing how the critical diameter,  $d_c$ , is defined for  $\text{CO}_2$ .**

split into three categories: macropores which have a diameter greater than 50 nm, mesopores which have a diameter between 2 and 50 nm and micropores which are smaller than 2 nm (Dabrowski & Meurant 1999). Figure 2.41 shows the internal structure of activated carbon and differing pore sizes. Activated carbons are produced from materials with a naturally high carbon content e.g. coal. This is then activated using steam or chemicals to expand the pore network in the adsorbent. The 3 – 10 mm activated carbon pellets used for this project were obtained from Brownell Limited (UK) and they have a surface area between 800 and 1200  $\text{m}^2 \text{g}^{-1}$ , which is larger than that of Zeolite 13X.

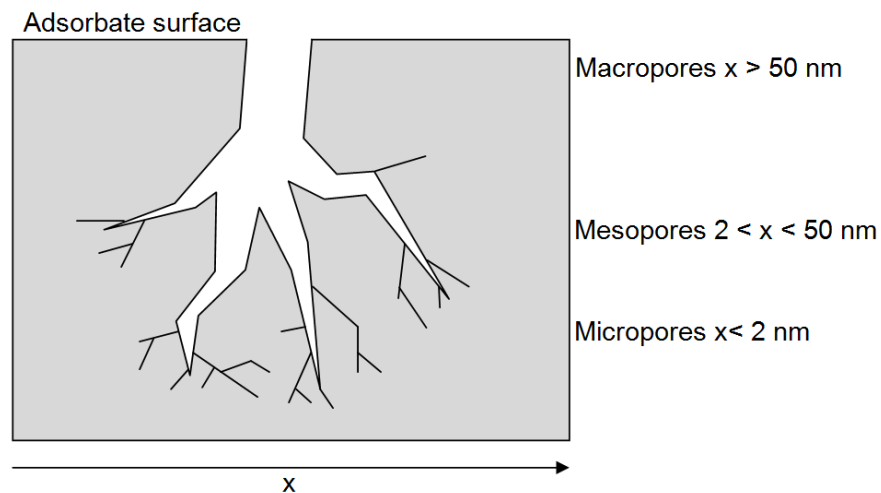


**Figure 2.41. Diagram showing the structure of macropores, mesopores and micropores.**

The pressure of the adsorption system has an influential effect on the capacity of the adsorbent because as pressure increases the volume of the gas decreases. This means that for the same adsorbent surface area more molecules can be attracted to the surface because they take up less room. The temperature of the system affects the capacity because adsorption is an exothermic process. As adsorbate molecules are attracted to the surface of the adsorbent this results in a decrease in excess surface energy which in turn results in a loss of heat, hence exothermic. According to Le Chatelier's Principle (Brunauer 1944) exothermic reactions are more favourable at lower temperatures. This means that if the system temperature of an adsorption process is increased from equilibrium then the system will try and cool itself down. To do this it will absorb the extra heat added to the system, reducing the number of exothermic reactions and also providing the adsorbed molecules more energy to escape. If the system temperature is reduced the system will try to bring the temperature up by favouring the exothermic reaction, thus capacity is increased at lower temperatures.

The selectivity can be defined as the ratio of adsorbate to other gas molecules adsorbed at a set adsorbate concentration (Talbot 1997). Although the adsorbent should preferentially adsorb the adsorbate over carrier gas molecules there will still be some other gas molecules captured at the surface. Each adsorbent material will have different selectivity for different gas mixtures so it is important that the selectivity is considered based on the adsorbate and carrier gas used.

It is desirable for an adsorbent to be effectively regenerable. This means that an adsorbent can be used repeatedly with uniform performance by regenerating the bed after use. Two common methods of a regenerative adsorption process are Pressure

Swing Adsorption (PSA) and Temperature Swing Adsorption (TSA). With PSA the temperature of the system is kept constantly low and the pressure is increased to encourage adsorption. Once the adsorption column is saturated the pressure is released and the captured adsorbate is flushed out of the column due to the reduction in capacity (Gomes & Yee 2002; Chahbani & Tondeur 2000). With TSA the pressure of the system is kept constantly high and the temperature is reduced to encourage adsorption. Once the adsorption column is saturated the temperature would be raised to decrease the capacity of the adsorbent allowing the captured adsorbate to be flushed out (Merel et al. 2008). Adsorbent compatibility mentioned earlier can affect the regenerability of the adsorbent and refers to the ability of the adsorbent material to withstand potential physical or chemical damage from the adsorbate or carrier. For this reason the adsorbent should be inert to the carrier phase and the operating conditions should be such that the temperature or pressure of the system does not cause permanent damage to the adsorbent affecting the regenerability.

Finally the adsorbent cost must be considered for industrial purposes as this process will be performed on a large scale meaning large quantities of adsorbent would be required which can be very expensive depending on the material chosen.

Now the specifications of the adsorbent material are understood the efficiency of the adsorption process under different operating conditions can be considered. The efficiency of the separation of molecules from the gas phase is essentially a result of the binding energy which is holding the molecules. The magnitude of the binding energy, the depth of the potential well, is dependent on a number of factors which affect the excess potential energy at the surface of the adsorbent and the net force between adsorbate and adsorbent. The separation of adsorbate molecules from the

bulk is also dependent on the probability of an adsorbate molecule making contact with a surface vacancy with the right properties for capture. Thus far the theoretical process of adsorption has been discussed which assumes instantaneous capture of an adsorbate molecule as it makes contact with a vacancy. However, the mass transfer rate of adsorbate from gas to solid phase is dependent on the adsorbate molecule having kinetic energy lower than the binding energy and colliding with an empty site. The variable operating conditions of adsorption will now be discussed in terms of separation efficiency.

The first condition discussed is the feed flow rate of the gas mixture which varies the probability of an adsorbate molecule colliding with an empty site. At a lower flow rate the gas molecules will spend more time in the vicinity of empty adsorption sites increasing the chance of adsorption. By increasing the flow rate the probability of an adsorbate molecule being adsorbed is decreased because it will spend less time in the proximity of surface vacancies meaning the adsorbate will breakthrough much before the adsorption column is saturated. In turn the concentration of adsorbate in the gas mixture will also affect the efficiency of the adsorption process. By increasing the number of adsorbate molecules present in the gas mixture the probability of a molecule coming into contact with a free site is increased and vice versa. It has been explained that the temperature and pressure of the system can affect the specific adsorbate uptake rate of the adsorbent which is described by mass transfer kinetics (Godish 1989). The mass transfer kinetics of the adsorbent can be described by the shape of the breakthrough curve. The term mass transfer kinetics refers to the net movement of the adsorbate from the gas phase to the solid phase in the MTZ. A sharp breakthrough curve would indicate fast kinetics and a broad curve would be produced from slow

kinetics. For a more complete understanding of adsorption it may be split into two categories: adsorption equilibria (thermodynamics) and adsorption kinetics. These topics are covered in sections 2.9.4 and 2.9.5 respectively.

#### **2.9.4 Adsorption equilibria**

Adsorption equilibrium refers to the point in the adsorption process where the amount of adsorbate entering the column is equal to the amount exiting and generally describes saturation. The first theory of adsorption was developed in 1918 by Langmuir (Langmuir 1918) and assumes that the adsorbate gas behaves like an ideal gas and that the theory of gas kinetics is applicable. The theory of gas kinetics states that a gas is made up of a large number of particles all moving rapidly and randomly colliding with each other and container walls and Langmuir's theory states that the constant bombardment of gas molecules at the wall is equal to the number of molecules evaporating from the surface (desorption) at equilibrium. This gives a net accumulation of zero on the surface. There are three main assumptions of Langmuir's adsorption model:

1. The surface of the adsorbent is flat and homogeneous, meaning the adsorption energy is constant over the whole surface
2. Adsorption on the surface occurs in distinct localised points called sites
3. Each site can only hold one molecule

The rate at which the gas particle will strike the surface is given by the kinetic theory of gas and is known as the impingement rate  $\Phi$ :

$$\Phi = \frac{n\bar{v}}{4} \qquad \mathbf{2.21}$$

and is measured as the number of molecules per unit time per unit area ( $\text{s}^{-1} \text{m}^{-2}$ ). Here  $n$  is the molecular density of the gas ( $\text{m}^{-3}$ ) and  $\bar{v}$  is the average molecular velocity ( $\text{m s}^{-1}$ ):

$$\bar{v} = \sqrt{\frac{8RT}{\pi M}}. \quad 2.22$$

Here  $R$  is the universal gas constant ( $\text{J K}^{-1} \text{mol}^{-1}$ ),  $M$  is molar mass ( $\text{kg mol}^{-1}$ ) and  $T$  is temperature (K). With adsorption a fraction of the gas molecules striking the surface will be captured by the van der Waals force of the surface and will be held there until they are desorbed. The rate of particles being adsorbed in moles per surface area per unit time,  $R_a$ , is given by the impingement rate multiplied by a sticking coefficient,  $\alpha$  (dimensionless) (Coulson & Richardson 1994):

$$R_a = \frac{\alpha n \bar{v}}{4}. \quad 2.23$$

If a particle strikes a site that is already occupied then it will essentially bounce back as per assumption number 3 (only one molecule can occupy a site). This means that the adsorption rate of a partially occupied surface is dependent on the number of available sites, or vacancies:

$$R_a = \frac{\alpha P}{\sqrt{2\pi MRT}} (1-\theta), \quad 2.24$$

where  $\theta$  is the fractional coverage and is defined as the ratio of sites occupied to total number of sites. This rate is also dependent on pressure,  $P$ , as an increase in pressure increases the total number of sites. The rate at which the particles are desorbed from the surface is given by

$$R_d = k_d \theta = k_{d\infty} e^{\left(-\frac{E_a}{RT}\right)} \theta, \quad 2.25$$

where  $R_d$  is rate of desorption,  $k_d$  is the rate constant for a saturated surface,  $k_{d\infty}$  is the rate constant for desorption at infinite temperature and  $E_a$  activation energy for desorption. The activation energy is the energy required to escape the potential well at the surface so is equal to  $E_0$ .

The average time that an adsorbate molecule will be held by the adsorbent is dependent on the magnitude of  $E_0$  and is defined as

$$\tau_a = \tau_{d\infty} e^{\left(\frac{E_a}{RT}\right)}. \quad 2.26$$

This is known as the residence time of adsorption,  $\tau_a$ , where  $\tau_{d\infty}$  is the adsorbed atoms period of thermal vibrations and  $\tau_{d\infty} = 1/k_{d\infty}$ . It can be seen from equation 2.26 that the residence time increases with increased activation energy, meaning the deeper the potential well at the surface the longer an adsorbed molecule will be held. These equations lead to the formation of Langmuir's isotherm. By equating the rate of adsorption to the rate of desorption the fractional coverage can be written in terms of fractional loading

$$\theta = \frac{bP}{1+bP} \quad 2.27$$

where

$$b = \frac{\alpha}{k_{d\infty} \sqrt{2\pi MRT}} e^{\left(\frac{E_a}{RT}\right)}. \quad 2.28$$

Here  $b$  is known as the affinity constant and represents the strength of the bond between the adsorbate molecule and the adsorbent surface and is dependent on temperature.

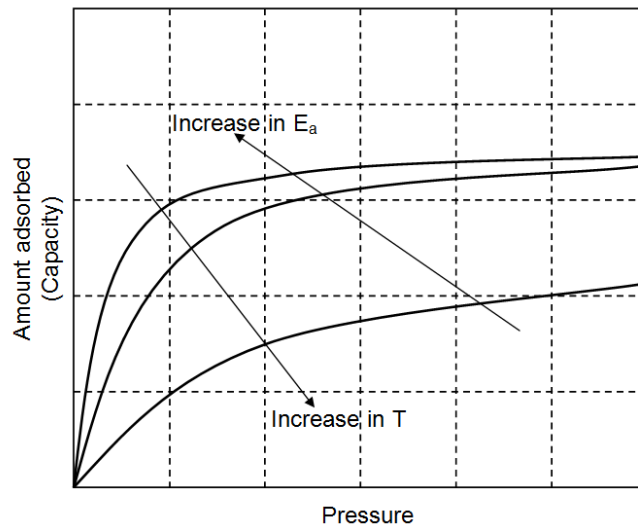


**Figure 2.42. Example of Langmuir isotherms.**

Figure 2.42 shows the behaviour of the Langmuir isotherm as the amount of adsorbate adsorbed against partial pressure of the adsorbate. As Langmuir's theory assumes one molecule per site and that the adsorbent surface consists of an array of localised sites this means that Langmuir's theory assumes monolayer coverage. This means that the amount of adsorbate adsorbed is directly proportional to the fractional surface coverage,  $\theta$ . It can be seen from Figure 2.42 that as the pressure increases the amount adsorbed tends towards a maximum capacity value, signified by a plateau. The isotherm examples also show that as temperature increases the capacity of the adsorbent decreases and as the activation energy increases, meaning an increase in  $b$ , the capacity increases. In order to evaluate the isotherm equations in terms of amount adsorbed against pressure the adsorption affinity is dependent on temperature:

$$q = q_m \frac{bP}{1+bP} \quad 2.29$$

Here  $q$  is the amount of adsorbate adsorbed ( $\text{mol kg}^{-1}$ ) and  $q_m$  is the saturated amount adsorbed ( $\text{mol kg}^{-1}$ ). The Langmuir isotherm equations form the basis for the majority of equations developed since 1919 (Foo & Hameed 2010). Equation 2.30 shows a modification developed in 1971 by Toth to account for heterogeneous adsorbent surface (Cavenati et al. 2004):

$$q = q_m \frac{bP}{[1+(bP)^{C_{T0}}]^{1/C_{T0}}} \quad 2.30$$

where the heterogeneity parameter  $C_{T0}$  is defined as

$$C_{T0} = A+BT . \quad 2.31$$

Here  $A$  and  $B$  are parameters specific to the adsorbate.

There are many more modified adsorption isotherm equations developed to include characteristics such as adsorbent surface roughness, interactions between adsorbate molecules and to allow for multiple adsorbate molecules to occupy one site. It was deemed sufficient to explore the Toth isotherm equations for the purposes of this project as the initial study presented in this thesis concentrates on the general uptake of  $\text{CO}_2$  onto two different adsorbents. The investigation gives an idea of the extent of the observable interactions within the column using the imaging technique and the applicability of using more complex models is discussed in section 6.2.

### 2.9.5 Kinetics

In order to describe the mass transfer kinetics of the adsorbate uptake in the system a mass transfer rate equation is required. For the purposes of this project the Linear Driving Force (LDF) approximation equation will be considered. This is a commonly used first order kinetics equation that relates the fluid phase and adsorbed phase by a

single mass transfer resistance. The LDF approximation is given by equation 2.32 (McCabe et al. 1993b).

$$\frac{\partial q}{\partial t} = k_{eff}(q_m - q) \quad 2.32$$

Here  $k_{eff}$  is the intraparticle mass transfer coefficient of the adsorbent particle and is given by:

$$k_{eff} = \frac{15 D_e}{r^2}. \quad 2.33$$

Here,  $D_e$  is an effective intraparticle diffusion coefficient which is dependent on adsorbate molecule size and the porosity of the adsorbent and  $r$  is the radius of the spherical adsorbent bead. For an adsorbent pellet of infinite length the factor 15 would be replaced by 8. The overall mass transfer coefficient is dependent on the external coefficient and an effective internal coefficient. The external coefficient relates to the diffusion of adsorbate through the fluid film on the surface of the adsorbent and can be considered almost instantaneous. The internal coefficient, however, relates to the diffusion through the adsorbent pores to the internal adsorption sites and the value for the internal coefficient will change with time as the molecules must travel further and further to reach a vacant site. This leads to the expectation that two different mass transfer rates should be observable using the gas imaging technique: the instantaneous surface adsorption rate and the slower internal adsorption rate. An approximate internal mass transfer coefficient,  $k_{int}$ , is given by equation 2.34 and is applicable for spherical adsorbent beads (Wilcox 2012).

$$k_{int} \approx \frac{10 D_e}{d_p}. \quad 2.34$$

Here  $d_P$  is the adsorbate particle diameter and this leads to a reasonable estimate of the overall mass transfer:

$$\frac{1}{k_{eff}} \approx \frac{1}{k_{ext}} + \frac{1}{k_{int}} \approx \frac{1}{k_{ext}} + \frac{d_P}{10D_e}, \quad 2.35$$

where  $k_{ext}$  is the external mass transfer coefficient and is given by

$$k_{ext} \approx \frac{5 D_e d_P}{r^2}. \quad 2.36$$

For the purposes of analysing the breakthrough curves the LDF approximation will be used as the mass transfer coefficient is an overall coefficient that covers both internal and external adsorption rates and had proven to be sufficient for analysing simple adsorption processes (Liaw et al. 1979).

There are more detailed kinetic models that have been developed such as the Lagergren pseudo-first order and the pseudo 2<sup>nd</sup> order kinetics (Rashidi et al. 2013). The feasibility of using the proposed imaging technique to produce results that can verify complex kinetics models has been discussed in section 6.2.

### 2.9.6 Measurement techniques

This section will give a general overview of a few different measurement techniques used to calculate the adsorbent capacity at equilibrium.

The technique used to verify capacity calculations' using the imaging technique was through effluent analysis as it was possible to use this method simultaneously with the imaging technique. By passing the outlet stream of the adsorption column through a gas analyser the amount of adsorbate held in the column can be calculated. The result of using a gas analyser is a breakthrough curve as described in section 2.9.3 and shown in Figure 2.37. This gives an adsorbate concentration of the total output gas as

a function of time. As the total gas flow of the adsorbate and carrier gas entering the adsorption column is known the breakthrough curve can be plotted in terms of volume of adsorbate exiting the column against time. By taking away the amount of adsorbate that exits the column from the amount that enters the column one is left with the total amount of adsorbate held by the adsorbent in the column.

For more accurate measurements of absolute adsorbent capacity volumetric and gravimetric measurements techniques are available. It is expected that if the imaging technique presented here was developed to allow quantitative measurements of CO<sub>2</sub> capacity within the bed the techniques described below would provide a determination of the relationship between activity and capacity.

Once an adsorbent particle is fully saturated and is said to be at equilibrium it will be wholly covered in a film of adsorbate. This changes two distinct characteristics of the adsorbate, its mass and its volume. Techniques have been developed to measure the change in mass and volume from clean and regenerated adsorbent particles to fully adsorbed to give an amount of adsorbate that has been captured (Belmabkhout et al. 2004). Volumetric methods are based on the principle that as adsorbate molecules are removed from the bulk gas mixture to bind with the surface of the solid to create a tightly packed film this means there is a net decrease in gas molecules in the fluid phase. This gives a decrease in pressure of the bulk gas mixture. The change in pressure for a known gas volume can be measured and this value is used to calculate the amount of adsorbate that has been removed from the fluid phase. Gravimetric methods of measuring the amount of adsorbate captures essentially use a mass balance to determine the weight of an adsorbent particle at different pressures. As the

molecular mass of one molecule of adsorbate is known and the mass of the adsorbent is known a total amount of adsorbate captured can be calculated.

## **2.10 HARDWARE**

### **2.10.1 SPECT camera**

The Positron Imaging Centre in the University of Birmingham operates an ADAC Forte gamma camera and has been modified for PEPT work, a full description of which can be found in (Parker et al. 2002). The gamma camera used consists of two camera heads mounted upon a gantry. These heads consist of one flat sodium iodide crystal plane, or detector, for each head which are optically coupled to an array of 55 photomultiplier tubes. The gantry is connected to a computer system that both controls the operation of the camera as well as acquisition and storage of acquired images. The system to be imaged is placed in between the two gamma camera heads with collimators attached. Collimators were used on the camera heads as a way of obtaining spatial information about the gamma emissions from the gamma emission source. The collimators consist of a sheet of lead tungsten alloy of thickness 54 mm with an array of thousands of parallel holes through it of diameter 2.03 mm and separation of 0.152 mm. The gamma camera heads detect the incident photons and the collimators restrict the incident direction of the photons with an angular range of  $\pm 2^\circ$ , meaning that the vast majority of all gamma rays emitted will not be detected due to their angle of incidence. The transmitted photons are spatially correlated and thus serve to form the basis of an image of the radioactivity distribution within the camera plane with a spatial resolution of 5-8 mm.

### 2.10.2 PET camera

The PET camera used for this project was the University of Birmingham's Siemens ECAT ART PET scanner. The high resolution ECAT ART scanner is capable of 3D dynamic imaging and has two sets of opposing banks of detectors where each bank is composed of 11 x 3 blocks of detectors. Each block of detectors has 8 x 8 bismuth germinate (BGO) detector crystals which gives the equivalent of 24 virtual rings. The rings are called virtual because although there is not a full ring of detectors when the detector banks rotate around the FoV the partial rings of blocks act as full rings. Each of the crystals is 6.75 x 6.75 mm with a depth of 20 mm and there are 16 crystals per Photo-Multiplier Tube (PMT). The diameter of the crystal rings is 82.5 cm and the axial length is 16.2 cm and the user manual states a spatial resolution of about 6 mm. The ECAT ART acquires data for 192 angles of view.

The default protocol used for acquiring and processing image data was a two stage protocol. The first stage was the dynamic emission stage, of which the parameters and definitions are taken from the operators manual (Siemens 1996) and are listed below:

- Upper Limit of Detection (ULD) of 650 keV and Lower Limit of Detection (LLD) of 350 keV – these limit define the energy window of the detectors. Anything outside these limits will not be registered as a detection
- Timing window of 12 ns for true coincidences
- Trues only sinogram mode – prompts and delayed are not recorded

The second stage of the protocol is the image reconstruction. The default set-up used for the PET studies presented in this thesis was as follows, unless specified otherwise. The definitions of each setting were found in the software operators manual (Siemens 1996):

- Reconstruction method: FBP
- Image size: 47 planes of 256 x 256 pixels
- Radial filter: Gaussian kernel FWHM: 6 mm
- Axial filter: All pass (cut-off frequency 0.5)

In the second stage of the protocol the projection data is multiplied pixel-by-pixel with normalisation data which consists of corrections for varying crystal efficiency and PMT gains. This normalisation process is applied to provide a uniformly scaled count rate for each pair of detectors. A decay correction is also applied in the image reconstruction stage of the protocol. For frame duration less than 1/3 of the radioactive tracer half-life an approximation method is used and the decay correction is computed by a Taylor series.

The resulting image array is 47 axial planes of 256 x 256 pixels which are 2.54 x 2.54 mm which equates to an image FoV of 650 x 650 mm spaced 3.45 mm apart unless stated otherwise.

## 3 PRELIMINARY STUDIES

This chapter discusses the preliminary experiments performed to determine the limitations of SPECT and PET for imaging dynamic gaseous flow processes. The spatial and temporal resolutions of each technique were investigated and the ability to identify specific process characteristics was determined. The final section of the chapter summarises the findings from both techniques and a conclusion is made about the technique which shows the most potential to continue this study.

### 3.1 SPECT INVESTIGATION

#### 3.1.1 Fluidised bed study

##### 3.1.1.1 Introduction

The first nuclear imaging technique applied to the investigation of a chemical process in this project was using SPECT to study a fluidised bed. This feasibility study describes the experimental method and summarises the results in comparison to what was expected from literature.

##### 3.1.1.2 Experimental procedure – Fluidised bed

The first SPECT study carried out was using a fluidised bed, a description of which can be found in section 2.7. The equipment used was set up as shown in Figure 3.1. The dimensions of the pseudo 2D fluidised bed were a height of 1 m, width of 30 cm and thickness of 2 cm. The bed was placed in between the two gamma camera heads with parallel-hole collimators attached to obtain spatial information about the location of the gamma emissions from the  $^{81}\text{Kr}^m$ . As described in section 2.3.2.2 parallel-hole collimators allow direct correlation between the detected event and point of emission.

This means that the raw image data does not need to be processed to create an image, however there is no way to define the distance travelled by the photon before detection so there is no depth information, thus the resulting acquisition data is a projected image.

The bed was set on an adjustable table so that the height of the bed as a whole could be changed in order to observe different sections of the bed. Fine glass ballotini particles were poured into the bed to a height of around 30cm. The particle size was measured using a laser diffraction size analyser giving a mean particle diameter of  $5\ \mu\text{m}$  hence the particles belong to Geldart group A (see section 2.7.2). The gas used was  $^{81}\text{Kr}^{\text{m}}$  which was produced by a  $^{81}\text{Rb}/^{81}\text{Kr}^{\text{m}}$  generator as described in section 2.6.1. The  $^{81}\text{Kr}^{\text{m}}$  gas is extracted by blowing air through the ion exchange column.

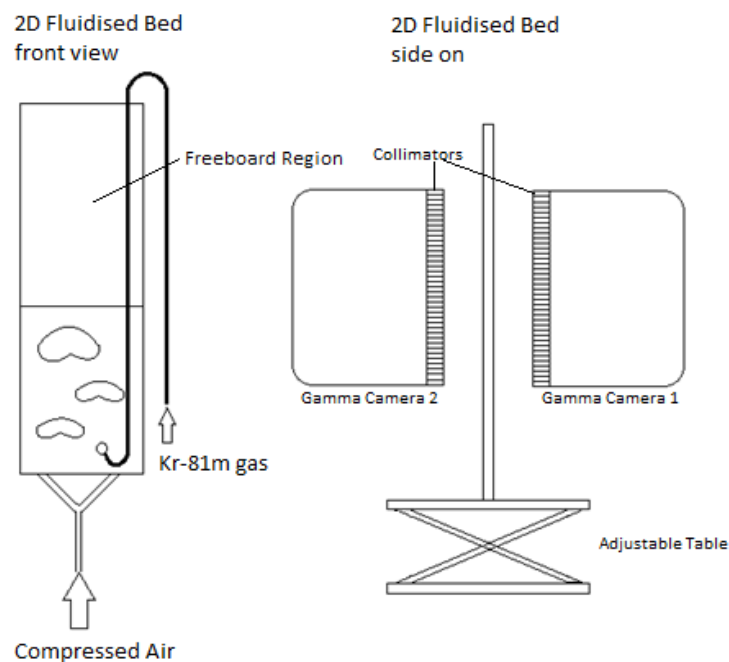


**Figure 3.1. Experimental set up of the fluidised bed study. The pseudo 2D fluidised bed was placed in between the two gamma camera heads and compressed air was used to fluidise the solid particles.**

Krypton-81m undergoes isomeric decay, has a half-life of 13.1 seconds and the main emission is 191 keV gamma rays, which may be detected by gamma cameras and used for creating images. The krypton generator was positioned close to the bed, and using a metal tube with an internal diameter of about 1 mm the gas was fed to the bottom of the bed, keeping the residence time of the krypton in the tube as low as possible. Air was passed through to the generator from an air pump which produced a flow rate of 1 l min<sup>-1</sup> to carry the <sup>81</sup>Kr<sup>m</sup> gas. It became apparent that using the krypton alone did not produce a sufficient superficial velocity to fluidise the bed so compressed air was also required which was connected to the base of the bed below a distributor plate. The compressed air was passed through a rotameter, which was used to adjust input airflow, and into the base of the bed. The fluidisation regime observed was bubbling fluidisation (see section 2.7.2) and it was expected that relatively large volumes of <sup>81</sup>Kr<sup>m</sup> would be observed travelling up the height of the bed. Data was acquired for a variety of bed heights and flow rates from the compressor.

### **3.1.1.3 Discussion of Results – Fluidised bed**

The images shown in Figure 3.2 are constructed from data acquired for a compressed air flow rate of 2 l min<sup>-1</sup> and a bed height of around 30 cm unfluidised, where each image is a 1 second recording of event rates with dimensions 700 mm width and 900 mm height. The initial activity of the generator used for this run was estimated to be between 2.7 and 5.6 GBq and for these frames the maximum instantaneous count rate was 80 kHz. A higher number of images per second were attempted, but due to the low activity of the <sup>81</sup>Kr<sup>m</sup> gas the difference between background noise and

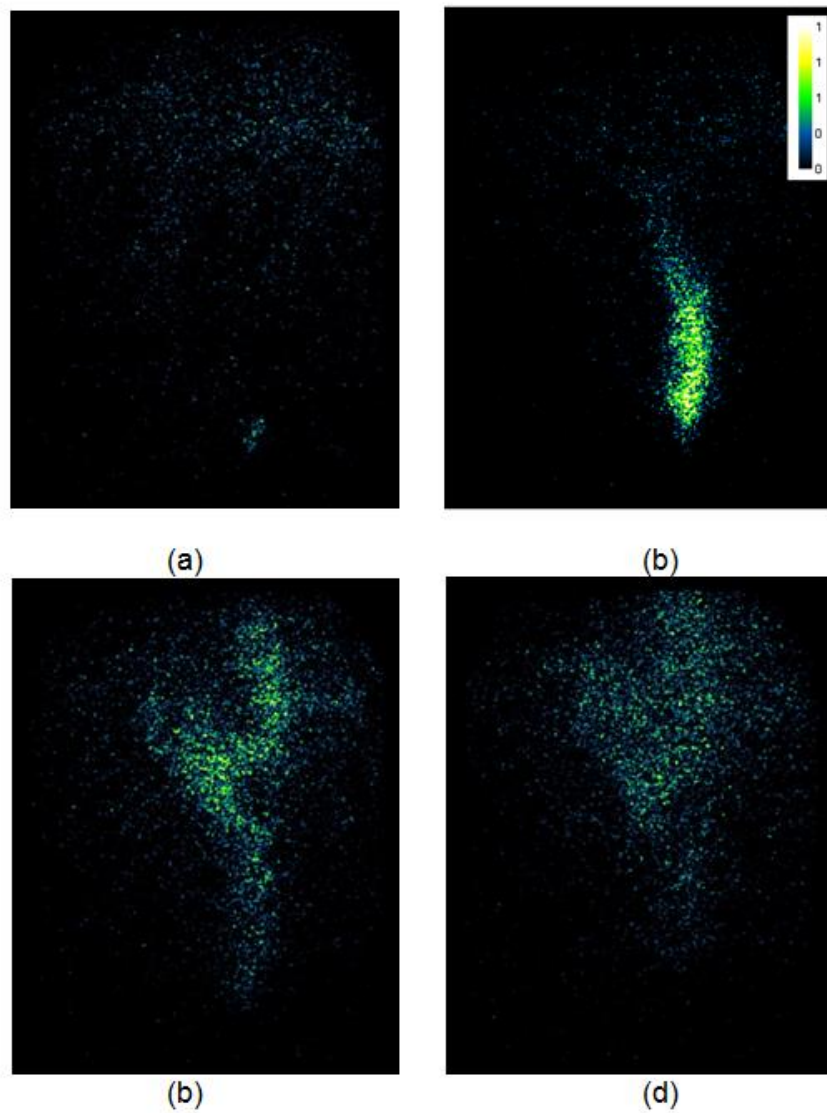


**Figure 3.2.** Image data acquired for a bed height of 30 cm and feed flow rate of  $2 \text{ l min}^{-1}$ . Each image from (a) to (d) shows a consecutive 1 second image frame from the initial introduction of  $^{81}\text{Kr}^m$  to 4 seconds into the run.

gas within the bed was minimal, and although it was possible to display some acquired information the gas processes could not be observed. With the frame rate at 1 image per second it can be seen that although the general path the  $^{81}\text{Kr}^m$  gas takes may be observed, no individual bubbles may be discerned. All of the obtained data for this experiment has been examined and it may be concluded that the experimental set up

was flawed and instead of observing the  $^{81}\text{Kr}^m$  occupying the bubbles passing through the bed the dispersion of the gas through the solid particles is seen. Also the ratio of meaningful data to background noise was too low, thus it was not possible to study the gas processes of the fluidised bed in any great detail. One possible reason for this is that it was necessary to position the  $^{81}\text{Kr}^m$  generator close to the bed to minimise the residence time between the generator and the FoV resulting in high levels of background radiation which were almost comparable to the levels of the gas within the fluidised bed. This resulted in high levels of noise in the image, decreasing the possibility of differentiating between noise and desirable data. Another issue with the experimental set up was the fact that the bed could not be fluidised with the  $^{81}\text{Kr}^m$  gas alone. As compressed air was required to fluidise the bed the  $^{81}\text{Kr}^m$  gas would have been diluted and dispersed and the behaviour of individual bubbles would not be observed. It was expected that the bubbly fluidisation regime would be clear from the image data, however because the majority of the compressed air being passed into the column formed bubbles instantly the  $^{81}\text{Kr}^m$  was excluded from the bulk behaviour. Along with the high velocity of the gas passing through the bed, further decreasing the ability to observe bubbles, it can be seen that the data acquired during this experiment is not adequate for reaching the objective of studying gas processes in detail without major changes to experimental design. The conclusion of this preliminary test was that the activity of the  $^{81}\text{Kr}^m$  gas would need to be increased in future studies and the experimental design would need to incorporate mixing the  $^{81}\text{Kr}^m$  into the bulk gas phase before introduction to the system.

### **3.1.2 Bubble column study**

#### **3.1.2.1 Introduction**

Following the conclusion of the fluidised bed study a request for new generators with higher initial activity was made as this would increase the event rate, which in turn leads to better temporal resolution.

For this reason a second experiment was carried out using the SPECT imaging technique and krypton generator, but this time using a bubble column. A bubble column was chosen for the ability to control the viscosity of the fluid through which the gas bubbles travel; and therefore the velocity of the bubbles. Also krypton generators with higher initial activity were used to increase the event rate of the  $^{81}\text{Kr}^m$  gas, which would lead to an improvement in signal to noise ratio. A way of keeping the generator away from the column was found and extra shielding was used.

#### **3.1.2.2 Experimental procedure – Bubble column**

A bubble column was used for the second SPECT study, a description of which can be found in section 2.8. The column is filled with a fluid and then gas is introduced to the base of the column which forms a stream of bubbles, which in turn allows gas exchange. With a bubble column the gas flow may be controlled to a certain degree by altering the viscosity of the fluid within the column and the rate of flow at which the gas is introduced to the column. The reason for deciding to use a bubble column was the ability to better define the gas bubbles and determine characteristics such as bubble velocity, bubble-bubble interactions, data rates, imaging frame rates and spatial and temporal resolution limitations of SPECT as an imaging technique.

The column used was 2 m tall with a cross-sectional radius of 0.04 m and maximum volume of 10 l. The fluid used within the column was a solution consisting of water and sodium carboxymethyl cellulose (CMC), the concentration of which varied depending on the viscosity desired for the fluid (Yang & Zhu 2007). The gas used was  $^{81}\text{Kr}^m$  which was produced using a  $^{81}\text{Rb}/^{81}\text{Kr}^m$  gas generator, as with the previous experiment with the fluidised bed. The equipment was set up as shown in Figure 3.3. The same  $1 \text{ l min}^{-1}$  air pump as used in the fluidised bed study was used to pass air through the  $^{81}\text{Kr}^m$  generator and collect the radioactive gas which would enter the column at its base and proved to be sufficient to produce bubble flow without external assistance from compressed air. This followed the recommendation from the fluidised bed study that the  $^{81}\text{Kr}^m$  would need to be mixed with the bulk gas phase before entering the column.

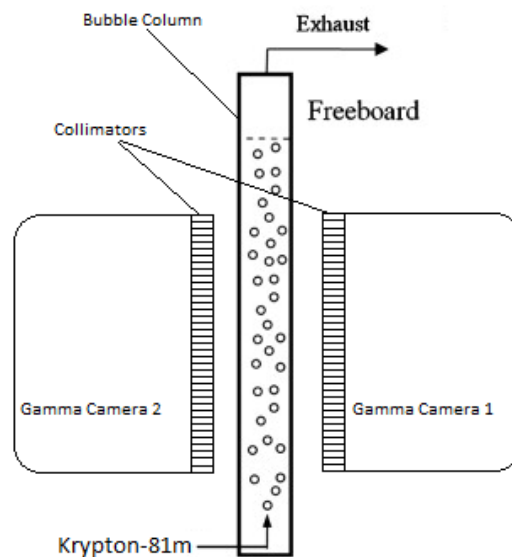


**Figure 3.3.** The bubble column was placed vertically between the two gamma camera heads.

A tap was introduced to the output of the pump in order to control the flow rate of the gas entering the column. The  $^{81}\text{Kr}^m$  generator was placed on the floor and extra lead bricks and sheeting were placed around the generator to reduce background noise. A thin tube with inner diameter of 1.1 mm was used to carry the gas from the generator to the column to keep residence time as low as possible. As the  $^{81}\text{Kr}^m$  gas has a half-life of only 13.1 seconds, if the residence time in the tube was too great then there was the risk of the gas not remaining active through the entire field of view of the cameras. In this case the tube was about 1 m long, giving a residence time of roughly 0.06 seconds in the tube which is approximately 0.5% of the half-life. The column was placed between the parallel gamma cameras and positioned so that the lowest section of the column was in the field of view of the cameras to ensure the  $^{81}\text{Kr}^m$  gas was imaged in its most active state. As with the fluidised bed study parallel-hole collimators were used on the camera heads in order to produce direct 2D images. The initial concentration of CMC in the solution for the fluid was 1.3%, or 65 grams of CMC in every 5 litres of water. Eight litres of this solution was created the night before by adding the CMC powder slowly to the water and left to mix overnight. This method was also used to make a solution of 2% concentration of CMC for use when higher viscosity was required.

Table 1 describes the conditions under which the bubble column was imaged, i.e. CMC concentration, whether data was acquired for a continuous stream of bubbles or if it was recorded for individual bubbles sent up through the column, the age of the generator at time of measurement, the initial generator activity and the approximate generator activity at time of measurement. The age of the generator is important because the activity of the  $^{81}\text{Rb}^m$  would reduce with time, the half-life being

approximately 4.5 hours. The generators are made at about 9.30pm, which is when the generators would be most active. By the following day at least three  $^{81}\text{Rb}^m$  half-lives would have passed by 11am, decreasing the activity of  $^{81}\text{Rb}^m$  and thus the production of  $^{81}\text{Kr}^m$ . In equilibrium conditions, either when no  $^{81}\text{Kr}^m$  gas is being eluted or when a steady flow of gas passes through the generator, the krypton activity is equal to the rubidium activity, therefore the  $^{81}\text{Kr}^m$  concentration reduces with the half-life of  $^{81}\text{Rb}$  which is every 4.5 hours. Once the  $^{81}\text{Kr}^m$  has been extracted from the generator it decays with its characteristic half-life of 13.1 seconds. The overnight recordings

**Table 1. Experimental conditions of the bubble column study including initial generator activity, generator age, generator activity at time of use and feed flow rate.**

Experiment No.	CMC Concentration	Krypton activity when made* (MBq)	flow rate (l min <sup>-1</sup> )	Cont./single	Estimated generator activity at time of use (MBq)
1	No Fluid	13,000	1	continuous	1,625
2	1.30%	13,000	1	continuous	1,625
3	1.30%	13,000	0.5	continuous	1,625
4	1.30%	17,000	1	single	17,000
5	1.30%	17,000	0.5	continuous	17,000
6	1.30%	17,000	1	continuous	2,125
7	1.30%	17,000	1	single	2,125
8	1.30%	17,000	0.5	continuous	2,125
9	2%	18,642	1	single	18,642
10	2%	18,642	1	continuous	18,642
11	2%	18,642	0.5	continuous	2,330
12	2%	18,642	1	single	2,330
13	0%	N/S	0.5	continuous	-
14	0%	N/S	1	continuous	-
15	0%	N/S	1	single	-
16	0%	N/S	0.75	continuous	-
17	0%	N/S	0.5	continuous	-

\*N/S – Not Supplied.  $^{81}\text{Kr}^m$  activity is not stated

would have the new generators with maximum activity and the day time recordings would have reduced activity, thus reduced  $^{81}\text{Kr}^m$  concentration and reduced event rates. Advantageously by running with a fresh generator overnight it was possible to measure the count rate performance of the imaging system and determine the optimum generator activity required for this work. It will be shown that the fresh generators had sufficient activity to saturate the cameras and thus the maximum data rate was found.

### **3.1.2.3 Discussion of Results – Bubble Column**

The images in Figure 3.4 are produced from data acquired while running the system with solution at 1.3% CMC concentration,  $0.5 \text{ l min}^{-1}$  air flow rate through the generator and using generator with initial activity of 17 GBq (experiment number 5). These images display the differences in image quality for 1, 10, 100 and 200 frames per second (fps) at approximately the same time into the experimental run. Using ImageJ (Abràmoff et al. 2005) software the information displayed in Table 2 was calculated regarding pixel intensity.

**Table 2. Table containing the relative difference in pixel intensity, mean pixel density and total intensity of the image frame for 1, 10, 100 and 200 fps.**

<b>Number of Frames per Second</b>	<b>Max. Pixel Intensity</b>	<b>Mean Pixel Density</b>	<b>Integrated Intensity of Image Frame</b>
1	36.952	0.801	504909
10	2.619	0.037	23378
100	1.19	0.008	5277
200	0.429	0.002	1228

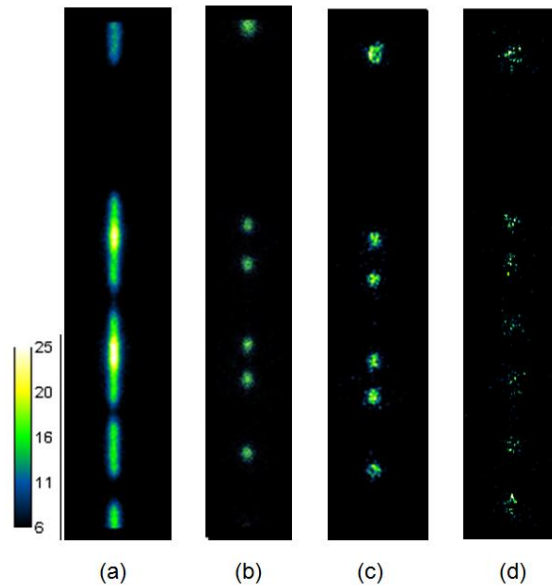


**Figure 3.4. These images all show the same data but with different acquisition rates. (a) is 1 fps, (b) is 10 fps, (c) is 100 fps and (d) is 200 fps.**

From the data obtained it was possible to determine several attributes of the bubbles within the bubble column from both the images produced and the raw count rate data. Characteristics calculated were bubble velocity, bubble volume, bubble activity and what happens when two bubbles coalesce.

Data obtained for the overnight run of the system at 2% CMC concentration and  $1 \text{ l min}^{-1}$  bursts of gas, with initial activity of 18.6 GBq, to create single bubbles (experiment 9), was used to calculate average bubble velocity in this scenario. To calculate bubble velocities graphs were created showing the instantaneous count rate data from the recorded data file as the points, with a rolling average trend line included purely for observational ease. The peaks of these graphs show peaks of activity within the field of view of the cameras, inferring that a  $^{81}\text{Kr}^m$  bubble was rising through the column at this point. By noting between which times the peaks occur the length of time the bubble is within the field of view of the cameras can be determined, thus their

velocity. Figure 3.5 is a graph displaying data obtained for 1 data point per second. For bubble 1 the total time in field of view is from about 16 to 24.5 seconds, giving a time of  $8.5 \pm 2$  seconds to travel 900 mm. This gives a velocity of about  $0.106 \pm 0.02 \text{ m s}^{-1}$  for bubble 1. The calculations were repeated for bubbles 2 and 3, giving velocities of  $0.056 \pm 0.006 \text{ m s}^{-1}$  and  $0.060 \pm 0.007 \text{ m s}^{-1}$  respectively. The decreasing intensity of bubble 2 is a result of the decay of krypton. To support these calculated velocities cross-correlation of two images of the same bubbles at different times was used, shown in Figure 3.6, which served as an approximate way of calculating the velocity. It can be seen that the 77<sup>th</sup> frame and 100<sup>th</sup> frames were used for (a) and (b) respectively and as the frame rate for these images is 10 fps this gives a time interval of 2.3 seconds. The change in bubble height for the two images is  $y = 718$  to  $y = 472$ , giving a distance of  $246 \pm 3 \text{ mm}$ , where the error in distance is half the spatial resolution of the camera.

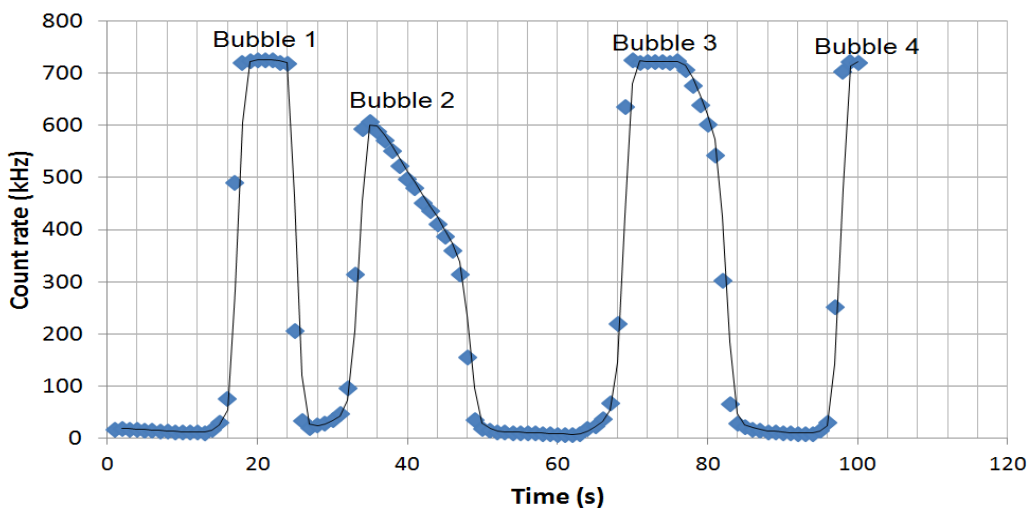


**Figure 3.5. Plot of counts detected against time. The peaks in event rate indicate the presence of a bubble in the FoV.**

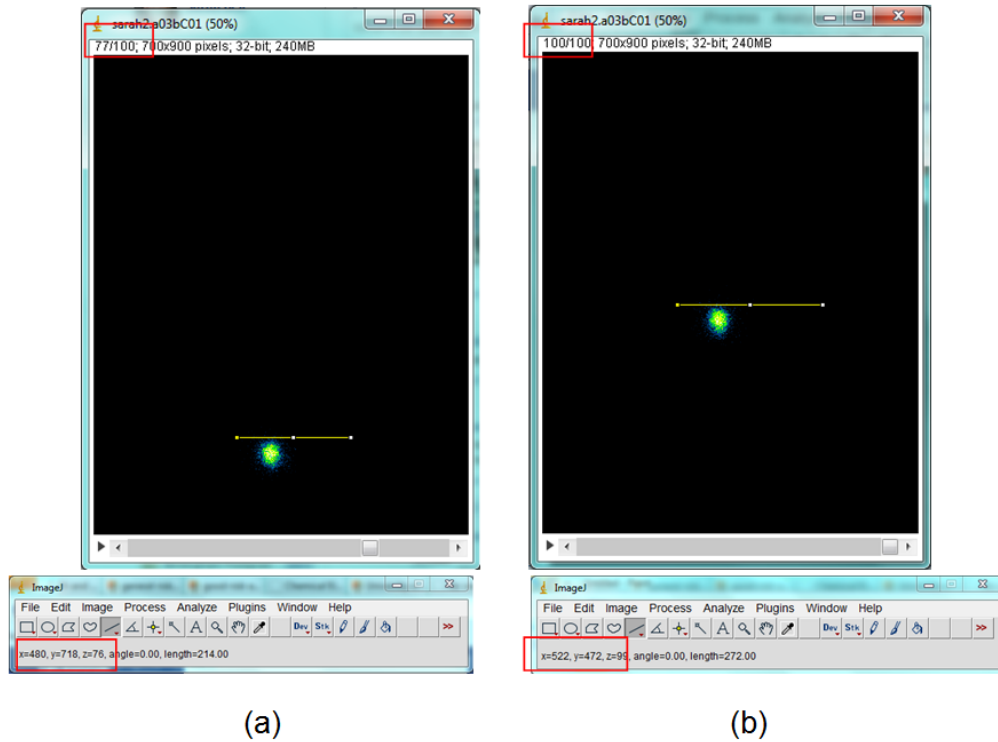
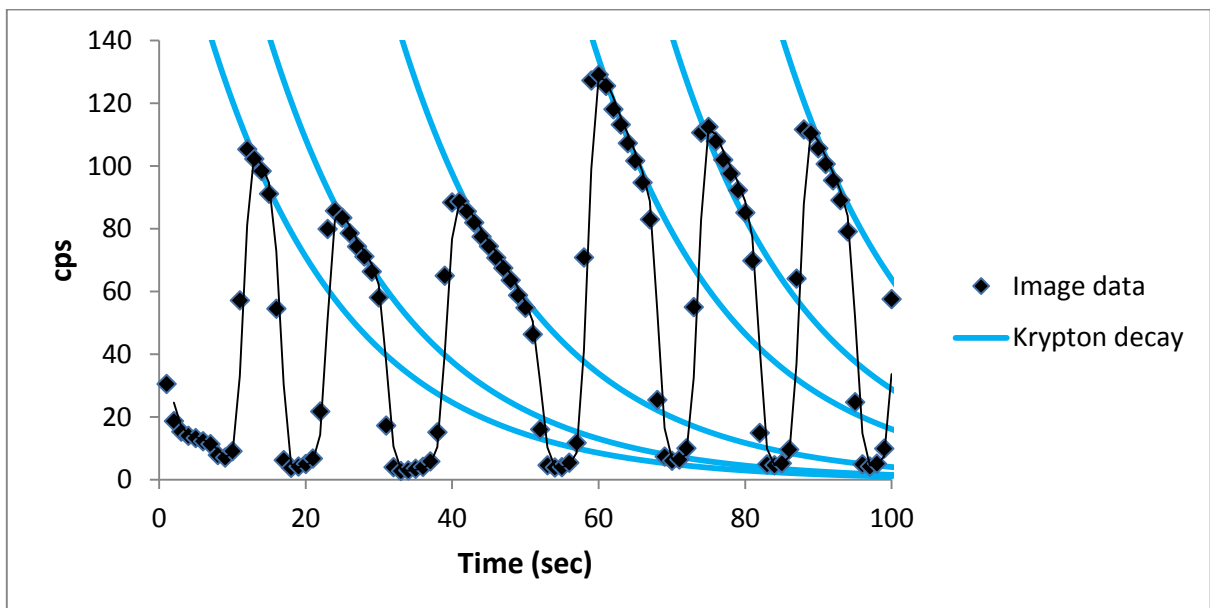


**Figure 3.6. (a) Shows bubble 1 at  $y = 718$  in frame 77 and (b) shows bubble 1 at  $y = 472$  in frame 100.**

This information leads to a calculated value of  $0.107 \pm 0.001 \text{ m s}^{-1}$  for the velocity of bubble 1. When compared to the value calculated from the raw data of  $0.106 \pm 0.02 \text{ m s}^{-1}$  it can be observed that these velocities have a difference of only  $0.001 \text{ ms}^{-1}$  which is within the error bounds of both calculations. This cross-correlation of images was repeated for bubbles 2 and 3 and velocities of  $0.051 \pm 0.001 \text{ m s}^{-1}$  and  $0.054 \pm 0.001 \text{ m s}^{-1}$  were calculated for bubbles 2 and 3 respectively. This method of calculating bubble velocity verifies the method of calculating velocity using the raw data. It may be concluded that it is possible to determine bubble velocity using the raw count rate data for single bubbles.

Figure 3.5 shows that the count rate for bubbles 1 and 3 plateaus at just above 720 kHz. This is due to the dead time of the gamma camera and at this point the

camera is saturated and cannot detect anymore. For this reason it is not possible to evaluate the effect the decay rate of the  $^{81}\text{Kr}^m$  gas may have on results from this set of data and also it is not possible to know the total maximum activity of the bubbles. With data on the total activity of each bubble it is expected that a correlation between bubble volume and bubble activity will be found. From this information it was possible to determine a relationship between bubble volume and bubble velocity. Below is a graph showing data obtained using the same set up as above, 2% CMC concentration and bursts of gas to create single bubbles (experiment 12). However this data was obtained during the following day, therefore the activity of the  $^{81}\text{Kr}^m$  gas was reduced and in turn the count rate is significantly reduced, meaning the dead time of the camera did not affect the number of events recorded.



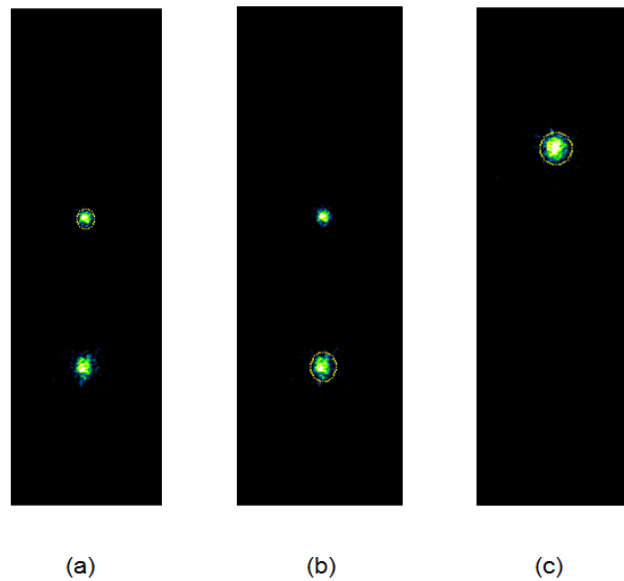
**Figure 3.7.** The black diamonds represent detected counts per second (cps) against time (sec) for experiment 12 and a peak in counts indicate a bubble of  $^{81}\text{Kr}^m$  passing through the FoV. The exponential decay of each bubble as it passes through the FoV of the camera is shown as the blue lines.

Figure 3.7 shows that it is possible to observe the krypton decay as the single bubbles pass through the FoV of the camera. As each bubble travels up through the column there is a decrease in intensity which corresponds to the exponential radioactive decay as indicated by the blue lines. The exponential trends were calculated using the equation for radioactive decay (equation 3.1), where  $A$  is activity (or counts in this instance),  $A_0$  is the initial activity (counts),  $t$  is time and  $\lambda$  is the decay constant (equation 3.2).

$$A = A_0 e^{-\lambda t} \quad 3.1$$

$$\lambda = \frac{\ln(2)}{t_{1/2}} \quad 3.2$$

This would imply that the count rate may be used to determine a quantitative measure of the activity of each Krypton bubble and thus discover if this is proportional to the bubble volume. It may be assumed that the larger the volume of the bubble the higher the count rate detected as there will be more gas emitting gamma rays. Determining a quantitative relationship between events detected and  $^{81}\text{Kr}^m$  concentration would be the next stage in further development of SPECT for study flow processes. In this preliminary study, however, it has been possible to verify a relationship between bubble volume, activity and velocity when two single bubbles coalesce. Data was used from the day time recording of initial generator activity of 17 GBq and 1.3% CMC concentration with single pulses sent through to create single bubbles (experiment 7). Figure 3.8 shows the bubbles which were analysed. Figure 3.8 (a) and (b) highlight bubble 1 and bubble 2 respectively before they coalesce. Figure 3.8 (c) is of the bubble produced after the two bubbles coalesce. Table 3 contains data calculated using ImageJ software and the cross-correlation method of calculating bubble velocity. The



**Figure 3.8. (a) Shows bubble 1 circled in yellow and (b) shows bubble 2 circled in yellow. (c) Is the resulting bubble after coalescence.**

calculated data appears to coincide with assumptions made about a relationship existing between bubble size, activity and velocity. The area of the combined bubble, after the two bubbles coalesce, is calculated have a difference of only 51 mm<sup>2</sup> from the summation of the areas of bubble 1 and bubble 2. It was expected that the volumes of bubble 1 plus bubble 2 would be equal to the volume of the combined bubble so a method of relating bubble activity to the cross sectional area of a bubble in order to determine bubble volume will be developed. A more accurate method of calculating the cross sectional area of a bubble would be through the activity data, however this would involve taking <sup>81</sup>Kr<sup>m</sup> decay rates into account and knowing the concentration of <sup>81</sup>Kr<sup>m</sup> in the gas mixture entering the column so this would be done for a continuation of investigating SPECT as a gaseous flow imaging technique. It may be observed that the velocity of the smallest bubble, bubble 1, is lower than the velocity of bubble 2, which is a larger bubble. Also the velocity of the combined bubble is yet larger, as is

its area. In potential future studies the viscosity of the fluid would be calculated which would provide enough information to predict bubble rise velocity (Talaia 2007).

**Table 3. This table shows relative cross-sectional area, pixel intensity, pixel density and velocity of bubble 1, 2 and the resulting combined bubble.**

	Area (mm <sup>2</sup> )	Max. Pixel intensity	Integrated Density of Bubble	Velocity (ms <sup>-1</sup> )
Bubble 1	907	1.714	521.238	0.07
Bubble 2	1410	2.286	910.476	0.23
Combined	2368	2.381	1636.143	0.27

### 3.1.3 SPECT study conclusion

These preliminary SPECT studies have tested the limitations of applying SPECT to the study of gaseous flow processes. The availability of <sup>81</sup>Rb/<sup>81</sup>Kr<sup>m</sup> generators at the University is beneficial for ease of access, relatively low cost and time management flexibility; however the short half-life of only 13 seconds introduces a number of complications. It would be difficult in the time available to perform a measurement of absolute <sup>81</sup>Kr<sup>m</sup> concentration in the resulting air-<sup>81</sup>Kr<sup>m</sup> mixture meaning quantitative measurements of bubble volume could not be made from the detected events. The balance between having activity so high that the camera is saturated, meaning any variations in <sup>81</sup>Kr<sup>m</sup> concentration within the FoV is indefinable losing potential quantitative analysis, and having activity too low so that the Krypton has decayed to a point that the meaningful statistical information has been lost would be a challenge to optimise. Although SPECT has proven to be capable of imaging a bubble column there are existing imaging studies in place for the investigation of bubble columns using SPECT, as described in section 2.8.3, and using an entirely different imaging technique called Electrical Capacitance Tomography (ECT). ECT is becoming a

standard technique for the study of both bubble columns and fluidised beds for the verification of mathematical models and Computational Fluid Dynamics (CFD) simulation (Warsito & Fan 2003; Wang et al. 2008; Zhang et al. 2015).

## **3.2 PET INVESTIGATION**

### **3.2.1 Steady state PET study**

#### **3.2.1.1 Introduction**

Using PET for the imaging of radioactive gases is a relatively new line of research for the University of Birmingham so it was necessary to perform some control and preliminary studies in order to develop a practical Standard Operating Procedure (SOP) for apparatus set-up in the camera, optimal acquisition conditions and consistent data analysis approach. For a full description of this PET investigation see (Bell et al. 2013) which has been included in the Publications section. To become familiar with the equipment and to determine the imaging limitations a control test was performed in steady state. The main aims of this steady state study were to determine:

- Spatial resolution
- Practical imaging protocol
- Image analysis technique
- Reliability of PET as an imaging technique for varying material density and voidage

#### **3.2.1.2 Experimental procedure**

For this initial PET study three different vessels containing a variety of objects of differing sizes and densities were filled with  $^{11}\text{CO}_2 + \text{N}_2$  and imaged. Table 4 shows the various vessel and media combinations used for this study.

**Table 4. The object combinations that were imaged for the steady state PET study are defined here.**

<b>Experiment number</b>	<b>Vessel</b>	<b>Vessel Dimensions (mm)</b>	<b>Media</b>	<b>Media Density (g cm<sup>-3</sup>)</b>
1	Spherical glass bottle	125 mm Ø	Empty	-
2	Spherical glass bottle	125 mm Ø	3 mm zirconium silicate spheres	4.5
3	Conical glass bottle	35 mm Ø - top 110 mm Ø - base	13 mm steel spheres	7.9
4	Plastic column	30 mm Ø	25 mm steel spheres	7.9

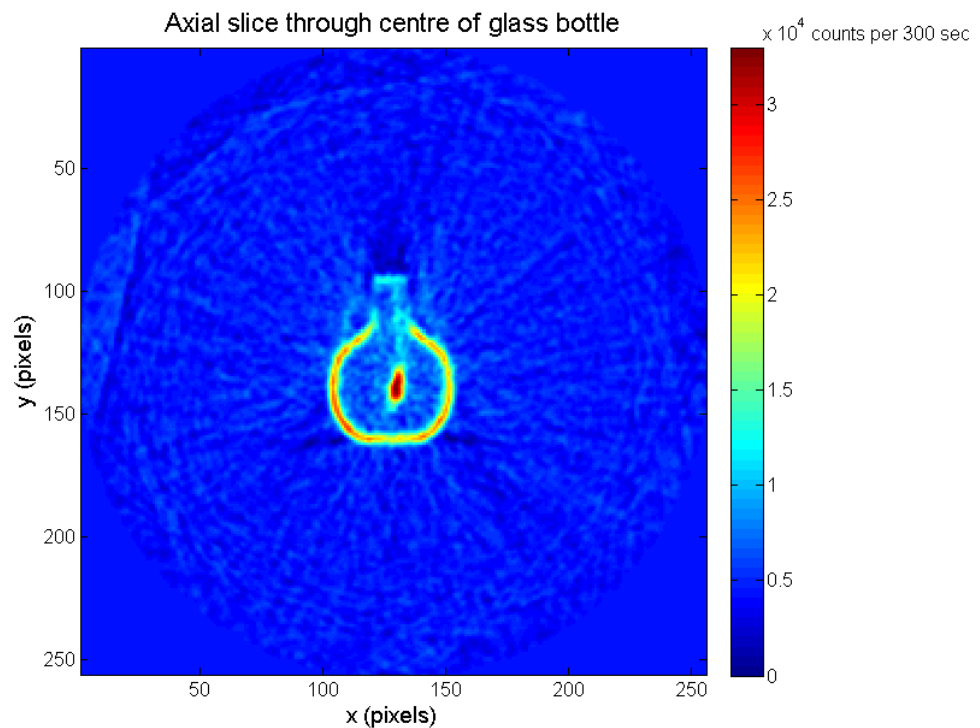
The MC40 cyclotron at the university supplied a two litre gas cylinder containing a mixture of positron emitting <sup>11</sup>CO<sub>2</sub> and N<sub>2</sub> which was produced as described in section 2.6.2. The gas cylinder had a pressure slightly higher than atmospheric pressure which was enough to fill each vessel in turn. Once filled with radioactive gas it was possible to image each vessel. The concentration and activity of <sup>11</sup>CO<sub>2</sub> contained within each vessel at the time of imaging was unknown.

The default imaging protocol was followed when performing the emission scans with one imaging frame of 600 sec followed by FBP reconstruction of the images. As described in section 2.10.2 these reconstructed images consisted of 47 planes, each with dimensions 256 x 256 pixels. In the transverse plane the pixel dimensions are 2.54 x 2.54 mm and in the axial plane the pixel dimensions are 2.54 x 3.45 mm.

### **3.2.1.3 Steady state results**

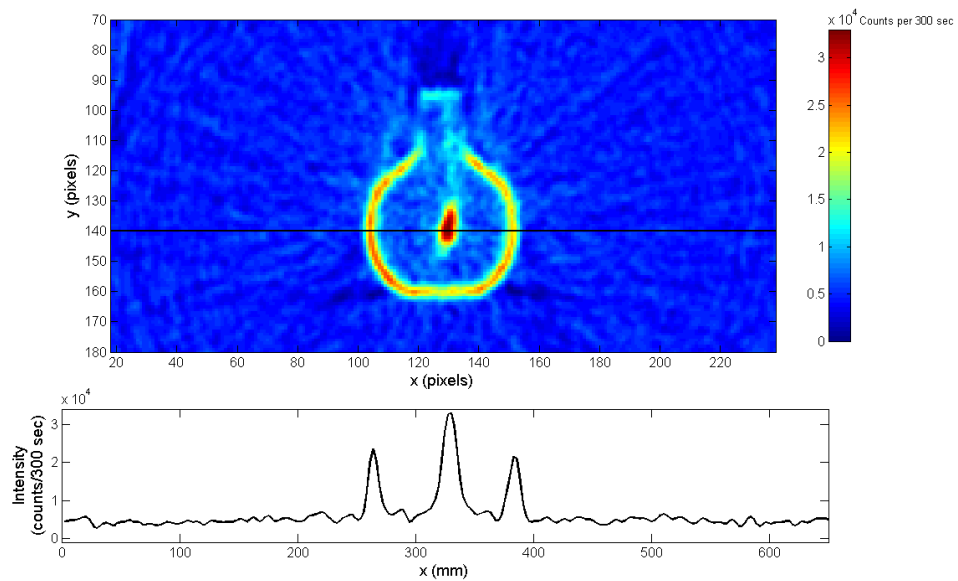
The aim of this steady state investigation was to determine the limitations of qualitative image analysis. The physical characteristics of each vessel were calculated from the images produced and a comparison of media density and size for each vessel was made.

Figure 3.9 shows a slice through the centre of the empty spherical glass bottle in the axial plane. This image clearly shows the star artefact inherent in FBP reconstruction as described in section 2.5.2. As a Gaussian filter with a 6 mm convolution kernel was used to remove high frequency noise it was expected that this combined with attenuation and scatter would produce some amount of blurring at the edges of the vessel walls. Despite the presence of blurring around the edges, the walls of the vessel and gas inlet tube are clearly visible and have minimal statistical noise allowing quantitative a study of intensity values for comparison. As an emission will be detected at the location of a positron-electron annihilation it was expected that the vast majority of counts would be at a gas-solid intersection due to the relatively high electron density of solids. Knowing that peaks in intensity occur at the edges of a solid allowed the measurement of physical properties such as the dimensions of the vessels, gas inlet pipe and media.



**Figure 3.9. Axial slice through the centre of spherical glass vessel. The point of intensity at the centre of the vessel is the gas inlet pipe. This image clearly shows the star artefact inherent with FBP techniques and there is blurring at the edges as expected. The high intensity vessel walls, however, have minimal noise and provide good comparable intensity values which would differ for materials of different densities.**

By taking a closer look at the empty glass bottle and creating an intensity profile of one row of values in the x-direction as shown in Figure 3.10 measurements could be made. At this stage of the PET study the blurring effects of image reconstruction had not been investigated so the FWHM was taken to be the width of the intensity peak as the dimensions being measured were smaller or comparable to the spatial resolution of the PET camera (stated as 6 mm in the user manual). From the intensity profile shown in Figure 3.10 the FWHM at the surface of the wall of the glass bottle was measured



**Figure 3.10. The plot at the bottom of this figure is the intensity profile of the row of pixels highlighted in red across the image at the top of the figure. There are clear peaks at the walls of the glass vessel and a peak in the centre which is the gas inlet pipe.**

as 4 pixels, which equates to  $\sim 9.3$  mm. This is over three times larger than the wall thickness of 3 mm, however it is only known that the interface between the wall and the gas is being observed. Without being able to perform attenuation correction the actual structure of the vessel cannot be accounted for. An attenuation correction was attempted for these studies so that the attenuation of the photon pairs caused by solid objects in the FoV could be subtracted from the emission image; however the attenuation correction protocol was not working. A measured FWHM of 9.3 mm was larger than the stated spatial resolution of 6 mm so it is clear that the spatial resolution of the camera and the image reconstruction protocol will need to be investigated further. While Figure 3.10 shows an image of a vessel with higher density than the media within (glass =  $2.6 \text{ g cm}^{-3}$  and air =  $0.0012 \text{ g cm}^{-3}$ ) Figure 3.11 shows the plastic

column (density =  $0.9 \text{ g cm}^{-3}$ ) filled with the six 25 mm steel spheres (density =  $7.9 \text{ g cm}^{-3}$ ). The relatively high density steel spheres are indicated in the image as voids of activity as the positrons cannot penetrate the surface. The highest region of activity is the boundary between the gas and the rubber bung (density =  $1.34 \text{ g cm}^{-3}$ ). Unexpectedly the gas between the bung and the steel spheres has higher intensity than the boundary between the plastic column walls and the gas and the background level is relatively high. It is thought that this is due to the post processing normalization of the image. The regions inside the steel spheres have minimum emissions and although the background level will be low it won't be as small as the activity voids in the spheres so the background will look higher than normal in comparison.

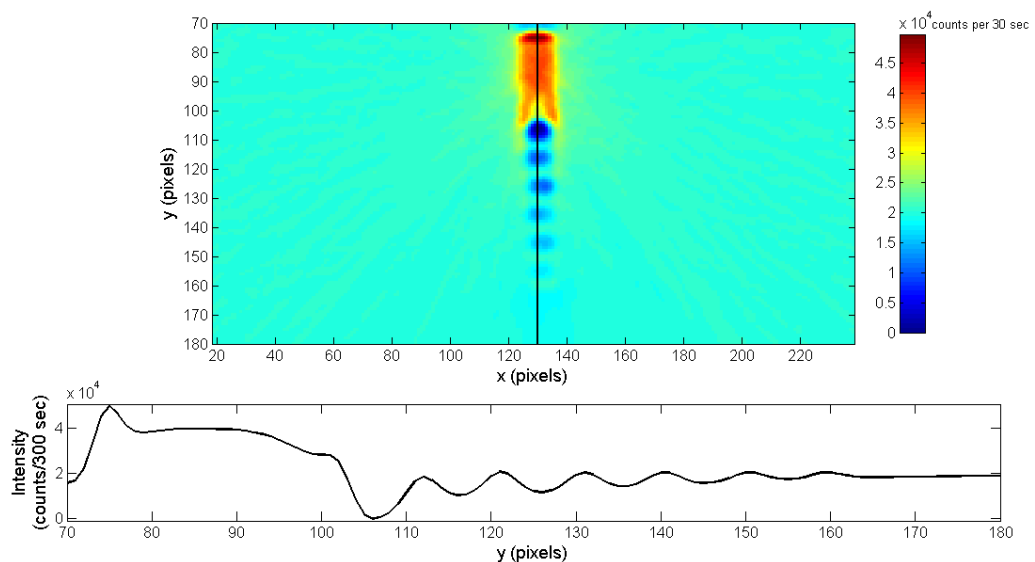


**Figure 3.11.** The image at the top shows the plastic column filled with six steel spheres. The intensity profile shows that the dense spheres have minimum activity and the highest region of activity is at the boundary between the gas and the rubber bung.

Measurements were made to determine the dimensions of the vessels and media and comparisons between density and relative intensity are provided in Table 5. The term CNM indicates that the dimensions of the media could not be measured. The zirconium silicate particles appeared as a solid void of activity and individual beads could not be discerned. For run 3 fluctuations in intensity could be observed where the gas was dispersed through the 13 mm spheres but there were no definite features that could be measured.

**Table 5. A comparison between the actual dimensions of the vessels and media and the measurements obtained from the image data. Also included is the relative intensity of events detected and gas-solid interfaces and the densities of the solids.**

No.	Vessel internal $\varnothing$ (mm)		Media $\varnothing$ (mm)		Density (g cm <sup>-3</sup> )		Intensity at solid-gas interface (% of max)		
	Actual	Image	Actual	Image	Vessel	Media	Vessel	Media	Bung
1	119	122	-	-	2.6	-	76	-	40
2 <sup>1</sup>	119	122	3	CNM <sup>2</sup>	2.6	4.5	100	32	68
3	104	97	13	CNM <sup>2</sup>	2.6	7.9	80	68	100
4	28	32	25	25	0.9	7.9	68	62	100

<sup>1</sup> $\varnothing$  measured at base of conical vessel    <sup>2</sup>CNM – Could Not Measure

By comparing the relative intensities at each on the gas-solid interfaces for each of the images material characteristics have been identified for each of the objects. For example, it was expected that the highest number of electron-positron annihilations would occur at the surface of the steel spheres as it has the highest density; however for the two runs with steel media the rubber bung had produced the maximum number of emissions. It is thought that the higher density of the steel would also contribute greatly to scattered events, attenuation and the possible absorption of photons decreasing the number of true coincidences detected.

By performing these steady state preliminary tests an imaging protocol was put in place and a standard technique for analysing the image data was developed. This directly led on to the investigation into dynamic imaging using PET.

### **3.2.2 Preliminary dynamic PET study**

#### **3.2.2.1 Introduction**

Once the data acquisition and image reconstruction protocols were understood a preliminary dynamic study was performed, also described in Bell et al. (2013). The steady state tests allowed a relationship between object density and observed count rates to be made, which was important to understand as attenuation correction could not be performed. With the image protocol in place a mock run of the proposed adsorption study at low pressure was performed to determine the feasibility of pursuing this line of research.

#### **3.2.2.2 Experimental procedure**

The experiment was set up as shown in Figure 3.12. The adsorption column used was a 250 mm long stainless steel pipe with a 25 mm internal diameter and a wall thickness of 1.5 mm. This column was packed with a 70 mm region of 3 mm beads of Zeolite 13X, acquired from Sigma Aldrich (USA), in the centre of the column and 3 mm glass beads at either end to replicate the packing of a fixed bed adsorption column. The feed gas used was a mixture of pure CO<sub>2</sub> and an N<sub>2</sub> + <sup>11</sup>CO<sub>2</sub> mixture supplied by the University's onsite MC40 cyclotron. As the pressure of the N<sub>2</sub> + <sup>11</sup>CO<sub>2</sub> is only slightly higher than atmospheric pressure it was necessary to pressurize it further, to 2 MPa, using a pure N<sub>2</sub> gas cylinder to ensure a constant feed for the duration of the experiment. The feed flow of gas was controlled using two Mass Flow Controllers

(MFCs) after which the two feed pipes connected to allow mixing of the bulk gas phase. Although Zeolite 13X is a CO<sub>2</sub> adsorbent the experimental rig was not set up to maintain a high system pressure while the N<sub>2</sub> + <sup>11</sup>CO<sub>2</sub> cylinder was connected to the system so it was not expected that adsorption would be observed. The purpose of this mock run was to determine the ability of the imaging system to measure the residence time of the gas flowing through the column by observing the progression of the gas through the bed and calculating the bulk velocity. The experimental issues with the set up were also defined allowing the procedure to be optimised for later studies.

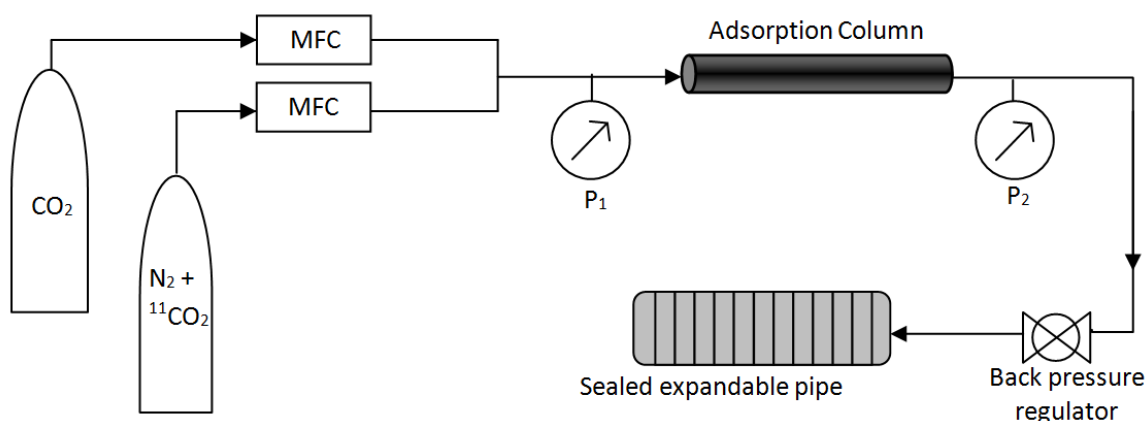


**Figure 3.12. Experimental set up of mock adsorption study.**

The adsorption column was positioned in the centre of the FoV parallel to the sagittal plane and a sealed expandable pipe was used to contain the radioactive effluent, which was shielded behind a lead brick wall. The first stage was to pass pure N<sub>2</sub> through the column at a flow rate of 400 ml min<sup>-1</sup> at atmospheric pressure for two hours to remove any molecules that weren't N<sub>2</sub>. After purging the column the N<sub>2</sub> was used to increase

the pressure of the system to approximately 2 MPa using the back pressure regulator after which the cylinder was removed and replaced with the N<sub>2</sub> + <sup>11</sup>CO<sub>2</sub> cylinder. The operating system pressure was approximately 0.3 MPa for the duration of the experiment. The CO<sub>2</sub> feed flow rate was 4.5 mln min<sup>-1</sup> and the N<sub>2</sub> + <sup>11</sup>CO<sub>2</sub> flow rate was set to 25.5 mln min<sup>-1</sup> to give a total bulk flow rate of 30 mln min<sup>-1</sup> and a CO<sub>2</sub> concentration of 15% volume. The units mln min<sup>-1</sup> refer to 'normal' millilitres per minute, where a normal millilitre is defined as a millilitre at a temperature of 0°C and pressure of 0.101 MPa. Imaging data was acquired over a two hour period at a rate of one frame every 45 seconds giving a total of 160 frames. As the gas is being passed through a packed bed of solid beads of adsorbent it is assumed that the positrons will on average not travel further than 1 mm before annihilating with an electron. This provides reasonable confidence that the event detected originates from the point of positron emission.

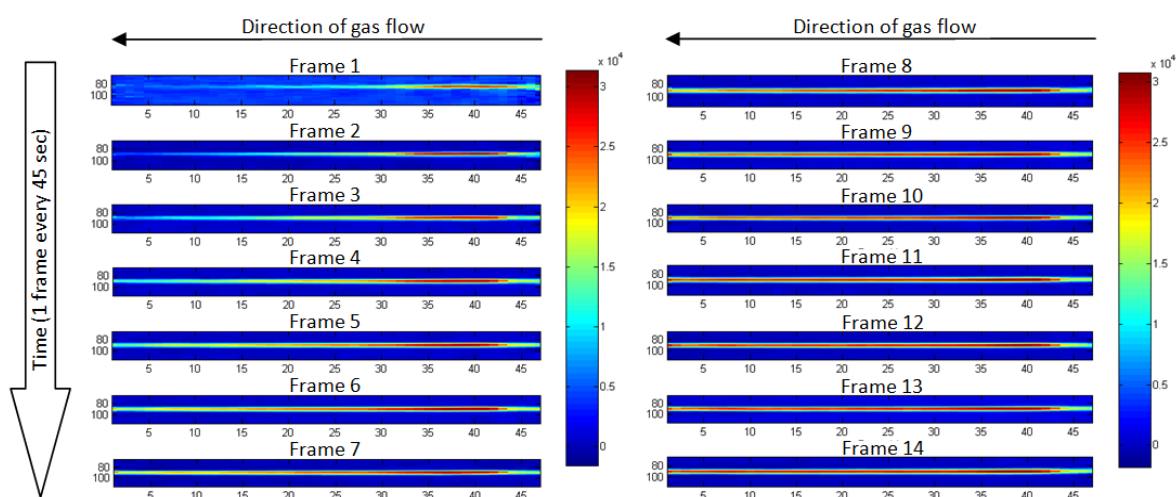
### **3.2.2.3 *Dynamic results***

Figure 3.13 shows the first fourteen image frames consecutively with the gas flowing from right to left. The first frame shows the initial introduction of <sup>11</sup>CO<sub>2</sub> to the column where the region of high concentration is indicated by red pixels. As time passes the progression of the gas through the length of the bed is observed up to the fourteenth frame (630 s). By applying the technique used to analyse the steady state systems it has been possible to make some observations about the flow of gas, including calculating residence time and gas velocity, by studying cross-sectional intensity profiles. At the 14<sup>th</sup> frame the bed appears to have reached full occupation, beyond this point there is no observable variation in the images produced. This implies that it

takes 630 s for the 42 planes of high intensity (145 mm) to fill with gas giving an actual velocity,  $v$ , of  $0.23 \text{ mm s}^{-1}$ . The ‘normal’ flow rate,  $Q$ , was calculated by

$$Q = \frac{vVP}{d}, \quad 3.3$$

where  $V$  is the volume of the column,  $P$  is pressure and  $d$  is distance travelled. A ‘normal’ flow rate of  $26 \pm 3.5 \text{ ml min}^{-1}$  was calculated, which is close to the  $30.00 \text{ ml min}^{-1}$  flow rate reading set by the MFCs. This implies that the process which can be observed from the data is not the progression of an adsorption front, rather the injection of radioactive gas into the column.



**Figure 3.13.** This series of images shows the bed packed with Zeolite 13X filling with  $^{11}\text{CO}_2$  over 14 image frames where each frame contains data acquired over 45 seconds. In these images the gas is flowing from right to left.

As the feed flow rate of  $30 \text{ ml min}^{-1}$  lies close the error margins of the calculated rate of flow it can be assumed that the emission data intensity profiles may be used to approximate the velocity of the gas. The flow regime of the gas passing through the packed bed can be determined by calculating the Reynolds number as given in

equation 2.16 (section 2.7.2). For the experiment presented here the Reynolds number is less than 1 which implies laminar flow as the limit for laminar flow in a packed bed is 10 (McCabe et al. 1993c).

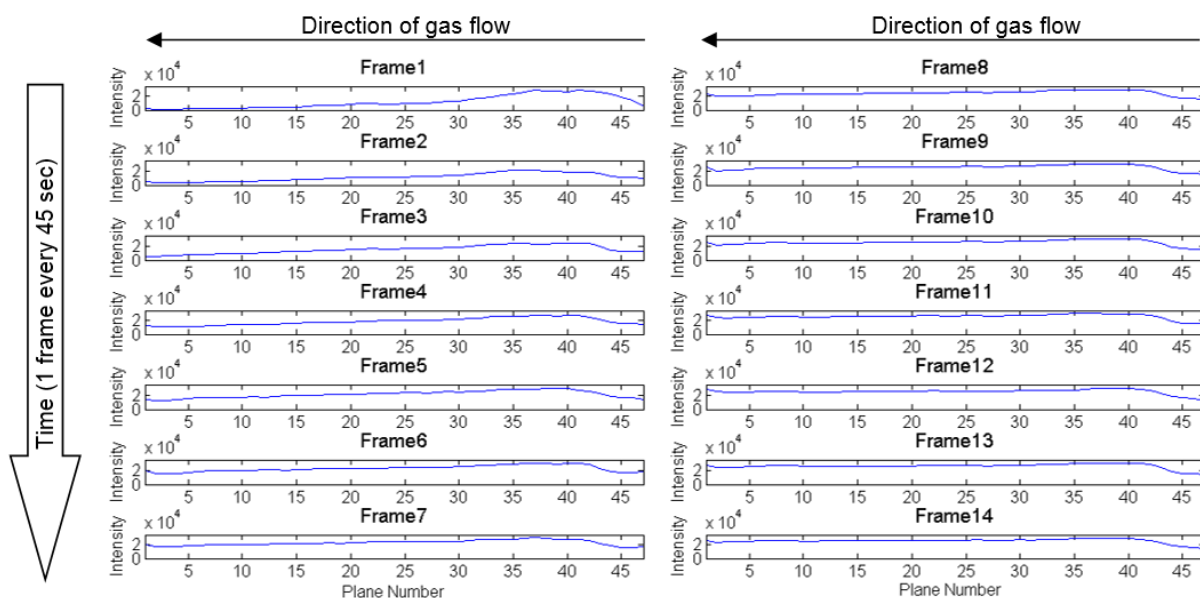


**Figure 3.14.** This series of intensity profiles shows the distribution of  $^{11}\text{CO}_2$  concentration along the length of the column for the first 14 image frames.

Figure 3.14 shows the cross sectional intensity profiles through the centre of the column for the first 14 frames. Frame 1 shows a peak in intensity of 444 cps per pixel at the 43<sup>rd</sup> plane as the radioactive gas is introduced to the system. However, over the following 585 s it can be seen that the width of the peak increases until the intensity throughout the column is constant. This confirms that the section of the column in the field of view of the camera is completely occupied by the radioactive gas by frame 14.

Although this trial run did not result in the observation of adsorption, which was expected due to the low pressure, the preliminary trial has suggested a data analysis protocol which has resulted in the development and implementation of an adsorption

study which is discussed in the following chapter (section 4). This study has proved that it is possible to observe the progression of radioactive gas flowing through the bed using 45 s acquisition frames. In order to determine the optimal acquisition time per frame a number of preliminary adsorption experiments were performed using a CO<sub>2</sub> analyser to monitor the CO<sub>2</sub> concentration in the effluent as described in section 2.9.6. Figure 3.15 shows the resulting breakthrough curve for Zeolite 13X at a system pressure of 3 MPa and a CO<sub>2</sub> feed concentration of 27%. The feed flow rate of N<sub>2</sub> was 140 mln min<sup>-1</sup> and the flow rate of CO<sub>2</sub> was 54 mln min<sup>-1</sup>. The curve clearly shows an output concentration of zero until about 35 minutes which implies that the MTW progresses through the bed with a bulk velocity of 0.3 mm s<sup>-1</sup> (2 mm min<sup>-1</sup>). The curve doesn't plateau at its maximum value until about 100 minutes into the experiment, which defines the minimum experiment duration. By taking both of these factors into account it was deemed that a consistent frame acquisition length of 1 minute would be suitable for each of the adsorption runs as the PET camera will not acquire more than 175 frames per imaging session and as the plane separation is 3.45 mm a progression of about 2 mm per image frame would be observable.

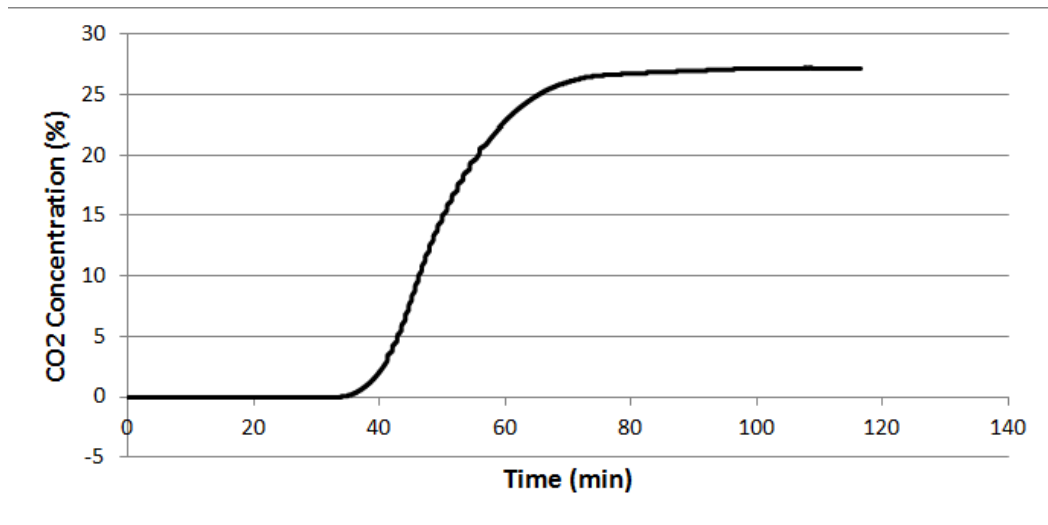


**Figure 3.15.** This breakthrough curve was obtained with experimental conditions 3 MPa system pressure and 27% CO<sub>2</sub> feed concentration. The error in CO<sub>2</sub> concentration is  $\pm 1\%$  and the error in time is  $\pm 2.25$  minutes. This curve was used to determine optimal imaging acquisition frame duration.

### 3.2.3 PET study conclusions

The PET feasibility studies presented here have yielded results that show the potential of using PET to study gaseous flow processes. Although the resulting reconstructed images show blurring, which loses a level of detail, an investigation into the axial sensitivity of the camera and the blurring in the images would be made before a continuation of the PET study allowing this systematic problem to be accounted for. The dynamic study has proved that the temporal resolution of the camera is adequate for the purposes of imaging adsorption and an optimal acquisition rate was determined using breakthrough data obtained using a CO<sub>2</sub> analyser. During the process of these feasibility studies a standard imaging protocol was put in place and a technique for image analysis was developed.

### **3.3 SPECT vs. PET**

From a comparison of the SPECT and PET studies presented here it was concluded that PET would be the imaging technique to continue the study of gaseous flow processes. The SPECT study proved that it was possible to image gas flow in a bubble column with high temporal resolution but the short half-life of  $^{81}\text{Kr}^m$  would not allow the detail that existing published studies already provide. During the dynamic PET study an emission acquisition protocol and image analysis technique were developed and an optimal acquisition frame rate was determined for the study of  $\text{CO}_2$  adsorption.

## **4 MATERIALS AND METHODS**

### **4.1 PET CAMERA CALIBRATION**

Once it was concluded that PET would be the desired imaging technique for the continuation of this project it was necessary to calibrate the camera and the method of analysis. As discussed in sections 2.5.2 and 2.10.2 there is an inherent blurring in the x and y directions due to Filtered Backprojection (FBP) reconstruction and blurring in the z direction due to axial smoothing. In order to effectively account for these known problems and determine the spatial resolution in z and y a series of tests were performed.

#### **4.1.1 Sensitivity and resolution tests**

The first series of tests were to check the sensitivity of the detectors for the full axial length of the FoV to ensure uniformity. To do the sensitivity tests a 2 mm  $\beta$  emitting Manganese 52 particle with an activity of 104  $\mu\text{Ci}$  and half-life of 5.6 days was moved in 10 mm increments along the axial FoV. The particle was left in each position for five 30 second frames before being moved to the next position. The desired position of the column was considered to be central in the FoV so the particle was moved in this position. For this test the camera continuously acquired data as the particle was repositioned from 0 mm to 160 mm according to the laser FoV display. This test also allowed a review of the inherent blurring due to axial smoothing. The image data has been analysed in two ways: 1). Intensity profiles made from single pixel intensities axially through the centre of the particle and 2). Intensity profiles made from the summation of pixel intensities for each cross-sectional plane.

Method 1 was used for the first stage of analysis. Figure 4.1 shows an example of a single intensity profile at 90 mm along the FoV in the z direction for one 30 second image frame for single pixel intensities along the axial FoV.

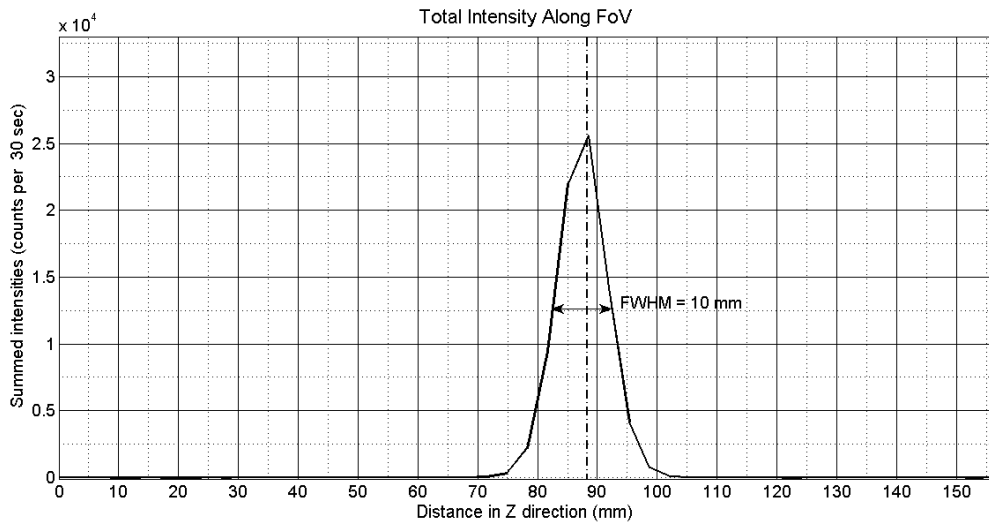


**Figure 4.1. Single intensity profile along z direction for 2 mm spherical particle at 90 mm measured by the ruler and 88 mm in the image data with FWHM = 10 mm.**

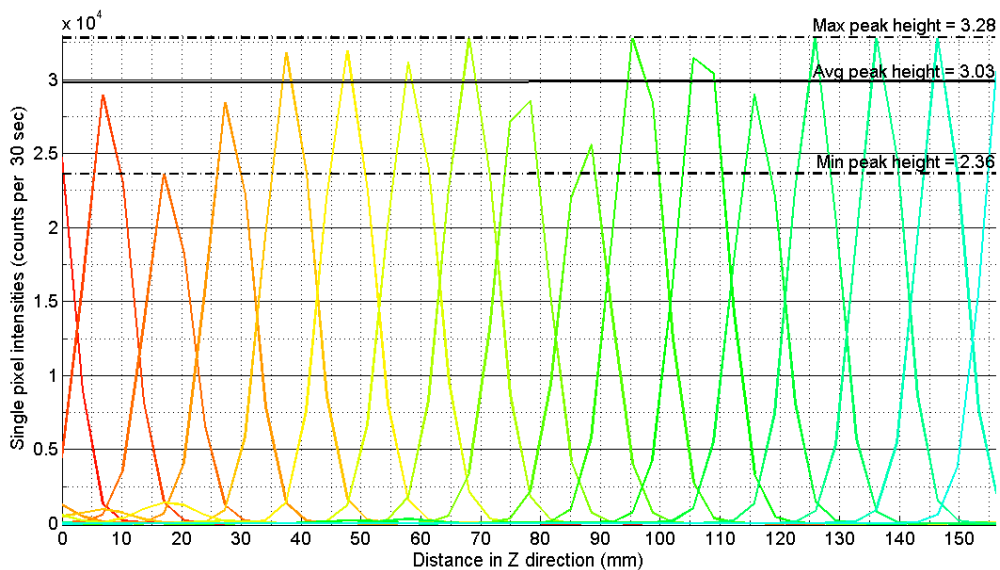


**Figure 4.2. Super imposed single pixel intensity plots for each 10 mm position.**

**Table 6. Maximum peak height and FWHM for the irradiated particle for 10 mm increments along the FoV for the single pixel intensity profiles across the particle.**

<b>Actual position in z direction (mm)</b>	<b>Measured position in z direction (<math>\pm 3.45</math> mm)</b>	<b>Distance between peaks (<math>\pm 1</math> mm)</b>	<b>Max peak height (<math>\times 10^4 \pm 0.05 \times 10^4</math> counts/30 sec)</b>	<b>FWHM (<math>\pm 1</math> mm)</b>
0	0	-	2.47	-
10	6.81	6.81	2.9	9
20	17.02	10.21	2.36	10
30	27.23	10.21	2.85	9
40	37.45	10.22	3.18	9
50	47.66	10.21	3.2	9
60	57.87	10.21	3.12	9
70	68.08	10.21	3.28	9
80	76.54*	8.46	2.78*	10
90	86.61*	10.07	2.38*	10
100	95.32	8.71	3.28	10
110	106.48*	11.16	3.09*	10
120	115.74	9.26	2.9	10
130	125.96	10.22	3.28	9
140	136.17	10.21	3.28	9
150	146.38	10.21	3.28	9
160	156.6	10.22	2.98	-
<b>Average</b>	-	9.79	3.03	9.4
<b>Standard deviation</b>	-	1.03	0.30	0.51
<b>Std as % of avg</b>	-	10.50	10.05	5.39
<b>Mode</b>	-	10.21	3.28	9

\* Calculated using weighted average of two consecutive high points of intensity

Each incremental position has been superimposed on the same plot, shown in Figure 4.2 and each position profile was a studied to determine the maximum peak intensity, peak location and FWHM which are shown in Table 6. The bottom section of the table shows the average peak height as multiples of  $10^4$  counts per 30 sec and the average FWHM in mm. The set location of the point source measured by the ruler along the

FoV is in the first column and the second column contains the measured location according to the intensity profiles. For the locations where the source is expected to be between two data points (e.g. ~80 mm, ~90 mm and ~110 mm) a weighted average was used to calculate the location and intensity. The middle column shows the separation distance of the peaks to check for consistency.

From Table 6 it is seen that the average peak height is  $3.0 \pm 0.05 \times 10^4$  counts per 30 sec with a standard deviation of  $0.3 \times 10^4$  counts per 30 sec, which is 10.0% of the average value. This standard deviation shows a discernible variance in the intensity peaks along the FoV. The average FWHM of the intensity profiles is about  $9.4 \pm 1$  mm with a low standard deviation of 0.51 mm, which is about 5.4% of the average value. Although this could be seen as a high percentage error it is smaller than the error in the measurement of the FWHM which is  $\pm 1$  mm or 10% of the average value. This shows reasonable consistency implying that the spatial resolution would be consistent along the axial FoV. However, the average FWHM displayed in the image data is about 10 mm which is slightly larger than the stated FWHM of 6 mm given by the manual. This increase is due to the axial smoothing filter which enhances the blurring effect. The next calibration text explores the spatial resolution in more detail.

The second column of the table shows the location of the maximum point of intensity for each particle placement. The mode of the peak separation distances is 10.21 mm, which is approximately three times the plane width of 3.45 mm. The other possible plane separation distances are  $2 \times 3.45 = 6.9$  mm or  $4 \times 3.45 = 13.8$  mm which coincides with the alternative separation distance that was not determined using a weighted average of 6.81 mm displayed in the table. This confirms that the error in determining distances from the image data is  $\pm 3.45$  mm in the axial direction. The variance in

intensity values for the particle along the FoV has led to the image data to be analysed using method 2. Instead of looking at one row of pixels through the centre of the particle location along the z direction a summation of each 2D plane was performed which allowed intensity profiles to be produced using all of the detected data in that time frame. Figure 4.3 shows the summed profile for the particle at about 80 mm along the FoV and Figure 4.4 shows the superimposed summed intensity plots for the particle at each 10 mm incremental position.

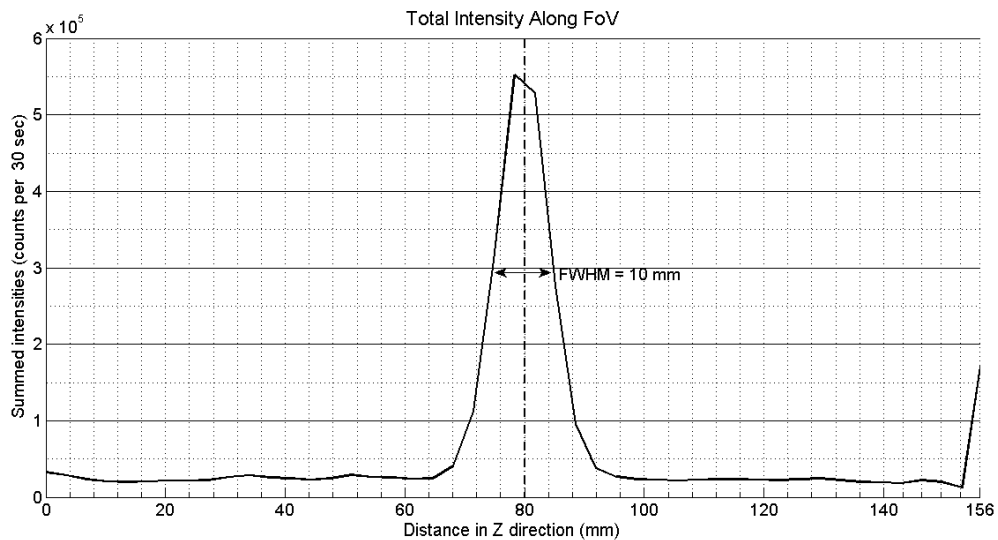


**Figure 4.3. Summed intensity plot for point source with peak at 80 mm. FWHM is 10 mm.**

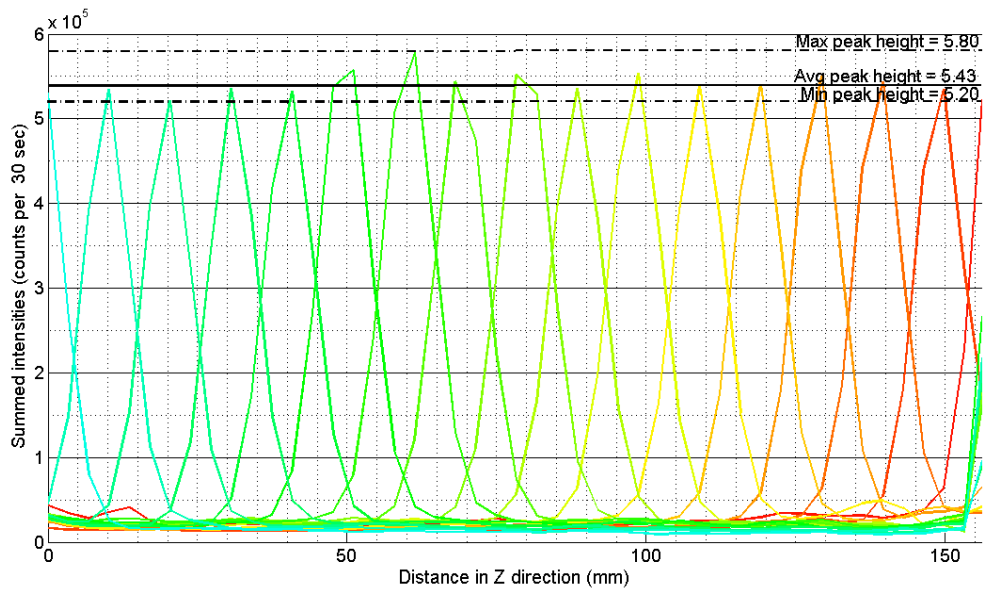


**Figure 4.4. Superimposition of all point source locations. The maximum peak height is  $5.8 \times 10^5$  counts per 30 sec at 100 mm, the minimum peak height is  $5.20 \times 10^5$  counts per 30 sec at 140 mm and the average peak height is  $5.44 \times 10^5$  counts per 30 sec.**

The same analysis was performed as previously and Table 7 shows the results for the summed intensity plots. By using all of the detected events for each time frame an average peak height of  $5.4 \pm 0.05 \times 10^5$  counts per 30 sec is observed with a standard deviation of  $0.14 \times 10^5$  counts per 30 sec, which is 2.76% of the average value. In comparison to the standard deviation of the single pixel peak heights, which was 10% of the average peak value, the peak heights of the summed data show much less variation and indicates increased axial sensitivity uniformity. The average measured FWHM of the point sources was  $10 \pm 1$  mm with a standard deviation of 1.10 mm (11% of the average value). This is larger than the measurements performed for the single pixel intensity profiles indicating that the blurring artefact is exaggerated when considering the entire image frame. The uncertainty of the measurement of the FWHM was 1 mm which is approximately equal to the standard deviation of 1.1 mm showing

that the uncertainty of the measurement is justified and there is reasonable consistency in the measurements. The stated FWHM provided by the PET user manual is 6 mm, which is less than the calculated value of 10 mm. This increase is due to the axial smoothing filter which enhances the blurring effect of the spatial resolution. The values marked with \* have been calculated using a weighted average. This is because there are two consecutive points of high intensity implying that the source is likely to lie

**Table 7. Maximum peak height and FWHM for the irradiated particle for 10 mm increments along the FoV for the cross-sectional summation intensity profiles across the particle.**

Actual position in z direction (mm)	Measured position in z direction ( $\pm 3.45$ mm)	Distance between peaks ( $\pm 1$ mm)	Max peak height ( $\times 10^5 \pm 0.05$ counts per 30 sec)	FWHM ( $\pm 1$ mm)
0	0	-	5.3	-
10	10.21	10.21	5.3	9
20	20.42	10.21	5.2	8
30	30.64	10.22	5.4	9
40	40.85	10.21	5.3	10
50	49.28*	8.43	5.5*	12
60	61.30	12.02	5.8	10
70	68.08	6.78	5.4	10
80	79.93*	11.85	5.4*	11
90	88.50	8.57	5.4	10
100	98.72	10.22	5.5	11
110	108.9	10.18	5.4	10
120	119.25	10.35	5.4	11
130	129.36	10.11	5.5	10
140	139.57	10.21	5.4	8
150	149.79	10.22	5.4	10
160	156.00	6.21	5.7	-
Average	-	9.75	5.43	10.00
Standard deviation	-	1.55	0.14	1.10
Std as % of avg	-	15.93	2.66	11.07
Mode	-	10.21	5.4	10.00

\* Calculated using weighted average of two consecutive high points of intensity

somewhere between the two. As with the single pixel profiles the mode of the peak separation distances is 10.21 mm, which correlates to approximately three plane separations (10.35 mm).

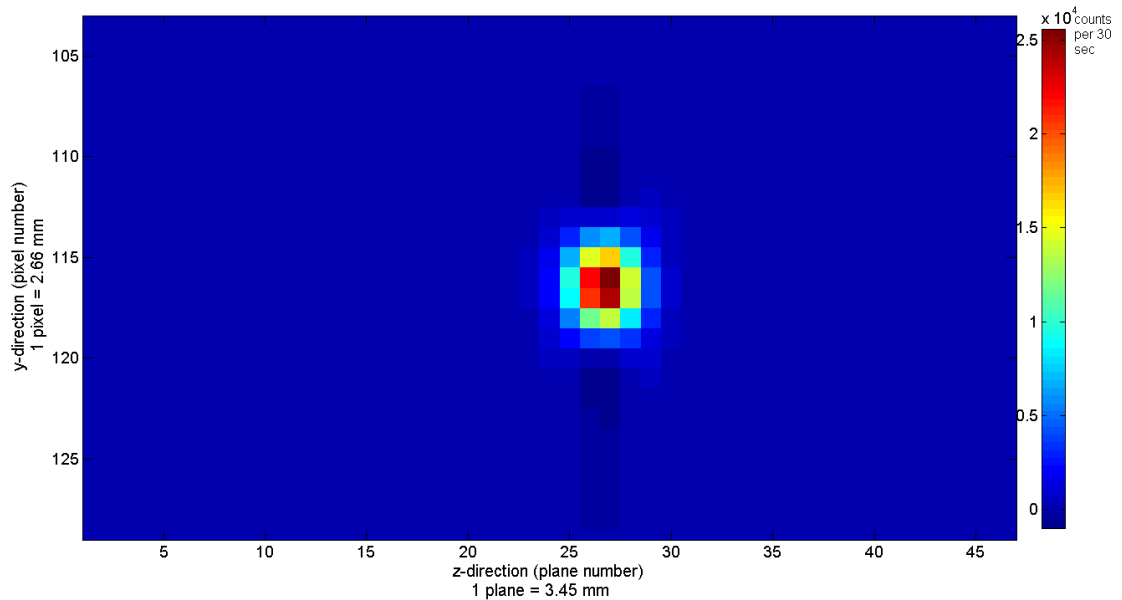


**Figure 4.5. An image of the point source at 90 mm (plane 26). This is an example of how the blurring is observable in the images. The maximum point of intensity ( $2.56 \times 10^5$  counts per 30 sec) is indicated by the dark red pixel and the range of yellow to light blue pixels show the blurring.**

The image shown in Figure 4.5 shows qualitatively what the blurring of a point source in an image looks like. The red pixels show the high intensity of the point source peak and the light blue pixels around this is the blurring effect.

The second series of tests were an investigation into the spatial resolution of the PET camera. From section 2.2 (Global Considerations) it is known that the spatial resolution is defined as the separation between point sources required for individual identification. This is also the same as the FWHM of the point source profile which is stated as 6 mm

for by the user manual. The following pages show a photo of each resolution test set-up and the resulting intensity plots across the irradiated particles and image of the test in order. Five different point sources of varying activities were separated by varying distances along the FoV in the z direction. The point sources used were irradiated steel particles and are described in Table 8. The ruler with the point sources was placed in the camera's FoV so that the end of the ruler labelled "FRONT" was at the side of the camera closest to the user. In the images this translates to  $z = min$  and the end of the ruler labelled "BACK" is  $z = max$ . The 4 cm mark on the ruler was lined up with the edge of the laser display closest to the user and the farthest laser marker lined up with the 20 cm mark on the ruler. This means that when analysing the image data  $z = 160 mm$  is 20 cm on the ruler and  $z = 0 mm$  is 4 cm on the ruler. For the displayed intensity profiles of the point source the line marking the peak location has been shown as the same colour of the marker showing the locations of the point sources on the ruler in the photos. The only colour that does not match is for point source 1 which has a yellow marker in the photos but to distinguish the peak from source 4 in the intensity profiles a purple line has been used. The intensity profiles appear to be cut short at just past 156 mm where the expected FoV is 160 mm. The reason for this is that the 160 mm FoV is split into 47 discrete planes. This means that all of the data acquired in plane 1, 0 – 3.45 mm, is stored in element 1, 3.45 – 6.9 mm is stored in element 2 and so on until element 47 which contains data between 156.55 – 160 mm. This is the technique that has been adopted for all image analysis.

**Table 8. Point source specifications for resolution test.**

Particle Number	Type	Colour indicator	Size (mm)*	Activity ( $\mu\text{Ci}$ )
1	Sphere	Purple	$\text{\O} = 3$	42
2	Pellet	Green	$\text{\O} = 3, L = 8$	208
3	Pellet	Blue	$\text{\O} = 3, L = 7$	108
4	Pellet	Yellow	$\text{\O} = 3, L = 7$	200
5	Sphere	Orange	$\text{\O} = 4$	86

\*  $\text{\O}$  is diameter and  $L$  is length of pellet



**Figure 4.6. Photo of set up for resolution test 1. The orange marker indicates the position of source 5 and the yellow marker indicates the position of source 5 (a purple line is used in the image analysis for the location of this source).**

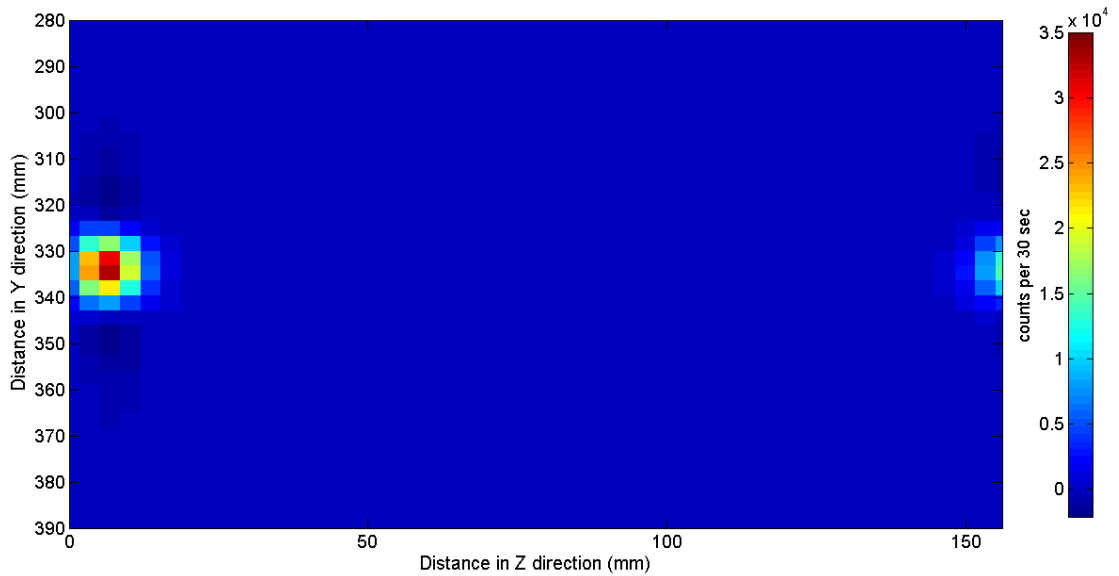


**Figure 4.7. Image of resolution test 1. The position of source 1 is 200 mm on the ruler which should correspond to 156 mm in the image. The position of source 5 is at 40 mm on the ruler and should correspond to 0 mm in the image; however the point of intensity is 3 pixels from the left which equates to 6.9 mm as pixel 1 = 0 mm. The maximum intensity of source 1 at the edge of the FoV is  $\sim 1/3$  of source 5 which leads to the assumption that source 1 is just outside the FoV of the camera.**

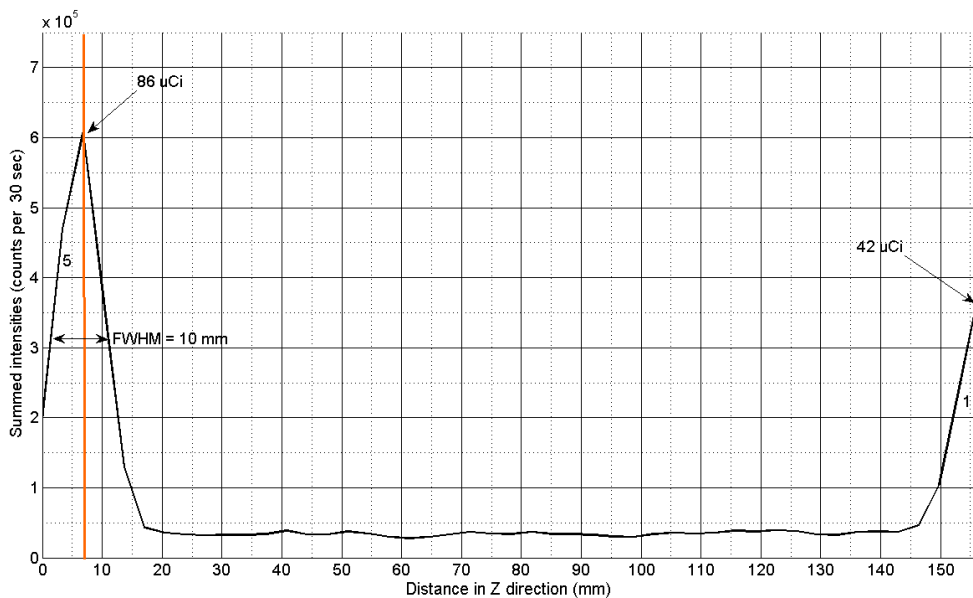


**Figure 4.8. Resolution test 1: Source 1 measured at the edge of or outside the FoV (156 mm) and source 5 measured at 6.9 mm (FWHM = 10 mm). See Table 9 for separation measurements.**

The axial FoV is expected to be 160 mm and in resolution test 1 (Figure 4.7 and Figure 4.8) source 1 and source 5 were placed 160 mm apart to test this. Both particles were expected to be at the edge of the FoV according to the laser display. It can be seen that the source on the left (source 5) is within the FoV with a FWHM of 10 mm but the source on the right (source 1) is assumed to be at the edge or outside of the FoV as there is no clear peak. In the image this is displayed as a hot point of intensity for source 5 and an increased intensity at the edge of the FoV in the left of the image for source 1 and minimum background intensity between the two sources. The displayed location offset could be caused by the size of the particles, which vary from 3 to 8 mm. This is comparable to and larger than the plane separation of 3.45 mm meaning the exact location of the particles could vary by 6.9 mm. Another reason for this apparent displacement could be that the laser display of the FoV wasn't exactly calibrated to the actual FoV of the detectors.



**Figure 4.9. Photo of set up for resolution test 2. The central yellow marker indicates the position of source 4. Source 4 is a spherical source and source 5, also identified by a yellow marker, is a pellet.**

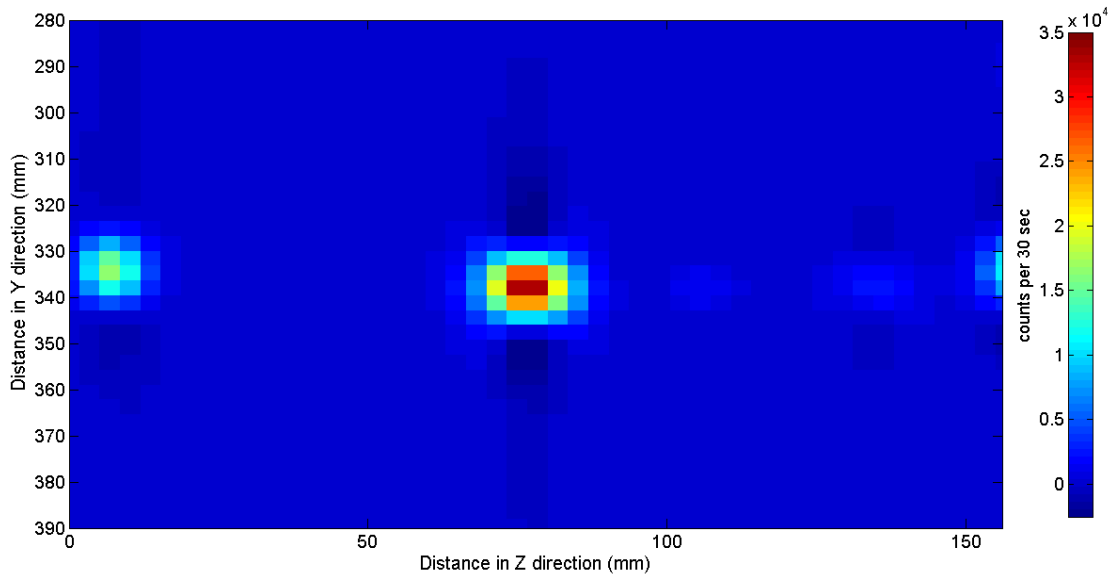


**Figure 4.10. Image of resolution test 2. The position of sources 1 was the same as the previous test and source 5 was moved 10 mm to 50 mm on the ruler (10 mm in the image data). Source 4 was placed between the two at 120 mm on the ruler (80 mm in the image data). The observed location of source 4 was measured to be 78 mm and the observed location of source 5 was the same as the previous measurement of 6.9 mm.**

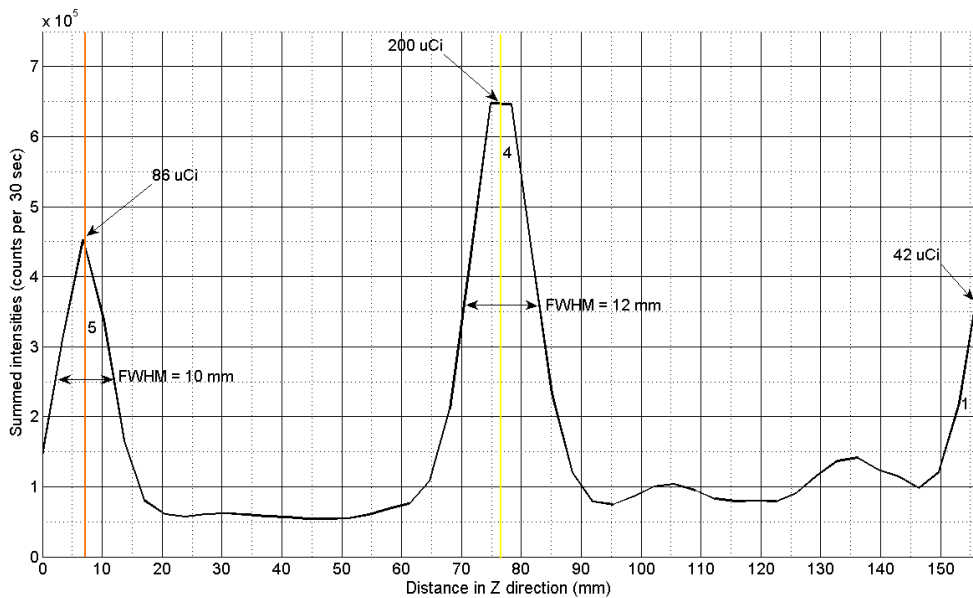


**Figure 4.11. Resolution test 2: Source 1 measured at 156 mm, source 4 measured at 78 mm (FWHM = 12 mm) and source 5 measured at 6.8 mm (FWHM = 10 mm) in the z direction. See Table 9 for separation measurements.**

The second test (Figure 4.10 and Figure 4.11) was to investigate how placing a third particle (particle 4) between the two edge particles would affect the intensity of the peaks and the minimum intensities between the peaks. The peak for particle 5 drops from about  $6 \times 10^5$  counts to around  $5 \times 10^5$  counts and the minimum values between peaks rises from about  $0.4 \times 10^5$  to around  $1 \times 10^5$  counts, with the profile no longer completely smooth on the right side of the central peak. The measured FWHM of source 4 was 12 mm and 10 mm for source 5.



**Figure 4.12. Photo of set up for resolution test 3. The blue marker indicates the location of source 3 and the green marker indicates the location of source 2.**

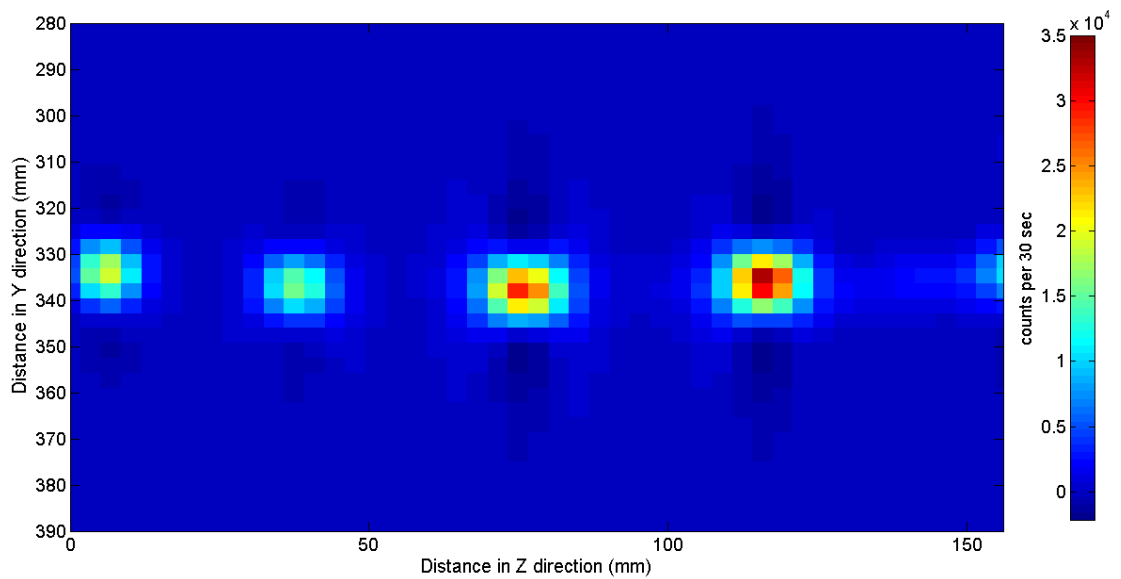


**Figure 4.13. Image of resolution test 3. Source 1 is still positioned at 200 mm (156 mm in the image data), source 2 was positioned at 160 mm (120 mm in the image data), source 4 was still positioned at 120 mm (80 mm in the image data), source 3 was positioned at 80 mm (40 mm in the image data) and source 5 was kept at 50 mm (10 mm in the image data).**

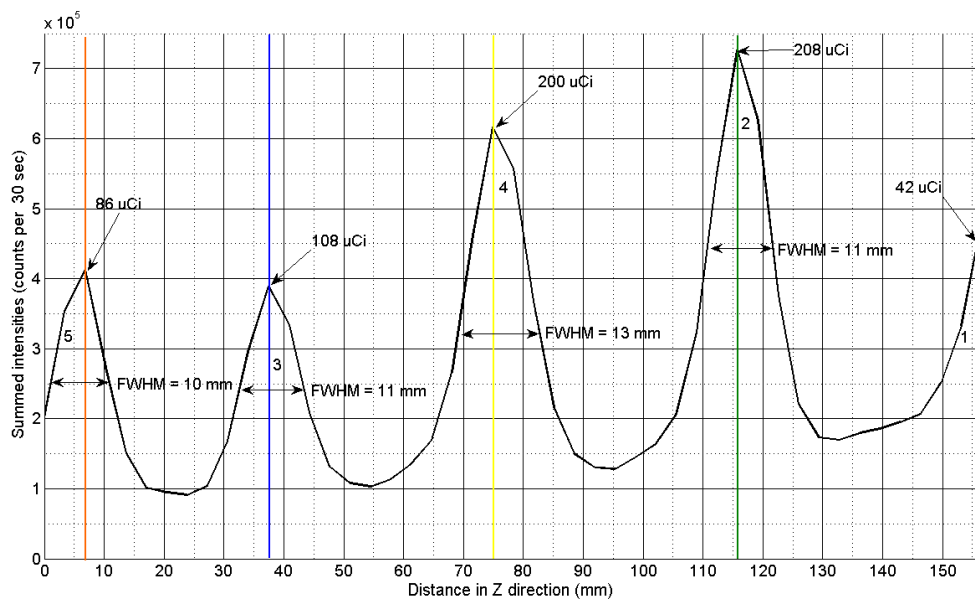


**Figure 4.14. Resolution test 3: Source 1 measured at 156 mm, source 2 measured at 115 mm (FWHM = 11 mm), source 4 measured at 76 mm (FWHM = 13 mm), source 3 measured at 37 mm (FWHM = 11 mm) and source 5 measured at 7 mm (FWHM = 10 mm). Sources are separated by 30 or 40 mm which is 3 – 4 times the observable spatial resolution of the camera. See Table 9 for separation measurements.**

In the third test (Figure 4.13 and Figure 4.14) all five particles of varying activity were placed in the FoV: Source 1 at ~ 156 mm, source 2 at ~ 115 mm, source 4 at ~ 76 mm, source 3 at ~ 37 mm and source 5 at ~ 7 mm. It is possible to see four distinct peaks of the particles that are within the FoV, particles 5, 3, 4 and 2. Particle 1 is still visible at the edge of the FoV and the background level between particle 1 and 2 are slightly higher than the other three minima. Again the average values of the background between peaks have risen by about  $0.5 \times 10^5$  counts. It is observed that the FWHM of sources 2, 3 and 4 are slightly larger than the measured FWHM of 10 mm from the previous calibration test. This is likely to be due to the length of these pellets (7 and 8 mm) being larger than the plane separation of 3.45 mm.



**Figure 4.15. Photo of the set up for resolution test 4. The sources have been re-ordered to 5, 4, 2, 3 and 1 and moved closer to each other, separated by 20 mm with source 1 positioned 30 mm away.**

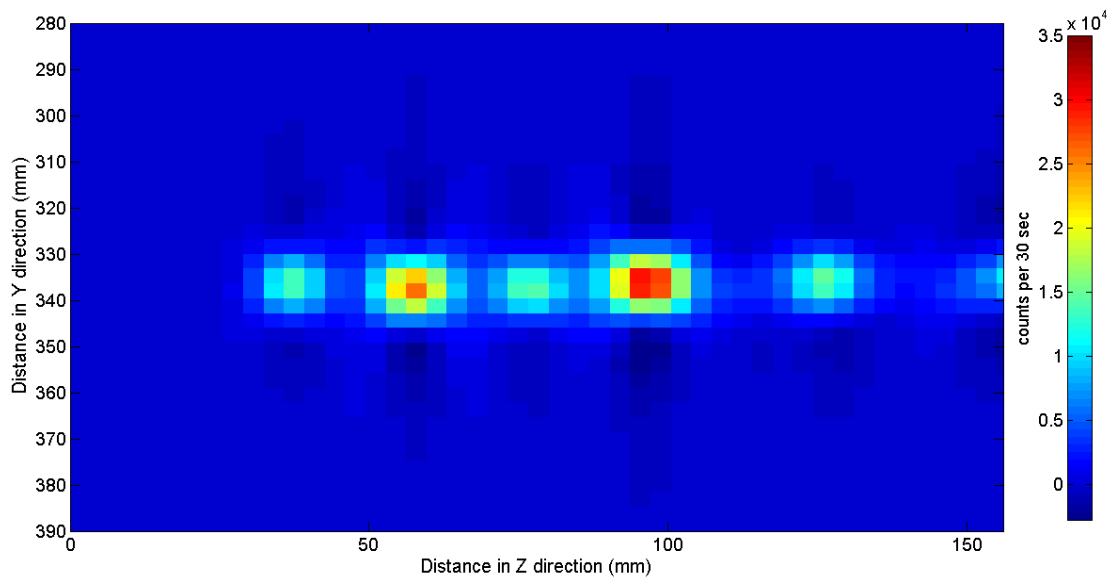


**Figure 4.16. Image of resolution test 4. Source 1 was moved to 170 mm (130 mm in the image data), source 2 was positioned at 140 mm (100 mm in the image data), source 3 was positioned at 120 mm (80 mm in the image data), source 4 was positioned at 100 mm (60 mm in the image data) and source 5 was moved to 80 mm (40 mm in the image data).**

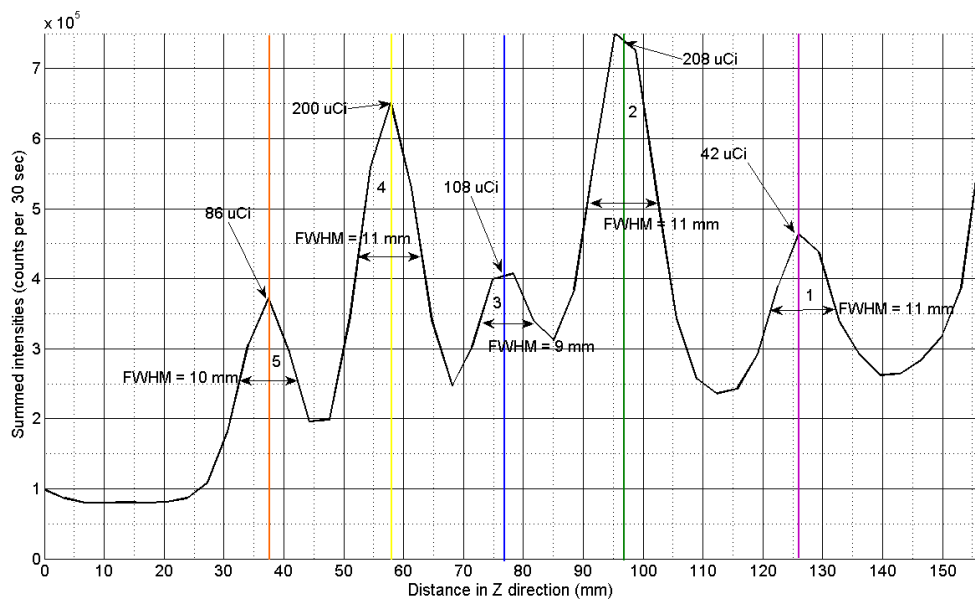


**Figure 4.17. Resolution test 4: Source 1 measured at 126 mm (FWHM = 11 mm), source 2 measured at 97 mm (FWHM = 11 mm), source 3 measured at 77 mm (FWHM = 9 mm), source 4 measured at 57 mm (FWHM = 11 mm) and source 5 measured at 38 mm (FWHM = 10 mm). Sources are separated by 2 or 3 cm which is which is 2 – 3 times the observable spatial resolution of the camera. See Table 9 for separation measurements.**

In the fourth test (Figure 4.16 and Figure 4.17) all five particles were repositioned to: Source 1 at ~ 126 mm, source 2 at ~ 97 mm, source 3 at ~ 77 mm, source 4 at ~ 57 mm and source 5 at ~ 38 mm. Although the separation between most of the particles has been reduced to 20 mm individual peaks of intensity are clear in the profile and the points are distinguishable in the image. Five distinct peaks can now be seen within the FoV but there still appears to be a peak to the right of the FoV where particle 1 had been located previously. This was an unexpected artefact in the image data and was monitored to determine if it was consistent and it was concluded that this is likely to be caused by a memory clearing problem of the PET camera. A separate series of tests were performed to investigate this issue where one point source was moved in 10 mm increments along the axial FoV and separate acquisition sessions were performed for each location. There were clear signs of peaks of intensity in the previous location of the point source along with the current location. This indicates an issue with the PET camera not effectively clearing the acquisition data between sessions. This was particularly a problem for imaging sessions performed within quick succession. For sessions performed several hours apart there was no apparent memory clearing problem so it was hoped that this would not cause an issue for the imaging of the adsorption column as the runs were performed on separate days. However it was noted in the event unexpected artefacts were observed. The minima between peaks observed in Figure 4.17 are now greatly increased showing that the spatial resolution of the camera is being approached. The FWHM of each of the peaks are all within 10 - 11 mm apart from source 3 which is smaller at 9 mm. This is due to the background level either side of the peak, approximately  $3 \times 10^5$  counts per 30 sec, being  $\frac{3}{4}$  of the

value of the peak,  $4 \times 10^5$  counts per 30 sec. This results in a less defined peak and a difficult to determine FWHM.



Figure 4.18. Photo of set up for resolution test 5. Similar set up to test 4 but with source 5 placed 30 mm away from the rest of the sources which are separated by 20 mm.

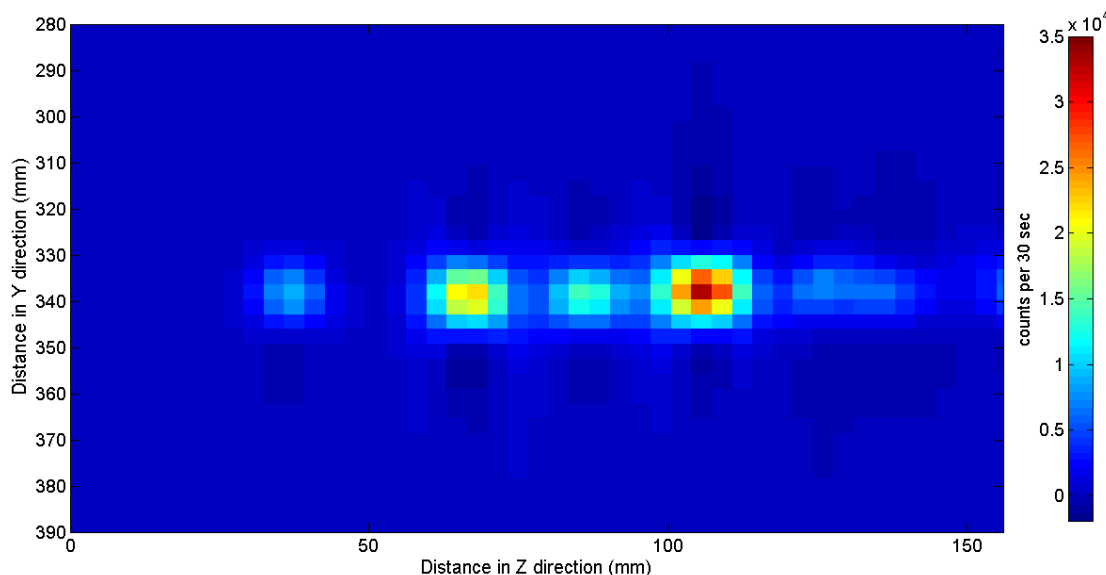
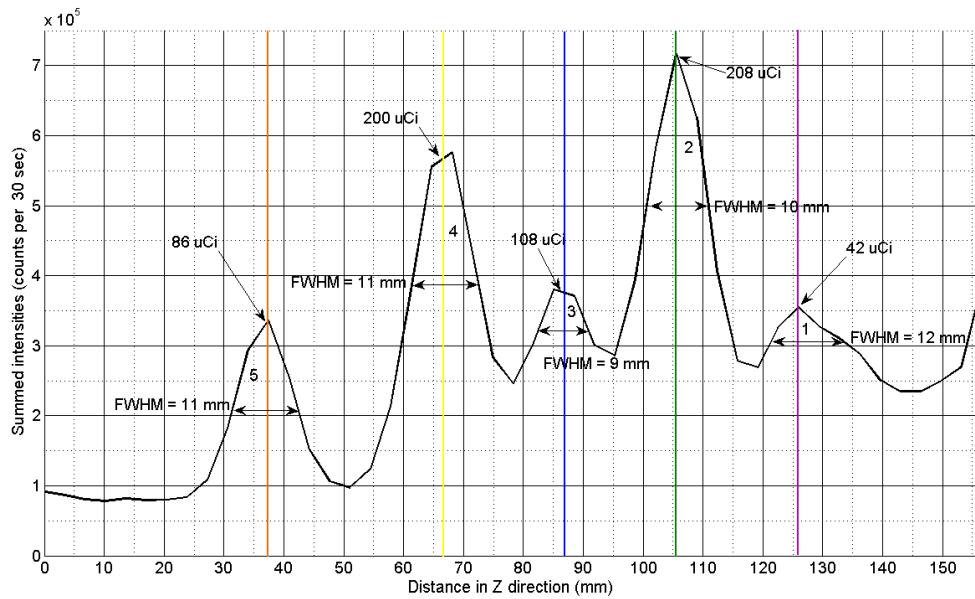


Figure 4.19. Image of resolution test 5. Source 1 was kept at 170 mm (130 mm in the image data), source 2 was moved to 150 mm (110 mm in the image data), source 3 was positioned at 130 mm (90 mm in the image data), source 4 was positioned at 110 mm (70 mm in the image data) and source 5 was kept at 80 mm (40 mm in the image data).



**Figure 4.20. Resolution test 5: Source 1 measured at 126 mm (FWHM = 12 mm), source 2 measured at 105 mm (FWHM = 10 mm), source 3 measured at 87 mm (FWHM = 3 mm), source 4 measured at 67 mm (FWHM = 11 mm) and source 5 measured at 38 mm (FWHM = 11 mm). Sources are separated by 2 or 3 cm which is which is 2 – 3 times the observable spatial resolution of the camera. See Table 9 for separation distance measurements.**

In the fifth sensitivity test (Figure 4.19 and Figure 4.20) all five particles were used and the locations were measured: source 1 at ~ 126 mm, source 2 at ~ 105 mm, source 3 at ~ 87 mm, source 4 at ~ 67 mm and source 5 at ~ 38 mm. The artefact on the right hand side of the intensity plots is still observable; however it has reduced from  $5.7 \times 10^5$  counts per 30 sec to  $3.7 \times 10^5$  counts per 30 sec. The profile produced for test 5 is very similar to that of test 4 although source 1 has a less defined peak and larger FWHM of 12 mm.



**Figure 4.21. Photo of set up for resolution test 6. All five sources are spaced 10 mm apart.**

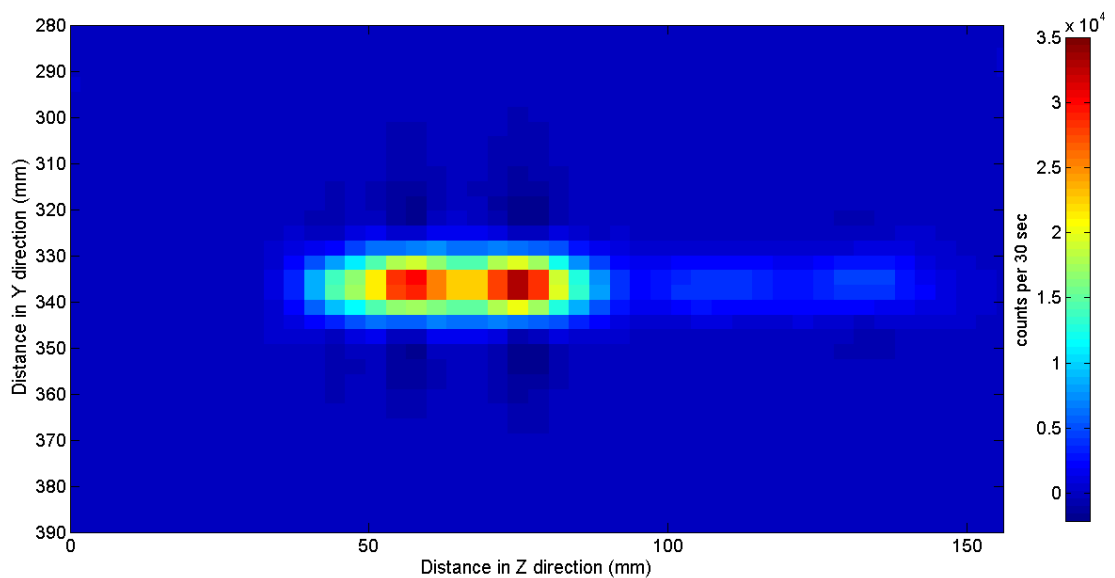


**Figure 4.22. Image of resolution test 6. The sources were all moved so that each was separated by 10 mm. Source 1 was moved to 130 mm (90 mm in the image data), source 2 was moved to 120 mm (80 mm in the image data), source 3 was positioned at 110 mm (70 mm in the image data), source 4 was positioned at 100 mm (60 mm in the image data) and source 5 was moved to 90 mm (50 mm in the image data).**

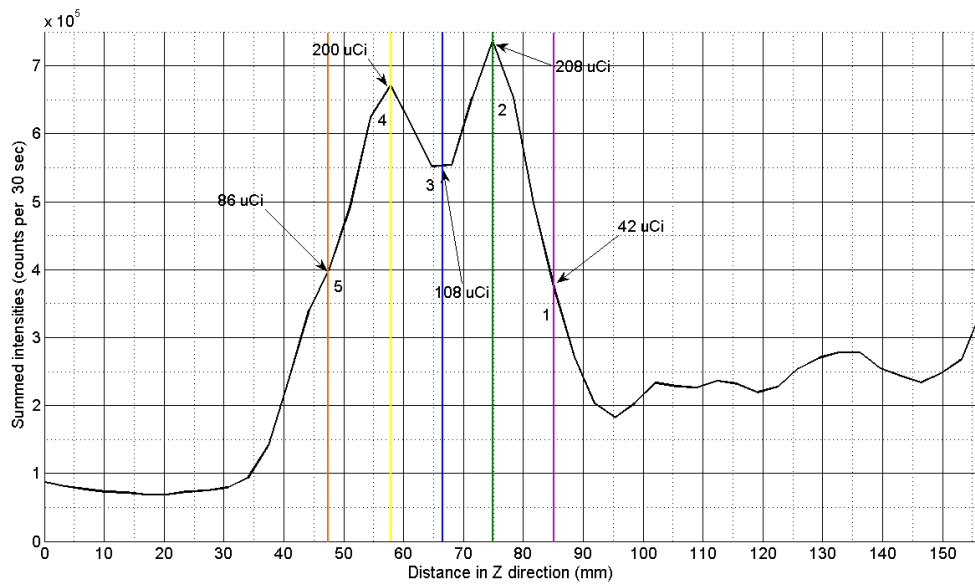


**Figure 4.23. Resolution test 6: Source 1 assumed to be 85 mm, source 2 measured at 75 mm, source 3 assumed to be 67 mm, source 4 measured at 58 mm and source 5 assumed to be 47 mm. Sources are separated by 10 mm which has been determined to be equal to the spatial resolution. There are no clear peaks so FWHM and location separation could not be determined.**

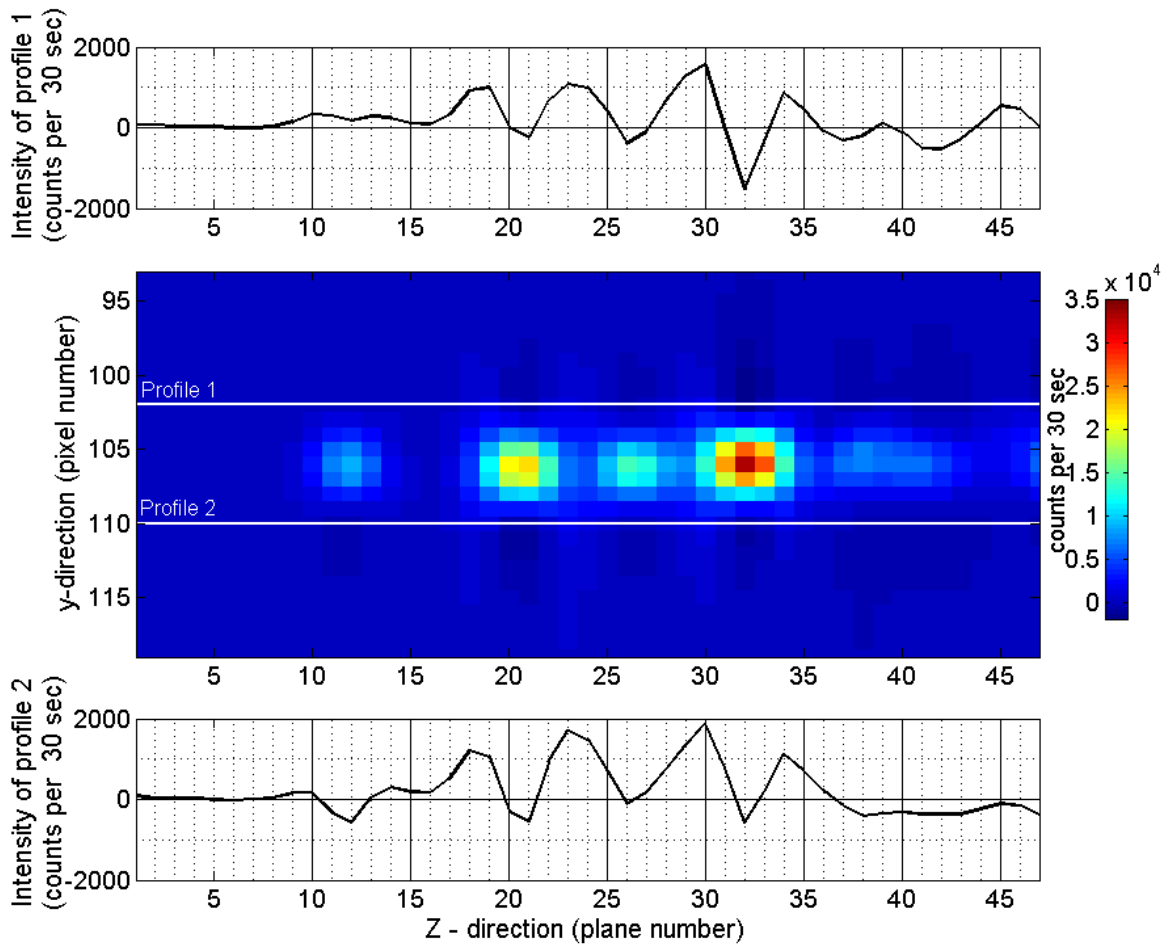
The final test (Figure 4.22 and Figure 4.23) shows all five particles spaced 10 mm apart in the middle of the FoV in the order 5, 4, 3, 2, 1. It is no longer possible to see 5 distinct peaks. The two particles with highest activity (2 and 4) were placed either side of particle 3 to see what affect that would have. The result is an intensity increase for particle 3 to  $5.5 \times 10^5$  counts. This is due to an accumulated intensity contribution from the blurring of particles 2 and 4. The area to the right of the particles show a clear and reduced minimum profile, however the area to the left of the particles is noisy with greater average intensity than the right hand side. There is still an increased intensity at the edge of the FoV on the left hand side.

**Table 9. Set and measured separation distances between point sources.**

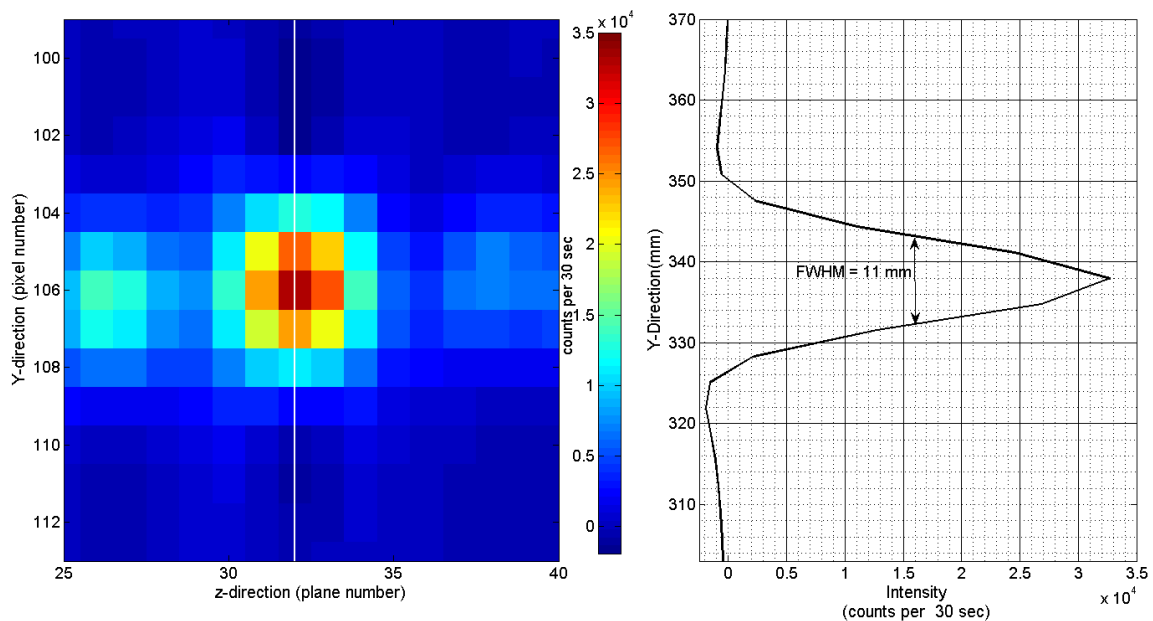
<b>Test number</b>	<b>Source order</b>	<b>Set separation (<math>\pm 1</math> mm)</b>	<b>Measured separation (<math>\pm 6.9</math> mm)</b>
1	5, 1	160	149
2	5, 4, 1	70, 80	71, 78
3	5, 3, 4, 2, 1	30, 40, 40, 40	30, 39, 39, 41
4	5, 4, 3, 2, 1	20, 20, 20, 30	19, 20, 18, 21
5	5, 4, 3, 2, 1	30, 20, 20, 20	29, 20, 18, 21
6	5, 4, 3, 2, 1	10, 10, 10, 10	-

Table 9 displays the set source separation distances for each test and the corresponding measured separations from the image data. It is observed that the measured separations are comparable to the set distances giving confidence to the ability to locate specific intensity characteristics.

In all six resolution test images transaxial blurring may be observed in the dark regions above and below the points of intensity (in the  $y$  direction) which indicate negative intensity which is an expected artefact of the Filtered Backprojection (FBP) reconstruction technique. This has been shown in more detail for resolution test 5 in Figure 4.24. Axial intensity profiles were produced above the locations of the point sources, profile 1, and below the point sources, profile 2. Both profiles clearly show minimum points of negative intensity directly above and below the maximum intensity of the point sources in the  $y$ -direction. The locations of the minimum intensities of the profiles and maximum intensities of the image correspond to the same plane number. To investigate this further a profile across source 2, the most active source, in the  $y$ -direction was produced and is shown in Figure 4.25.



**Figure 4.24.** An image of resolution test 5 with axial profiles of the regions of blurring above (profile 1) and below (profile 2) the point sources included.



**Figure 4.25. A close up image of point source 2 from resolution test 5 and the corresponding intensity profile in the y-direction across the centre of the source.**

The transaxial intensity profile for point source 2 in resolution test 5 shows a peak with FWHM of 11 mm. There are negative points of intensity either side of the peak due to the Gaussian filter applied in the image reconstruction (see section 2.5.2). The FWHM is consistent with the measurements made from the axial profiles showing that the spatial resolution is equal in the axial and transverse planes. The increase of observed spatial resolution from the resolution claimed by the manufacturer shows that the FBP technique and axial smoothing has a noticeable effect on the observable spatial resolution of the image data. The degraded resolution could also be an effect of the deterioration of the PET camera due to old age.

## 4.2 EXPERIMENTAL PROCEDURE

Once the capabilities and limitations of the PET camera for static imaging were investigated and reviewed it was possible to apply the adapted technique to the study of CO<sub>2</sub> adsorption onto a pressurised packed bed. From the preliminary investigation (section 3.2.2) and calibration tests (section 4.1.1) it was possible to determine optimal imaging conditions and solve any engineering issues for the system set-up.

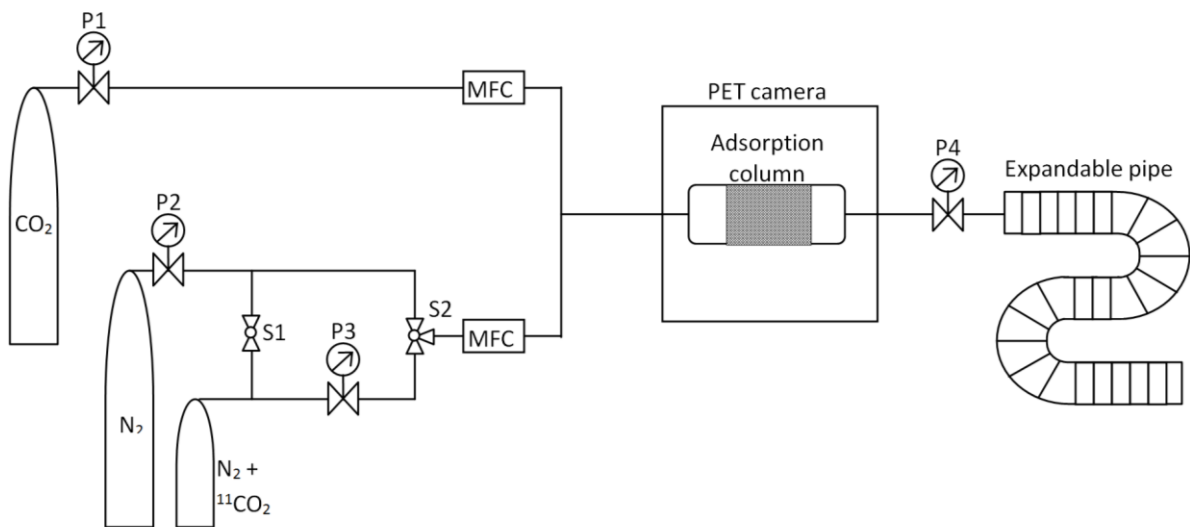


**Figure 4.26. Experimental set-up for the adsorption study.**

From the dynamic PET preliminary investigation it was concluded that a more efficient way of connecting the <sup>11</sup>CO<sub>2</sub> cylinder to the system was required to enable system pressurisation before the arrival of the gas and to maintain constant pressure whilst connecting the cylinder. It was also necessary to pressurise the <sup>11</sup>CO<sub>2</sub> – N<sub>2</sub> cylinder once it was connected to the system as the pure N<sub>2</sub> cylinder would already be connected for the pressurisation phase. The experimental set-up is shown in Figure 4.26. The three-way valve, S2, allows: 1) the system to be pressurised using pure N<sub>2</sub>, 2) the system to be isolated whilst attaching and pressurising the <sup>11</sup>CO<sub>2</sub> cylinder and

3) to switch the inlet gas to the  $^{11}\text{CO}_2 - \text{N}_2$  mixture. The two-way valve,  $S_1$ , is used to

- 1) isolate the system from the  $^{11}\text{CO}_2$  cylinder so that the regeneration and pressurisation of the bed may happen without the presence of the  $^{11}\text{CO}_2$  cylinder and
- 2) the  $^{11}\text{CO}_2$  cylinder may be pressurised using the  $\text{N}_2$  once it has been attached.

The system pressure was controlled using backpressure regulator  $P_4$  and the flow rate of the feed gas was controlled using two Mass Flow Controllers (MFCs). The feed flow of  $\text{CO}_2$  and  $\text{N}_2$  (or  $^{11}\text{CO}_2 - \text{N}_2$ ) was controlled separately. Each gas cylinder has a pressure gauge and regulator attached:  $P_1$  controlled the outlet pressure of the pure  $\text{CO}_2$  cylinder,  $P_2$  controlled the outlet pressure of the pure  $\text{N}_2$  cylinder and  $P_3$  controlled the outlet pressure of the  $^{11}\text{CO}_2 - \text{N}_2$  cylinder. The adsorption column was positioned in the FoV of the PET camera and the expandable pipe was sealed and used to contain the radioactive effluent of the adsorption column. The expandable pipe was shielded behind a lead brick wall to reduce exposure to radiation. The risk assessment describing the safety precautions of this experiment is included in section 8.1. A description of the equipment and materials used follows.

## **4.2.1 Materials**

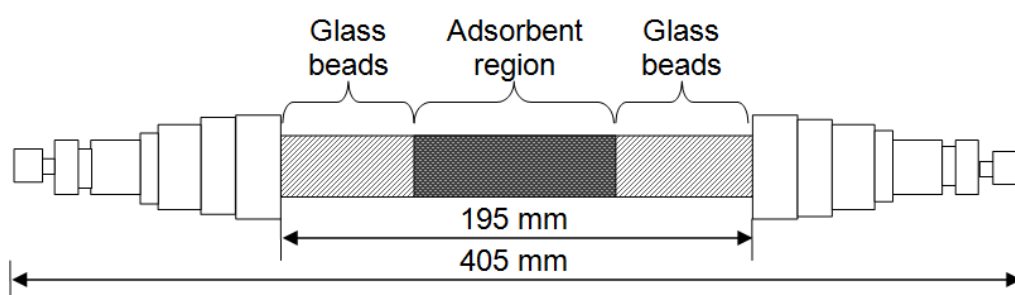
### ***4.2.1.1 Adsorption bed***

A photo and diagram of the adsorption bed used can be seen in Figure 4.27. The column was made from a stainless steel tube with an internal diameter of 22 mm and a wall thickness of 1.5 mm. The tube was 250 mm long and Swagelok reducers were used to connect the column to the 1/8" stainless steel pipes at the inlet and outlet. For the project it was desirable to see the full length of the adsorbent region in the image data so the ends of the column were packed with 3 mm glass beads and the adsorbent

region was 70 mm for Zeolite 13x and 79 mm for Activated Carbon as depicted in Figure 4.27 (b). The packing of the bed was random and steel mesh disks were used to separate the glass beads from the adsorbent.



(a)



(b)

**Figure 4.27. (a) Is a photograph of the stainless steel adsorption column with Swagelok fittings and (b) is a diagram displaying the dimensions of the column and the adsorbent region has been highlighted.**

#### **4.2.1.2 Adsorbent Zeolite 13X**

The zeolite used for the first set of experiments was Zeolite 13X acquired from Sigma Aldrich (USA). The 13X type synthetic zeolite in 3 mm bead form has pore diameter of 0.1 nm and a bulk density of  $689 \text{ kg m}^{-3}$ , measured using a pycnometer, and a surface area of about  $750 \text{ m}^2 \text{ g}^{-1}$  (Vyas et al. 2004). Figure 4.28 shows a photo of the zeolite 13X beads used.



**Figure 4.28. Photo of 3 mm Zeolite 13X beads.**

#### ***4.2.1.3 Adsorbent Activated Carbon***

The activated carbon used was from Brownell's (UK). Figure 4.29 shows a photo of the 3 – 10 mm activated carbon pellets used for the second part of the experiment. The bulk density was  $486 \text{ kg m}^{-3}$ , measured using a pycnometer, and the high degree of microporosity due to a network of pores with diameters ranging up to 50 nm means that per gram of activated carbon the surface area is between  $800 \text{ to } 1200 \text{ m}^2 \text{ g}^{-1}$  (Dabrowski & Meurant 1999).



**Figure 4.29. Photo of the 3mm to 10 mm pellets of Activated Carbon.**

#### **4.2.1.4 CO<sub>2</sub> analyser**

The CO<sub>2</sub> analyser used for the purpose of this study was a Servomex 5200 Multi-Purpose portable benchtop gas analyser. It has a CO<sub>2</sub> measurement range of 1-100 vol.% CO<sub>2</sub> in the gas and the intrinsic error associated with this measurement is  $\pm 2\%$  of the full scale range. The analyser has an operational pressure range between 6.9 kPa gauge to 68.9 kPa gauge. The manufacturer states a response time of 75 seconds with a drying tube fitted to the inlet and high and low calibrations were performed regularly as recommended by the manufacturer. To record the data a simple data logger was used.

#### **4.2.1.5 Mass Flow Controllers**

Mass Flow Controllers (MFCs) were used to control the feed flow of gas into the column. Specifically two Brooks 5850 thermal mass flow controllers were used, one to control N<sub>2</sub> input and one to control CO<sub>2</sub>. The N<sub>2</sub> flow controller was calibrated for a maximum 'normal' flow rate of 400 mln min<sup>-1</sup>, where 'normal' conditions are considered to be 0°C and atmospheric pressure. The CO<sub>2</sub> flow controller was calibrated to have a maximum flow rate of 100 mln min<sup>-1</sup>. Both controllers could be used up to a pressure of 10 MPa. A correction factor that depended on CO<sub>2</sub> cylinder pressure was required for the set CO<sub>2</sub> flow and is given in section 8.2. An IGI Systems dIGIbox combined USB-RS485 communication and power supply was used to interface the MFCs with the operating computer and the IGI control software was used to control and record the flow rates.

#### **4.2.1.6 Backpressure regulator**

A high sensitivity general purpose Swagelok backpressure regulator was used to control the pressure of the system. It featured a nonperforated diaphragm with a metal-to-metal diaphragm seal and could control pressures up to 6.8 MPa at temperatures up to 200°C. The operating conditions of the adsorption study included system pressure up to 3.1 MPa and each experimental run was performed at 19°C so the backpressure regulator was adequate for this purpose. The laboratory was air conditioned and temperature controlled.

#### **4.2.2 Experimental method**

The first stage of the experimental procedure was to regenerate the bed. To do this pure N<sub>2</sub> was passed through the bed at atmospheric pressure at a flow rate of 200 ml min<sup>-1</sup> controlled using the N<sub>2</sub> MFC. The CO<sub>2</sub> analyser was set to monitor the outlet of the column and once the analyser reported a CO<sub>2</sub> concentration of 0% the pressure of the system was raised to desired pressure for the specific experimental conditions. Regeneration would take between 1 to 3 hours depending on initial conditions and previous experimental conditions. (Regeneration could be done more efficiently by raising the temperature of the bed as done in Temperature Swing Adsorption (TSA) but as it was necessary to keep the bed in the FoV of the PET camera this was not possible.) Once the system was pressurised it was possible to maintain this pressure by switching the 3-way valve to “closed” and stopping the MFCs. Upon arrival of the <sup>11</sup>CO<sub>2</sub> – N<sub>2</sub> gas cylinder from the cyclotron (a description of the production of <sup>11</sup>CO<sub>2</sub> is provided in section 2.6.2) the cylinder was connected to the system and pressurised to 60 bar using N<sub>2</sub> by opening the 2-way valve. The 2-way valve was then closed and the 3-way valve was switched to “<sup>11</sup>CO<sub>2</sub>” and the MFCs were set to start

the flow of gas at the desired flow rates as specified by the experimental conditions, which can be found in Table 10.

**Table 10. Table describing the desired experimental conditions used for each adsorption run.**

Run no.	Adsorbent	System Pressure (MPa)	CO <sub>2</sub> conc. (%)	N <sub>2</sub> flow (mln min <sup>-1</sup> )	CO <sub>2</sub> flow (mln min <sup>-1</sup> )	Time (min)
1	Zeolite 13X	3.1	10	180	20	160
2		2.6	30	140	60	160
3		2.6	50	100	100	160
4		1.7	10	180	20	170
5		1.6	30	140	60	160
6		1.6	50	100	100	160
7	Activated Carbon	2.8	10	180	20	180
8		2.6	30	140	60	160
9		2.6	50	100	100	150
10		1.6	10	180	20	180
11		1.6	30	140	60	150
12		1.6	50	100	100	150

Once the imaging of the system was complete the CO<sub>2</sub> and N<sub>2</sub> supply would be turned off and the system would be depressurised by releasing the back pressure regulator. Gas from the <sup>11</sup>CO<sub>2</sub> cylinder would continue to be passed through the system in order to safely depressurise the cylinder and keep the exhausted radioactive gas contained within the lead shielding. After the cylinder reached ambient pressure it would be disconnected from the system and returned to the cyclotron ready for the next run. The exhausted radioactive gas would be left inside the expandable ducting pipe overnight to allow the <sup>11</sup>CO<sub>2</sub> to decay down to background levels, after which point the gas would be safely released into the atmosphere.

The MFC and CO<sub>2</sub> analyser data was then retrieved and the actual CO<sub>2</sub> feed concentration and flow rate was determined. This information allowed a verification study to prove that the process being imaged was CO<sub>2</sub> adsorption and an approximate capacity of the adsorbents used was calculated. Adsorption isotherms from experimental data were produced and compared to literature and are discussed in section 5.1.

After the Unix PET computer had finished processing and reconstructing the images they would be checked and then transferred to a computer with Windows OS where they could be converted to usable ascii files and analysed using MATLAB and Excel. The raw image files containing the image data would be presented in the form of one continuous array starting with a main acquisition header and separated by frame sub headers. In the process of converting the raw data to ascii files the header and sub headers were removed to enable easier matrix manipulation. In ascii form it has been possible to analyse the image data qualitatively and quantitatively and this analysis is discussed in the following chapter.

## 5 RESULTS

### 5.1 CO<sub>2</sub> ANALYSER RESULTS

#### 5.1.1 Capacity and isotherms

The first stage of results analysis was to study the data recorded by the CO<sub>2</sub> analyser in order to verify and calibrate image data obtained by the PET camera. For confirmation that the process being studied for this section of the project was CO<sub>2</sub> adsorption values for capacity and breakthrough were extracted and compared to the well established Toth isotherm model (Cavenati et al. 2004). A code was written using MATLAB to calculate these values.

The Mass Flow Controllers (MFCs) control the flow of feed gas according to normal millilitres per minute. The term normal millilitres defines the volume of the gas in 'normal' conditions which are considered as an atmospheric pressure,  $P'$ , of 101,325 Pa and a temperature,  $T'$ , of 273.15 K as defined by the CO<sub>2</sub> analyser manufacturer (Servomex). From the MFC data the total 'normal' volumetric flow rate of N<sub>2</sub>,  $Q'_{N_2}$ , that enters the system is known. As stated in section 4.2.1.5 there is a systematic difference between the CO<sub>2</sub> flow rate that the MFC provides and the actual flow rate that enters the system that is inherent to the equipment which is corrected for in the results analysis. The actual normal flow rate of CO<sub>2</sub>,  $Q'_{CO_2}$ , was determined using  $Q'_{N_2}$  and the equilibrium concentration of CO<sub>2</sub>,  $C_{max}$ , provided by the CO<sub>2</sub> analyser as this is equal to the feed concentration.

$$Q'_{CO_2} = \frac{Q'_{N_2} 100}{100 - C_{max}} \text{ (mln min}^{-1}\text{)} \quad 5.1$$

It is expected that the flow rate of N<sub>2</sub> that exits the system,  $Q'_{N_2}$ , will be higher than the flow of N<sub>2</sub> that enters it as during adsorption CO<sub>2</sub> molecules will displace N<sub>2</sub> molecules already in the column. However, this change in flow rate is small and for simplicity the flow of N<sub>2</sub> is assumed to be constant giving equation 5.2.

$$Q'_{N_2exit} = Q'_{N_2} \text{ (mln min}^{-1}\text{)}. \quad 5.2$$

The exit flow rate of CO<sub>2</sub> varies proportionally according to the breakthrough curve of the column. As a higher volume of CO<sub>2</sub> exits the column this relates to a higher flow rate,  $Q'_{CO_2exit}$ . The varying flow rate was calculated as shown in equation 5.3 and is dependent on the amount of time that has passed  $t$ .

$$Q'_{CO_2exit,t} = \frac{Q'_{N_2}C_t}{(100-C_t)} \text{ (mln min}^{-1}\text{)}, \quad 5.3$$

where  $C_t$  denotes the CO<sub>2</sub> concentration at the exit at time  $t$ . An example plot of  $Q'_{CO_2exit}$  against  $t$  is shown in Figure 5.1. The solid line shows the varying CO<sub>2</sub> exit flow rate and the bold dashed line highlights feed  $Q'_{CO_2}$ . The dotted lines indicate the points considered to be breakthrough and saturation, 5% and 95% of the feed flow rate respectively. This type of plot clearly shows the point at which the adsorption column reaches equilibrium, i.e. the point when  $Q'_{CO_2} = Q'_{CO_2exit}$ . The volume of CO<sub>2</sub> that passed through the system,  $V_{CO_2out}$  was determined by integrating  $Q'_{CO_2exit}$  with respect to  $t$  where  $t_0$  is the start time and  $t_{max}$  is the end time.

$$V_{CO_2out} = \int_{t_0}^{t_{max}} Q'_{CO_2exit,t} dt \text{ (ml)} \quad 5.4$$

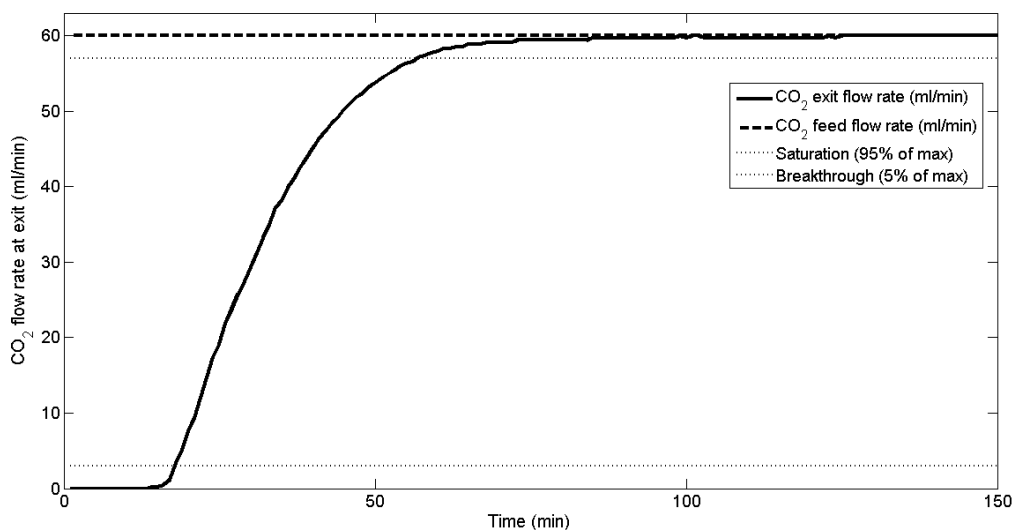


**Figure 5.1.** An example of a breakthrough curve from experimental data. The solid line shows the CO<sub>2</sub> exit flow rate (mln min<sup>-1</sup>), the bold dashed line shows the constant CO<sub>2</sub> feed rate (mln min<sup>-1</sup>) and the dotted lines highlight the points considered to be breakthrough (5% of feed) and saturation (95% of feed). This curve was produced using Activated Carbon at a system pressure of 1.6 MPa and CO<sub>2</sub> concentration of 30%.

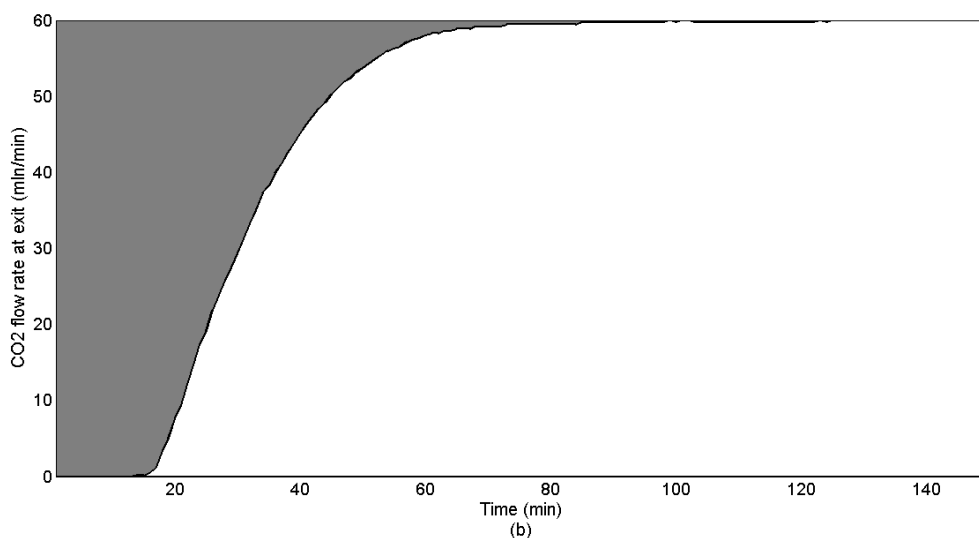


**Figure 5.2.** Plot showing the volume of CO<sub>2</sub> that exits the bed shaded in white under the curve (mln) and the volume of CO<sub>2</sub> captured by the column is shown by the grey region about the curve (mln).

Figure 5.2 shows the same  $Q'_{CO_2exit}$  against time plot as Figure 5.1 with the area under the curve shaded in white. This area gives the volume of CO<sub>2</sub> that passed through the bed in mln and is denoted by  $V_{CO_2out}$ . The grey area above is the volume of CO<sub>2</sub> that remains in the system, and therefore is assumed to be adsorbed, and is denoted by  $V_{CO_2ad}$  with units mln.  $V_{CO_2ad}$  was calculated by equation 5.5

$$V_{CO_2ad} = V - V_{CO_2out} \text{ (mln) ,} \quad \mathbf{5.5}$$

where  $V$  is the total volume of CO<sub>2</sub> that enters the system and is known by  $V = C_{CO_2} \cdot t$ . This volume of CO<sub>2</sub> adsorbed was used to determine the capacity,  $q_m$ , of the adsorbent for each experimental run using

$$q_m = n_{ad}/m \text{ (mol kg}^{-1}\text{),} \quad \mathbf{5.6}$$

where

$$n_{ad} = \frac{P_{CO_2} V_{CO_2ad}}{RT} \text{ (mol),} \quad \mathbf{5.7}$$

from the Ideal Gas Law, where  $P'_{CO_2}$  is the partial pressure of CO<sub>2</sub> in Pa and  $m$  is the mass of the adsorbent. Isotherms of partial pressure vs. capacity were made using values calculated for each experimental run and are shown in Figure 5.3 and Figure 5.4 for adsorbents Activated Carbon and Zeolite 13X respectively. Also included is the Toth model to provide a direct comparison between experimental data obtained and theoretically expected values.

**Table 11. Parameters of the Toth equation for Activated Carbon and Zeolite 13X.**

	$q_m$ (mol kg <sup>-1</sup> )	$C_{T0}$	$b$ (kPa)
Activated Carbon <sup>1</sup>	16.8	0.583	35.19
Zeolite 13X <sup>2</sup>	9	0.2784	0.14

<sup>1</sup> Values taken from Himeno et al. (2005)

<sup>2</sup> Values taken from Cavenati et al. (2004)

An explanation of the Toth model is provided in section 2.9.3 and the parameters used are given in Table 11. As explained in the literature review (section 2.9.6) the method for calculating capacity described in this project does not include the use of a micro balance or an atmospheric micro reactor (techniques used by Cavenati et al. (2004) and Siriwardane et al. (2001) respectively). For this reason the capacity values obtained from the presented calculations cannot be considered absolute values of capacity, instead they are taken as approximate values and treated as such. Figure 5.3 and Figure 5.4 both show that the approximate capacities obtained experimentally are relatively close to the values produced from the Toth model, especially when the error in calculating these approximations is taken into consideration. The main source of error is from the inherent uncertainties of the CO<sub>2</sub> analyser and MFCs,  $\pm 2\%$  and  $\pm 1\%$  respectively. The average error on the calculated capacities is about  $\pm 0.8$  mol kg<sup>-1</sup>. The calculated results show reasonable consistency with the theoretical Toth model, however it is noted that the capacities calculated for a CO<sub>2</sub> partial pressure of 1.3 MPa (50% CO<sub>2</sub> feed concentration at a system pressure of 2.6 MPa) for both Activated Carbon and Zeolite 13X are higher than expected. However, as the majority of results follow the expected trend the calculated approximate values are deemed to be applicable. Included is Figure 5.5 which shows the isotherms for Activated Carbon and Zeolite 13X. This plot shows the differences an increase in pressure has on the

capacity of each adsorbent. The Zeolite 13X shows a rapid increase in capacity at low pressures (up to about 0.1 MPa) but plateaus relatively quickly unlike the Activated Carbon which has a more gradual increase in capacity which continues to increase at higher pressure. This means that the Zeolite has a higher capacity at low pressures and the Activated Carbon has a higher capacity at high pressures. According to the Toth model the pressure at which the capacity of Activated Carbon exceeds that of the Zeolite is about 0.55 MPa and is illustrated as the cross over point for the two curves in Figure 5.5.

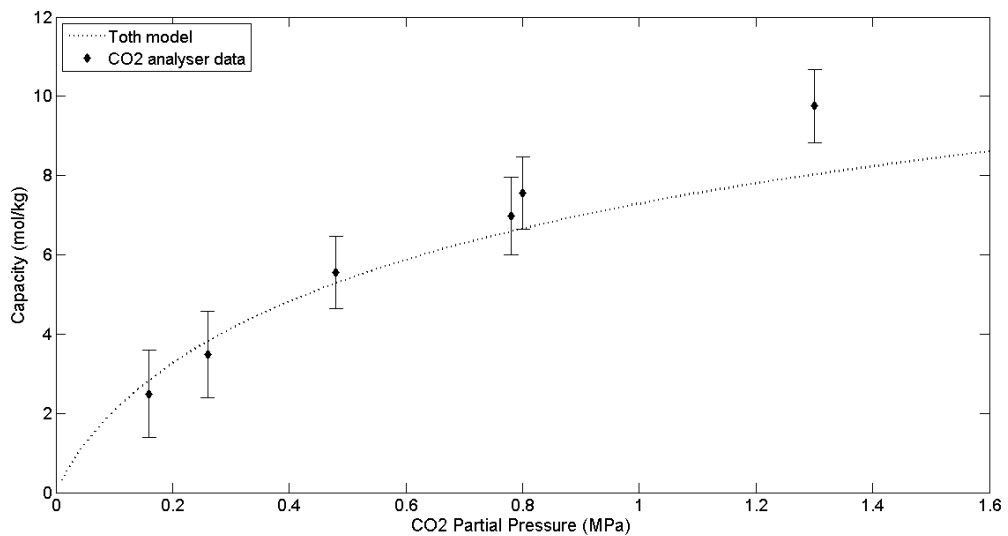


**Figure 5.3. Isotherm for Activated Carbon at 292K using CO<sub>2</sub> analyser data. The Toth model has been included for comparison using parameters from Table 11.**

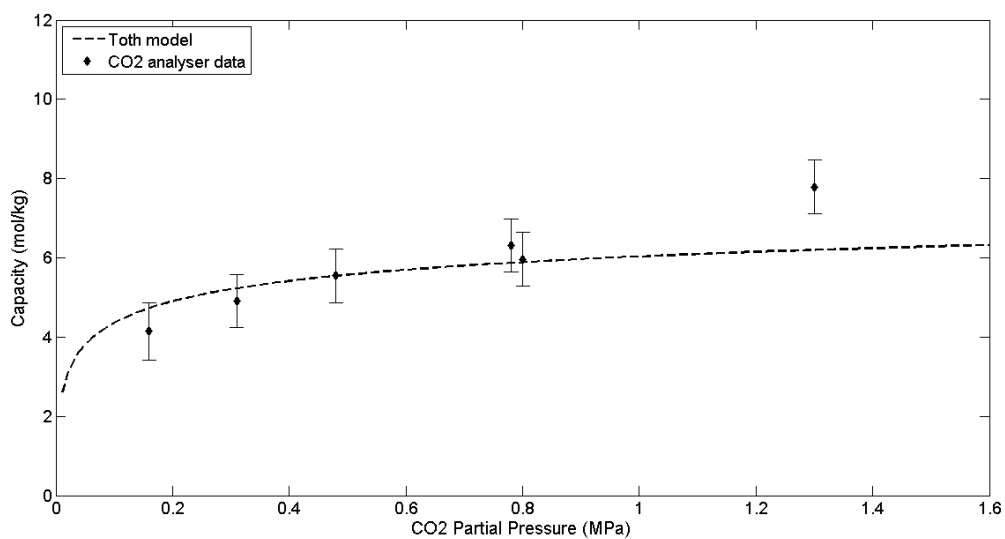


**Figure 5.4. Isotherm for Zeolite 13X at 292K using CO2 analyser data. The Toth model has been included for comparison using parameters from Table 11.**

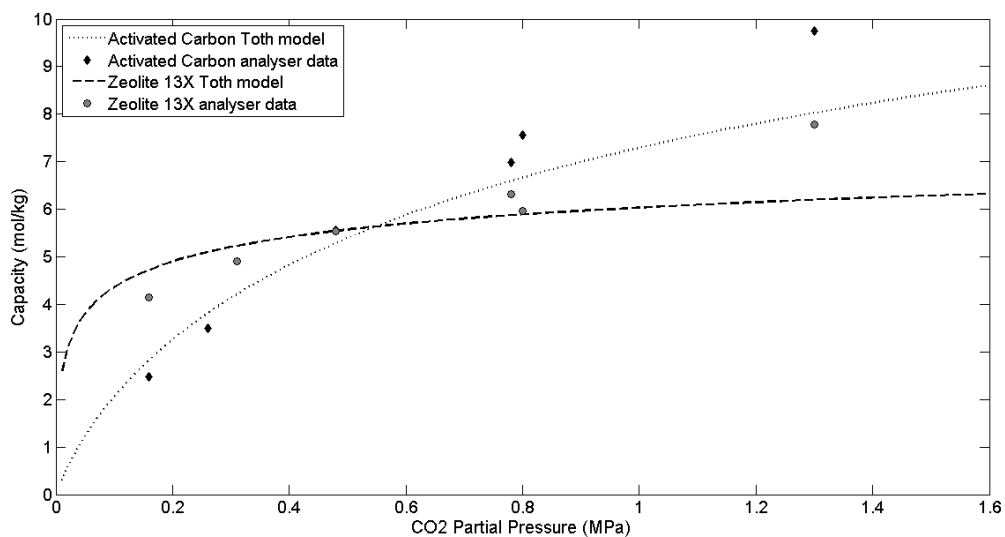


**Figure 5.5. Isotherm for Activated Carbon and Zeolite 13X at 292K using CO2 analyser data. The Toth model has been included for comparison.**

### 5.1.2 Breakthrough

The efficiency of the adsorption process may be judged from the breakthrough curve of the CO<sub>2</sub> exiting the bed (section 2.9.3). The feasibility of using the imaging technique developed to perform the same studies as commonly used techniques such as the CO<sub>2</sub> analyser was investigated. For this reason simultaneous measurements were performed using the CO<sub>2</sub> analyser and the imaging system to allow direct comparison. This section discusses the results obtained using the CO<sub>2</sub> analyser which are displayed in Figure 5.6 to Figure 5.9. The breakthrough curves show exit CO<sub>2</sub> concentration normalised with respect to the feed concentration,  $C_{max}$  to allow direct comparison between the different experimental set-ups. Characteristics of the breakthrough curves have been identified and time to breakthrough,  $t_{bt}$ , and time to full saturation,  $t_{sat}$ , have been calculated for each experimental run and are presented in Table 12. The time uncertainty for both calculations,  $\sigma_t$ , is the CO<sub>2</sub> analyser response time of 75 seconds plus the uncertainty on the recorded data, 30 seconds (half of the logging time increment of 1 minute).

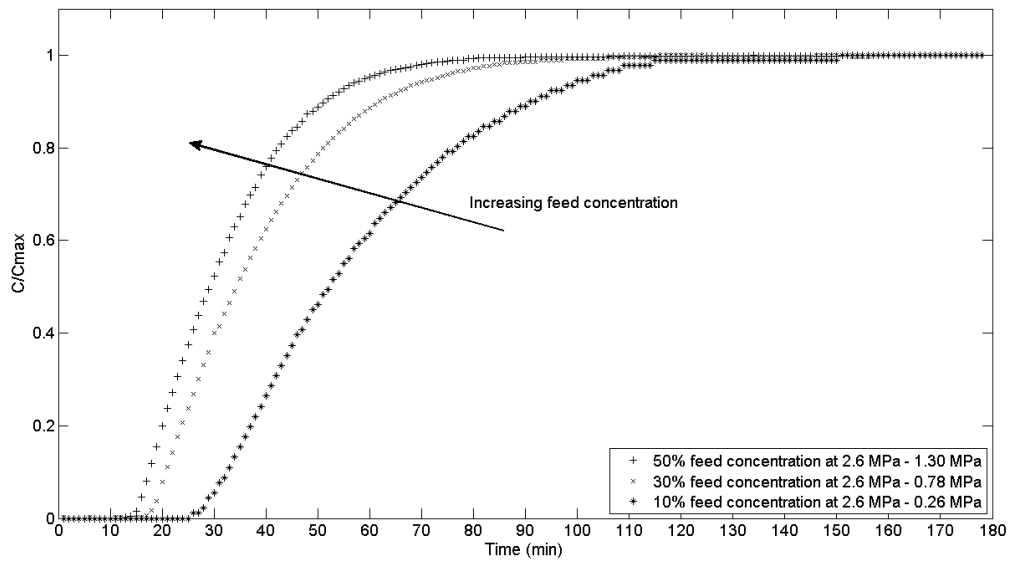


Figure 5.6. Breakthrough plots of normalised exiting CO<sub>2</sub> concentration with respect to maximum CO<sub>2</sub> concentration ( $C/C_{max}$ ) against time for Activated Carbon at total system pressure of 2.6 MPa.

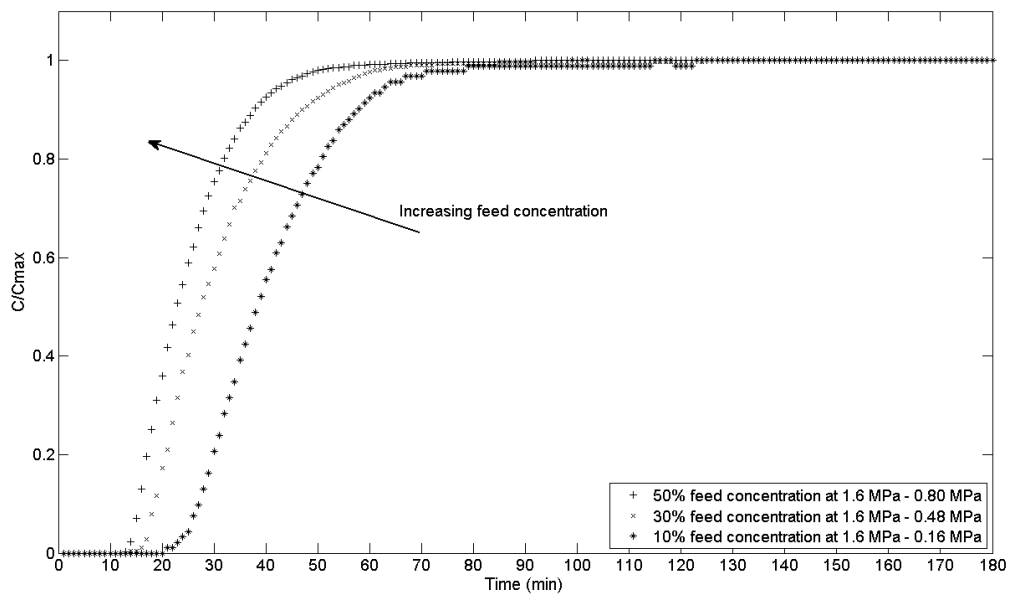


Figure 5.7. Breakthrough plots of normalised exiting CO<sub>2</sub> concentration with respect to maximum CO<sub>2</sub> concentration ( $C/C_{max}$ ) against time for Activated Carbon at total system pressure of 1.6 MPa.

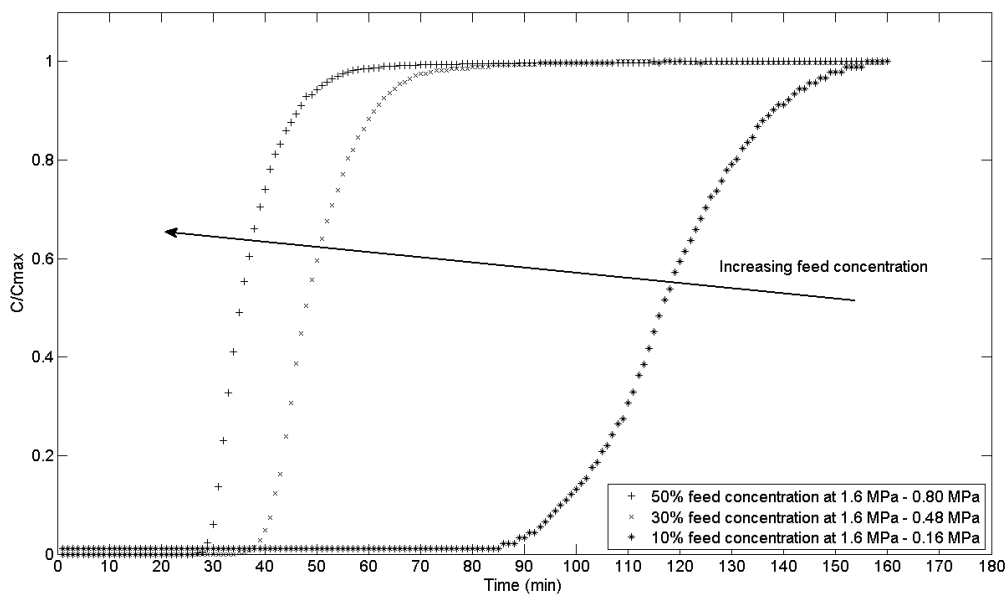


Figure 5.8. Breakthrough plots of normalised exiting CO<sub>2</sub> concentration with respect to maximum CO<sub>2</sub> concentration ( $C/C_{max}$ ) against time for Zeolite 13X at total system pressure of 2.6 MPa (10% CO<sub>2</sub> concentration at 3.1 MPa).

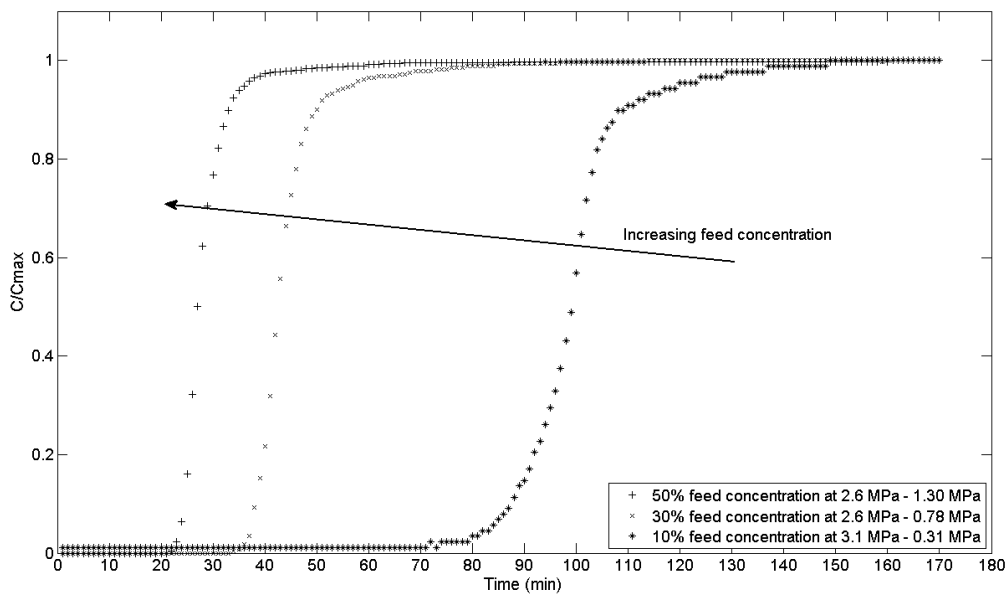


Figure 5.9. Breakthrough plots of normalised exiting CO<sub>2</sub> concentration with respect to maximum CO<sub>2</sub> concentration ( $C/C_{max}$ ) against time for Zeolite 13X at total system pressure of 1.6 MPa.

**Table 12. Calculated time to breakthrough,  $t_{bt}$ , and saturation,  $t_{sat}$ , for experimental data measured using the CO<sub>2</sub> analyser. The capacity of the column at  $t_{bt}$ ,  $q_{bt}$ , and at  $t_{sat}$ ,  $q_{sat}$  has been included and the percentage of saturation capacity at breakthrough is given.**

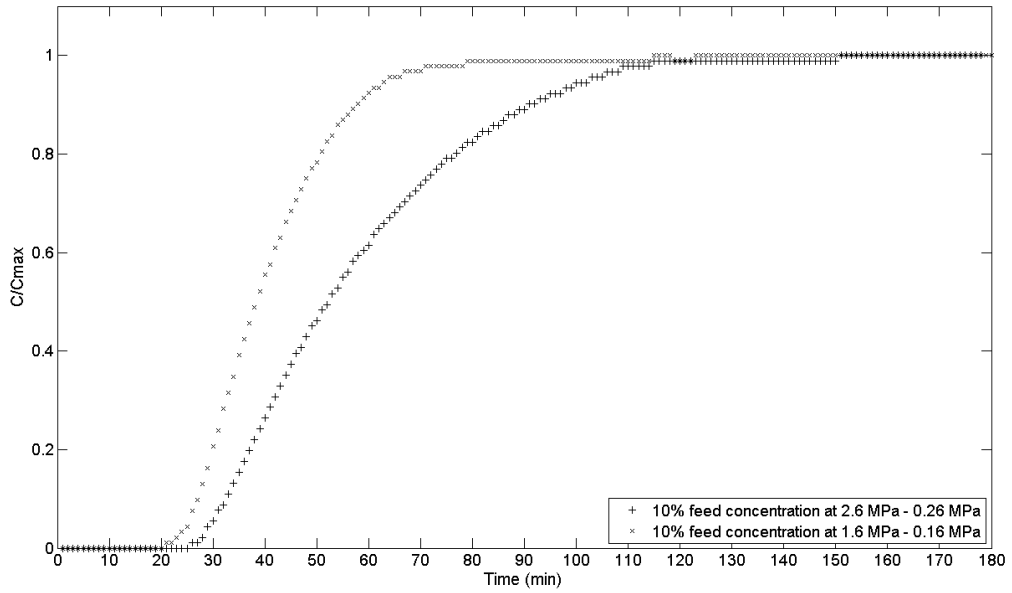
	$C_{max}$ (%)	$P_{sys}$ (MPa)	$P_{CO_2}$ (MPa)	Time (min)			Capacity (mol kg <sup>-1</sup> )			% of $q_{sat}$ adsorbed at $t_{bt}$
				$t_{bt}$	$t_{sat}$	$\sigma_t$	$q_{bt}$	$q_{sat}$	$\sigma_q$	
Activated Carbon	50	2.6	1.30	17	60	1.75	5.15	9.55	0.92	54
	30		0.78	20	73	1.75	3.63	6.86	0.98	53
	10		0.26	30	103	1.75	1.82	3.45	1.09	53
	50	1.6	0.8	15	44	1.75	4.55	7.43	0.92	61
	30		0.48	18	54	1.75	3.28	5.44	0.92	60
	10		0.16	26	64	1.75	1.58	2.43	1.00	65
Zeolite 13X	50	2.6	1.30	30	51	1.75	6.33	7.69	0.68	82
	30		0.78	41	66	1.75	5.18	6.24	0.67	83
	10	3.1	0.31	93	145	1.75	3.88	4.90	0.68	79
	50	1.6	0.8	24	37	1.75	5.06	5.81	0.68	87
	30		0.48	38	57	1.75	4.83	5.45	0.67	88
	10		0.16	84	120	1.75	3.5	4.11	0.71	85

As expected from literature (section 2.9.2) with increased CO<sub>2</sub> concentration the time to breakthrough decreases as there are more CO<sub>2</sub> molecules in the feed which increases the probability of a CO<sub>2</sub> molecule coming into close proximity of a vacancy on the adsorbents surface. Increasing the system pressure increases the time to breakthrough as it increases the number of vacancies on the surface of the adsorbent which will be filled by CO<sub>2</sub> molecules. Table 12 includes the calculated capacity in mol kg<sup>-1</sup> at  $t_{bt}$  and  $t_{sat}$  for each experiment,  $q_{bt}$  and  $q_{sat}$  respectively. The percentage of saturation at breakthrough provides an indication of the efficiency of the system and the size of the MTZ. It is observed that the percentage of saturation at breakthrough for Zeolite 13X is between 79% and 88% implying an efficient process as the bed is close to full saturation capacity at breakthrough, particularly for the experiments at a system pressure of 1.6 MPa. Activated Carbon, however, is only 53-54% saturated at

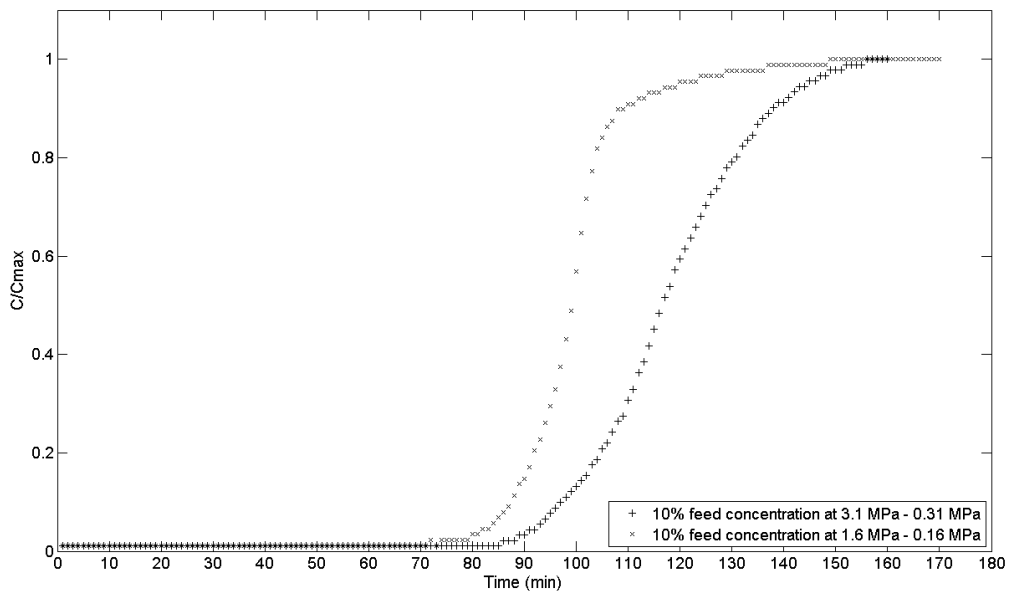
a system pressure of 2.6 MPa which increases to 60-65% at 1.6 MPa. This implies a large MTZ for Activated Carbon and indicates low efficiency.

Figure 5.6 and Figure 5.7 show the breakthrough curves of Activated Carbon produced at system pressures 2.6 MPa and 1.6 MPa respectively. Each plot shows the data obtained from CO<sub>2</sub> feed concentrations of 50%, 30% and 10% and the resulting partial pressure of the CO<sub>2</sub> is used to identify the different curves. From the figures it may be seen that the curves for Activated Carbon are relatively shallow, particularly for higher system pressure. This agrees with the relatively low percentage of saturation capacity at breakthrough and implies poor efficiency, especially for conditions 2.6 MPa and 10% CO<sub>2</sub> displayed in Figure 5.6 with partial pressure 0.26 MPa, where breakthrough occurs after 30 minutes and the bed does not saturate until 103 minutes into the experiment. This is a difference of 73 minutes and it may be observed that the shape of curve is one long shallow curve with no noticeable linear region implying a large MTZ. It is expected that for the experimental runs performed at the higher pressure of 2.6 MPa a large MTZ will be observed in the image data. For the systems at lower pressure the MTZ is expected to be relatively small. In comparison the plots for Zeolite 13X (Figure 5.8 and Figure 5.9) generally show a much steeper incline with larger linear regions and sharper curves as the system reaches saturation. It is expected that the MTZ's for Zeolite 13X will be relatively small in comparison to Activated Carbon. The size of the MTZ and the shape of the adsorption front have been investigated in section 5.3.4, however it is not possible to perform this direct observation using the CO<sub>2</sub> analyser, hence the requirement for direct imaging. The phenomenon that causes the shallow curve on approaching full saturation which is apparent in all of the plots is

fully investigated in the image data and a relationship between this phenomenon and adsorption kinetics is established in section 5.3.3.



**Figure 5.10. Two runs at different pressure but the same CO<sub>2</sub> feed concentration of 10% for Activated Carbon.**



**Figure 5.11. Two runs at different pressure but the same CO<sub>2</sub> feed concentration of 10% for Zeolite 13X.**

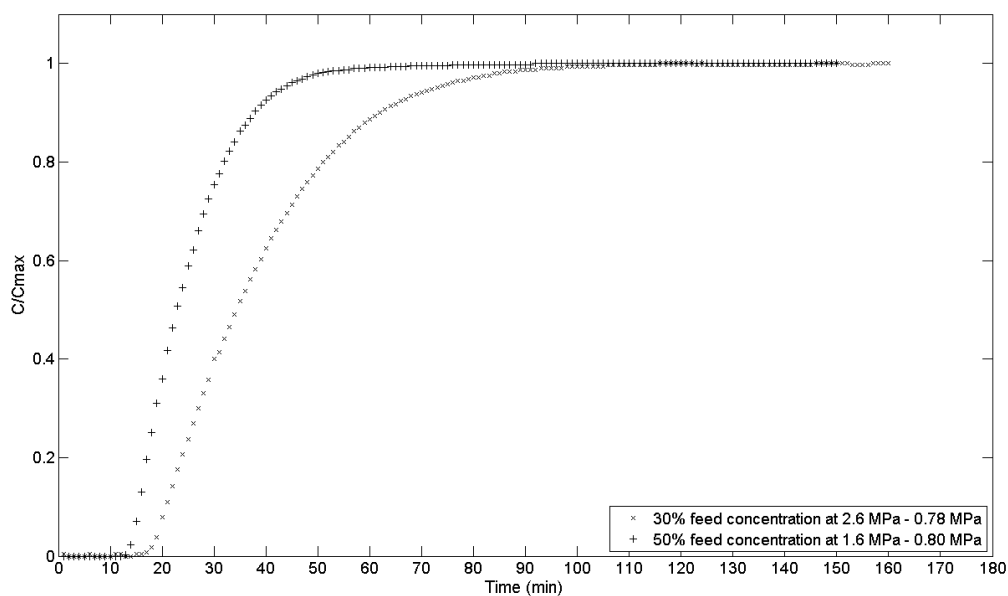


**Figure 5.12. Two runs with similar CO<sub>2</sub> partial pressure (~0.8 MPa) but different CO<sub>2</sub> feed concentrations for Activated Carbon.**

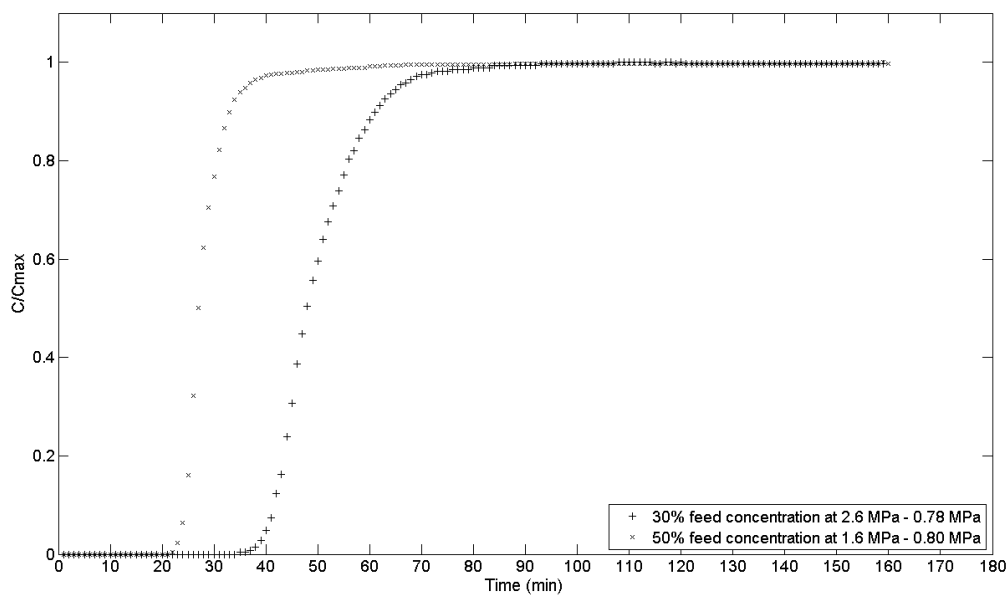


**Figure 5.13. Two runs with similar CO<sub>2</sub> partial pressure (~0.8 MPa) but different CO<sub>2</sub> feed concentrations for Zeolite 13X.**

Figure 5.10 and Figure 5.11 show the breakthrough curves of the two experimental runs at the same CO<sub>2</sub> feed concentration of 10% but different system pressures for Activated Carbon and Zeolite 13X respectively. This is to demonstrate the effect that increasing the system pressure has on the shape of the breakthrough curve. The systems at lower pressure breakthrough more quickly and have a steeper curve than the systems at higher pressure. Likewise, plots have been produced using data from experiments with similar CO<sub>2</sub> partial pressures of around 0.8 MPa but different CO<sub>2</sub> feed concentrations (50% and 30%). The plots for Activated Carbon and Zeolite 13X are shown in Figure 5.12 and Figure 5.13 respectively. As expected the systems with higher CO<sub>2</sub> concentration of 50% reach breakthrough faster than the systems with 30% concentration. The curve is also steeper implying greater efficiency.

## **5.2 IMAGE DATA RESULTS**

### **5.2.1 Capacity and isotherms**

This section of the results discusses the capability of the imaging technique to perform comparable measurements to that of the CO<sub>2</sub> analyser. A comparison between CO<sub>2</sub> analyser data, image data and what is expected from theory is provided. Section 6.2 goes into greater detail about the potential of the technique to add further levels of investigation and understanding to the measurements provided by the CO<sub>2</sub> analyser. Figure 5.14 to Figure 5.16 display how the image data is manipulated to provide the same information as that obtained by the CO<sub>2</sub> analyser. As the analyser and image data were obtained simultaneously direct comparisons have been possible and are provided.

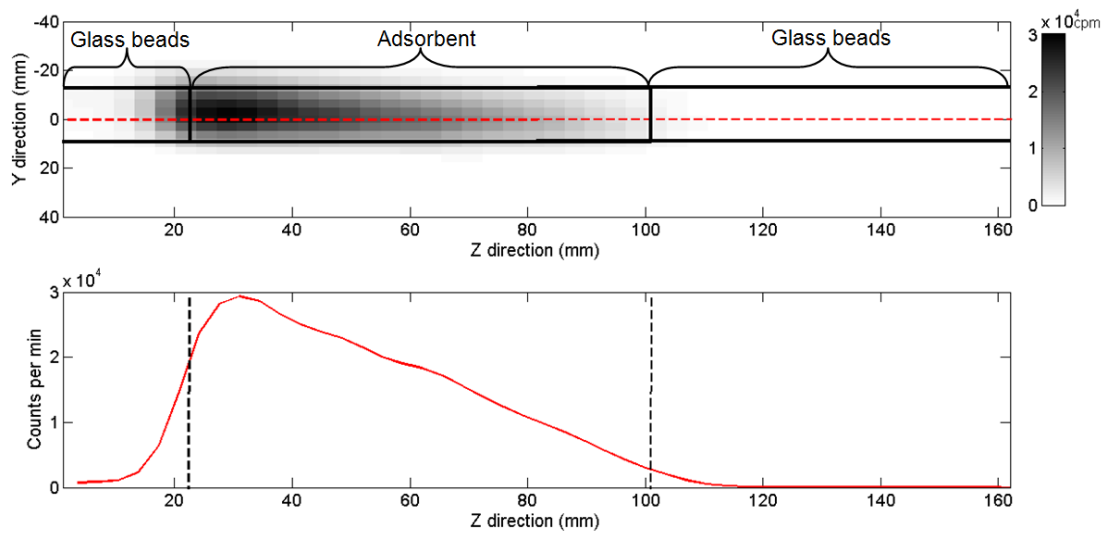


Figure 5.14 The image at the top of this figure shows the position of the adsorption column in the FoV. The ends of the column are packed with glass beads and the middle section contains the adsorbent (Activated Carbon in this example). The red dashed line through the centre of the column defines the pixels used to make the intensity profile at the bottom of the figure. The intensity is measured in counts per minute (cpm) and is a direct indication of the concentration of  $^{11}\text{CO}_2$ . This image shows the column 20 minutes into the experiment at  $P_{\text{sys}} = 1.6 \text{ MPa}$  and  $C_{\text{max}} = 10\%$ .

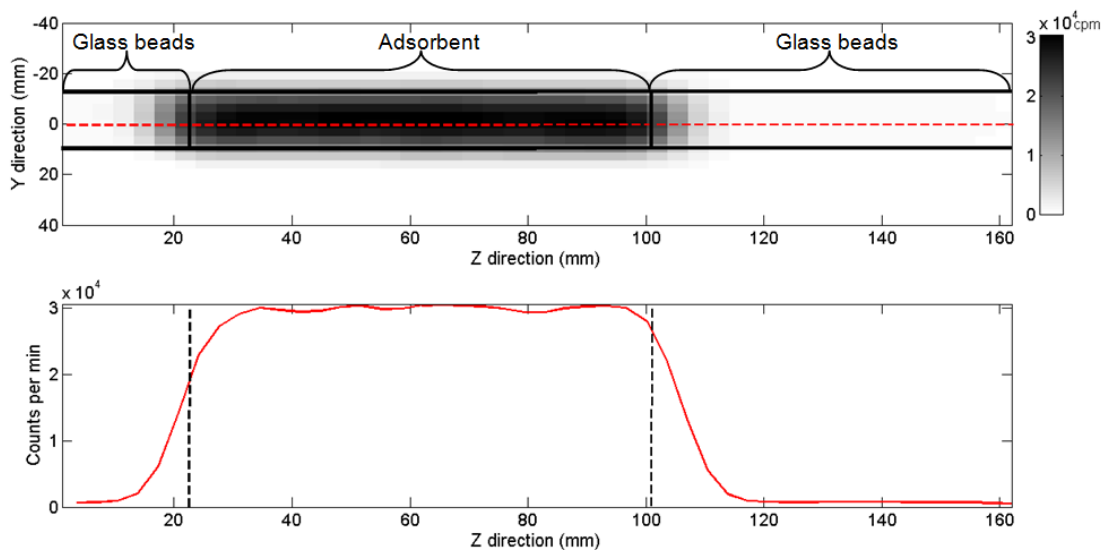
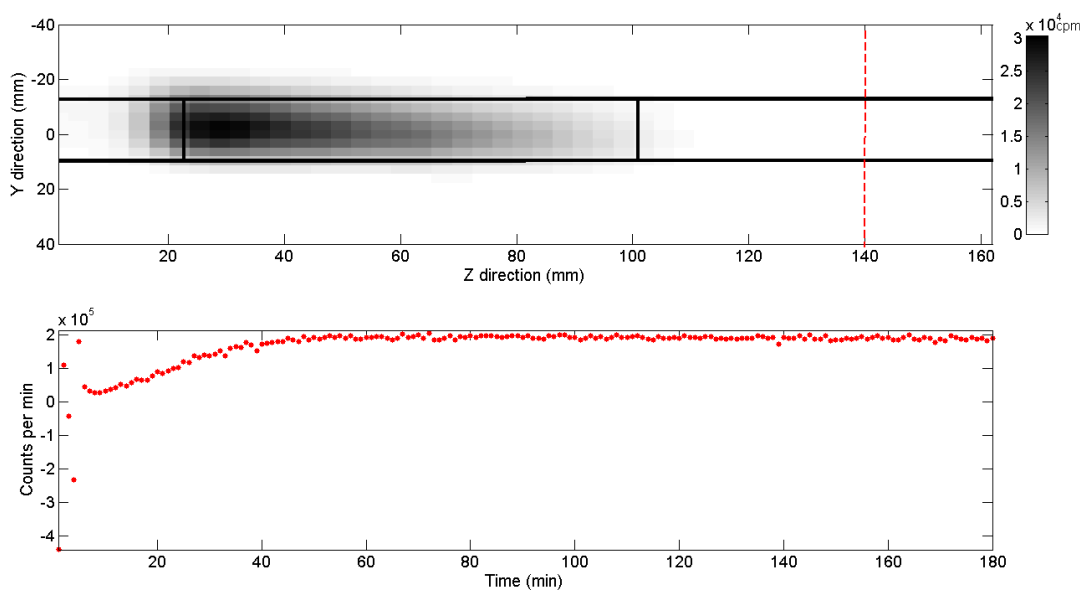


Figure 5.15. The adsorption column at 100 minutes into the same experiment illustrated in Figure 5.14. By this point the column is at full saturation. The smearing at the ends of the column which are clearly seen in the intensity profile at the bottom of the figure is due to axial smoothing in the reconstruction technique (section 2.5.2 and 2.10.2).



**Figure 5.16** Figure showing how the breakthrough curves are created from the same image data as Figure 5.14. To make the curves comparable to the  $\text{CO}_2$  analyser data information was taken from the outlet of the adsorbent region. The total cpm for each pixel in the transverse slice at plane 40 ( $z = 140 \text{ mm}$ ), indicated by the dashed red line, was summed for each time frame. The resulting breakthrough curve is shown in the plot at the bottom of this figure.

Figure 5.14 and Figure 5.15 show how profiles of the intensity distribution along the length of the column were created. The intensity is measured in counts per minute (cpm) and is the result after decay correction, dead time correction and normalization (see sections 2.2 and 2.10.2). The intensity is assumed to be directly representative of the distribution of  $\text{CO}_2$  as  $^{11}\text{CO}_2$  behaves as  $\text{CO}_2$  and is assumed to be evenly mixed into the  $\text{CO}_2 - \text{N}_2$  mixture. The concentration profiles along the column show that at the outlet of the column the amount of  $^{11}\text{CO}_2$  detected outside the adsorbent region of the bed is very low in comparison the maximum intensity inside the region which is about  $3 \times 10^4 \text{ cpm}$ , however it is non zero. This indicates that the amount of  $^{11}\text{CO}_2$  exiting the adsorbent region may be monitored making a comparable measurement to

that of the CO<sub>2</sub> analyser. In order to reduce statistical noise the total number of counts for a transverse plane at the outlet of the column were summed for each time frame to produce a breakthrough curve as shown in Figure 5.16. The curve shown at the bottom of the figure shows a high level of noise at the beginning of the data acquisition including a small number of negative points. This is due to very high statistical noise from a low count rate and as the <sup>11</sup>CO<sub>2</sub> gas has not yet entered the FoV of the PET camera. The imaging protocol has also corrected for background noise and scattered detections which results in negative counts as a scatter value has been subtracted from zero true detections. The point at which the noise is drastically reduced is the time at which the gas enters the column, for this reason the noisy frames preceding the introduction of <sup>11</sup>CO<sub>2</sub> for each run were removed. Another technique used to reduce the noise shown in the breakthrough curves was to apply a 10 point rolling ball average to smooth the data. The standard deviation of each data point is given by the standard deviation of the 10 values used to calculate the mean for each point. At the beginning of the image session the standard deviation is relatively large due to the high statistical noise from a low count rate in the FoV. The standard deviation falls as the amount of radioactive gas in the FoV increases but because the <sup>11</sup>CO<sub>2</sub> has a half-life of 20 minutes after a time the loss of counts due to decay will be greater than the increase due to adsorption so the statistical noise increases giving a higher standard deviation.

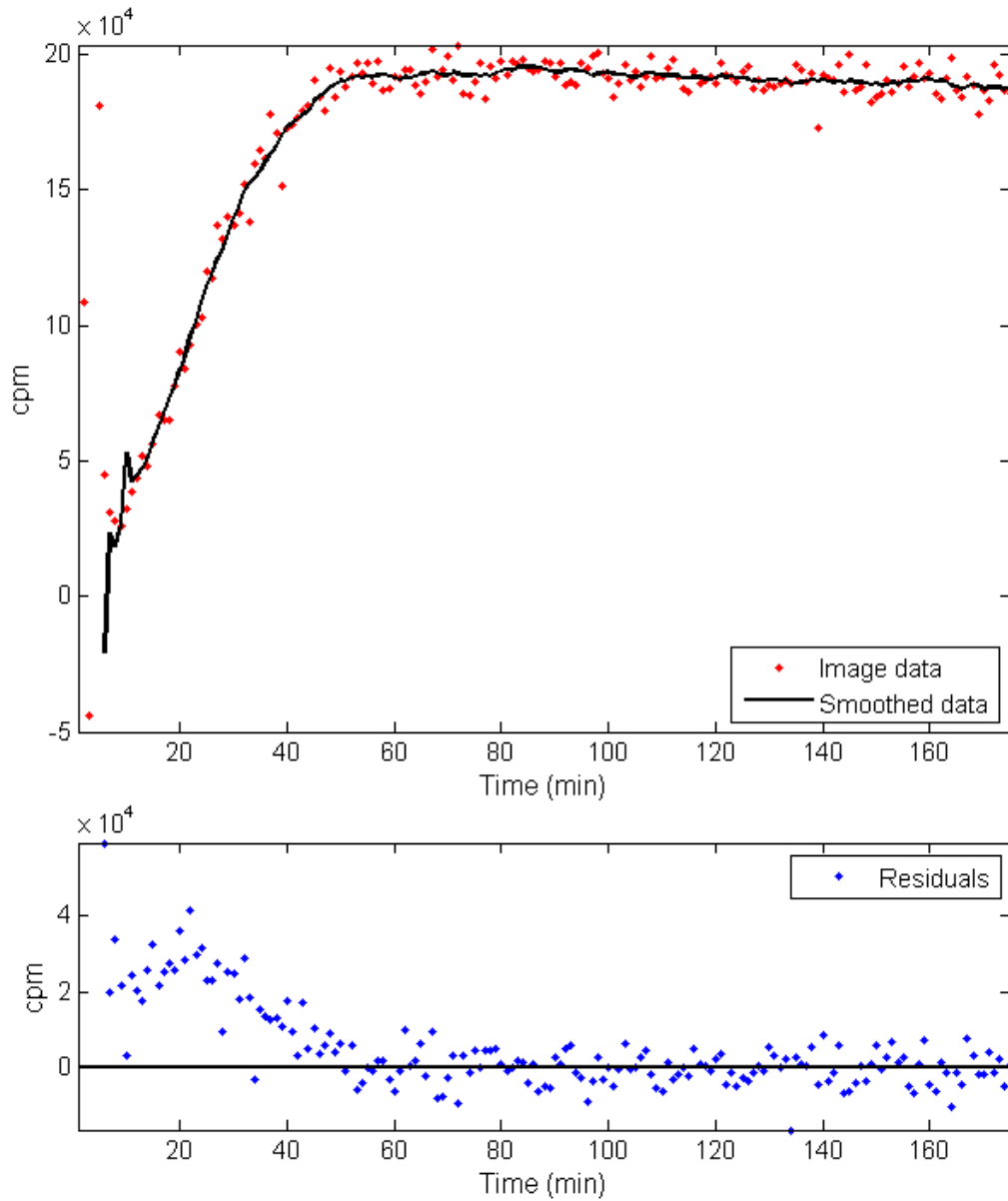


**Figure 5.17.** The original image data is subject to noise, particularly for long imaging sessions due to the decay of the radioisotope and hence a reduction in count rate, so a 10 point rolling ball average was applied to the breakthrough curves to smooth the data. This plot shows the same breakthrough data as Figure 5.16. The plot of residuals shows a relatively large difference between the original image data and smoothed data in the breakthrough region and a fairly even distribution at saturation.

By normalising the image data with respect to the known feed flow rate of CO<sub>2</sub> the capacity of each experimental run could be calculated in the same manner as the data obtained by the CO<sub>2</sub> analyser described in section 5.1.1. The area below the breakthrough curve is equal to the volume of CO<sub>2</sub> that exits the system so by subtracting the total feed volume of CO<sub>2</sub> the volume that remains in the bed can be determined. The error on capacity was determined by the standard deviation of the smoothed breakthrough curves and the error on total feed volume and exit volume. Figure 5.18 displays an example of a normalised breakthrough curve including the standard deviation.

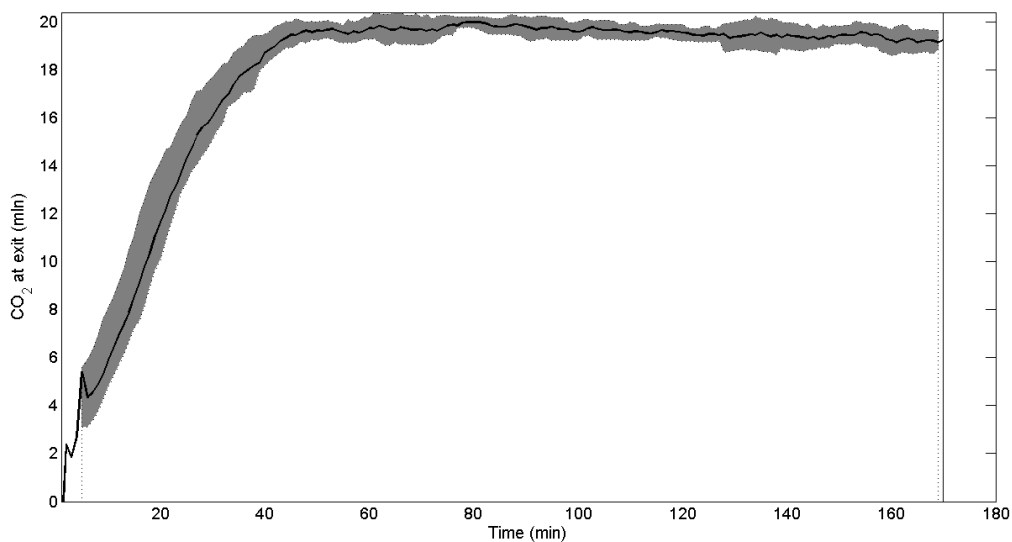


**Figure 5.18.** The region highlighted in grey is the area within the standard deviation of the smoothed image data and shows the possible variation between maximum captured CO<sub>2</sub> volume and the minimum.

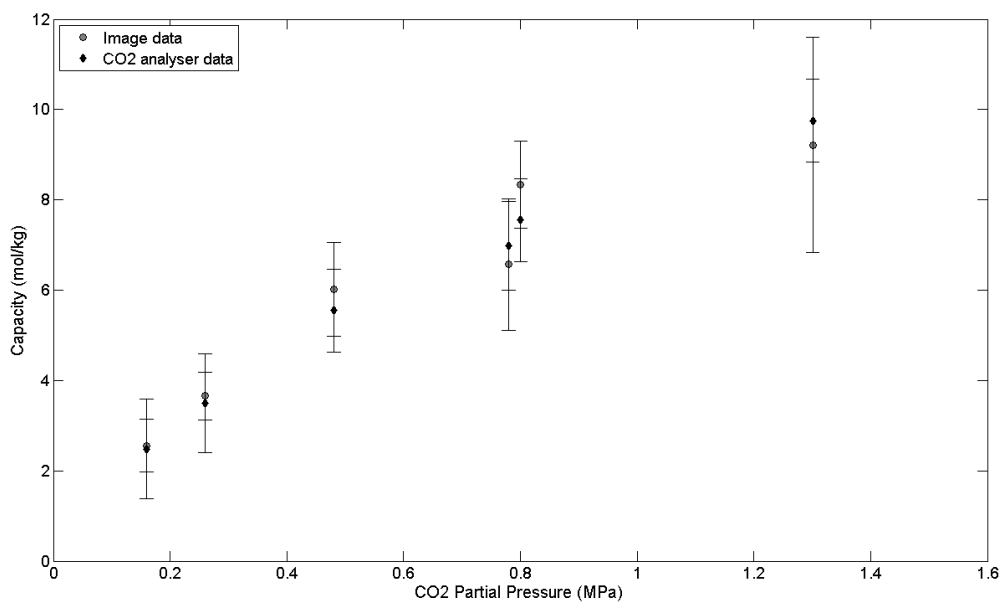


**Figure 5.19. Isotherm created using image data and CO<sub>2</sub> analyser data for Activated Carbon at 292 K.**

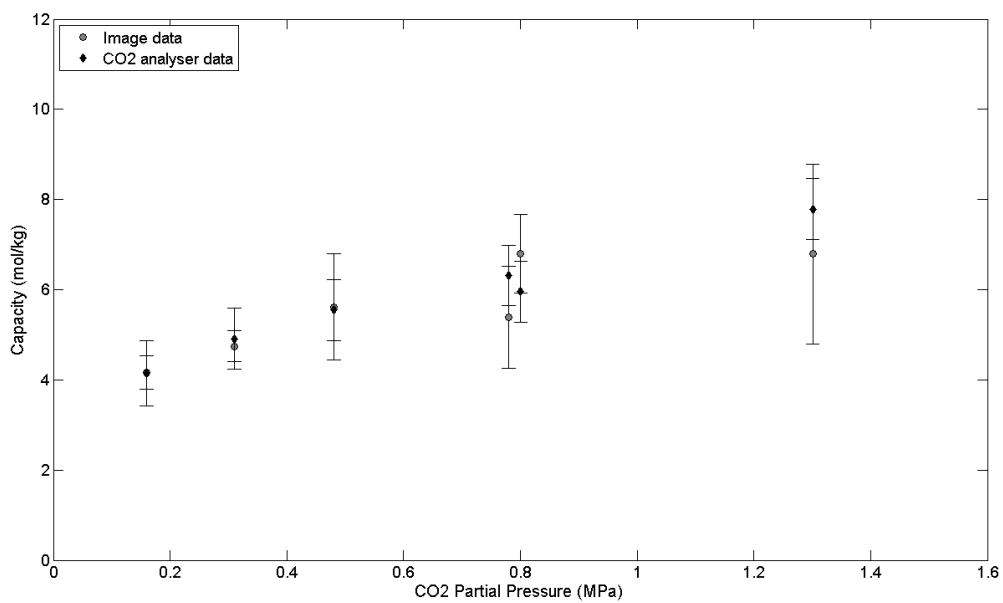


**Figure 5.20. Isotherm created using image data and CO<sub>2</sub> analyser data for Zeolite 13X at 292 K.**

Figure 5.19 and Figure 5.20 show the isotherms calculated from the image data, depicted as grey circles, and CO<sub>2</sub> analyser data, black diamonds, for Activated Carbon and Zeolite 13X respectively. Both plots show good similarity between the capacity values calculated using the CO<sub>2</sub> analyser and the image data, particularly at lower pressures where the uncertainty on calculated values is smaller. This similarity gives confidence in the imaging technique as a means of determining capacity as the data was acquired simultaneously providing verification of the imaging technique.

## 5.2.2 Breakthrough

### 5.2.2.1 Activated Carbon breakthrough curves from image data

Each of the breakthrough curves obtained from image data for each of the Activated Carbon runs has been displayed in Figure 5.21 and Figure 5.22 for system pressures 2.6 and 1.6 MPa respectively.

The breakthrough curves show increasing time to breakthrough with decreasing pressure. The general gradient of the curves appear to be relatively equal up to about  $C/C_{max} = 0.8$  where the curves for 0.26 MPa (Figure 5.21) and 0.8 MPa (Figure 5.22) show a gradual curve to the maximum concentration, whereas the other curves show a sharper curve as they approach the maximum. The curve for partial pressure 0.48 MPa, 1.6 MPa system pressure and 30% feed concentration, begins to fluctuate after the maximum has been reached. This continual fluctuation is unexpected and at this point cannot be explained and has been investigated further in section 5.3.1. It was observed during the further investigation that the data set for this particular experimental run was inconsistent with the data acquired for each of the other experiments. For the purposes of calculating the capacity and for comparison to the

other breakthrough curves the data for 1.6 MPa system pressure and 30% feed concentration was normalised with respect to the average of the final twenty data points.

The next stage was to compare the breakthrough curves obtained using CO<sub>2</sub> analyser data and image data. As the breakthrough curve can provide information about the mass transfer kinetics of the process good similarity is important.

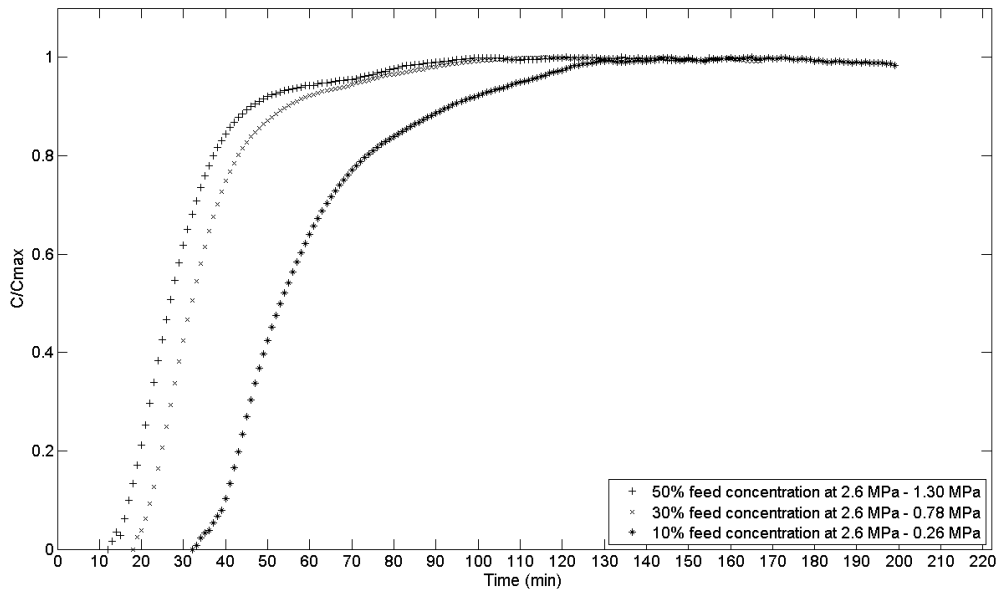


**Figure 5.21. Breakthrough plots of normalised exiting CO<sub>2</sub> concentration with respect to maximum CO<sub>2</sub> concentration ( $C/C_{max}$ ) against time for Activated Carbon at total system pressure of 2.6 MPa using smoothed image data.**

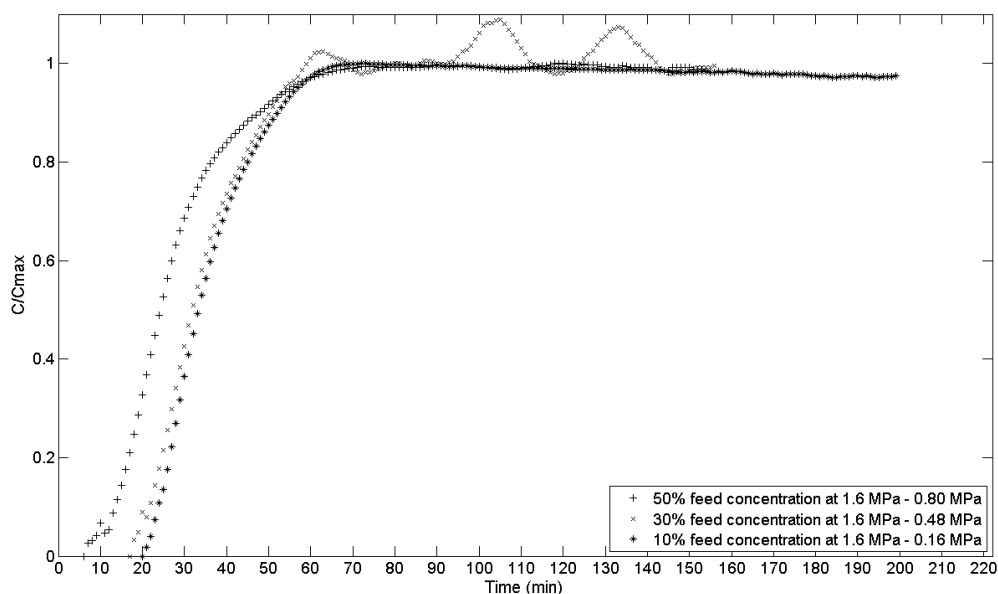


**Figure 5.22. Breakthrough plots of normalised exiting CO<sub>2</sub> concentration with respect to maximum CO<sub>2</sub> concentration ( $C/C_{max}$ ) against time for Activated Carbon at total system pressure of 1.6 MPa using smoothed image data.**

### **5.2.2.2 Activated Carbon breakthrough curves comparison**

The first set of curves shown from Figure 5.23 to Figure 5.25 are for Activated Carbon at 2.6 MPa for CO<sub>2</sub> feed concentrations 50%, 30% and 10%. The image data has been plotted using a dotted line and the analyser data is shown by a dashed line. The time offset between the acquisition of the image data and CO<sub>2</sub> analyser data has been corrected and the calculated capacity of each experimental set up has been included in the legends. These first three breakthrough curves show reasonably good similarity with times to breakthrough within 5 minutes of each other. The initial incline for the image data at 50% and 30% feed concentration is slightly steeper, however the times to saturation are 6 and 1 minutes apart respectively, which is within the error of 7 minutes of the calculation of the time offset. Times to breakthrough, saturation and the errors on the calculations are given previously in Table 14. The shape of the curves

shown in Figure 5.25 both show a gradual increasing exit concentration with time taking 73 minutes from breakthrough to saturation for the analyser data and 74 minutes from the image data. Figure 5.26 is a plot of image breakthrough and saturation times against analyser breakthrough and saturation time to determine the similarity. A linear least squares fit (LSF) (equation 5.8) has been included to show the common trend of increasing time for decreasing concentration (Kirkup 1994). Each point has been labelled with the feed concentration of the data set. It is observed that there is great similarity between the two measurement techniques for Activated Carbon at 2.6 MPa as indicated by the gradient of  $1.04 \pm 0.09$  and y-intercept of  $0.47 \pm 5.23$  min. For data sets of the same values the resulting trend would be  $y = x$  ( $m = 1$  and  $c = 0$ ).

The equation to determine the gradient,  $m$ , of a linear LSF is given by:

$$m = \frac{\sum \frac{1}{\sigma_i^2} \sum \frac{x_i y_i}{\sigma_i^2} - \sum \frac{x_i}{\sigma_i^2} \sum \frac{y_i}{\sigma_i^2}}{\Delta}, \quad 5.8$$

and the y-intercept,  $c$ , is given by:

$$c = \frac{\sum \frac{x_i^2}{\sigma_i^2} \sum \frac{y_i}{\sigma_i^2} - \sum \frac{x_i}{\sigma_i^2} \sum \frac{x_i y_i}{\sigma_i^2}}{\Delta}, \quad 5.9$$

where subscript  $i$  denotes individual data points,  $n$  is the total number of points and  $\sigma$  is the uncertainty on the measured data. Equation 5.10 gives the calculation of  $\Delta$  and the standard deviation of the gradient and y-intercept are given by equations 5.11 and 5.12 respectively.

$$\Delta = \sum \frac{1}{\sigma_i^2} \sum \frac{x_i^2}{\sigma_i^2} - \left( \sum \frac{x_i}{\sigma_i^2} \right)^2 \quad 5.10$$

$$\sigma_m = \left( \frac{\sum \frac{1}{\sigma_i^2}}{\Delta} \right)^{1/2} \quad 5.11$$

$$\sigma_c = \left( \frac{\sum \frac{x_i^2}{\sigma_i^2}}{\Delta} \right)^{1/2} \quad 5.12$$

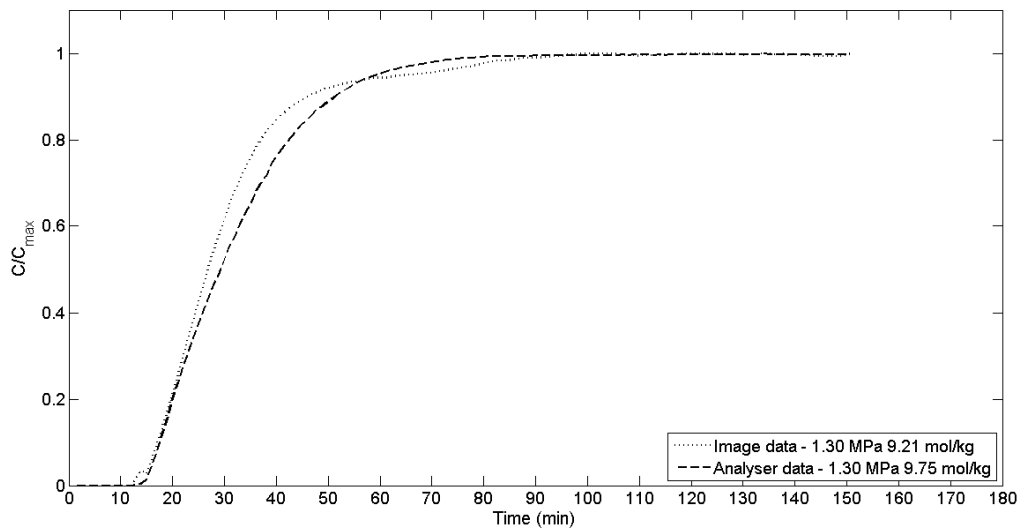


**Figure 5.23.** A comparison between breakthrough curves for Activated Carbon produced using image data and CO<sub>2</sub> analyser data with corresponding calculated capacities. The experimental conditions were system pressure of 2.6 MPa and CO<sub>2</sub> concentration of 50%.

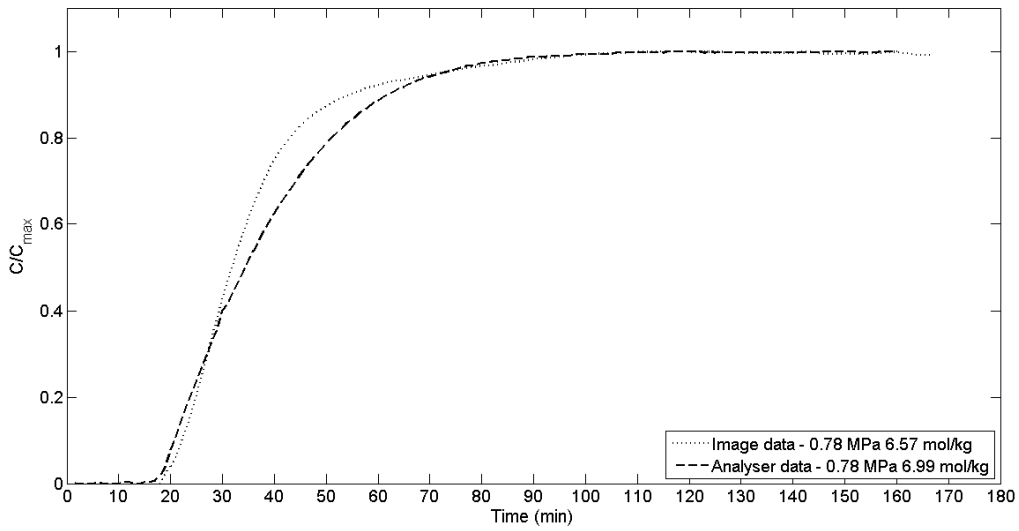


**Figure 5.24. A comparison between breakthrough curves for Activated Carbon produced using image data and CO<sub>2</sub> analyser data with corresponding calculated capacities. The experimental conditions were system pressure of 2.6 MPa and CO<sub>2</sub> concentration of 30%.**

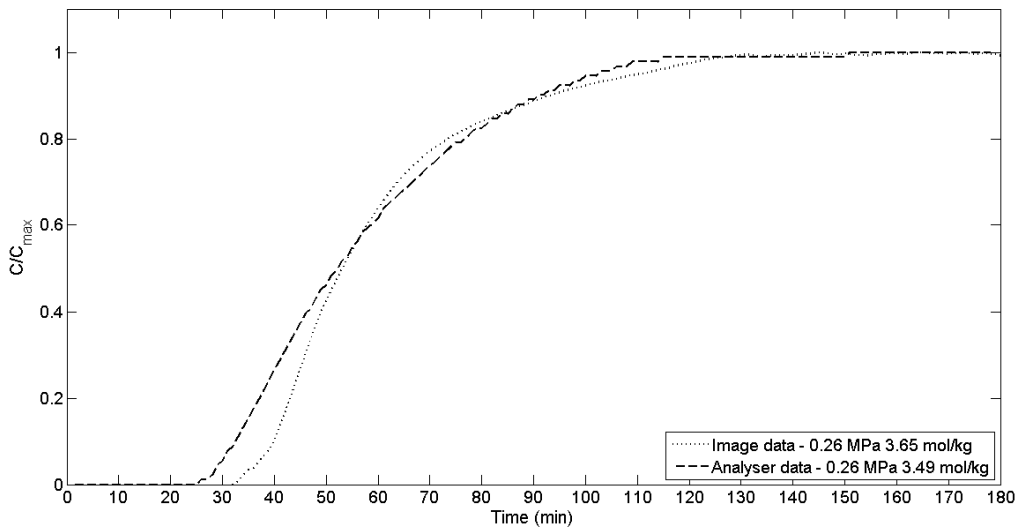


**Figure 5.25. A comparison between breakthrough curves for Activated Carbon produced using image data and CO<sub>2</sub> analyser data with corresponding calculated capacities. The experimental conditions were system pressure of 2.6 MPa and CO<sub>2</sub> concentration of 10%.**

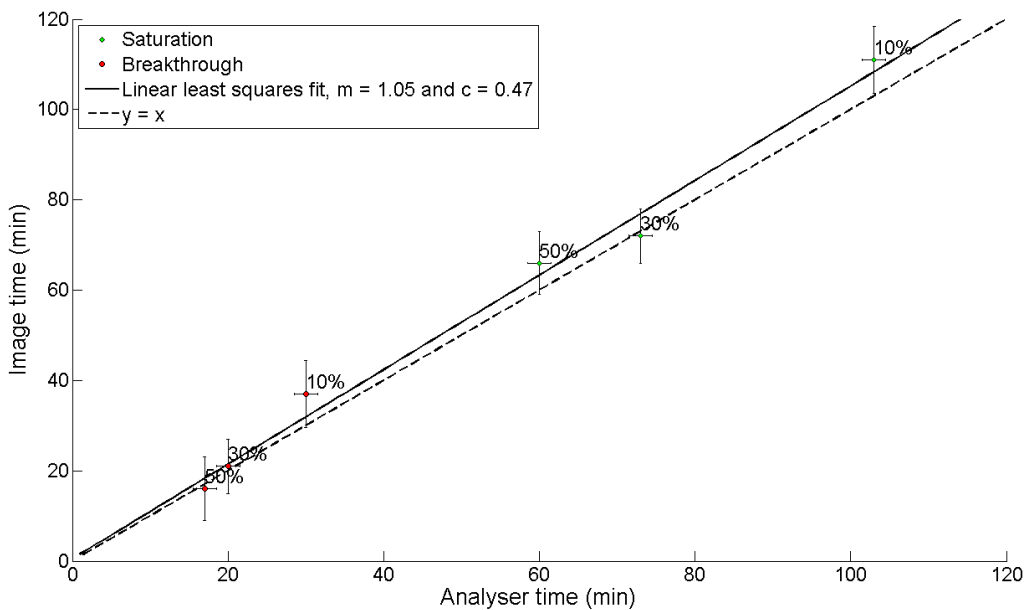


**Figure 5.26. Times to breakthrough and saturation calculated from image data and CO<sub>2</sub> analyser data for system pressure of 2.6 MPa using Activated Carbon. The results have been plotted against each other to clarify similarities between the two measurement techniques and a linear LSF has been applied ( $m = 1.04$ ,  $\sigma_m = 0.09$ ,  $c = 0.47$  and  $\sigma_c = 5.23$ ).**

The following three figures, Figure 5.27 to Figure 5.29, show the analyser and image breakthrough curves for Activated Carbon at 1.6 MPa from 50% to 10% feed concentration. Figure 5.27 shows noise in the image data at about 10 minutes and a shallower curve on approaching saturation than that of the CO<sub>2</sub> analyser data. This gives a difference of 17 minutes between the two data sets from breakthrough to saturation as the image data breaks through at 10 minutes and saturates at 56 minutes, whereas the analyser data shows breakthrough at 15 minutes and saturation at 44 minutes. However the following two figures for 30% and 10% concentration show very similar trends, particularly so for 10% feed concentration. The unusual fluctuations in the image data for 30% concentration make it difficult to confirm

with any certainty the curvature of the rate of increasing concentration on approaching maximum but the initial incline of the increasing uptake appears to have a very similar gradient to that of the analyser data.

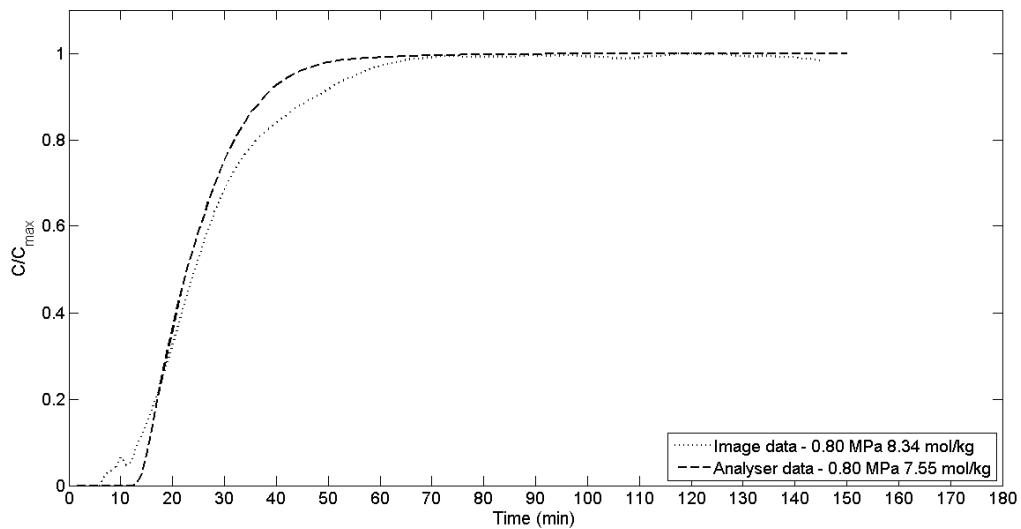


**Figure 5.27. A comparison between breakthrough curves for Activated Carbon produced using image data and CO<sub>2</sub> analyser data with corresponding calculated capacities. The experimental conditions were system pressure of 1.6 MPa and CO<sub>2</sub> concentration of 50%.**

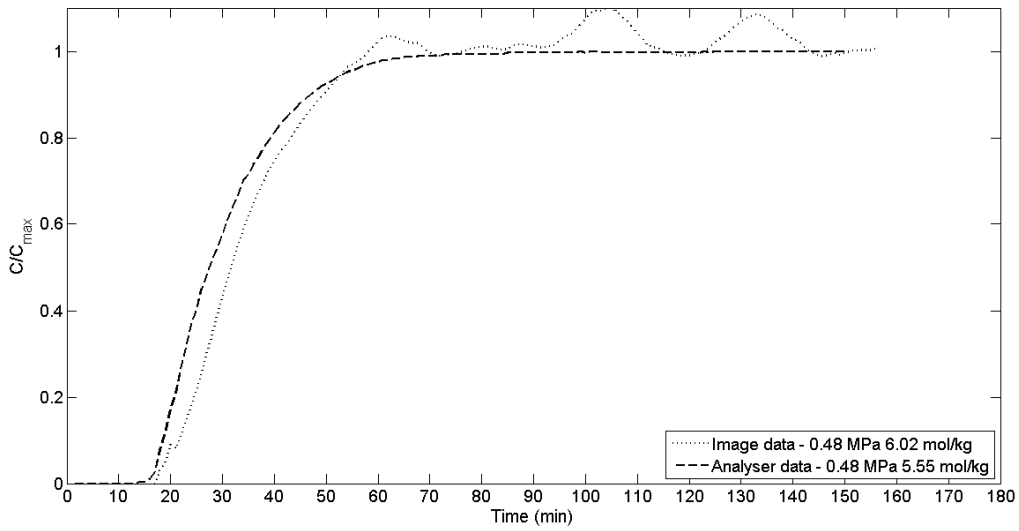


**Figure 5.28.** A comparison between breakthrough curves for Activated Carbon produced using image data and CO<sub>2</sub> analyser data with corresponding calculated capacities. The experimental conditions were system pressure of 1.6 MPa and CO<sub>2</sub> concentration of 30%.

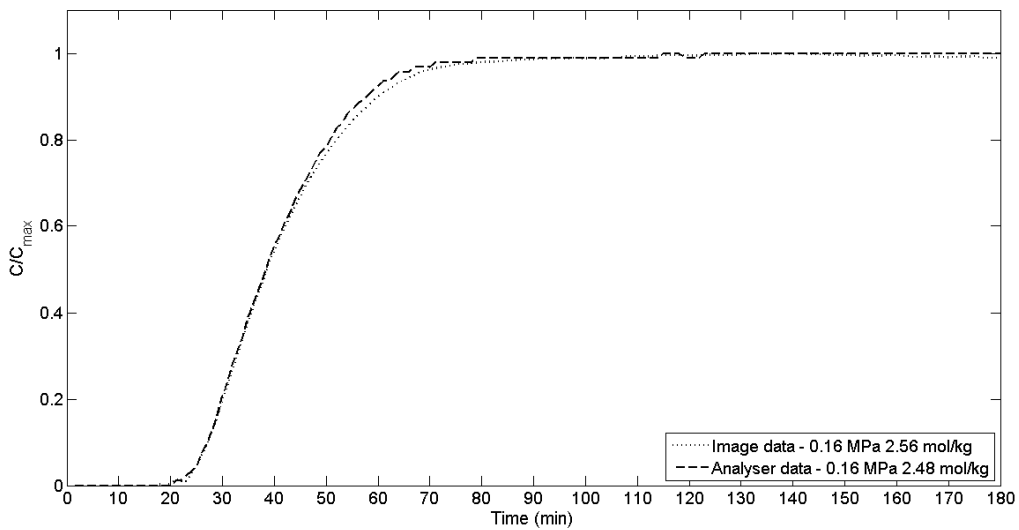


**Figure 5.29.** A comparison between breakthrough curves for Activated Carbon produced using image data and CO<sub>2</sub> analyser data with corresponding calculated capacities. The experimental conditions were system pressure of 1.6 MPa and CO<sub>2</sub> concentration of 10%.

The times to breakthrough and saturation for Activated Carbon at 1.6 MPa calculated using analyser data and image data have been plotted against each other as done previously and the resulting plot is shown in Figure 5.30. The times to breakthrough and saturation show a reasonably linear trend for the experiments at 10% and 30% concentration, however the points for 50% concentration appear to be inconsistent. This coincides with the comments regarding the curve for the image data as the rates of increasing concentration seems to drop off at about  $C/C_{max} = 0.8$ . However, the runs for 10% and 30% show good similarity between the analyser and image data for Activated Carbon at 1.6 MPa as indicated by the calculated LSF gradient of  $0.97 \pm 0.1$  and y-intercept of  $2.25 \pm 4.16$  min.

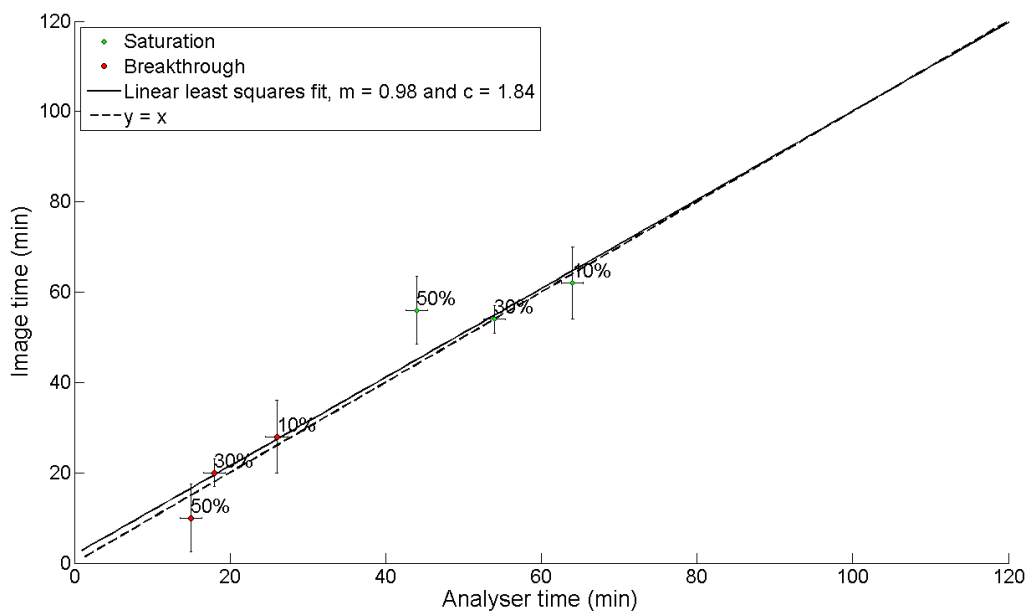


**Figure 5.30.** Times to breakthrough and saturation calculated from image data and CO<sub>2</sub> analyser data for system pressure of 1.6 MPa using Activated Carbon. The results have been plotted against each other to clarify similarities between the two measurement techniques and a linear LSF has been applied ( $m = 0.97$ ,  $\sigma_m = 0.1$ ,  $c = 2.25$  and  $\sigma_c = 4.16$ ).

### **5.2.2.3 Zeolite 13X breakthrough curves from image data**

The breakthrough curves obtained from the image data for Zeolite 13X are shown in Figure 5.31 and Figure 5.32 for system pressures 2.6 and 1.6 MPa respectively. The curves for 10% feed concentration for both system pressures show a relatively long time to breakthrough, about 80 minutes for 3.1 MPa system pressure and about 65 minutes for 1.6 MPa, partial pressures 0.31 MPa and 0.16 MPa respectively. These curves also show a gradual incline, taking about 60 minutes from breakthrough for partial pressure 0.31 MPa to reach saturation and about 100 minutes from breakthrough for partial pressure 0.16 MPa to saturate. The other curves at higher feed concentrations show steeper inclines from breakthrough and a sharper curve on approaching saturation. The systems with higher partial pressure are the first to breakthrough, about 15 minutes for 1.3 MPa and 5 minutes for 0.8 MPa. As 0.8 MPa is lower than 1.3 MPa its faster breakthrough time was unexpected. By looking at the curve for 0.8 MPa in Figure 5.32 the curve seems to increase in two stages, an initial steep incline from about 5 minutes followed by a reduced incline at about 60% of the maximum value for about 10 minutes at which point the incline increases again followed by a reasonably sharp curve to the maximum value. A similar inconsistency is observed at about 95% of the maximum value of the curve at 1.3 MPa and at 70% of the maximum for 0.78 MPa in Figure 5.31. This could be due to an unexpected artefact in the image data. The quality of the image data is discussed in section 5.3.1 where the image data has been analysed in greater detail.

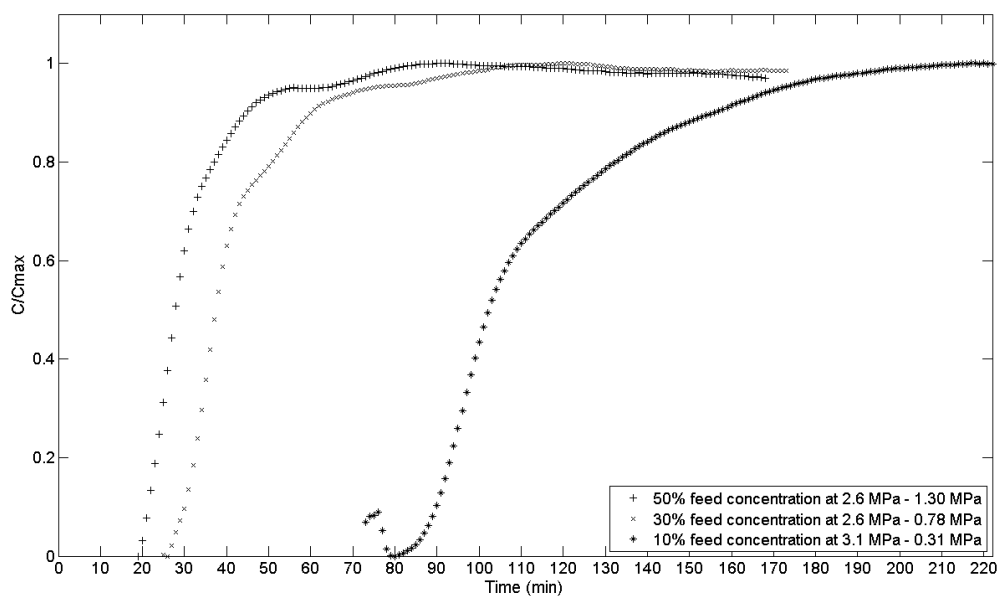


Figure 5.31. Breakthrough plots of normalised exiting CO<sub>2</sub> concentration (calculated using cpm) with respect to maximum CO<sub>2</sub> concentration ( $C/C_{max}$ ) against time for Zeolite 13X at total system pressure of 2.6 MPa using smoothed image data (10% CO<sub>2</sub> concentration at 3.1 MPa).

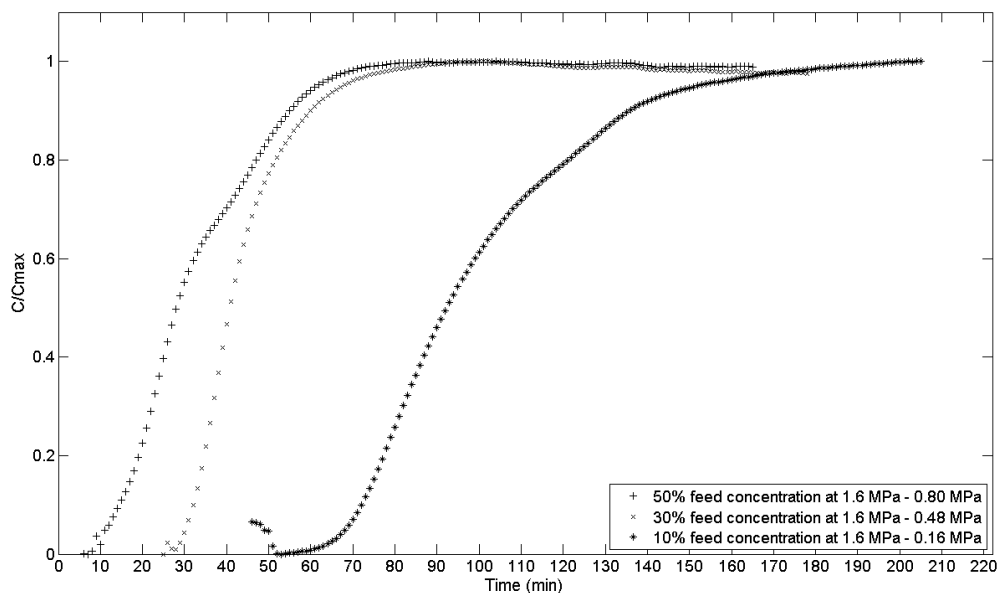
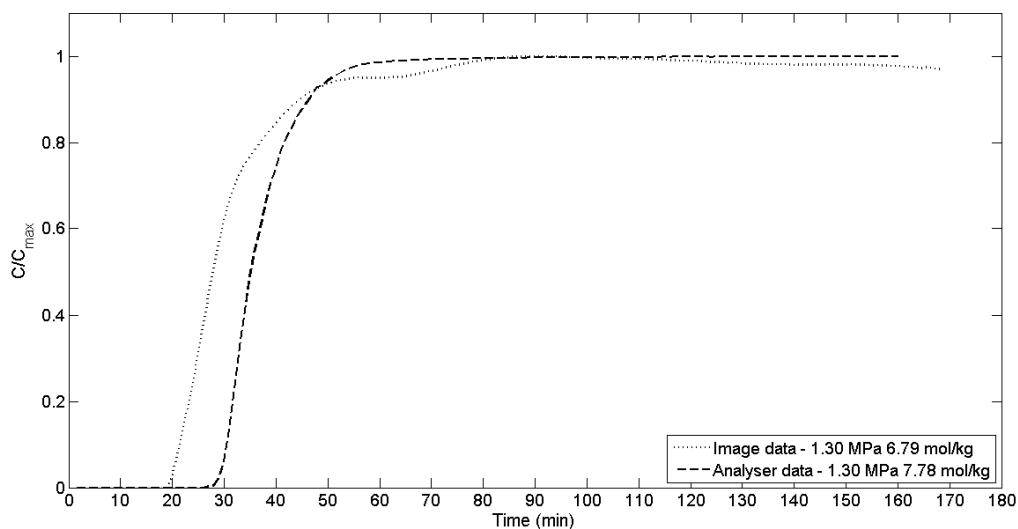


Figure 5.32. Breakthrough plots of normalised exiting CO<sub>2</sub> concentration (calculated using cpm) with respect to maximum CO<sub>2</sub> concentration ( $C/C_{max}$ ) against time for Zeolite 13X at total system pressure of 1.6 MPa using smoothed image data.

### **5.2.2.1 Zeolite 13X breakthrough curves comparison**

A comparison between the analyser and image data for adsorbent Zeolite 13X are displayed and discussed in this section. Figure 5.33 and Figure 5.34 show the breakthrough curves obtained at 2.6 MPa for concentrations 50% and 30% respectively and Figure 5.35 shows the data obtained at 3.1 MPa with 10% feed concentration. A common trend seen in the first two of the three comparison plots presented is that the initial gradient of increasing concentration with time is similar between the analyser and the image data up to about 70%. At this point the rate of increasing concentration drops off for the image data. By plotting the two sets of data obtained by the two different imaging techniques together, which shows how the image breakthrough curves should look, it appears that each of the image data sets could have actually reached the maximum concentration at about 70%, but for an unexplained reason the cpm continues to increase. If the maximum point was considered to be  $C/C_{max} = 0.7$  and the data was normalised with respect to this it is expected that the two measurement techniques would show very similar gradients and curves on approaching the maximum. The unusual trends shown by the image data has been investigated further in section 5.3.1.



**Figure 5.33. A comparison between breakthrough curves produced for Zeolite 13X using image data and CO<sub>2</sub> analyser data with corresponding calculated capacities. The experimental conditions were system pressure of 2.6 MPa and CO<sub>2</sub> concentration of 50%.**

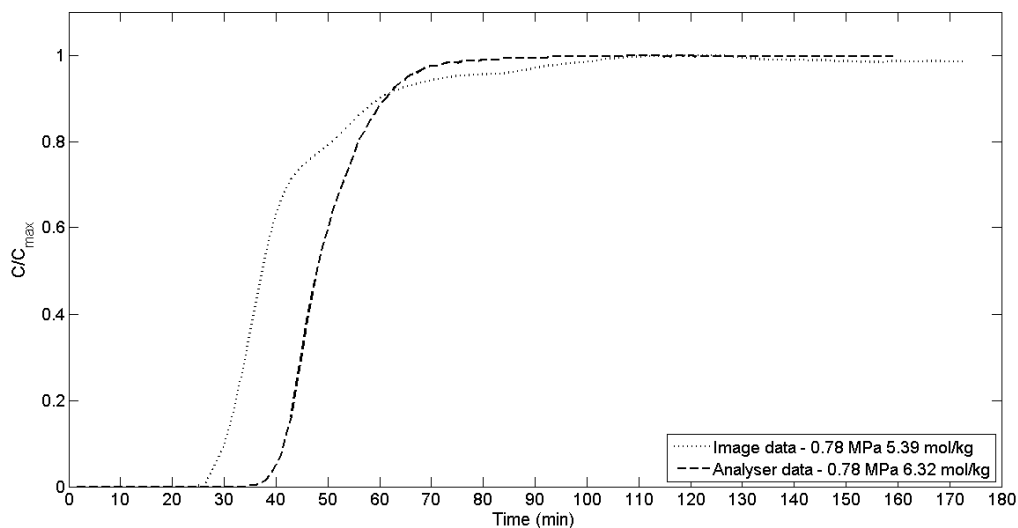


**Figure 5.34. A comparison between breakthrough curves for Zeolite 13X produced using image data and CO<sub>2</sub> analyser data with corresponding calculated capacities. The experimental conditions were system pressure of 2.6 MPa and CO<sub>2</sub> concentration of 30%.**

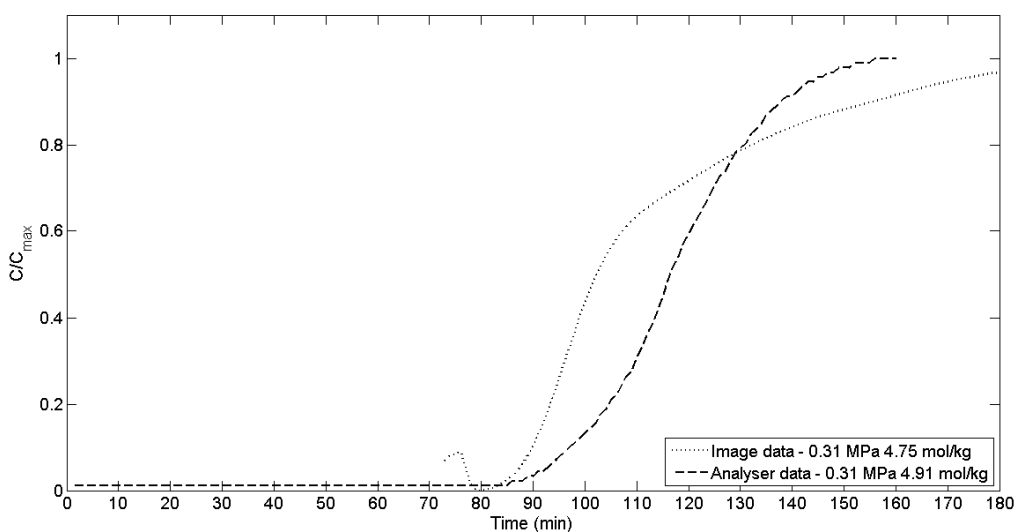


**Figure 5.35. A comparison between breakthrough curves for Zeolite 13X produced using image data and CO<sub>2</sub> analyser data with corresponding calculated capacities. The experimental conditions were system pressure of 3.1 MPa and CO<sub>2</sub> concentration of 10%.**

The plot of analyser breakthrough and saturation times against image times is displayed in Figure 5.36 and shows reasonably good linearity between the two measurement techniques and there is a clear trend of increasing time with decreasing feed concentration as expected, although the gradient of the linear LSF of  $1.28 \pm 0.07$  shows poor equality between the two measurement techniques. The calculated capacities shown on the legends of each of the plots are similar between the two techniques, however the general shape of the image data curves are inconsistent with the analyser data and from looking at this data alone the kinetics of the process could not be determined from the breakthrough curves for Zeolite 13X at 2.6 MPa (3.1 MPa for 10%).

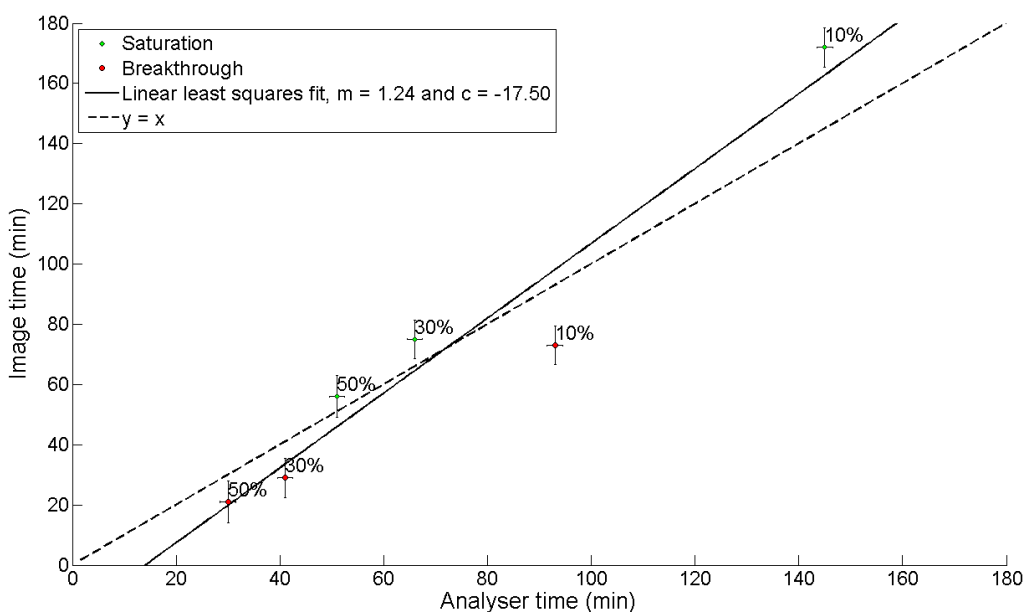


**Figure 5.36. Times to breakthrough and saturation calculated from image data and CO<sub>2</sub> analyser data for system pressure of 2.6 MPa (10% CO<sub>2</sub> concentration at 3.1 MPa) using Zeolite 13X. The results have been plotted against each other to clarify similarities between the two measurement technique and a linear LSF has been applied ( $m = 1.28$ ,  $\sigma_m = 0.07$ ,  $c = -17.45$  and  $\sigma_c = 5.23$ ).**

The following three plots show the data obtained for Zeolite 13X at 1.6 MPa. The curves produced from the image data do not show similar trends to the curves produced from the CO<sub>2</sub> analyser. Although the calculated capacity values are close the time between breakthrough and saturation for the image data is considerably greater than the times measured from the analyser. Figure 5.40 shows that although there is a general increase in time with decreasing concentration the points are not comparable and show poor linearity and equality with LSF gradient of  $1.23 \pm 0.07$  and y-intercept of  $-4.38 \pm 3.85$ . The data acquired for Zeolite 13X has proven to provide unexpected and inconsistent breakthrough profiles. This unusual behaviour has been discussed in section 5.3.1.

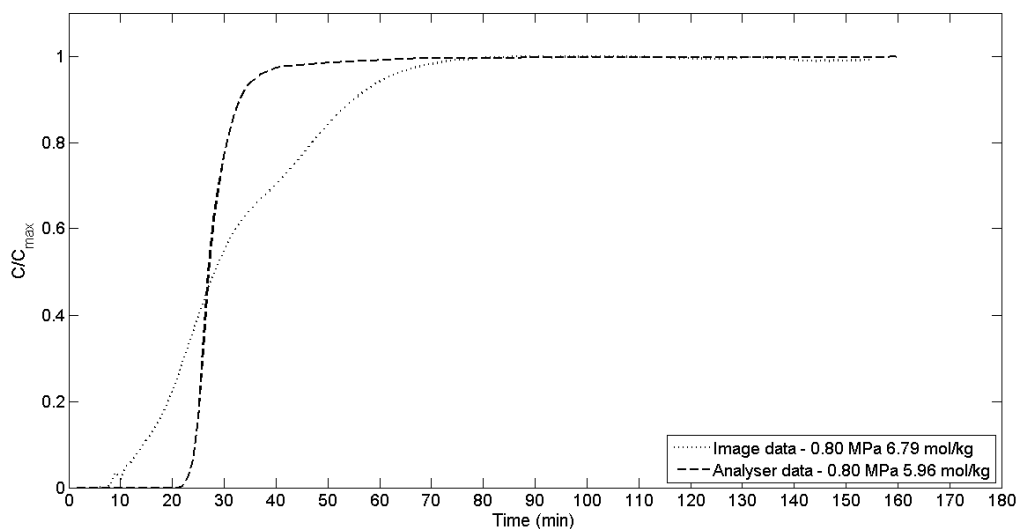


**Figure 5.37.** A comparison between breakthrough curves for Zeolite 13X produced using image data and CO<sub>2</sub> analyser data with corresponding calculated capacities. The experimental conditions were system pressure of 1.6 MPa and CO<sub>2</sub> concentration of 50%.

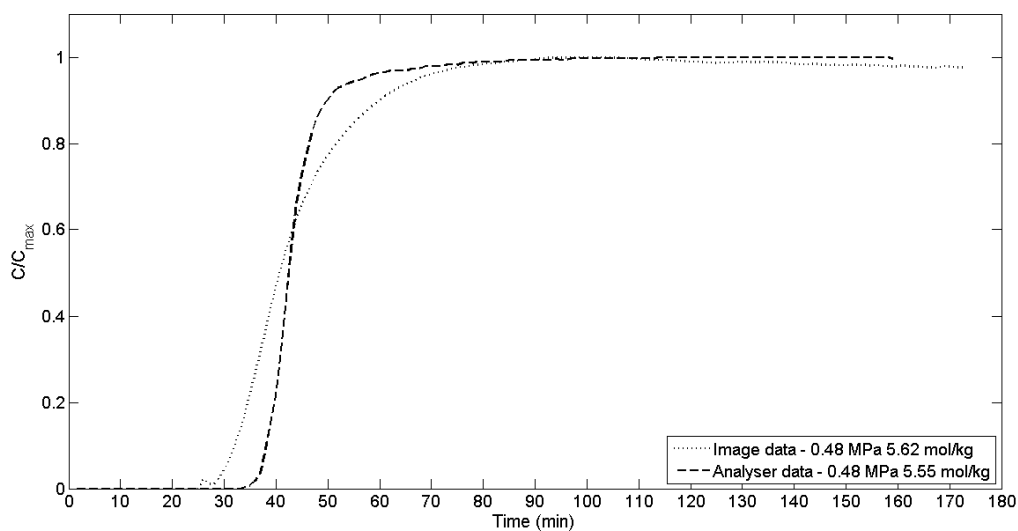


**Figure 5.38.** A comparison between breakthrough curves for Zeolite 13X produced using image data and CO<sub>2</sub> analyser data with corresponding calculated capacities. The experimental conditions were system pressure of 1.6 MPa and CO<sub>2</sub> concentration of 30%.

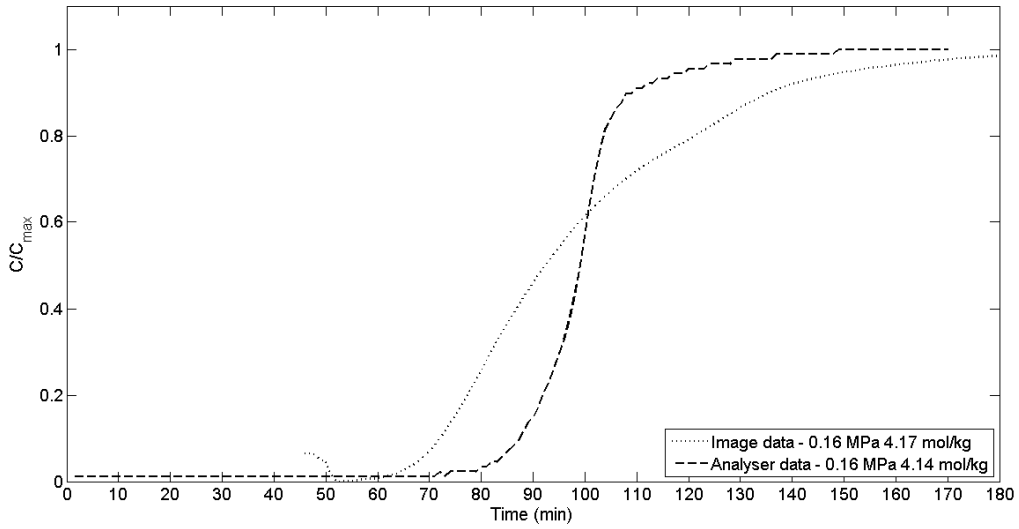


**Figure 5.39.** A comparison between breakthrough curves for Zeolite 13X produced using image data and CO<sub>2</sub> analyser data with corresponding calculated capacities. The experimental conditions were system pressure of 1.6 MPa and CO<sub>2</sub> concentration of 10%.

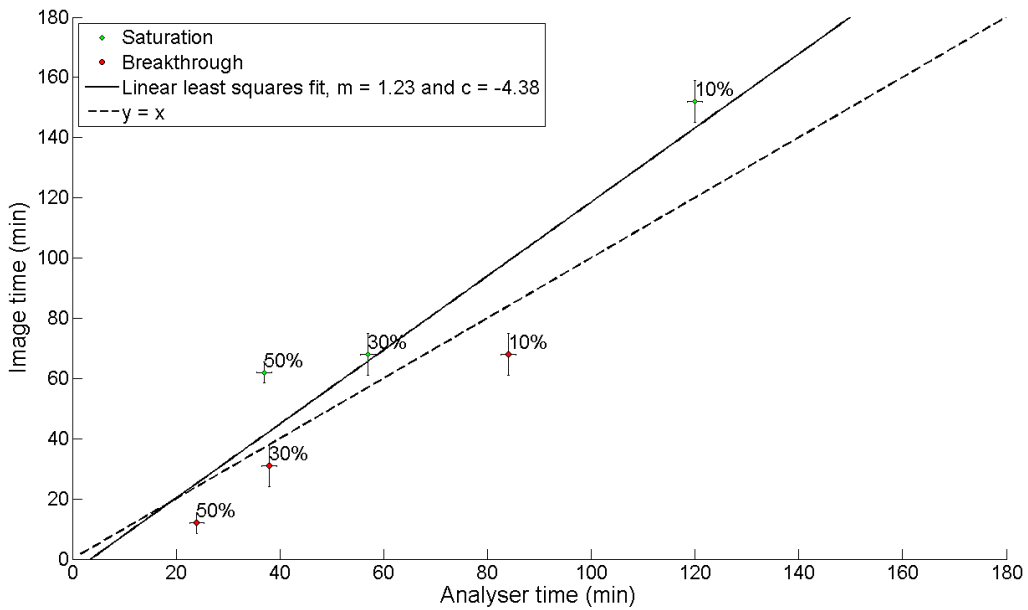


**Figure 5.40.** Times to breakthrough and calculated from image data and CO<sub>2</sub> analyser data for system pressure of 1.6 MPa using Zeolite 13X. The results have been plotted against each other to clarify similarities between the two measurement techniques and a linear LSF has been applied ( $m = 1.23$ ,  $\sigma_m = 0.07$ ,  $c = -4.38$  and  $\sigma_c = 3.85$ ).

**Table 13. Calculated time to breakthrough,  $t_{bt}$ , and saturation,  $t_{sat}$ , for image data. The capacity of the column at  $t_{bt}$ ,  $q_{bt}$ , and at  $t_{sat}$ ,  $q_{sat}$  has been included and the percentage of saturation capacity at breakthrough is given.**

	$C_{max}$ (%)	$P_{sys}$ (MPa)	$P_{CO2}$ (MPa)	Time (min)			Capacity (mol kg <sup>-1</sup> )			% of $q_{sat}$ adsorbed at $t_{bt}$
				$t_{bt}$	$t_{sat}$	$\sigma_t$	$q_{bt}$	$q_{sat}$	$\sigma_q$	
Activated Carbon	50	2.6	1.30	16	66	7	4.85	8.95	2.38	54
	30		0.78	21	72	6	3.82	6.39	1.46	60
	10		0.26	37	111	7.5	2.25	3.60	0.54	63
	50	1.6	0.8	12	56	3	3.59	8.09	0.97	44
	30		0.48	20	54	8	3.64	6.02	1.04	60
	10		0.16	28	62	7	1.70	2.45	0.58	70
Zeolite 13X	50	2.6	1.30	21	56	7	4.41	6.37	2.00	69
	30		0.78	29	75	6.5	3.66	5.20	1.12	70
	10		0.31	87	172	6.5	3.66	4.71	0.43	78
	50	1.6	0.8	12	62	3.5	2.50	6.65	0.87	38
	30		0.48	31	68	7	3.91	5.43	1.18	72
	10		0.16	68	152	7	2.85	4.13	0.37	69

Table 13 contains the breakthrough times and saturation time for each of the runs calculated from the image data breakthrough curves. The error in the time calculations is derived from the standard deviation of the smoothed breakthrough data and the uncertainty in the calculation of gas residence time between the column and the CO<sub>2</sub> analyser. As with the CO<sub>2</sub> analyser data the capacity at  $t_{bt}$  and  $t_{sat}$  have been included and the uncertainty,  $\sigma_q$ , was calculated as explained in section 5.2.1. The calculated percentage of saturation capacity at breakthrough for Activated Carbon at 2.6 MPa is within 54% and 63% which is reasonably consistent and indicates a relatively inefficient system. The percentage capacity at breakthrough for Zeolite 13X at 2.6 MPa (3.1 MPa for 10% feed concentration) are also reasonably consistent as they are between 65% and 70% which also indicates higher efficiency than Activated Carbon at the same pressure. However, for both adsorbents at the lower system pressure of 1.6 MPa the

capacity percentage at breakthrough for each run varies more considerably with particularly low values for  $C_{max} = 50\%$ . The following section provides a direct comparison between the CO<sub>2</sub> analyser data and image data.

#### **5.2.2.2 Comparison between CO<sub>2</sub> analyser and image data**

Table 14 provides a direct comparison between data obtained using the CO<sub>2</sub> analyser and the imaging technique. As expected from the comparison breakthrough plots presented in the previous section the times to breakthrough and saturation for each of the Activated Carbon experiments are comparable, and by referring to Table 12 and Table 13 it is observed that the values lie within each other's error bounds. This corresponds to relatively comparable percentage adsorbed at breakthrough with values within 10% of each other except for the data obtained for  $P_{sys} = 1.6$  MPa and  $C_{max} = 50\%$  which are 17% apart. The percentage of saturation capacity adsorbed at breakthrough for Zeolite 13X is generally higher than that of Activated Carbon implying greater efficiency, however greater differences between values obtained using the CO<sub>2</sub> analyser and imaging technique are observed, particularly for  $P_{sys} = 1.6$  MPa. It has been observed that the largest difference between the CO<sub>2</sub> analyser data and image data is for  $P_{sys} = 1.6$  MPa and  $C_{max} = 50\%$  for each adsorbent with a difference of 17% for Activated Carbon and 49% for Zeolite 13X. The differences for Zeolite 13X at  $P_{sys} = 1.6$  MPa and feed concentrations of 10% and 30% are both relatively high at 17%. These figures agree with the earlier conclusion that the breakthrough curves obtained using the image data for Activated Carbon agree well with the CO<sub>2</sub> analyser data, however the results for Zeolite 13X show inconsistencies between the image and analyser breakthrough curves, particularly observed for system pressure 1.6 MPa, despite the similar calculated capacities.

**Table 14. Comparison between CO<sub>2</sub> analyser data and image data for time to breakthrough, time to saturation and percentage of total saturated capacity adsorbed at breakthrough.**

	$C_{max}$ (%)	$P_{sys}$ (MPa)	$t_{bt}$ (min)		$t_{sat}$ (min)		% of $q_{sat}$ adsorbed at $t_{bt}$	
			Analyser	Image	Analyser	Image	Analyser	Image
Activated Carbon	50	2.6	17	16	60	66	54	54
	30		20	21	73	72	53	60
	10		30	37	103	111	53	63
	50	1.6	15	12	44	56	61	44
	30		18	20	54	54	60	60
	10		26	28	64	62	65	70
Zeolite 13X	50	2.6	30	21	51	56	82	69
	30		41	29	66	75	83	70
	10	3.1	93	87	145	172	79	78
	50	1.6	24	12	37	62	87	38
	30		38	31	57	68	88	72
	10		84	68	120	152	85	69

### 5.2.2.3 Discussion

The analysis of results presented in this section shows that the imaging technique is capable of performing similar saturation capacity measurements to the CO<sub>2</sub> analyser. The breakthrough curves obtained for Activated Carbon show good agreement although the results for Zeolite 13X show inconsistencies between the image and analyser breakthrough curves, particularly observed for system pressure 1.6 MPa, despite the similar calculated capacities. This has been investigated further in the following section.

The developed imaging technique has been verified as a comparable measurement technique to the CO<sub>2</sub> analyser, although it would be recommended to continue using the CO<sub>2</sub> analyser simultaneously to ensure the reliability of the results.

## **5.3 DETAILED ANALYSIS OF ADSORPTION USING THE DEVELOPED IMAGING TECHNIQUE**

This section discusses the full extent of information that can be provided using the imaging technique beyond the production of breakthrough curves. The ability of PET to non-invasively provide a direct observation of the internal process within an opaque system has resulted in the production of concentration profiles within the column, images of the progression of  $^{11}\text{CO}_2$  and an investigation into the MTZ of the adsorption column. The following results analysis provides a qualitative study of the kinetics of adsorption and discusses the future potential of quantitative measurements and the ability to utilise the results obtained for the verification of existing isotherm and kinetic models.

### **5.3.1 Concentration profiles**

Once the imaging technique was validated as a comparable measurement technique to the  $\text{CO}_2$  analyser the capabilities of the technique for providing extra information about the adsorption process were investigated. The imaging technique allows a non-invasive look at what is happening inside the column so the natural first stage of the investigation began with a qualitative study of the concentration profiles of the  $^{11}\text{CO}_2$  within the adsorption column at every stage of the process. Figure 5.41 demonstrates how the concentration profiles were created using image data. For each image plane in the  $z$  (axial) direction the number of counts in that plane was summed to give  $S_n$ , where  $n$  is plane number. By using the summation of each plane the number of counts increases which in turn decreases the statistical noise of the data used allowing the production of meaningful profiles. The intensity profiles created in this manner indicate the total number of counts detected in that plane per minute which is assumed to be

directly proportional to the amount of CO<sub>2</sub> present in that location, therefore the profiles are considered representative of CO<sub>2</sub> concentration profiles. This process is repeated for each time frame allowing the progression of CO<sub>2</sub> through the bed to be clearly visualised.

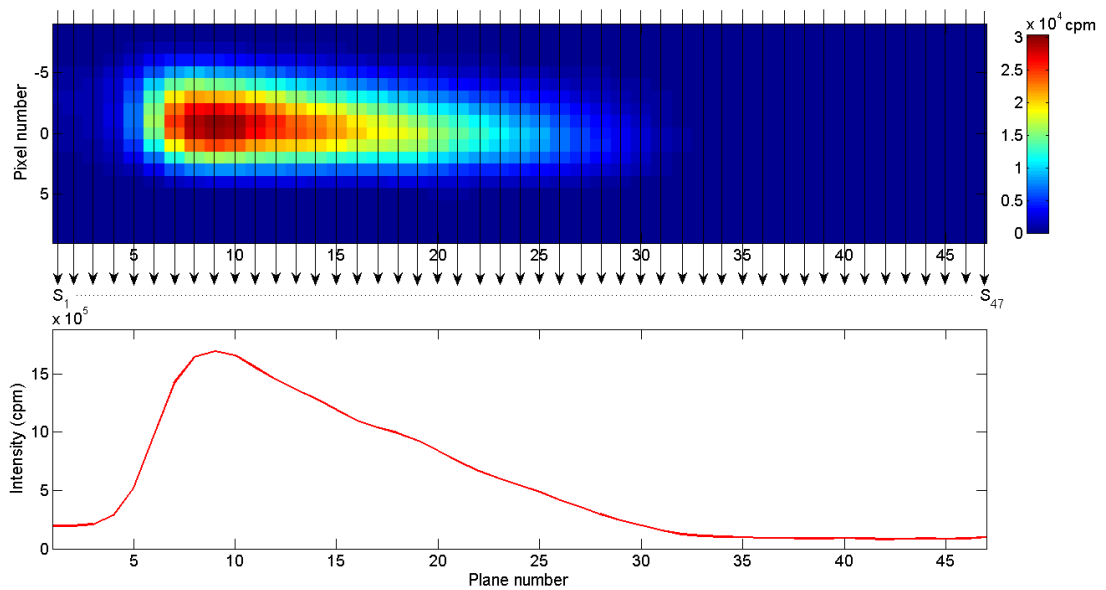


**Figure 5.41. 2D slice showing how the concentration profiles were created using the image data. The number of counts for each pixel across each plane for each time frame were summed to create an array of  $S_{n=1}$  to  $S_{n=47}$  where  $n$  is plane number. This example was created using data from experimental conditions 10% CO<sub>2</sub> at system pressure 1.6 MPa for adsorbent Activated Carbon at 20 minutes into the experiment.**

Figure 5.42 is an example of the range of concentration profiles produced for Activated Carbon at system pressure 1.6 MPa and CO<sub>2</sub> feed concentration of 10%. Each colour line of the plot from blue to red is the concentration profile of the column each consecutive minute from the start of the process to the end of the experiment. The black dashed lines indicate the ends of the adsorbent region of the bed. As described

in section 5.2.1 the data used does not include the initial image frames as the noise of the PET camera before a positron emitting source is present in the FoV renders the data unusable. This is the case for every image data set presented in this work and the first image frame used for each set after removing noisy frames is considered to be from the start of the process as this is the first frame  $^{11}\text{CO}_2$  is present in the FoV. This figure has been displayed as it highlights some initial characteristics and limitations of the imaging technique. As the profiles are created along the z axis axial smoothing is apparent in the data. It is seen that the effect of axial smoothing blurs what would be expected to be a sharp boundary at the edges of the adsorbent region. Instead, what is observed is a broadened base in the low count frequency range and a narrow plateau in the high frequency range. From section 2.5.2 this was anticipated and is a known inherent artefact of the reconstruction technique used and to correct for this problem is beyond the limits of this project. It was deemed sufficient for the purposes of this project to perform the sensitivity and resolutions tests (section 4.1.1) where the smearing from axial smoothing was found to an observable spatial resolution of 10 mm.

Another anticipated characteristic is the slightly oscillating count rate along the axial length of the bed due to uneven sensitivity of the camera along the FoV. This has been explained by the camera's user manual and is discussed in section 2.4.2.3. As this is an expected trait of the camera it has not caused significant problems with the analysis of the image data. In Figure 5.42 the amount of  $^{11}\text{CO}_2$  in the region between about 30 and 50 mm appears to rise to a maximum and then drop by about  $2 \times 10^5$  cpm. This is due to the dead time correction of the camera and is an indication that the initial activity

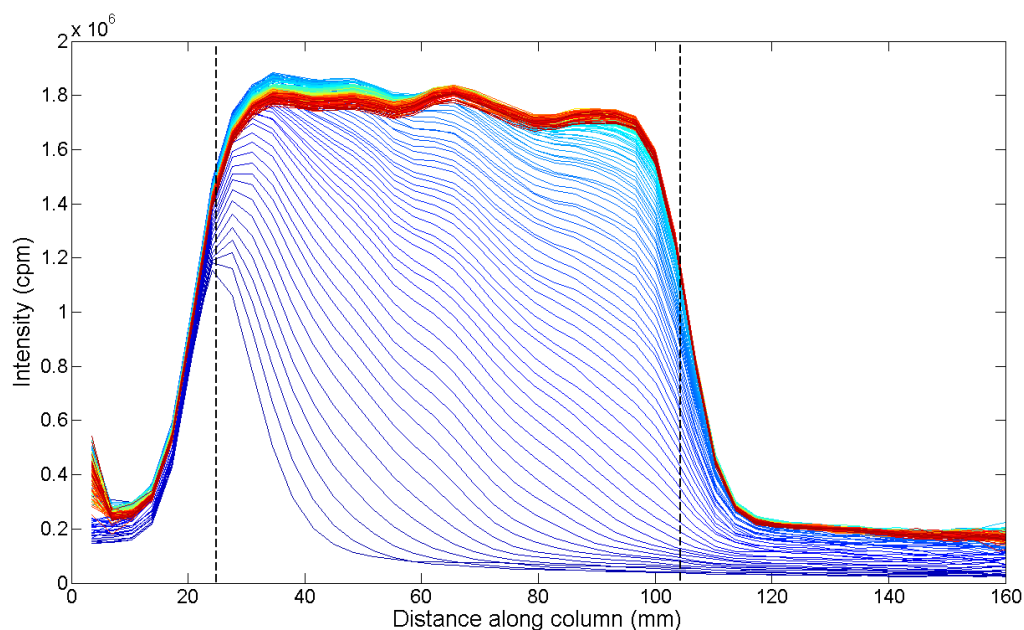


**Figure 5.42. Progressive intensity profiles along the adsorption column for each minute of the experiment. Data acquired for the first minute after the removal of noise is shown as dark blue and the final image frame is red. The dashed black lines indicate the location of the start and end of the adsorbent region.**

of the gas used was too high. As explained in section 2.2 there is a limit to the frequency of counts detectable by the scintillation crystal to enable the identification of distinguished coincidences. Above this frequency the PET camera cannot uniquely identify a true LOR as the detectors become ‘saturated’ and not all detections are recorded. The dead time correction would affect the normalisation process in the image reconstruction protocol as the image frames will be normalised to a limited maximum count rate that will not vary with varying concentration until the  $^{11}\text{CO}_2$  decays to an activity below the camera saturation threshold but a decay correction will still be applied. After sufficient time has passed for the  $^{11}\text{CO}_2$  gas to have decayed enough for the frequency of photons hitting the detectors to be below the threshold the dead time correction is no longer needed. At this point the decay correction applied to the

detected counts is the reason the level of intensity remains constant. It is confidently assumed that the phenomenon being witnessed in this region is not the desorption and displacement of  $^{11}\text{CO}_2$  molecules from the surface of the adsorbent, rather the application of the dead time correction. This leads to the recommendation that future work using his technique should have a preliminary optimal gas activity investigation, which would require the ability to measure the amount of  $^{11}\text{CO}_2$  produced by the cyclotron, the activity of a sample of the gas and the calculation of the distribution of  $^{11}\text{CO}_2$  in the gas flow mix entering the column. This has been discussed in greater detail in section 6.2. Figure 5.43 has been included to demonstrate consistent imaging traits for different experimental conditions. The concentration profiles shown in the figure were made from image data acquired for 50%  $\text{CO}_2$  feed concentration at a system pressure of 1.6 MPa for Zeolite 13X. The first important feature to be noted is the location of the adsorbent region within the FoV. The region of Activated Carbon was 24 to 103 mm along the column and the Zeolite 13X was 66 to 135mm. Ideally the adsorbent regions would have been placed centrally along the FoV, however, the attenuation correction programme on the PET camera was not working meaning the actual location of the adsorbent within the stainless steel column could not be identified until after the first imaging session. It was deemed more prudent to keep the column in the same place for each run of the same adsorbent material than to attempt to vary the location slightly. The different locations of the regions of interest have not caused any apparent complications or inconsistencies for the analysis of the data.

The similarities between Figure 5.42 and Figure 5.43 include the equal maximum summed intensity of around  $1.8 \times 10^6$  cpm. This is due to the normalisation performed post reconstruction as an integral part of the image reconstruction protocol. Another

common feature between all of the image data sets is the presence of noise at plane 1. This is unexpected from literature but is consistent with the findings from the sensitivity test (section 4.1.1) so it is thought that this is likely to be a result of the deterioration of the PET camera which is now at least 15 years old.

These concentration profiles have been used to perform qualitative analysis of adsorption characteristics for each experimental run. A number of features provide valuable insight to the progression of the process over time which is not possible to observe using other techniques. The overall rate of the adsorption process can be initially gauged by how tightly packed the profiles are. For example Figure 5.43 shows concentration profiles that are very close together which would imply a slow progression of the MTZ through the bed. Conversely, the concentration profiles shown in Figure 5.44 are much more spaced apart and the profiles begin to plateau at about 70% of the maximum intensity. This would indicate a relatively fast moving bulk adsorption front with the entire length of the adsorption region acting as an active MTZ with consistent  $^{11}\text{CO}_2$  uptake for the length of the bed from about 19 minutes into the experiment onwards.

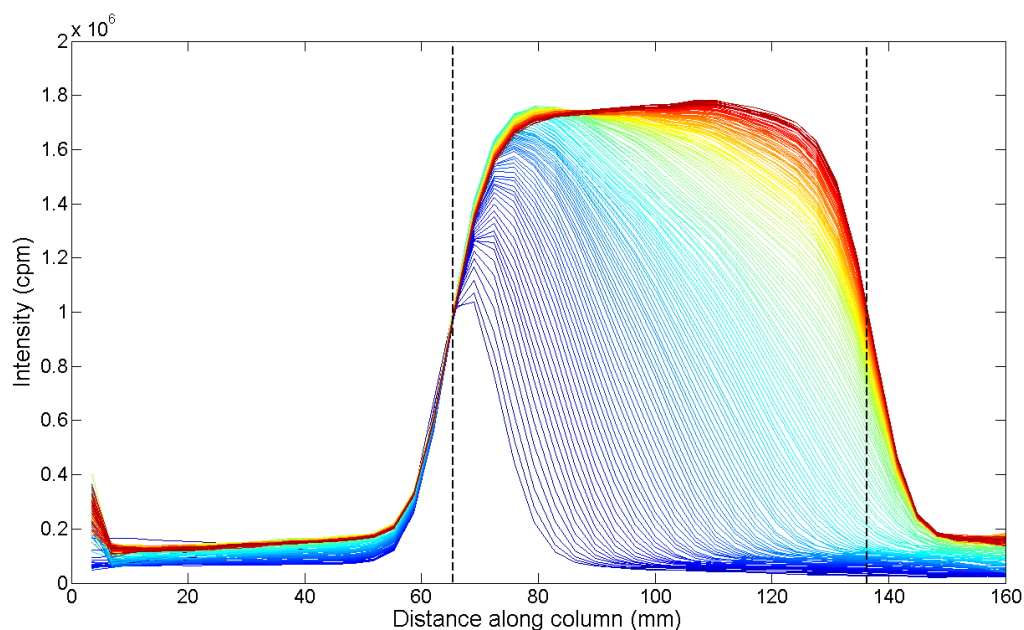


**Figure 5.43 Intensity profiles for Zeolite 13X at a system pressure of 1.6 MPa and CO<sub>2</sub> feed concentration of 10%. The lines ranging from blue to red are representative of concentration profiles from the first image frame to the last. The concentration profiles are close together which implies a slow progression of the MTZ through the bed.**

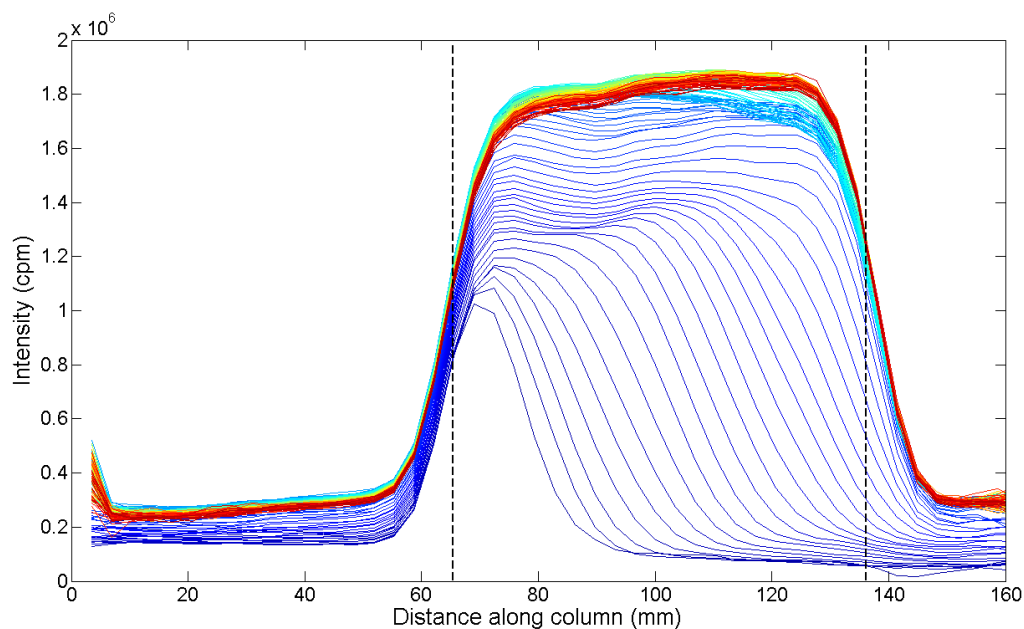


**Figure 5.44. Intensity profiles for Zeolite 13X at a system pressure of 2.6 MPa and CO<sub>2</sub> feed concentration of 50%. The lines ranging from blue to red are representative of concentration profiles from the first image frame to the last. These profiles are spaced apart indication a fast moving MTZ.**

In section 5.2.2 it was observed that the breakthrough curve produced using image data for Activated Carbon at 1.6 MPa and 30% feed concentration showed unusual fluctuations after saturation. Figure 5.45 shows the intensity profiled for this set up and the cause of the fluctuations is immediately apparent. There is a large amount of noise at the inlet and the column does not appear to reach full saturation. A definite cause of this behaviour is unknown but a possible reason could be that the feed gas used for this experiment was very active causing large dead time corrections, which when combined with the decay correction causes the unusual distribution and fluctuation of  $^{11}\text{CO}_2$  concentration observed.

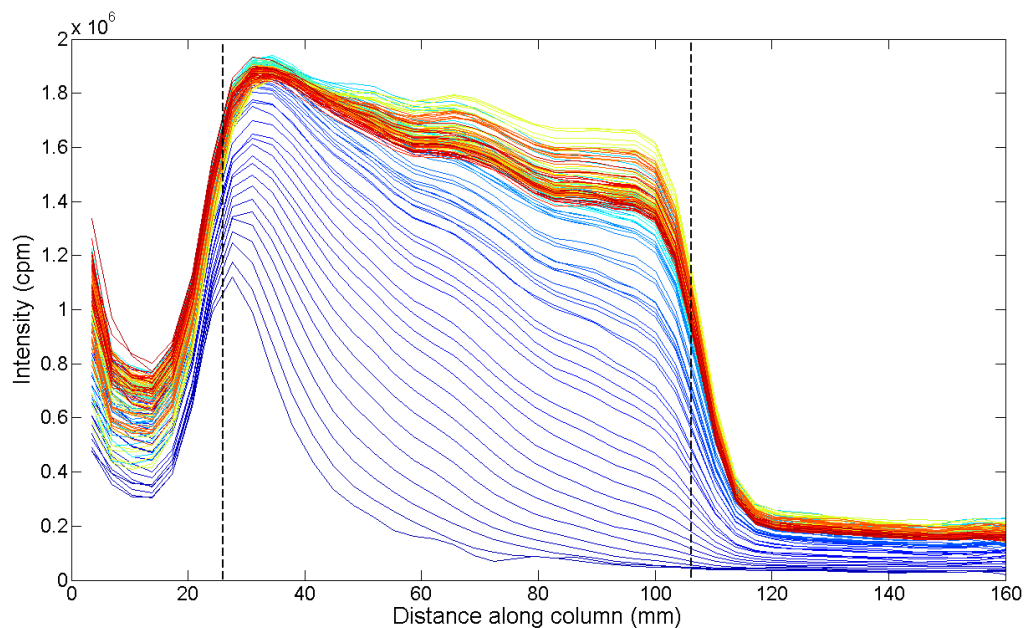


**Figure 5.45. Intensity profiles for Activated Carbon at 1.6 MPa and 30% feed concentration.**

The following sections contain the analysis of the velocity of the adsorption front through the column, the shape of the adsorption front and the rate of CO<sub>2</sub> uptake in specific locations in the bed and the relationship between these characteristics have been investigated. Concentration profiles for each of the 12 runs can be found in section 8.3.

### 5.3.2 Mass Transfer Wave velocity

From the concentration profiles produced using the image data a study of the bulk velocity of the adsorption front was made. Figure 5.46 shows how the velocity was determined for each data set. From the conclusions drawn from the resolution tests it is known that the point at half the maximum is the closest estimate to the actual location of the radioactive source so this has been taken as the leading point of the adsorption

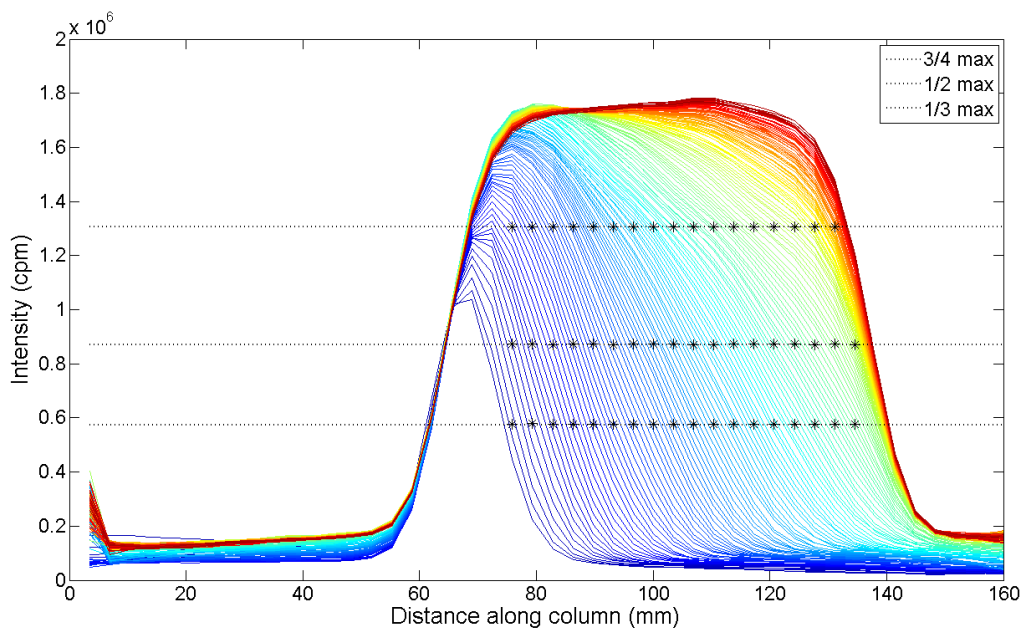


**Figure 5.46.** Figure showing how the velocity of the adsorption front was calculated for experimental conditions 10% CO<sub>2</sub> feed concentration and system pressure 1.6 MPa for Zeolite 13X. The time at which the intensity reaches a specified threshold (3/4, 1/2 and 1/3 of the maximum) has been marked by a \* and was recorded.

front. The time at which the intensity increased to half the maximum at each plane for a range of 14 planes for Activated Carbon (planes 12 to 26) and 16 planes for Zeolite 13X (planes 22 to 39) was determined through interpolation. From the shape of the profiles it has been observed that the progression of the adsorption front can vary depending on the threshold used so a brief investigation comparing velocities obtained using thresholds of 3/4, 1/2 and 1/3 of the maximum was performed. Figure 5.47 displays each of the points marked in Figure 5.46 as a plot of distance in mm against time in minutes. The uncertainties on the measurements come from the spatial resolution of the camera in the axial direction and the length of acquisition time for each

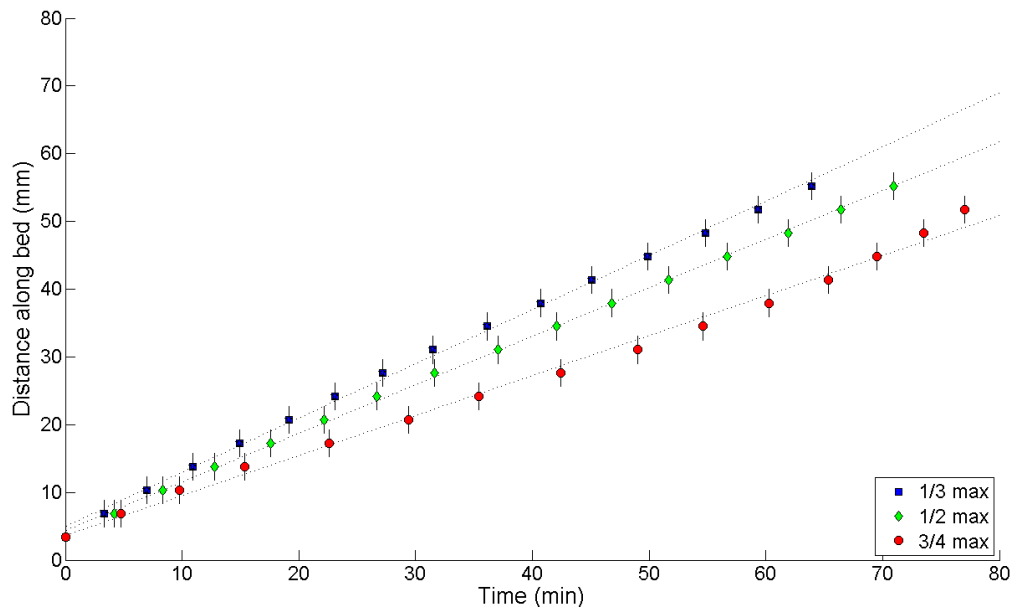


**Figure 5.47. Distance against time to show the progression of the adsorption front along the bed using different intensities as the leading point of the front. The linear least squares fit has been included, the gradient of which is the apparent velocity. This plot shows data obtained for 1.6 MPa 10% CO<sub>2</sub> using Zeolite 13X.**

frame. As the spatial resolution in the axial direction was found to be 10 mm this means the location of the emission could be within 5 mm either side of the displayed location, giving an uncertainty of  $\pm 5$  mm. As the length of one image frame is 1 minute this give a time uncertainty of  $\pm 0.5$  minutes. A linear least squares fitting technique was used to determine the gradient of each distance vs. time plot and the gradient is the apparent velocity of the adsorption front. Table 15 shows all of the calculated velocities for each experimental run using 3/4, 1/2 and 1/3 of the maximum velocities as reference points.

**Table 15. Comparison of calculated adsorption front velocities using 3/4 max, 1/2 max and 1/3 max as points of reference.**

Adsorbent	System Pressure (MPa)	CO <sub>2</sub> Concentration (%)	Front Velocity at 3/4 max (mm min <sup>-1</sup> )	Front Velocity at 1/2 max (mm min <sup>-1</sup> )	Front Velocity at 1/3 max (mm min <sup>-1</sup> )
Activated Carbon	2.6	50	5.07	5.78	6.09
		30	4.33	4.90	5.23
		10	2.00	2.62	3.47
	1.6	50	4.32	5.40	5.93
		30	2.85	4.14	4.39
		10	2.18	3.05	3.67
Zeolite 13X	2.6	50	2.76	3.60	3.68
		30	0.90	2.32	2.44
	3.1	10	0.66	0.78	0.89
	1.6	50	2.19	3.57	3.74
		30	0.94	2.07	2.24
		10	0.56	0.71	0.79

For each of the 12 experimental conditions the adsorption front velocity is faster at the bottom of the curve and slower at the top. The slower progression at high intensities has been investigated and is discussed later in this results section. The following figures are plots showing distance vs. time plots for each of the experimental runs at 1/2 maximum intensity.

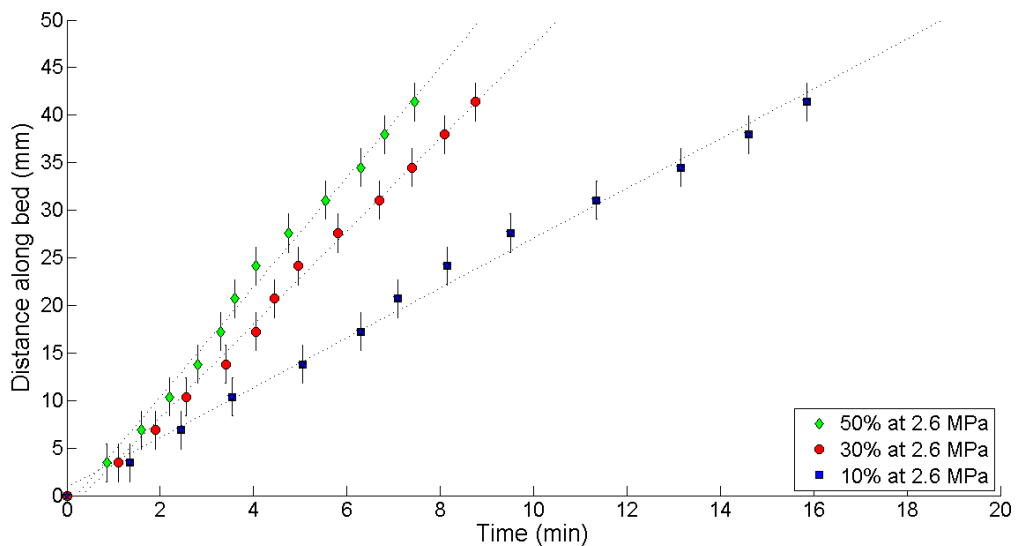


**Figure 5.48. Distance against time plots for Activated Carbon at 2.6 MPa for 50%, 30% and 10% CO<sub>2</sub> feed concentrations. The linear least squares fits used to calculate the velocity have been included to show linearity and the time scale has been kept consistent for all plots for easy comparison.**

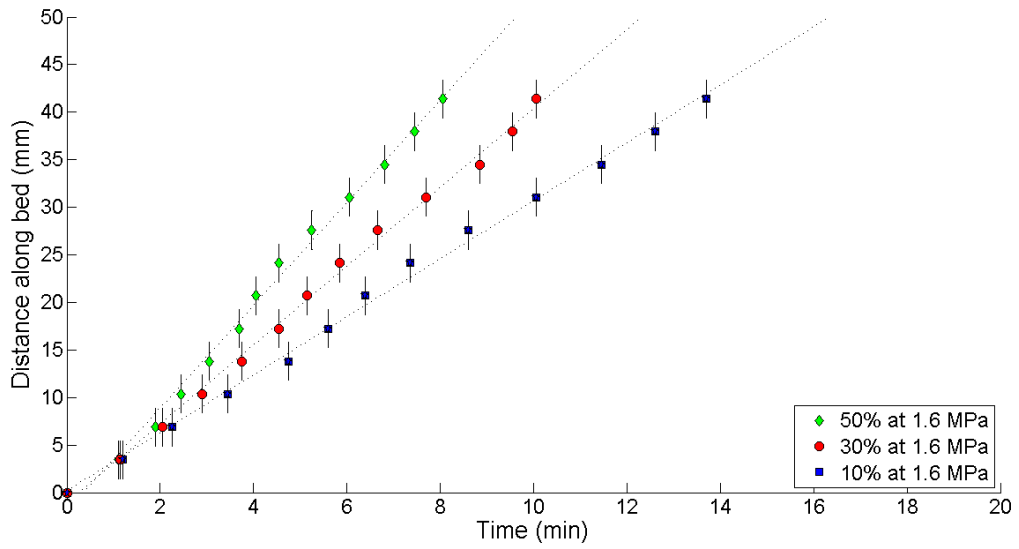


**Figure 5.49. Distance against time plots for Activated Carbon at 1.6 MPa for 50%, 30% and 10% CO<sub>2</sub> feed concentrations. The linear least squares fits used to calculate the velocity have been included to show linearity.**

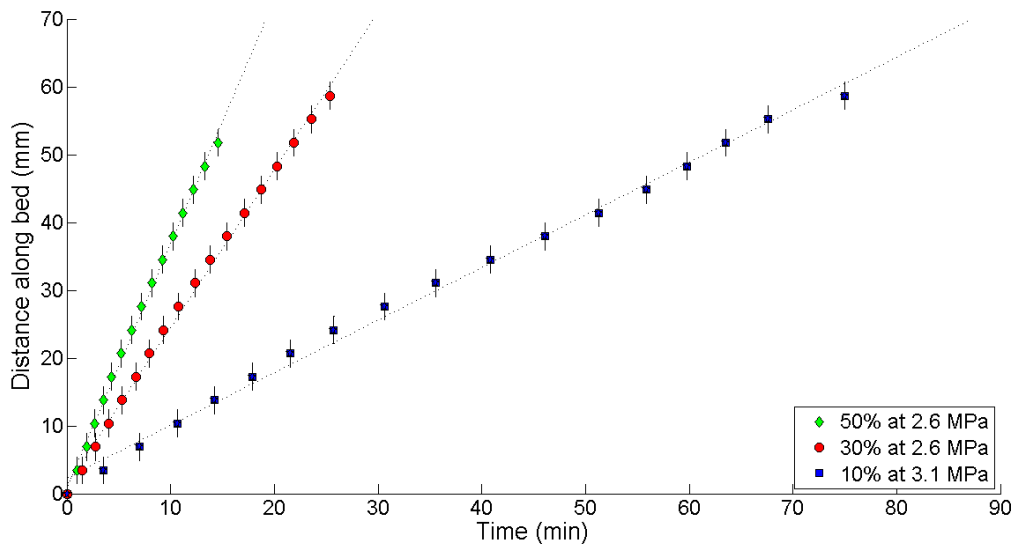


**Figure 5.50. Distance against time plots for Zeolite 13X at 2.6 MPa for 50%, 30% and 10% CO<sub>2</sub> feed concentrations. The linear least squares fits used to calculate the velocity have been included to show linearity.**

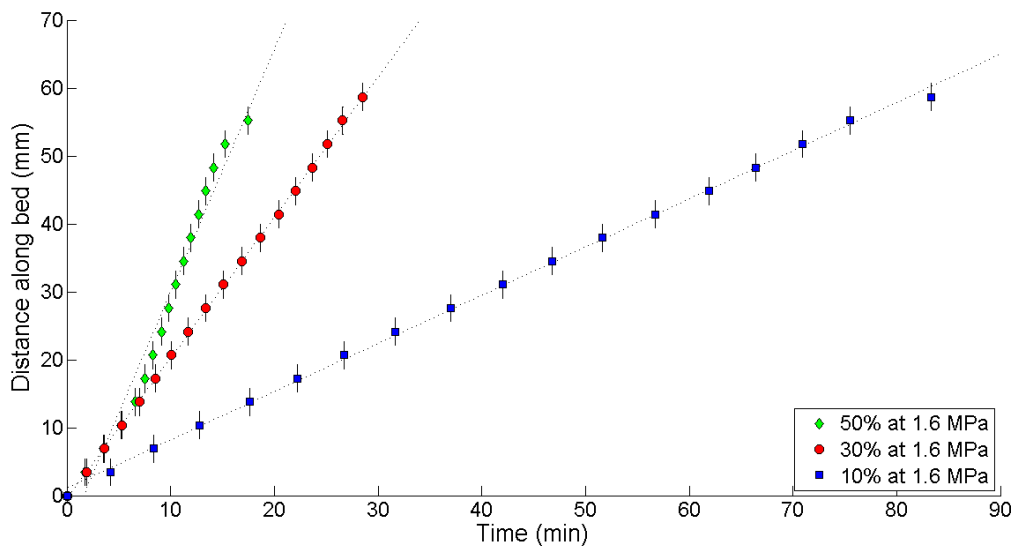


**Figure 5.51. Distance against time plots for Zeolite 13X at 1.6 MPa for 50%, 30% and 10% CO<sub>2</sub> feed concentrations. The linear least squares fits used to calculate the velocity have been included to show linearity.**

Table 16 summarises the calculated velocity data including the standard deviation of the distance vs. time linear least squares fit and the CO<sub>2</sub> feed flow rate. There is a clear proportionality between increasing CO<sub>2</sub> feed flow rate, which is dependent on desired CO<sub>2</sub> concentration, and the velocity of the adsorption front. By plotting CO<sub>2</sub> concentration against velocity this relationship has been investigated and the results are shown for Activated Carbon in Figure 5.52 and for Zeolite 13X in Figure 5.53. The plot for Zeolite 13X shows good linearity between velocity and feed concentration, and the velocity values for 2.6 MPa and 1.6 MPa are close together with the points at 10% and 50% within each other's error bounds. This would imply that the factor with greatest influence over the adsorption front velocity for Zeolite 13X is the CO<sub>2</sub> feed concentration, and in turn the feed flow rate of CO<sub>2</sub>, of the system rather than the system pressure. The plateau in capacity according to the Toth model for increasing

pressure beyond about 0.4 MPa (see Figure 5.20) shows agreement that pressure has very little influence over the velocity of the adsorption front. The plot for Activated Carbon shows good linearity at system pressure 1.6 MPa; however the point for 10% CO<sub>2</sub> feed at 2.6 MPa goes against the trend of higher velocity at higher system pressure and prevents a linear relationship from being confirmed for Activated Carbon at 2.6 MPa. Regardless, it is not possible to conclude with any certainty that a trend is linear from only three data points so a recommendation for any future investigations would be to examine this relationship for a greater range of feed concentrations and system pressures. However, for the purposes of this study an assumption that the point

**Table 16. Calculated adsorption front velocities.**

Adsorbent	P <sub>sys</sub> (MPa)	C <sub>max</sub> (%)	Q <sub>CO2</sub>		Front Velocity		σ	
			mln min <sup>-1</sup>	x 10 <sup>-5</sup> mol s <sup>-1</sup>	mm min <sup>-1</sup>	x 10 <sup>-5</sup> m s <sup>-1</sup>	mm min <sup>-1</sup>	x 10 <sup>-5</sup> m s <sup>-1</sup>
Activated Carbon	2.6	50	100	6.96	5.78	9.64	1.5	2.50
		30	60	4.18	4.90	8.16	1.3	2.17
		10	20	1.39	2.62	4.36	0.51	0.85
	1.6	50	100	6.96	5.40	8.99	1.42	2.37
		30	60	4.18	4.14	6.91	1.02	1.70
		10	20	1.39	3.05	5.08	0.64	1.07
Zeolite 13X	2.6	50	100	6.96	3.60	6.00	0.73	1.22
		30	60	4.18	2.32	3.87	0.4	0.67
	3.1	10	20	1.39	0.78	1.29	0.11	0.18
	1.6	50	100	6.96	3.57	5.95	0.72	1.20
		30	60	4.18	2.07	3.45	0.34	0.57
		10	20	1.39	0.71	1.18	0.1	0.17

for Activated Carbon at 2.6 MPa and 10% CO<sub>2</sub> goes against the trend and a velocity higher than that of 10% concentration at 1.6 MPa would be expected. Pressure is expected to have a small influence over the velocity of the adsorption front for Activated Carbon as the capacity does gradually increase with increasing pressure (see Figure 5.19). From comparison between the plots for Activated Carbon and Zeolite 13X the increase in velocity for Activated Carbon is smaller than that of Zeolite 13X if the point for 10% at 2.6 MPa is ignored. Activated Carbon increases from about 3 mm min<sup>-1</sup> to about 5 mm min<sup>-1</sup> and Zeolite 13X from about 0.7 mm min<sup>-1</sup> to about 3.5 mm min<sup>-1</sup>. This is a difference of 2 mm min<sup>-1</sup> and 2.8 mm min<sup>-1</sup> for Activated Carbon and Zeolite 13X respectively. However, the actual velocities of Activated Carbon are higher than those of Zeolite 13X.

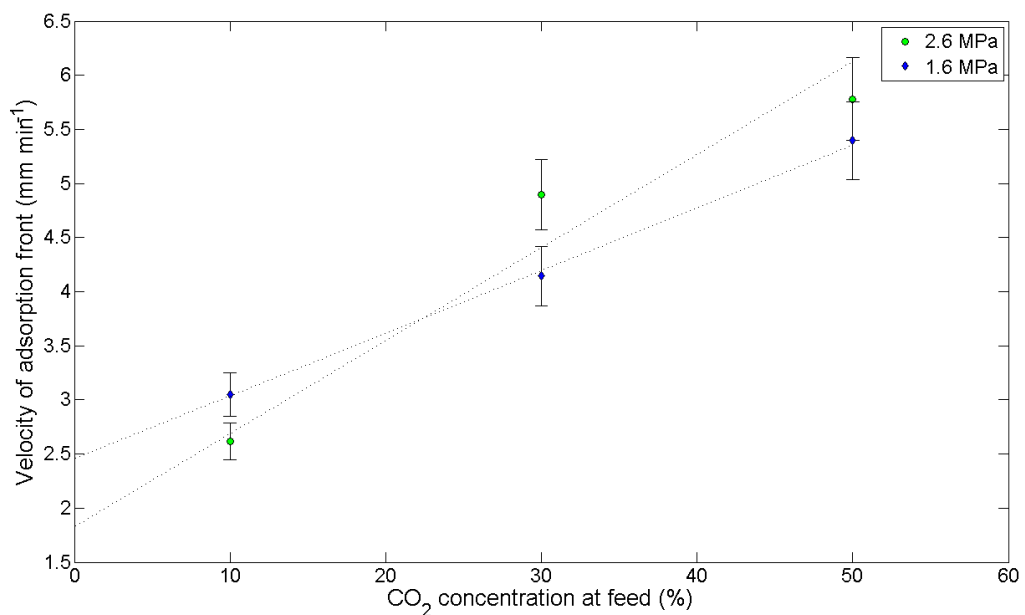


**Figure 5.52. Calculated velocity of the adsorption front against corresponding CO<sub>2</sub> feed concentration for system pressures 1.6 MPa and 2.6 MPa for Activated Carbon.**

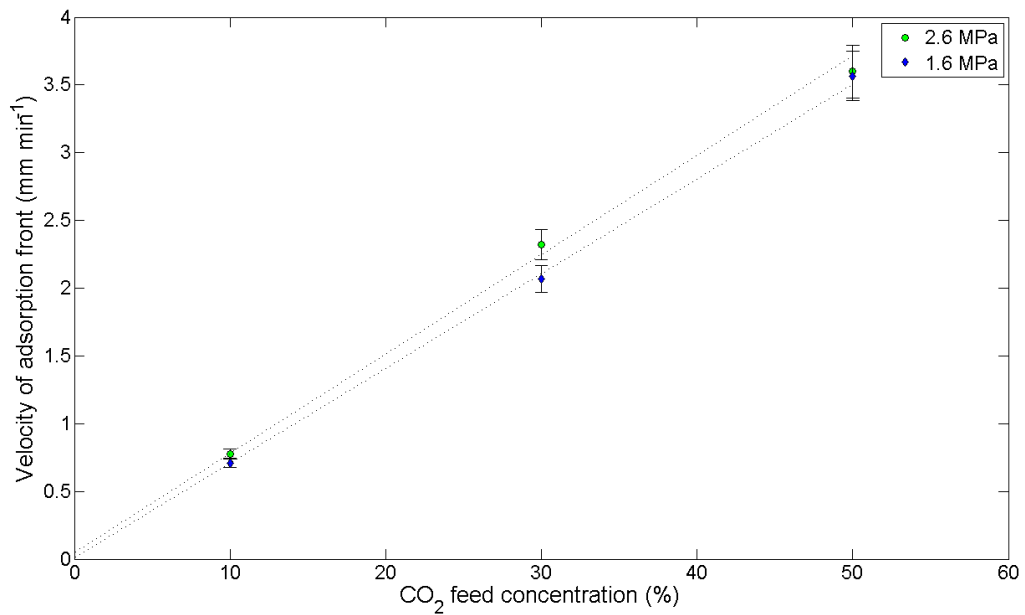


**Figure 5.53. Calculated velocity of the adsorption front against corresponding CO<sub>2</sub> feed concentration for system pressures 1.6 MPa and 2.6 MPa for Activated Carbon. The similarity between these plots implies very little effect of pressure.**

### 5.3.3 CO<sub>2</sub> accumulation

This section is a study of the accumulation of <sup>11</sup>CO<sub>2</sub> at a specified location within the bed. The results provided by the investigation into the varying adsorption front velocities using different intensity values as a reference point showed a lower velocity at higher intensity. This indicates that CO<sub>2</sub> is still being adsorbed even after the main MTZ has progressed past that point. By analysing the accumulation of CO<sub>2</sub> at a set location and comparing this uptake rate to the bulk velocity of the MTZ a relationship defining the overall mass transfer kinetics of the bed has been observed.

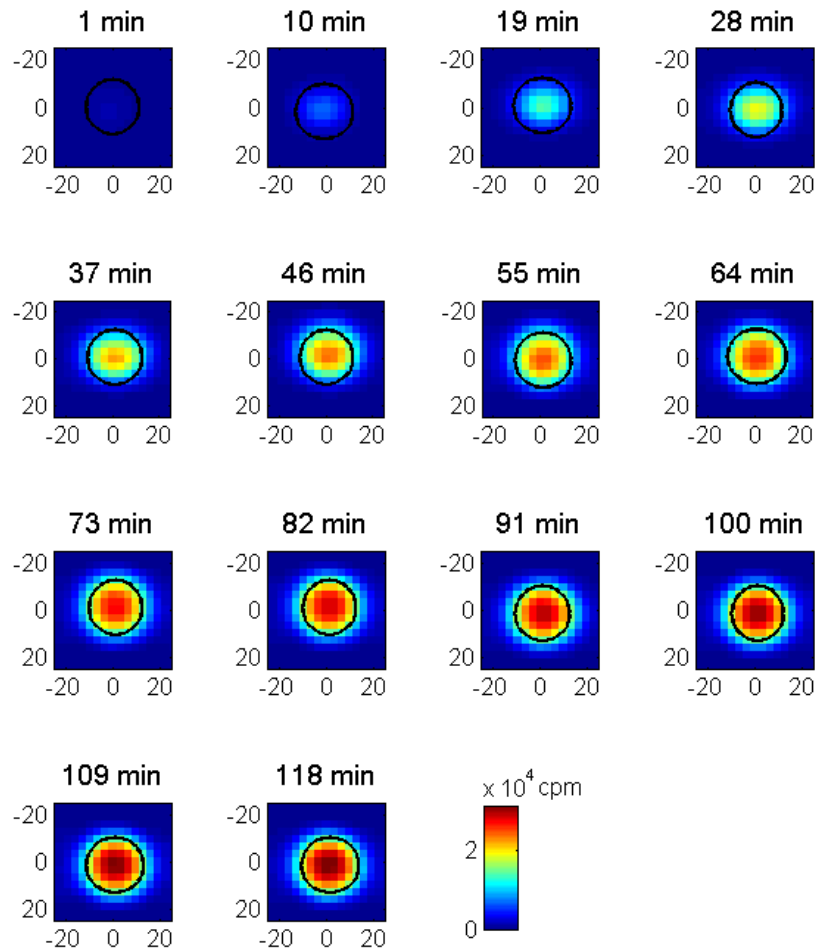


**Figure 5.54. Cross sectional slice at plane 35 for Zeolite 13X at  $P_{sys} = 1.6$  MPa and  $C_{max} = 10\%$  at nine minute intervals. Time = 1 min is the time at which  $^{11}\text{CO}_2$  is initially detected in the plane and the final image is a time at which the plane in question has reached its maximum intensity meaning it is saturated.**

In order to perform the comparison the accumulation at a specific location for each experimental run was analysed. Figure 5.54 shows an array of images displaying how the increasing amount of  $\text{CO}_2$  is observed qualitatively from the image data. Each image is of a cross sectional slice halfway along the adsorbent region of the bed

(plane 25, 86 mm, for Activated Carbon and plane 35,120 mm, for Zeolite 13X) and this example is for experimental conditions 10% CO<sub>2</sub> concentration at 1.6 MPa for Zeolite 13X. The top left image shows the point at which <sup>11</sup>CO<sub>2</sub> enters the central plane and the time of this is set to 1 minute. Each consecutive image from left to right shows the same plane every 9 minutes until the final bottom right slice at 118 minutes. At this point the central plane is fully saturated and no variance in the images can be observed. In order to have a more complete understanding of what is happening in the central slice intensity profiles across the width of column were made for the specified plane and a corresponding plot of average plane intensity, which is assumed to be indicative of the accumulation, with time. Figure 5.55 and Figure 5.56 display the intensity profiles from the time at which <sup>11</sup>CO<sub>2</sub> enters the system, blue, to the end of the experimental run, red, for data obtained for Activated Carbon and Zeolite 13X respectively. The right hand side of each figure is a plot of average intensity of the central plane against time for the same duration. The experimental conditions used for these example plots were 1.6 MPa system pressure and CO<sub>2</sub> feed concentration of 10%. A figure was created for each of the 12 experimental runs and the full range has been included in section 8.4. The plots on the right hand side of the figures show the average accumulation of <sup>11</sup>CO<sub>2</sub> at one point in the column and by normalising these plots with respect to equilibrium capacity of each run a rate of increasing CO<sub>2</sub> concentration can be determined. Plots of capacity in the central plane against time are shown in Figure 5.57 to Figure 5.60 for each adsorbent material and system pressure. More densely packed lines in the intensity profiles indicate a low accumulation rate and vice versa.

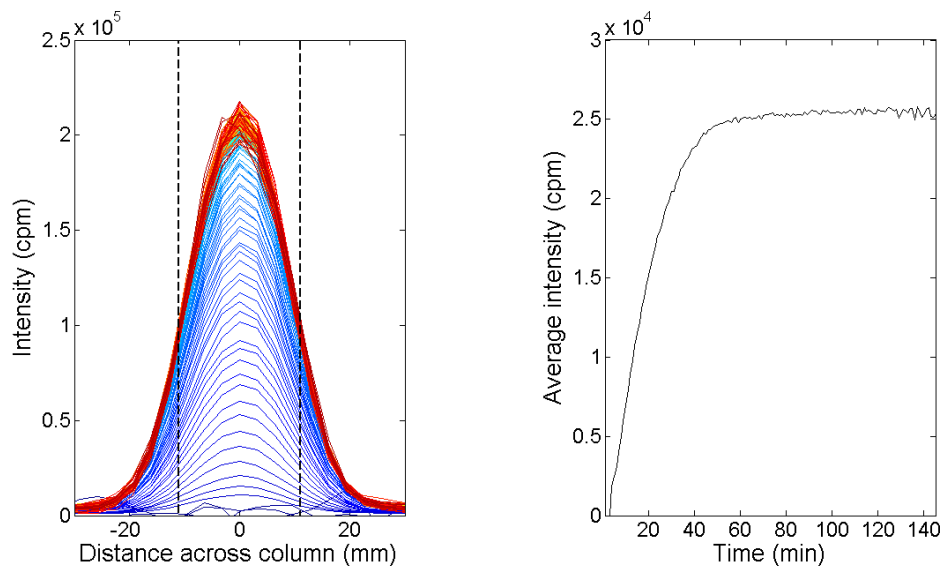


**Figure 5.55.** The left hand side of this figure shows intensity profiles across the column at the central slice (plane 25) of the adsorbent region from and the right hand side shows the increasing intensity average against time. This figure is for Activated Carbon at 1.6 MPa with CO<sub>2</sub> feed concentration of 10%.

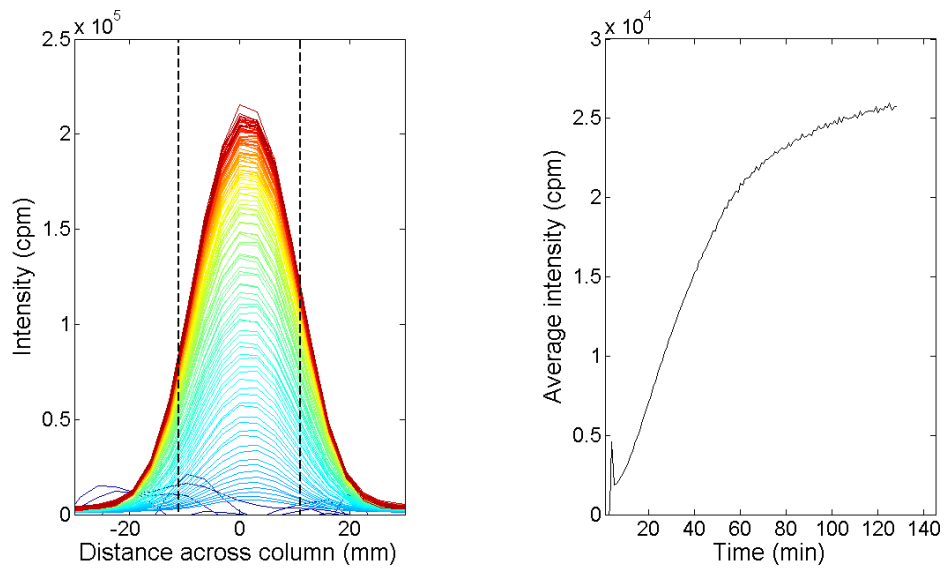


**Figure 5.56.** The left hand side of this figure shows intensity profiles across the column at the central slice (plane 35) of the adsorbent region from and the right hand side shows the increasing intensity average against time. This figure is for Zeolite 13X at 1.6 MPa with CO<sub>2</sub> feed concentration of 10%.

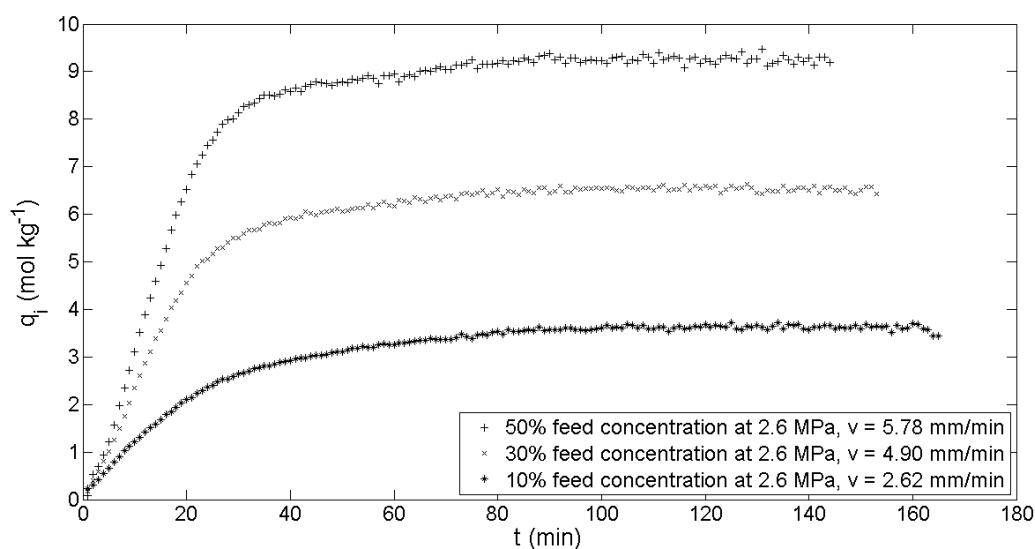


**Figure 5.57. Plot of increasing amount of CO<sub>2</sub> accumulating in the central plane with time for Activated Carbon at 2.6 MPa for feed concentrations 50%, 30% and 10%. The calculated velocities of the adsorption front have been included in the legend to help determine a relationship. These plots were produced normalising the average plane intensity with respect to equilibrium capacity of each run.**

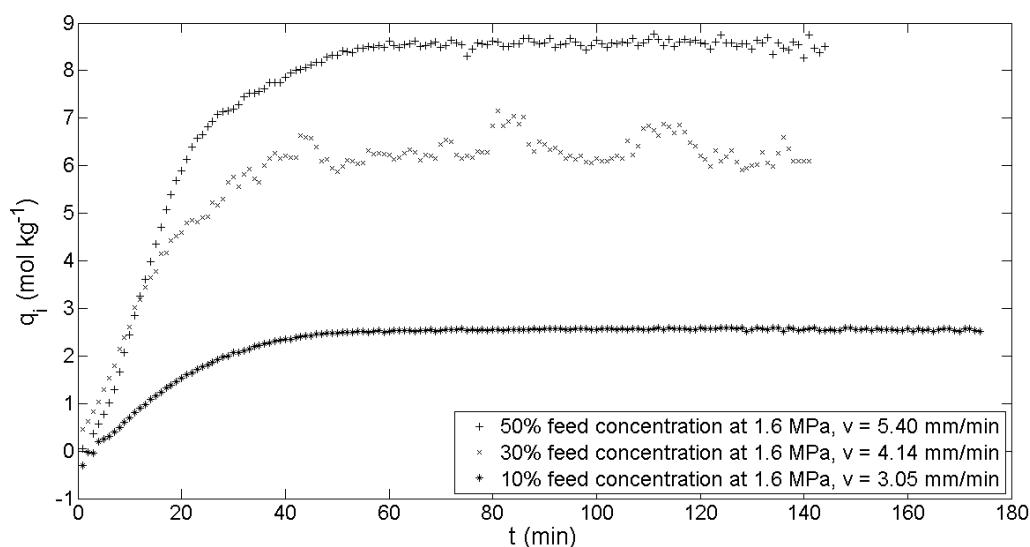


**Figure 5.58. Plot of increasing amount of CO<sub>2</sub> accumulating in the central plane with time for Activated Carbon at 1.6 MPa for feed concentrations 50%, 30% and 10%. The calculated velocities of the adsorption front have been included in the legend to help determine a relationship. These plots were produced normalising the average plane intensity with respect to equilibrium capacity of each run.**

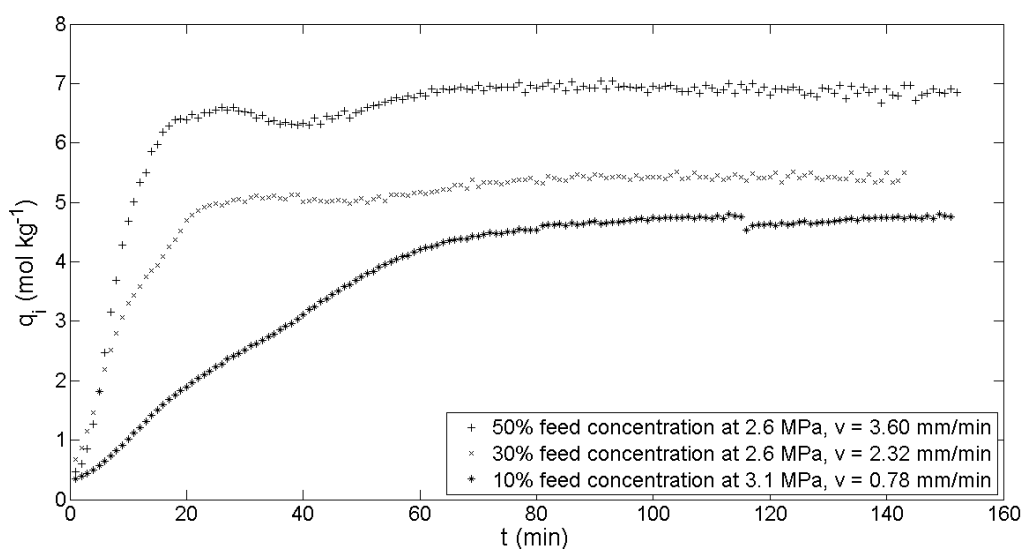


**Figure 5.59. Plot of increasing amount of CO<sub>2</sub> accumulating in the central plane with time for Zeolite 13X at 2.6 MPa for feed concentrations 50%, 30% and 10% (system pressure 3.1 MPa for 10% feed concentration). The calculated velocities of the adsorption front have been included in the legend to help determine a relationship. These plots were produced normalising the average plane intensity with respect to equilibrium capacity of each run.**

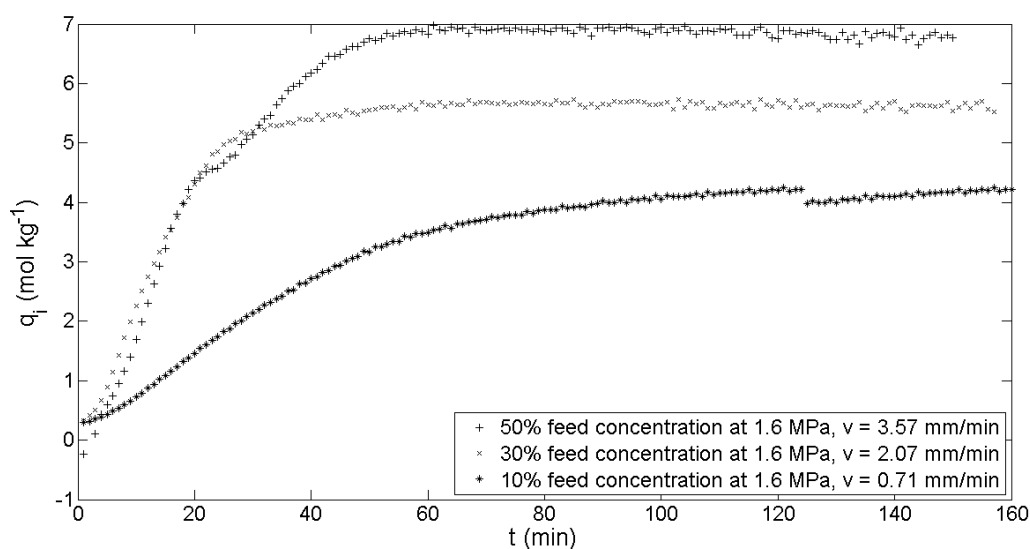


**Figure 5.60. Plot of increasing CO<sub>2</sub> concentration in the central plane with time for Zeolite 13X at 1.6 MPa for feed concentrations 50%, 30% and 10%. The calculated velocities of the adsorption front have been included in the legend to help determine a relationship. These plots were produced normalising the average plane intensity with respect to equilibrium capacity of each run.**

It is observed that a common trend for each of the plots is an initial rapid linear incline followed by a gradual curve as the capacity approaches its maximum value. It is thought that the initial linear regions of the plots are a direct result of the MTZ progressing through the bed and a linear relationship between the two is expected. In order to compare the progression of the MTZ through the bed and the CO<sub>2</sub> accumulation at a specific location a linear least squares fit was applied to the linear section of each curve, up to 60% of the maximum loading, and the gradient gives the rate of increasing capacity. Figure 5.61 to Figure 5.64 show a comparison between the linear trends for each adsorbent for the range of experimental conditions. The calculated rate of increasing loading has been given in the legends,  $\frac{\partial q}{\partial t}$ , and the error in capacity was determined by the average standard deviation of the normalised accumulation plots for each set up.

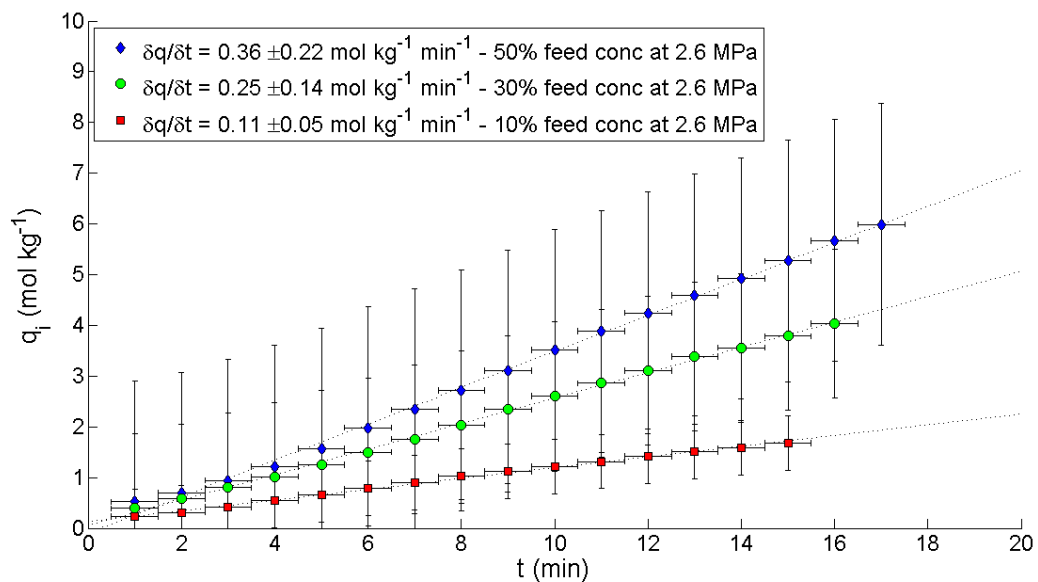


**Figure 5.61. Rate of increasing CO<sub>2</sub> loading for the central slice (plane 25) of Activated Carbon at 2.6 MPa.**

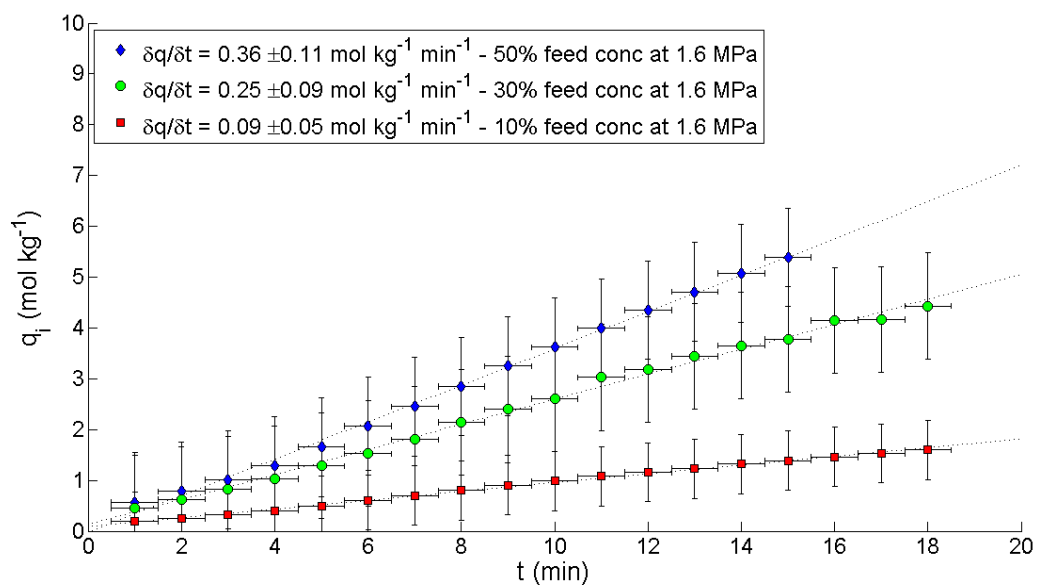


**Figure 5.62.** Rate of increasing CO<sub>2</sub> loading for the central slice (plane 25) of Activated Carbon at 1.6 MPa.

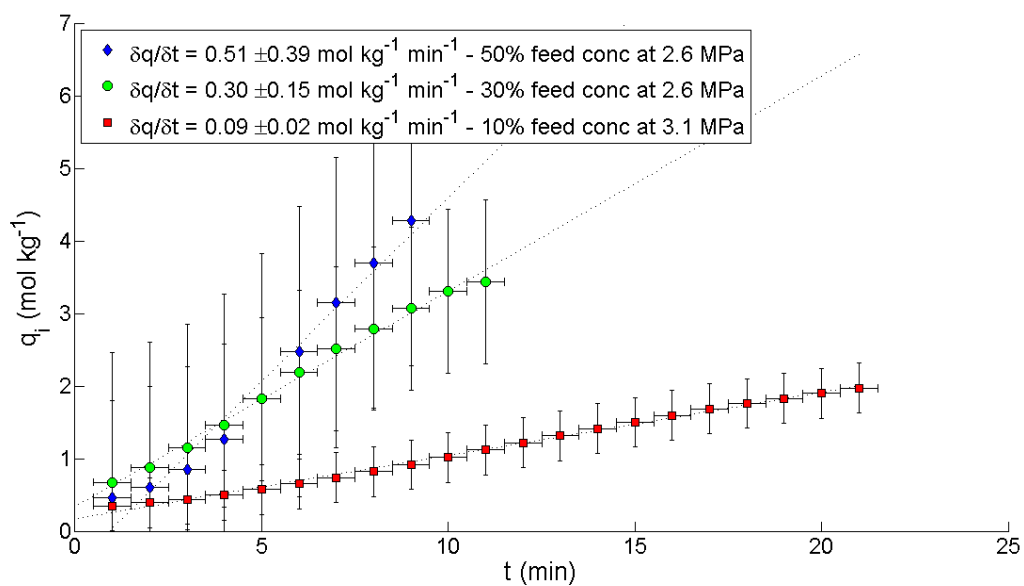


**Figure 5.63.** Rate of increasing CO<sub>2</sub> loading for the central slice (plane 25) of Zeolite 13X at 2.6 MPa (10% feed concentration at 3.1 MPa).

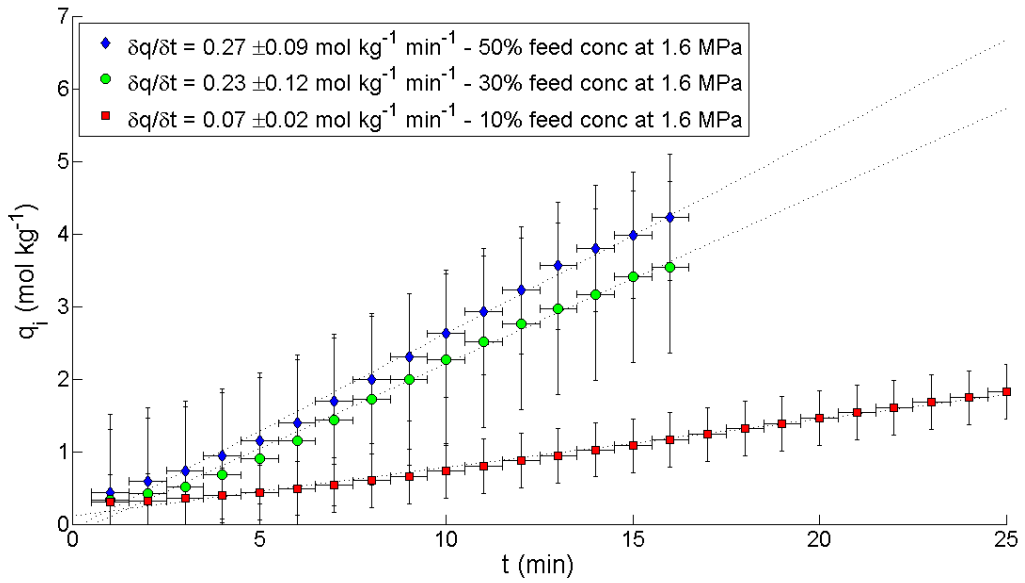


**Figure 5.64.** Rate of increasing CO<sub>2</sub> loading for the central slice (plane 25) of Zeolite 13X at 1.6 MPa.

**Table 17.** Calculated linear rate of CO<sub>2</sub> loading at the central slice of each adsorbent. The calculated adsorption front velocities have been included for comparison.

	$C_{max}$ (%)	$P_{sys}$ (MPa)	$dq_i/dt$ (mol kg <sup>-1</sup> min <sup>-1</sup> )	$\sigma_{dq}$ (mol kg <sup>-1</sup> min <sup>-1</sup> )	$v$ (mm min <sup>-1</sup> )	$\sigma_v$ (mm min <sup>-1</sup> )
Activated Carbon	50	2.6	0.36	0.22	5.78	0.38
	30		0.25	0.14	4.90	0.32
	10		0.11	0.05	2.62	0.17
	50	1.6	0.36	0.11	5.40	0.36
	30		0.25	0.09	4.14	0.27
	10		0.09	0.05	3.05	0.20
Zeolite 13X	50	2.6	0.51	0.39	3.60	0.19
	30		0.30	0.15	2.32	0.11
	10		0.09	0.02	0.78	0.04
	50	1.6	0.27	0.09	3.57	0.18
	30		0.23	0.12	2.07	0.10
	10		0.07	0.02	0.71	0.03

Table 17 summarises the calculated increase in capacity at the central slice of Activated Carbon and Zeolite 13X for each experimental run. It is observed that for decreasing adsorption front velocity with decreasing feed concentration there is a corresponding decrease in CO<sub>2</sub> accumulation. For Activated Carbon the same rate of accumulation has been calculated for 50% and 30% feed concentrations for both system pressures and the rates for 10% feed concentration have a difference of 0.02 mol kg<sup>-1</sup> min<sup>-1</sup>, which is less than the uncertainty of 0.05 mol kg<sup>-1</sup> min<sup>-1</sup>. This is observed more clearly in Figure 5.65, which shows a plot of rate of accumulation against adsorption front velocity. It has been observed that for Zeolite 13X the point at 3.6 mm min<sup>-1</sup> and 0.51 mol kg<sup>-1</sup> min<sup>-1</sup>, which corresponds to  $P_{sys} = 2.6$  MPa and  $C_{max} = 50\%$ , has relatively large uncertainty when compared to the other calculated rates and it lies quite far from the linear LSF for Zeolite 13X. This corresponds to a rapid initial accumulation as shown in Figure 5.59, where the gradient of the accumulation plot is much steeper for this data set than for the data obtained for 30% and 10% feed concentrations. This figure also shows a fluctuation at saturation that is consistent with dead time correction, which could be the cause of the slightly anomalous result.

Figure 5.65 is a plot of  $dq_i/dt$  against adsorption front velocity for each of the runs. As expected a linear trend is apparent between the two rates giving confidence to the theory that the linear region of the rate of accumulation is governed by the initial rapid external surface uptake (Wilcox 2012). By determining the length of time the accumulation is linear and multiplying this by the velocity an estimation of the length of the MTZ for each experiment has been made and the values are given in Table 18.

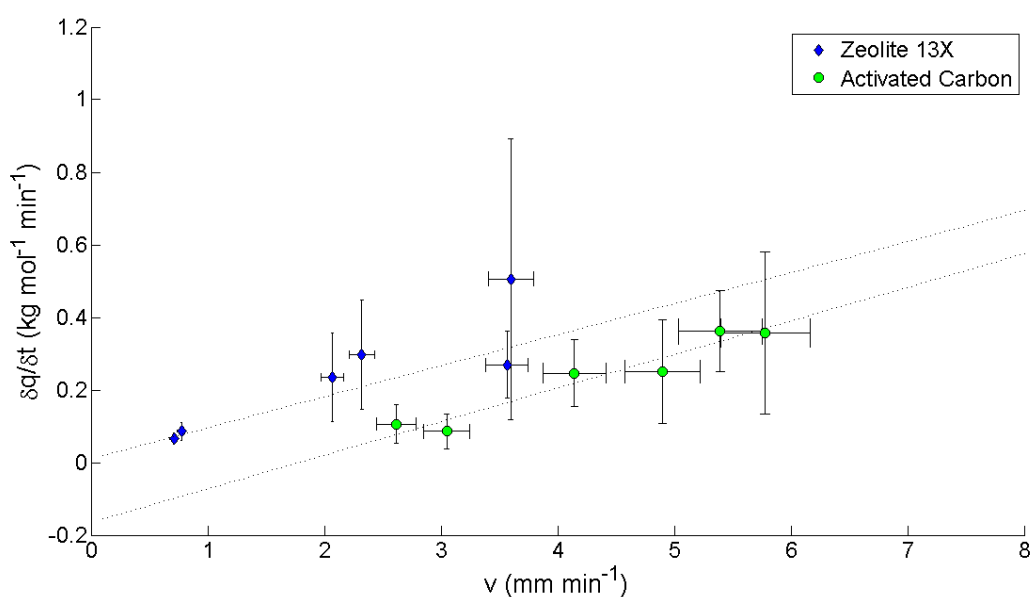


**Figure 5.65.** Plot of rate of increasing CO<sub>2</sub> capacity against the velocity of the adsorption front for Activated Carbon and Zeolite 13X. A linear LSF has been included to show the relationship between the two rates.

**Table 18.** Table showing calculated length of MTZ from the duration of linear accumulation and adsorption front velocity.

	$C_{max}$ (%)	$P_{sys}$ (MPa)	Velocity (mm min <sup>-1</sup> )	Time of linearity (min)	Length of MTZ (mm)	$\sigma$ of length (mm)
Activated Carbon	50	2.6	5.78	18	104.04	19.4
	30		4.90	16	78.4	18.0
	10		2.62	15	39.30	8.5
	50	1.6	5.40	17	91.80	16.9
	30		4.14	18	74.52	14.3
	10		3.05	19	57.95	11.1
Zeolite 13X	50	2.6	3.60	11	39.60	6.9
	30		2.32	11	25.52	6.8
	10	3.1	0.78	21	16.38	1.9
	50	1.6	3.57	19	67.83	9.7
	30		2.07	17	35.19	5.1
	10		0.71	38	26.98	3.3

Section 5.3.4 describes the investigation made into the shape of the adsorption front and the prudence of the calculated MTZ lengths is discussed. Before progressing to this topic, however, the shape of the CO<sub>2</sub> accumulation plots beyond the linear region has been examined. Figure 5.66 to Figure 5.69 show the non-linear regions of the CO<sub>2</sub> accumulation plots. Each of the plots have been normalised with respect to each average maximum concentration value for comparison.

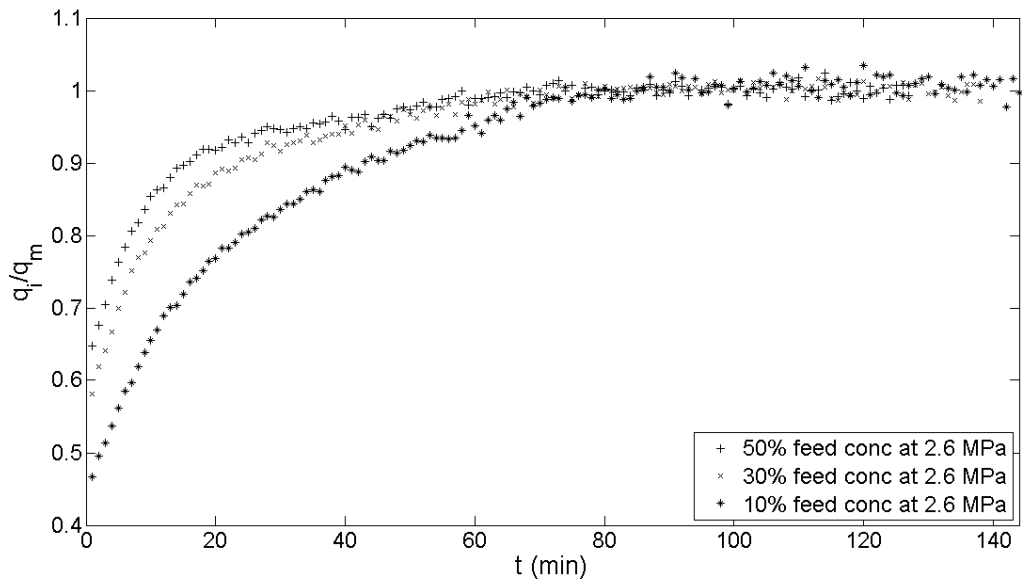


**Figure 5.66. Plot of normalised concentration against time for the non-linear region of the CO<sub>2</sub> accumulation at a specific point for Activated Carbon at 2.6 MPa.**

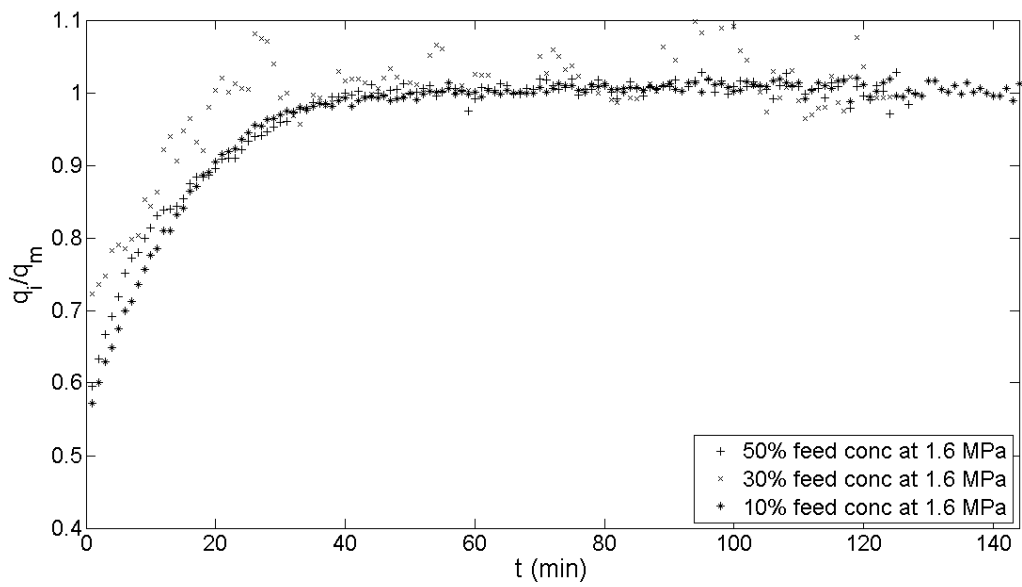


**Figure 5.67. Plot of normalised concentration against time for the non-linear region of the CO<sub>2</sub> accumulation at a specific point for Activated Carbon at 1.6 MPa.**

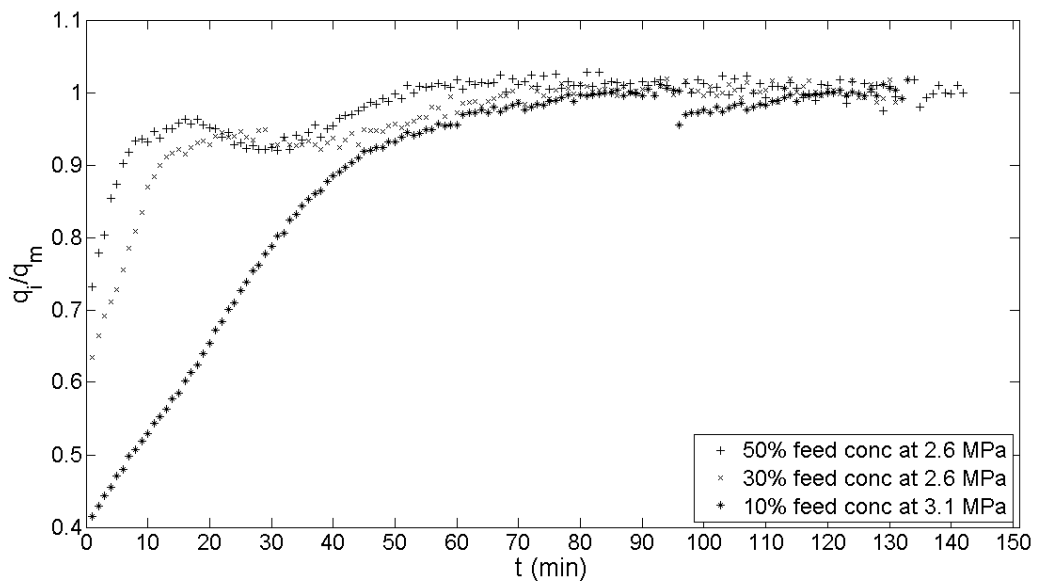


**Figure 5.68. Plot of normalised concentration against time for the non-linear region of the CO<sub>2</sub> accumulation at a specific point for Zeolite 13X at 2.6 MPa (3.1 MPa for 10% feed concentration).**

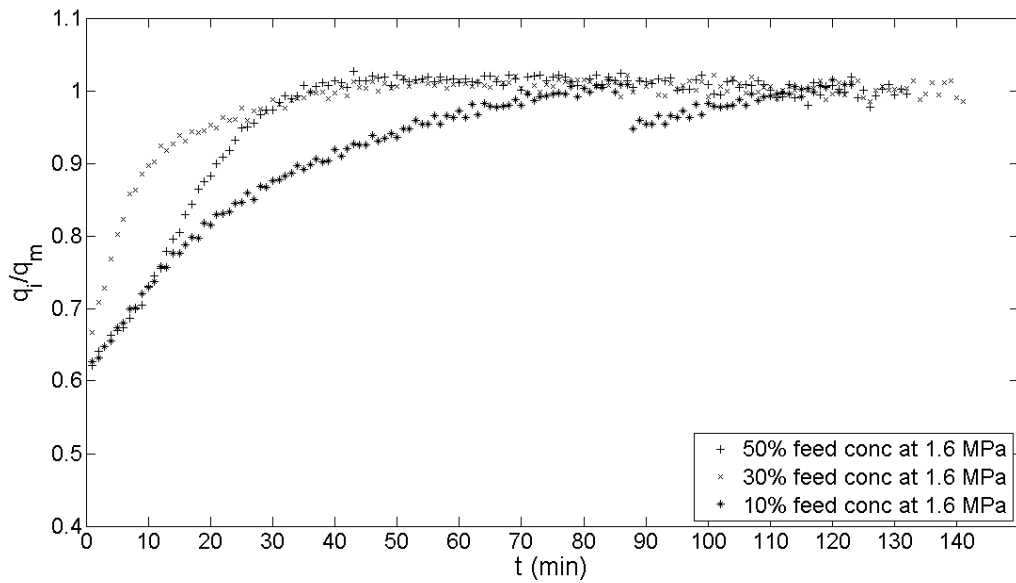


**Figure 5.69. Plot of normalised concentration against time for the non-linear region of the CO<sub>2</sub> accumulation at a specific point for Zeolite 13X at 1.6 MPa.**

It is thought that these plots show the secondary uptake of CO<sub>2</sub> molecules as explained in section 2.9.5. Once the initial, almost instantaneous, adsorption of CO<sub>2</sub> onto the surface of the adsorbent occurs the outer surface of the adsorbent becomes saturated. Over time the molecules on the outer surface of the adsorbent will diffuse into the pores leaving empty sites on the surface which will attract more molecules from the gas phase. This secondary uptake is slower than the initial rapid surface adsorption and the rate will decrease as the internal sites become occupied making it more difficult for surface molecules to diffuse through. Once all of the internal and external sites are occupied the system is at equilibrium and the net uptake will be zero. The figures show the general trend described here with decreasing rate of CO<sub>2</sub> uptake as time passes until saturation is reached. By accounting for the dead time correction the accumulation curves for Zeolite 13X at 2.6 MPa for 50% and 30% feed concentrations would be the sharpest implying that the MTZ progresses slowly enough that the majority of the

secondary internal adsorption would happen in the MTZ. However, the curves for 10% feed concentration for Activated Carbon at 2.6 MPa and Zeolite 13X at both 3.1 and 1.6 MPa show very gradual curves implying that the internal adsorption is the process dominating the shape of the accumulation curve. In the future an interesting direction of study would be to analyse the shape of these curves quantitatively to demonstrate numerically the relationship between the primary and secondary stages of adsorption.

#### **5.3.4 Mass Transfer Zone**

This section of the image analysis is to determine the ability of the imaging technique to investigate the shape of the adsorption front and in turn the size of the MTZ. As explained previously a known problem already encountered in this image analysis is the effect of axial smoothing on the shape of the concentration profiles. This does mean that absolute MTZ lengths and a defined shape cannot be concluded from the image data alone but this analysis should provide an idea of the potential of this technique for future studies as discussed in section 6.2. Figure 5.70 to Figure 5.73 show central cross sectional images along the length of the column for each experimental run at 20 minutes. Each figure shows the three images of 50%, 30% and 10% feed concentration for the specified adsorbent and system pressure and with the pixel intensities normalised so that a pixel at maximum intensity represents a saturation percentage of 100%. Underneath the images is a profile indicating the distribution of  $^{11}\text{CO}_2$  along the column as a percentage of its maximum observed capacity. The saturation percentage profiles have been created by summing the pixel columns as described in section 5.3.1 and normalised so that the maximum value shows 100% saturation.

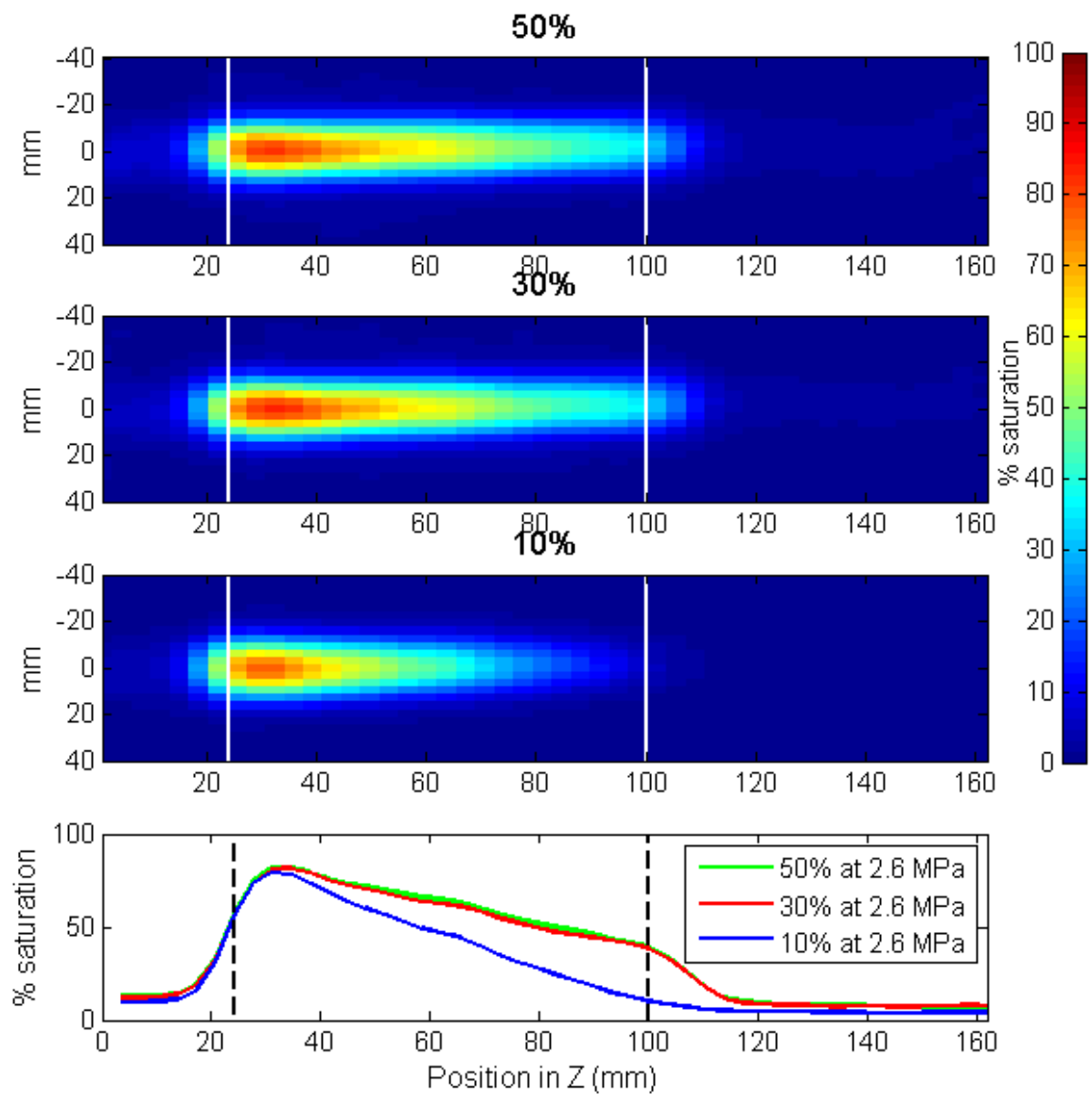


**Figure 5.70. Percent saturation of Activated Carbon at 2.6 MPa for feed concentrations 50%, 30% and 10% from top to bottom at 20 minutes into the experiment. The plot at the bottom of the figure shows a percent saturation profile along the column. The distributions for  $C_{max} = 50\%$  and  $30\%$  show a minimum of 40% saturation for the length of the adsorbent region implying a MTZ that is longer than the bed. The distribution for  $C_{max} = 10\%$  shows low saturation percentage at the exit of the bed implying a smaller MTZ.**

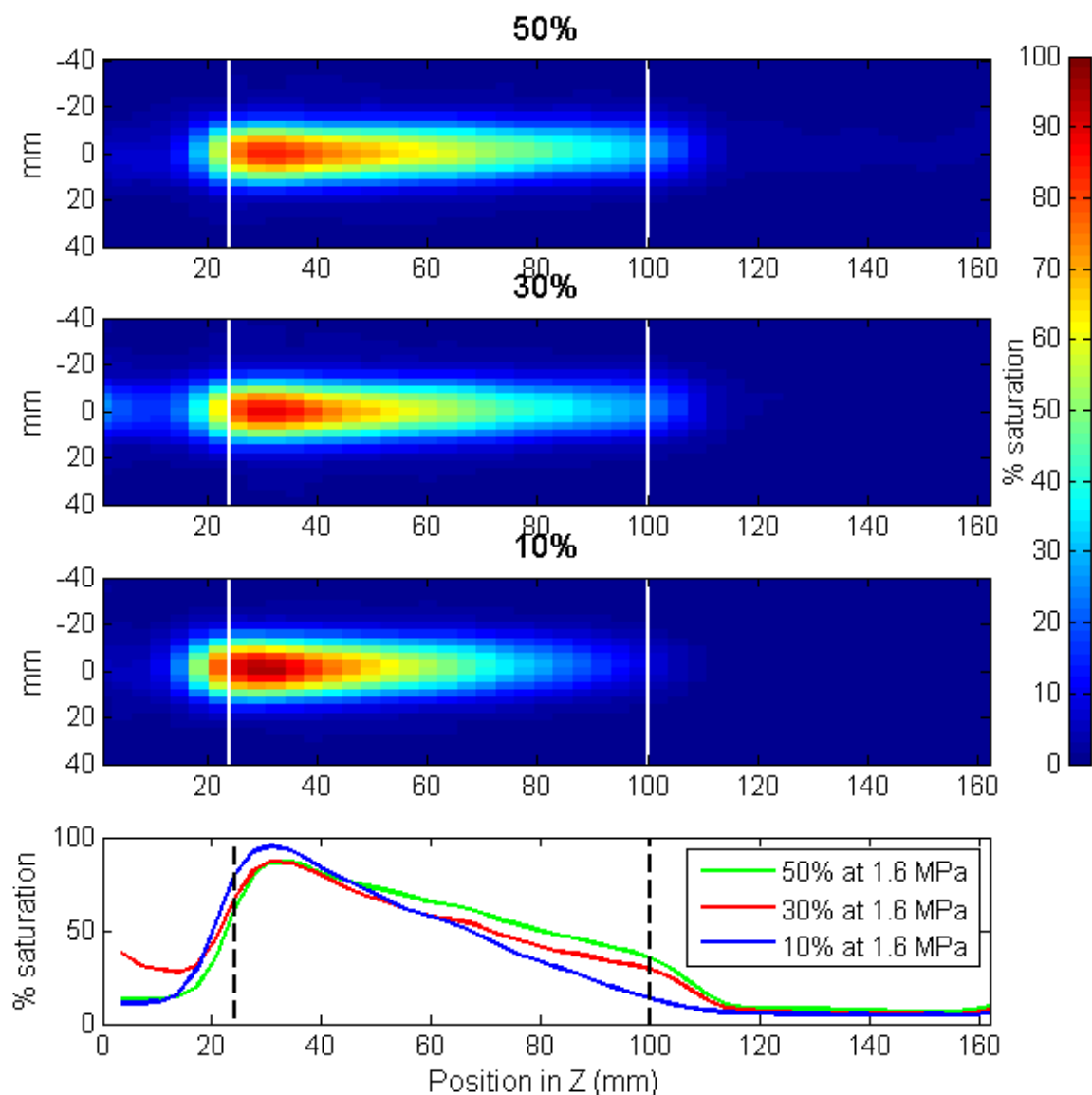


**Figure 5.71. Percent saturation of Activated Carbon at 1.6 MPa for feed concentrations 50%, 30% and 10% from top to bottom at 20 minutes into the experiment. The plot at the bottom of the figure shows a percent saturation profile along the column. The distributions for  $C_{max} = 50\%$  and  $30\%$  show a minimum saturation of about 35% at the exit of the adsorbent region implying a MTZ that is longer than the bed. The distribution for  $C_{max} = 10\%$  shows low saturation percentage at the exit of the bed implying a smaller MTZ. The saturation percentage at the inlet of the column is high at 95%.**

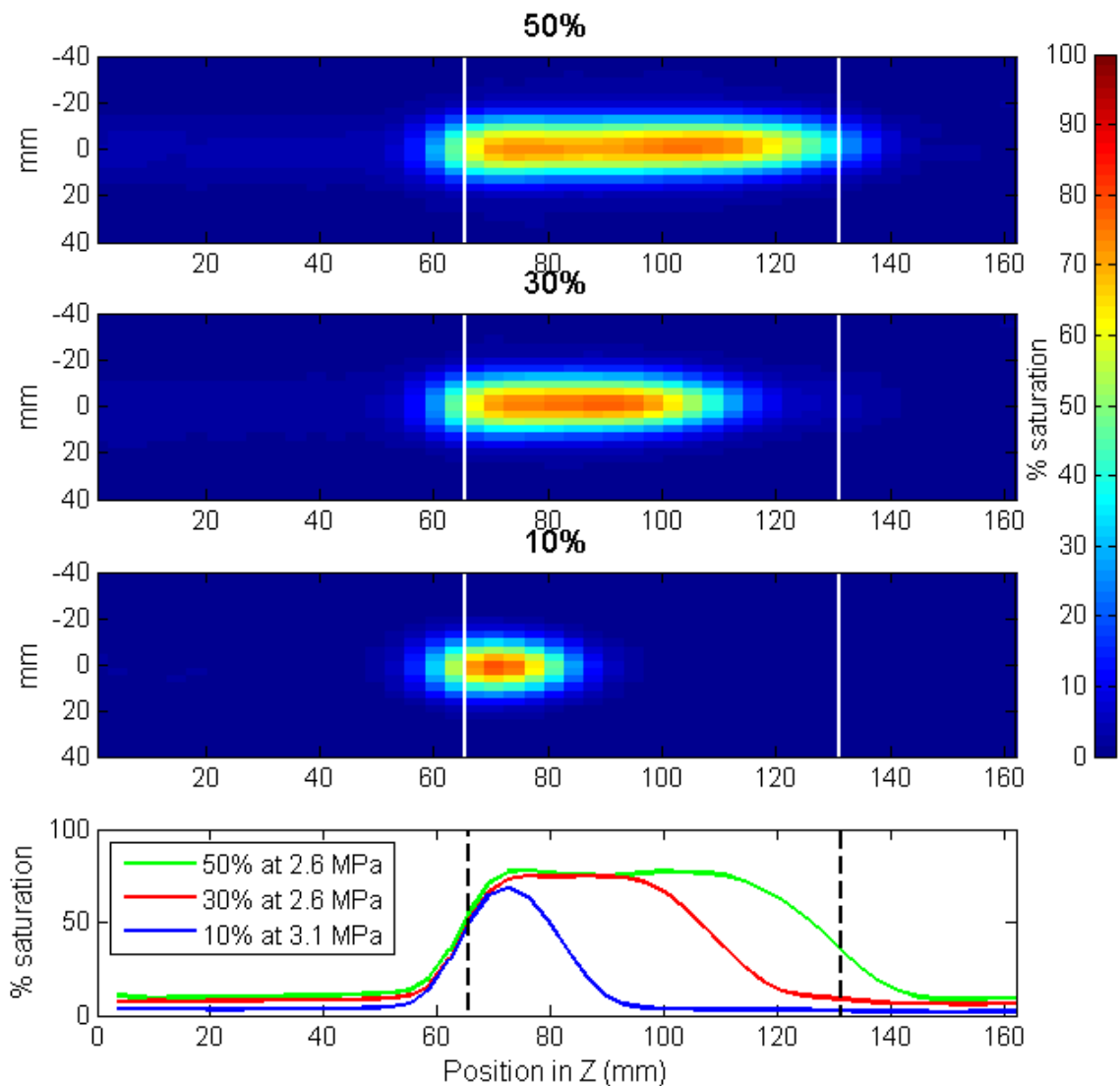


**Figure 5.72.** Percent saturation of Zeolite 13X at 2.6 MPa for feed concentrations 50%, 30% and 10% ( $P_{sys} = 3.1$  MPa for  $C_{max} = 10\%$ ) from top to bottom at 20 minutes into the experiment. The plot at the bottom of the figure shows a percent saturation profile along the column. All of the distributions plateau at a maximum of 75% saturation and each distribution shows a clear step down from 75% saturation to background level indicating a clear and relatively small MTZ.

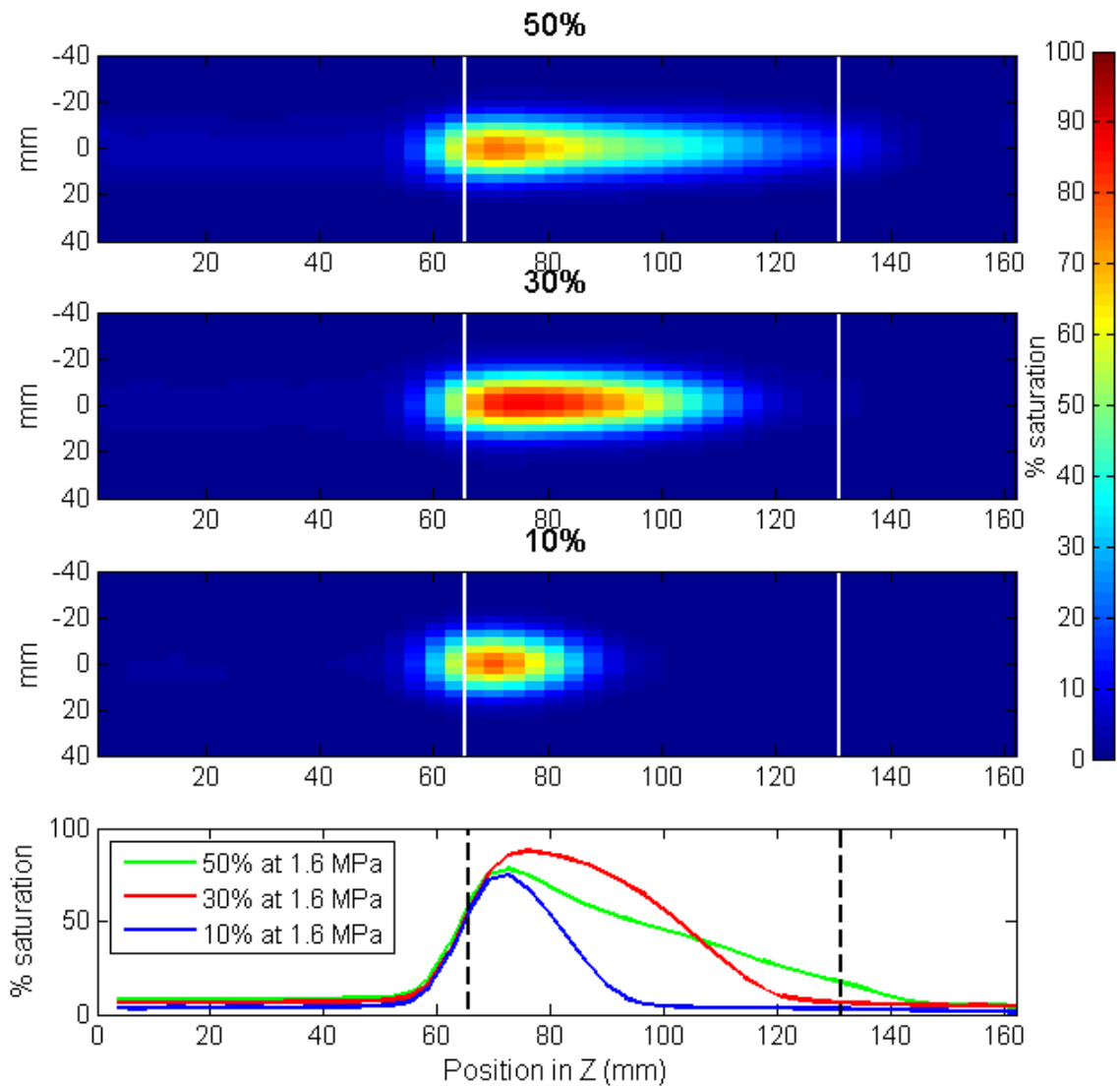


**Figure 5.73. Percent saturation of Zeolite 13X at 1.6 MPa for feed concentrations 50%, 30% and 10% from top to bottom at 20 minutes into the experiment. The plot at the bottom of the figure shows a percent saturation profile along the column. The profiles for 10% and 50% feed concentration have a maximum of 80% saturation at the inlet of the column. Unusually the profile for 30% feed concentration shows a higher percentage saturation of about 90% at the inlet which is expected to be due to considerable dead time correction for this data set.**

Figure 5.70 shows almost identical saturation percentage distribution along the column for 50% and 30% concentration at 20 minutes. From the images it is noted that the planes at the inlet of the column are only at 80% saturation yet  $^{11}\text{CO}_2$  has reached the exit at 40% saturation implying a MTZ comparable to the length of the bed. The image for 10% shows a more distinctive difference in occupancy between the inlet and outlet showing a relatively smaller MTZ. The occupancy at the inlet for each concentration is equal at 80% occupancy with 40% occupancy at the exit for 50% and 30% feed concentration.

Figure 5.71 shows that for the lower system pressure of 1.6 MPa the saturation percentage distributions for 50% and 30% are still very similar at 20 minutes. The occupancy at the inlet at these concentrations is 86% which gradually decreases to 35% for 50% feed concentration at 30% for 30% concentration. The occupancy profile for 10% feed concentration shows a high occupancy of 95% at the inlet which steadily decreases to 14% at the exit. This implies that the length of the MTZ for Activated Carbon at  $P_{\text{sys}} = 1.6 \text{ MPa}$  and  $C_{\text{max}} = 30\%$  and 50% is longer or comparable to the length of the adsorbent region of the column. The MTZ length of Activated Carbon at  $P_{\text{sys}} = 1.6 \text{ MPa}$  and  $C_{\text{max}} = 10\%$  is relatively small.

Figure 5.72 shows data obtained for Zeolite 13X at 2.6 MPa for 50% and 30% concentrations and 3.1 MPa for 10% feed  $\text{CO}_2$ . Unlike the plots for Activated Carbon the data presented here shows a clear and equal plateau at 75% saturation for feed concentrations 50% and 30%. There is a distinct drop from 75% to background level of 8% at different stages along the bed and the plots look more like what would be expected from theory implying a relatively small and distinct MTZ. As the MTZ appears

to progress along the column before saturation is reached this supports the discussion made in section 5.3.2.

Figure 5.73 shows similar initial saturation percentage of 75% at the column inlet for 50% and 10% feed concentrations at 1.6 MPa system pressure for Zeolite 13X. The occupancy of the run with CO<sub>2</sub> feed concentration 30% appears to be greater than the other two systems; however this is expected to be due to the dead time correction as the activity of the gas used was too high and saturated the PET camera. As the half-life of <sup>11</sup>CO<sub>2</sub> is about 20 minutes it is expected that any subsequent images will not be affected by this as the number of emissions will be halved. The distribution for 50% does not show a clear step down in occupancy which would indicate the front of the MTZ, instead a gradual decrease from 75% occupancy to 18% from inlet to outlet is observed.

By analysing the distribution of the occupancy along the column observations have been made about the nature of the adsorption process for each of the experimental conditions. An initial comparison between the two adsorbent materials at 20 minutes show that for Activated Carbon the general distribution of adsorbed CO<sub>2</sub> along the column shows a maximum occupancy at the inlet of the column with the remaining adsorbed molecules dispersed with gradually decreasing quantity to the end of the column. It is difficult to discern the MTZ from the diffusion and internal adsorption that follows the MTZ. This coincides with the shape of the breakthrough curves for Activated Carbon which show very fast breakthrough times and relatively long times to full saturation which indicates a less efficient system, therefore an undefined MTZ is not unexpected. Zeolite 13X, on the other hand, shows a more clearly defined MTZ, particularly for system pressure 2.6 MPa. This indicates a more efficient system, which

is backed up by the long breakthrough times and relatively short times to full saturation. There is a clearer distinction between the MTZ and the internal adsorption occurring after the passing of the MTZ.

#### **5.3.4.1 Length of MTZ**

This section provides a visual comparison of the MTZ lengths calculated in section 5.3.3 and the actual percent saturation of the column at 10 minutes, 20 minutes and 30 minutes into the run. Figure 5.74 to Figure 5.85 show the calculated MTZ for each run superimposed on the occupancy plots and progressing at the calculated velocities.

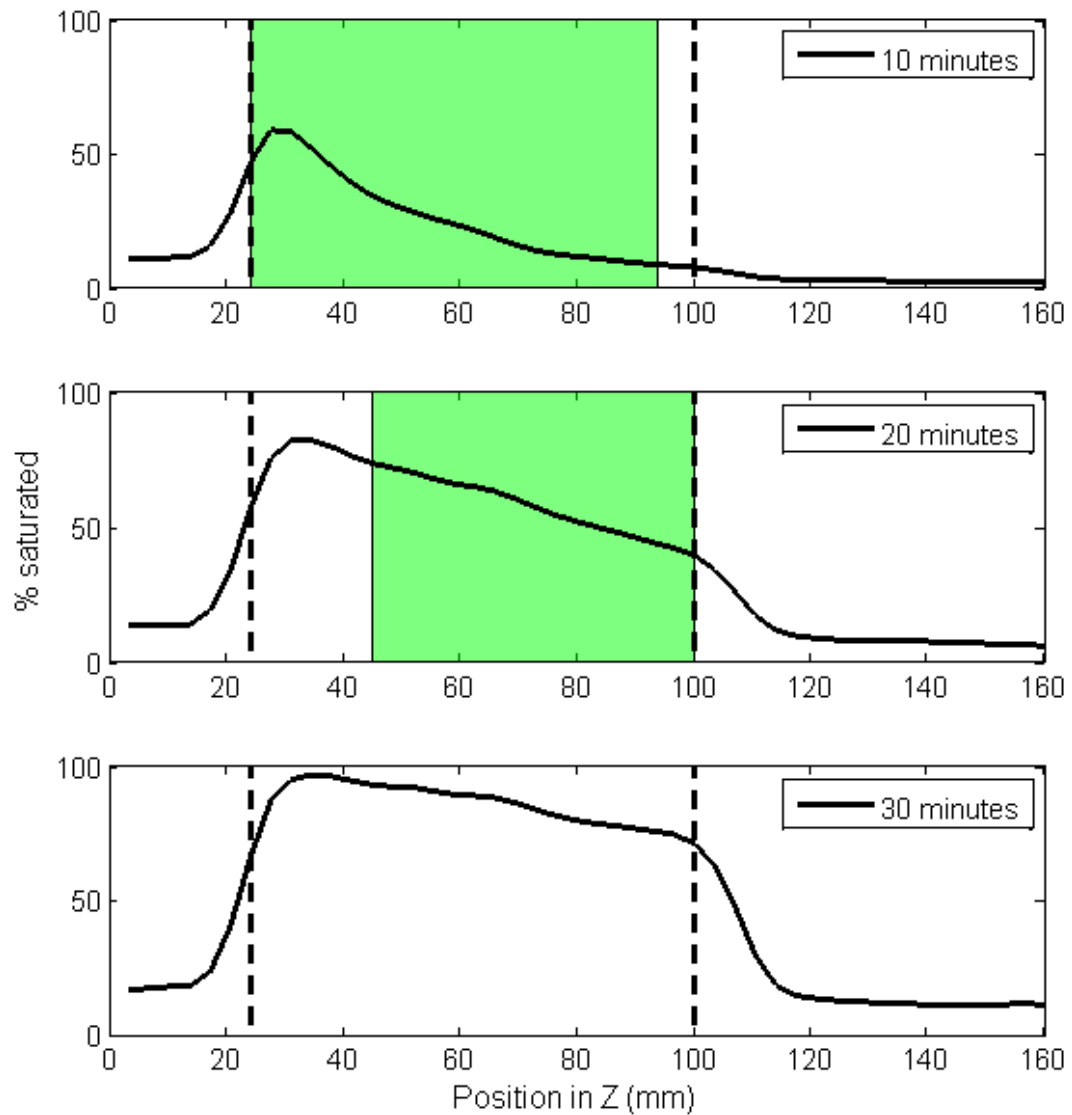


**Figure 5.74. Occupancy plots with superimposed calculated MTZ for Activated Carbon at 2.6 MPa for 50% feed concentration. The calculated MTZ length is 104 mm (30 planes) which is 25 mm longer than the length of the adsorbent region and the adsorption front velocity is 5.78 mm min<sup>-1</sup>.**

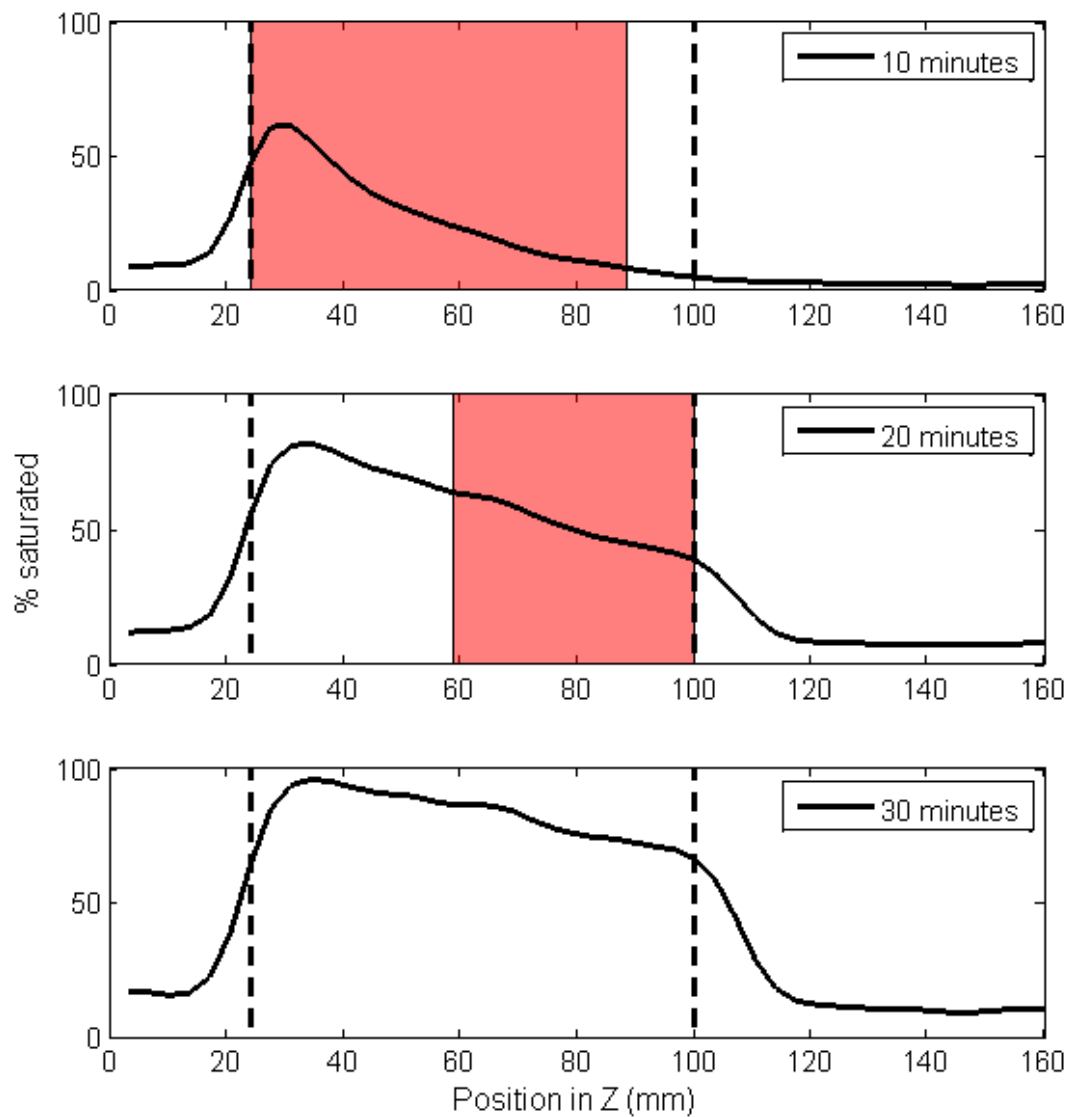


**Figure 5.75. Occupancy plots with superimposed calculated MTZ for Activated Carbon at 2.6 MPa for 30% feed concentration. The calculated MTZ length is 78 mm (23 planes) which is about the same length as the adsorbent region and the adsorption front velocity is 4.90 mm min<sup>-1</sup>.**

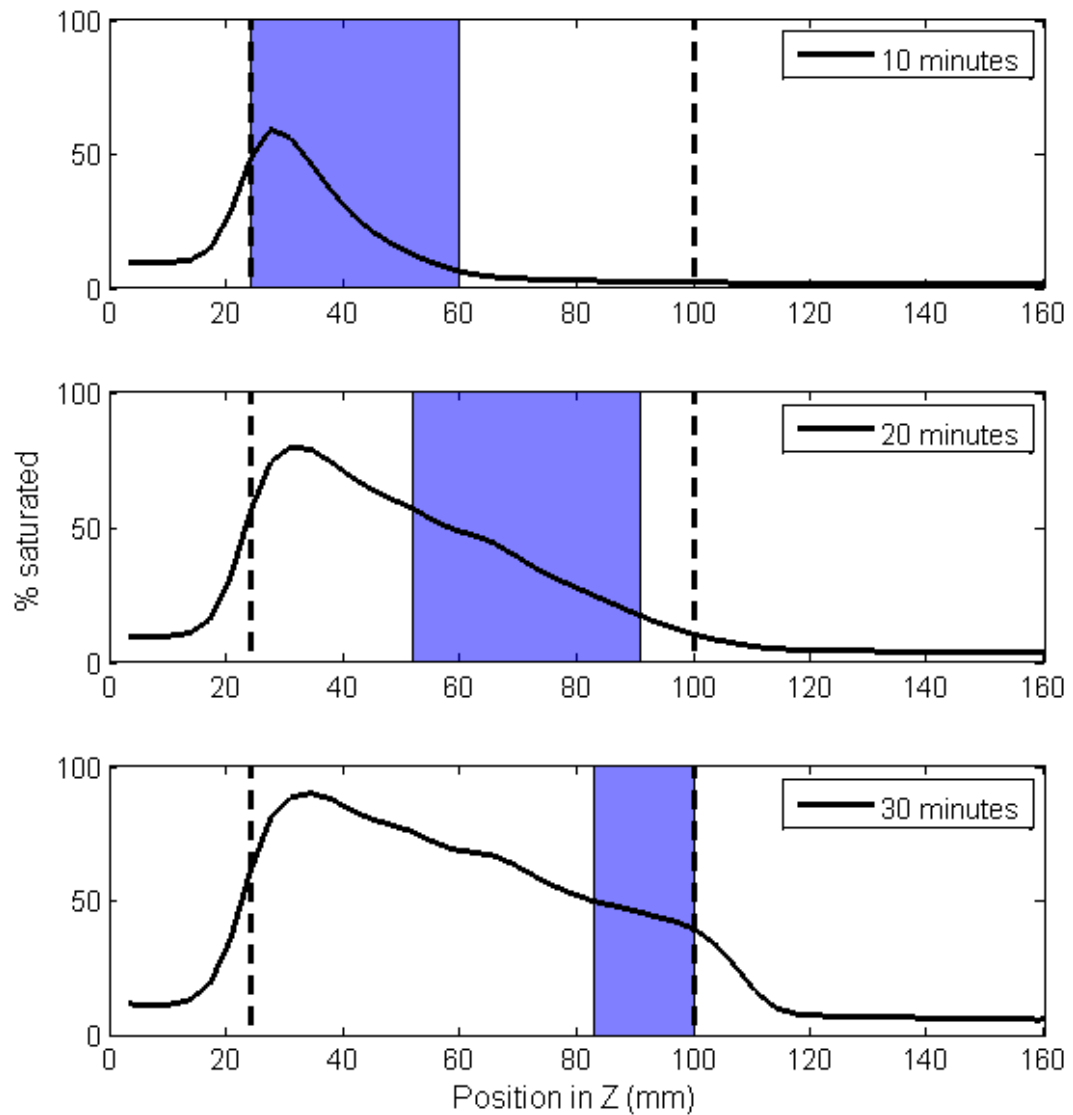


**Figure 5.76. Occupancy plots with superimposed calculated MTZ for Activated Carbon at 2.6 MPa for 10% feed concentration. The calculated MTZ length is 39 mm (11 planes) which is about half the length of the adsorbent region and the adsorption front velocity is  $2.62 \text{ mm min}^{-1}$ .**

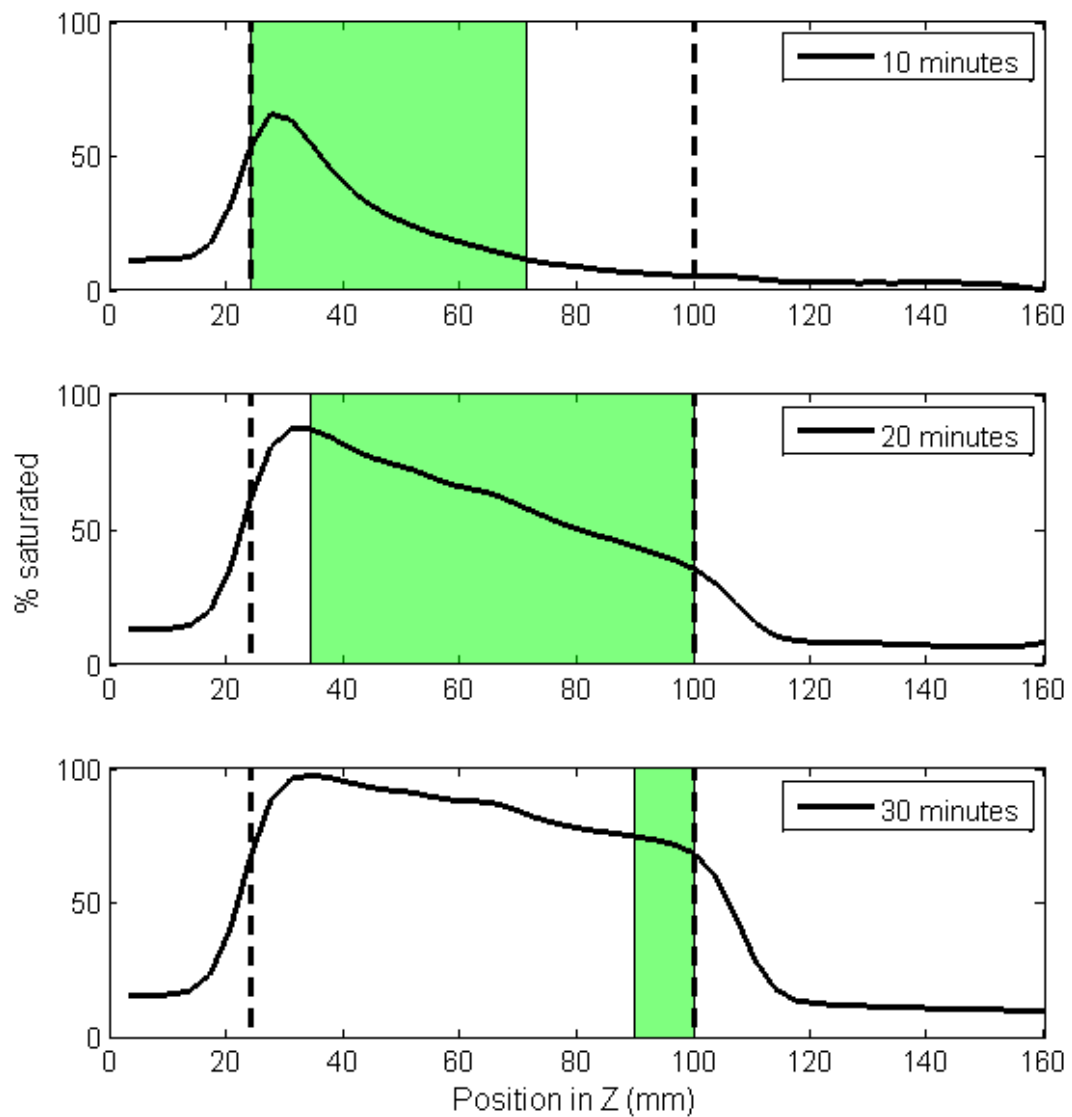


**Figure 5.77. Occupancy plots with superimposed calculated MTZ for Activated Carbon at 1.6 MPa for 50% feed concentration. The calculated MTZ length is 92 mm (27 planes) which is 13 mm longer than the adsorbent region and the adsorption front velocity is  $5.40 \text{ mm min}^{-1}$ .**

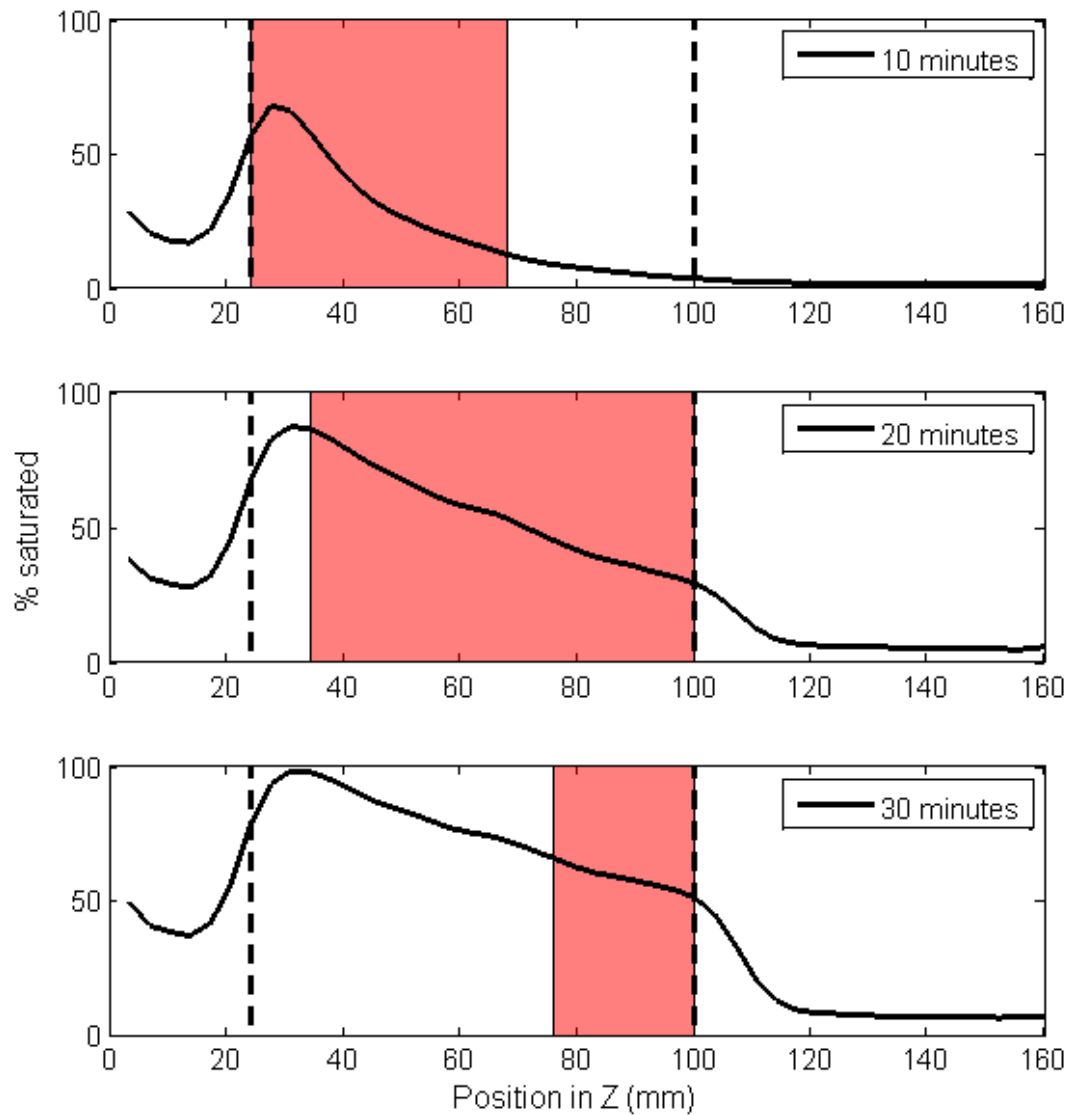


**Figure 5.78. Occupancy plots with superimposed calculated MTZ for Activated Carbon at 1.6 MPa for 30% feed concentration. The calculated MTZ length is 74 mm (22 planes) which is 4 mm longer than the adsorbent region and the adsorption front velocity is  $4.14 \text{ mm min}^{-1}$ .**

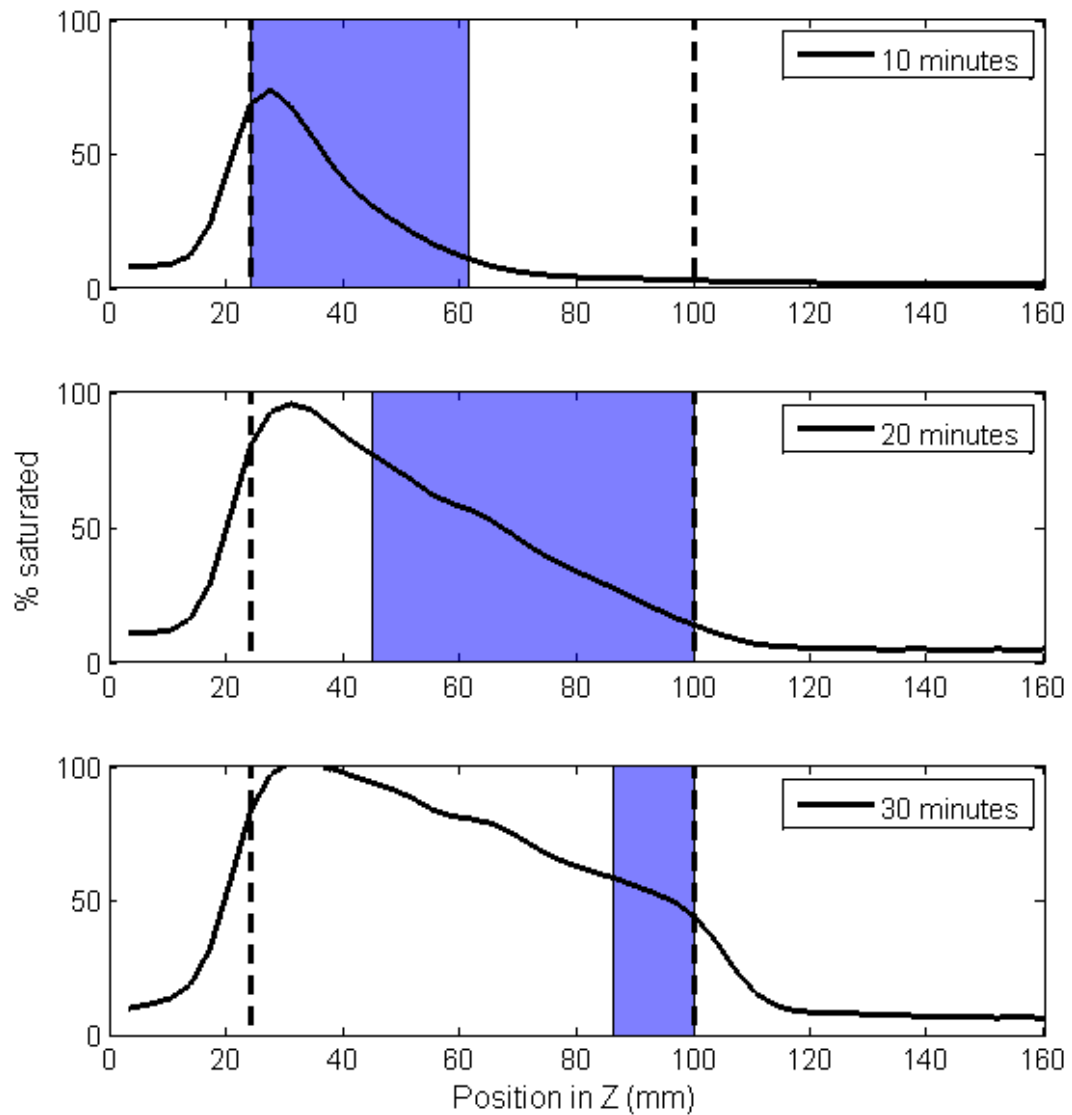


**Figure 5.79. Occupancy plots with superimposed calculated MTZ for Activated Carbon at 1.6 MPa for 10% feed concentration. The calculated MTZ length is 58 mm (14 planes) which is about 83% of the length of the adsorbent region and the adsorption front velocity is 3.05 mm min<sup>-1</sup>.**

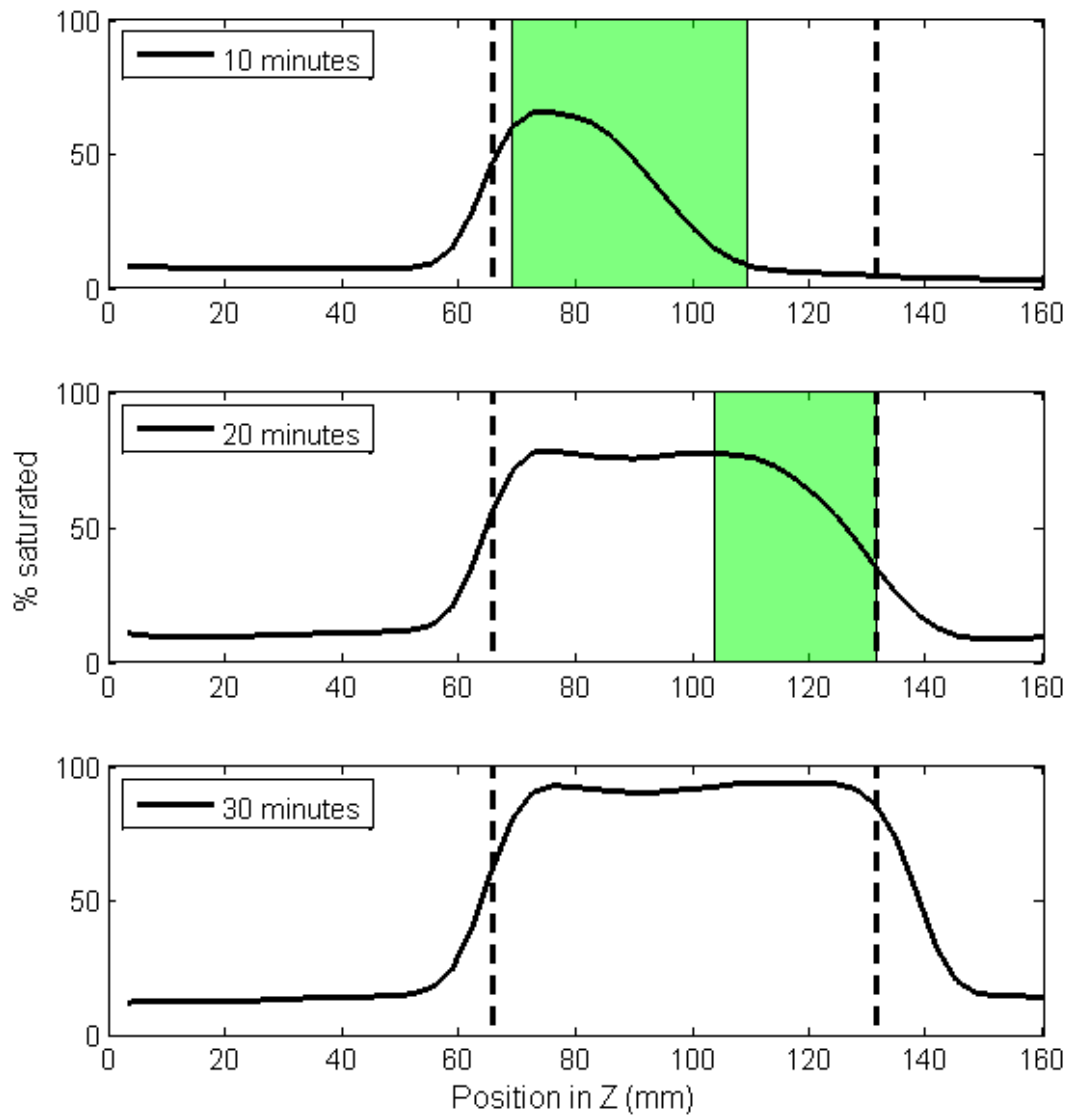


**Figure 5.80. Occupancy plots with superimposed calculated MTZ for Zeolite 13X at 2.6 MPa for 50% feed concentration. The calculated MTZ length is 40 mm (11 planes) which is about 57% of the adsorption region and the adsorbent front velocity is  $3.05 \text{ mm min}^{-1}$ .**

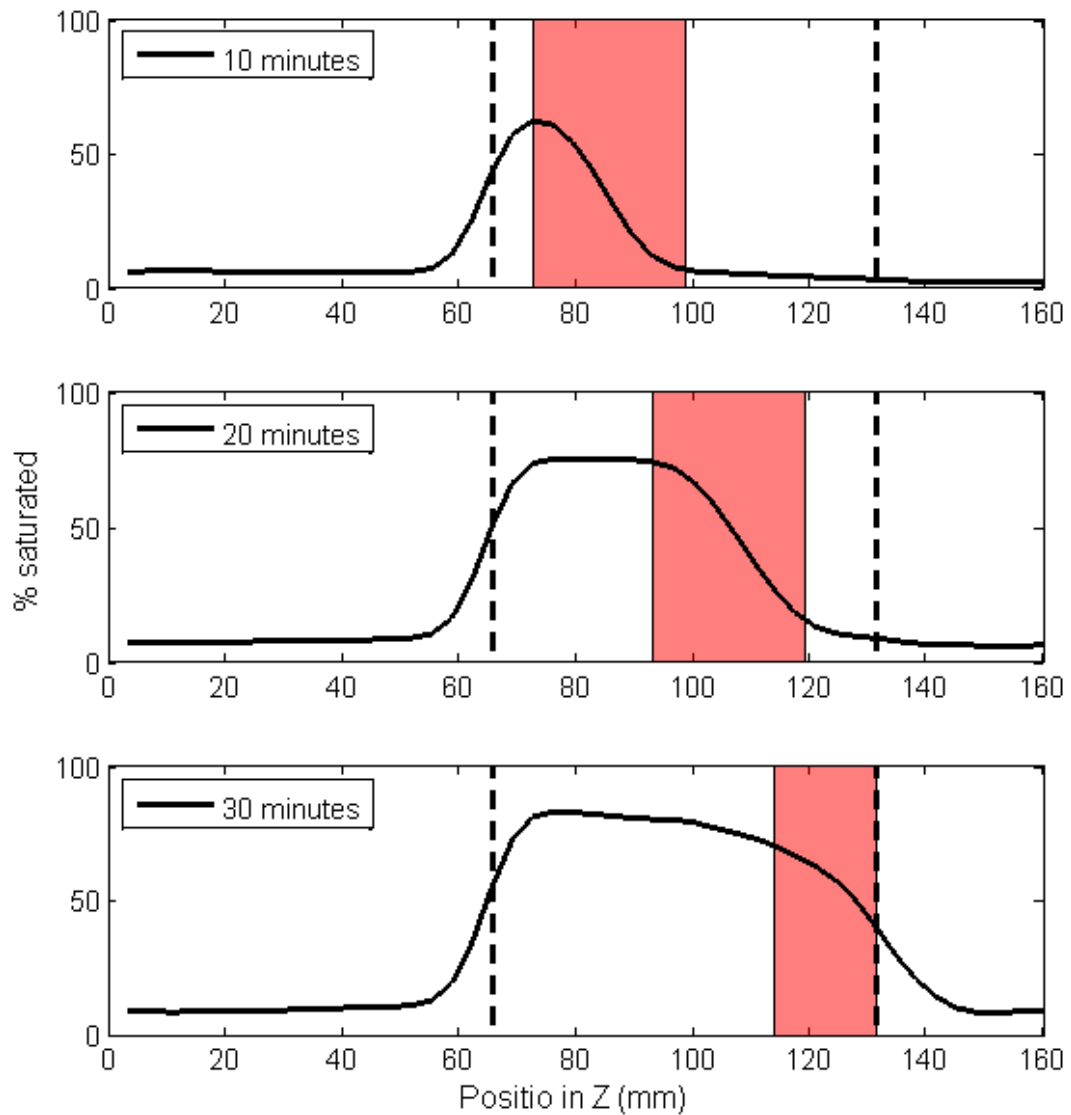


**Figure 5.81. Occupancy plots with superimposed calculated MTZ for Zeolite 13X at 2.6 MPa for 30% feed concentration. The calculated MTZ length is 26 mm (7 planes) which is about 37% of the adsorbent region and the adsorption front velocity is  $2.32 \text{ mm min}^{-1}$ .**

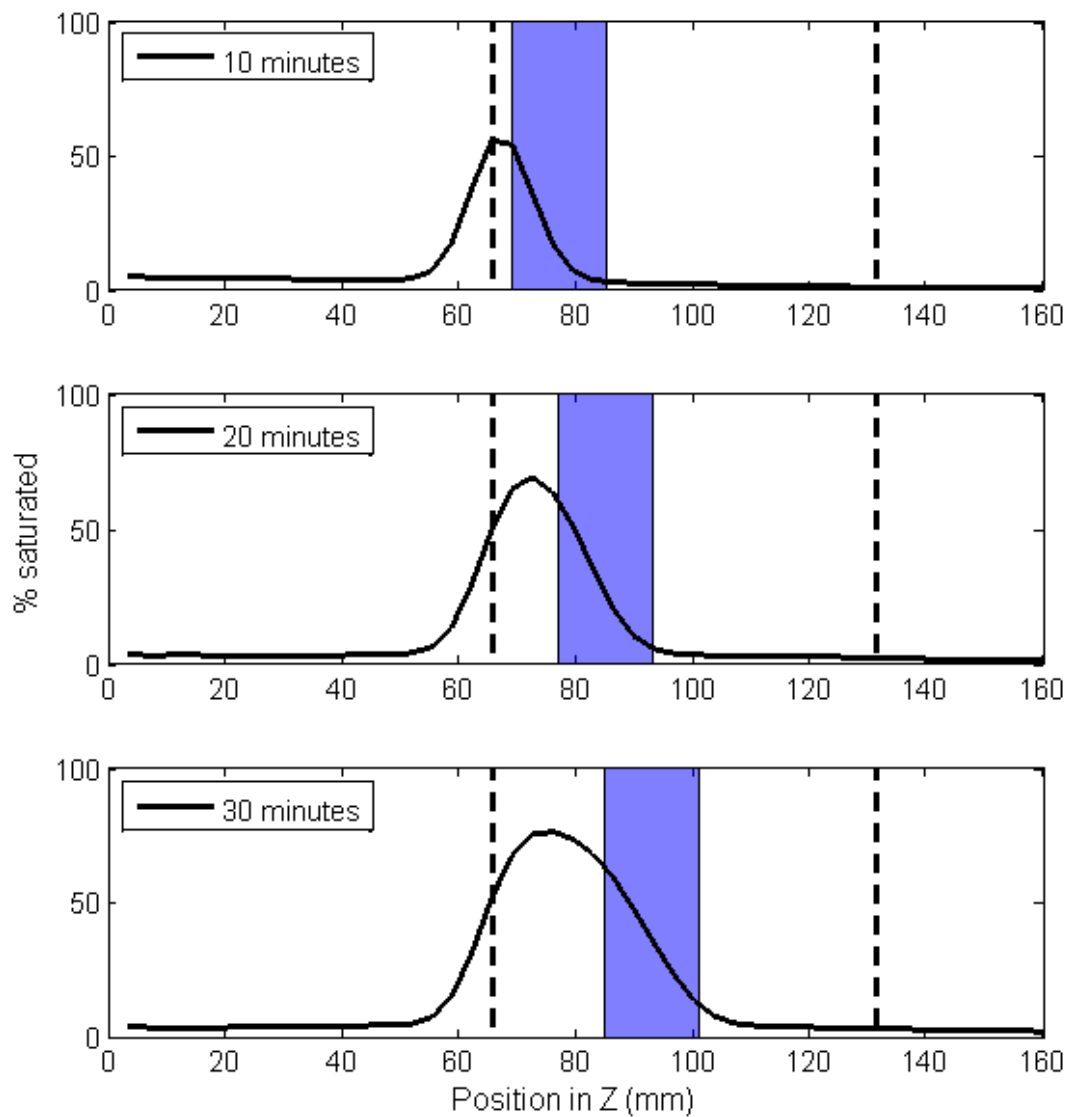


**Figure 5.82. Occupancy plots with superimposed calculated MTZ for Zeolite 13X at 3.1 MPa for 10% feed concentration. The calculated MTZ length is 16 mm (5 planes) which is about 23% of the adsorbent region and the adsorption front velocity is  $0.78 \text{ mm min}^{-1}$ .**

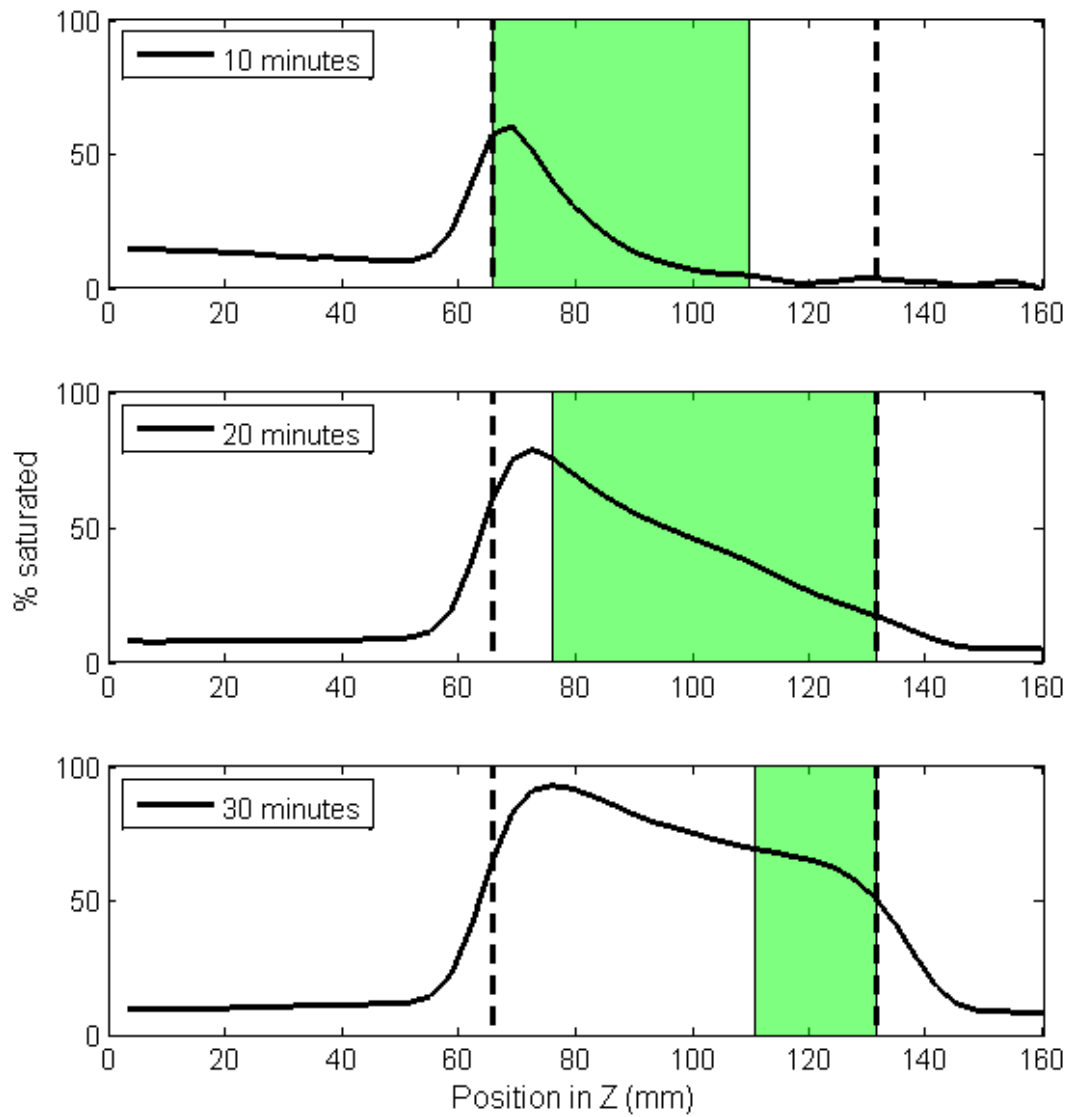


**Figure 5.83. Occupancy plots with superimposed calculated MTZ for Zeolite 13X at 1.6 MPa for 50% feed concentration. The calculated MTZ length is 68 mm (20 planes) which is about the same length of the adsorbent region (70 mm) and the adsorption front velocity is  $5.95 \text{ mm min}^{-1}$ .**

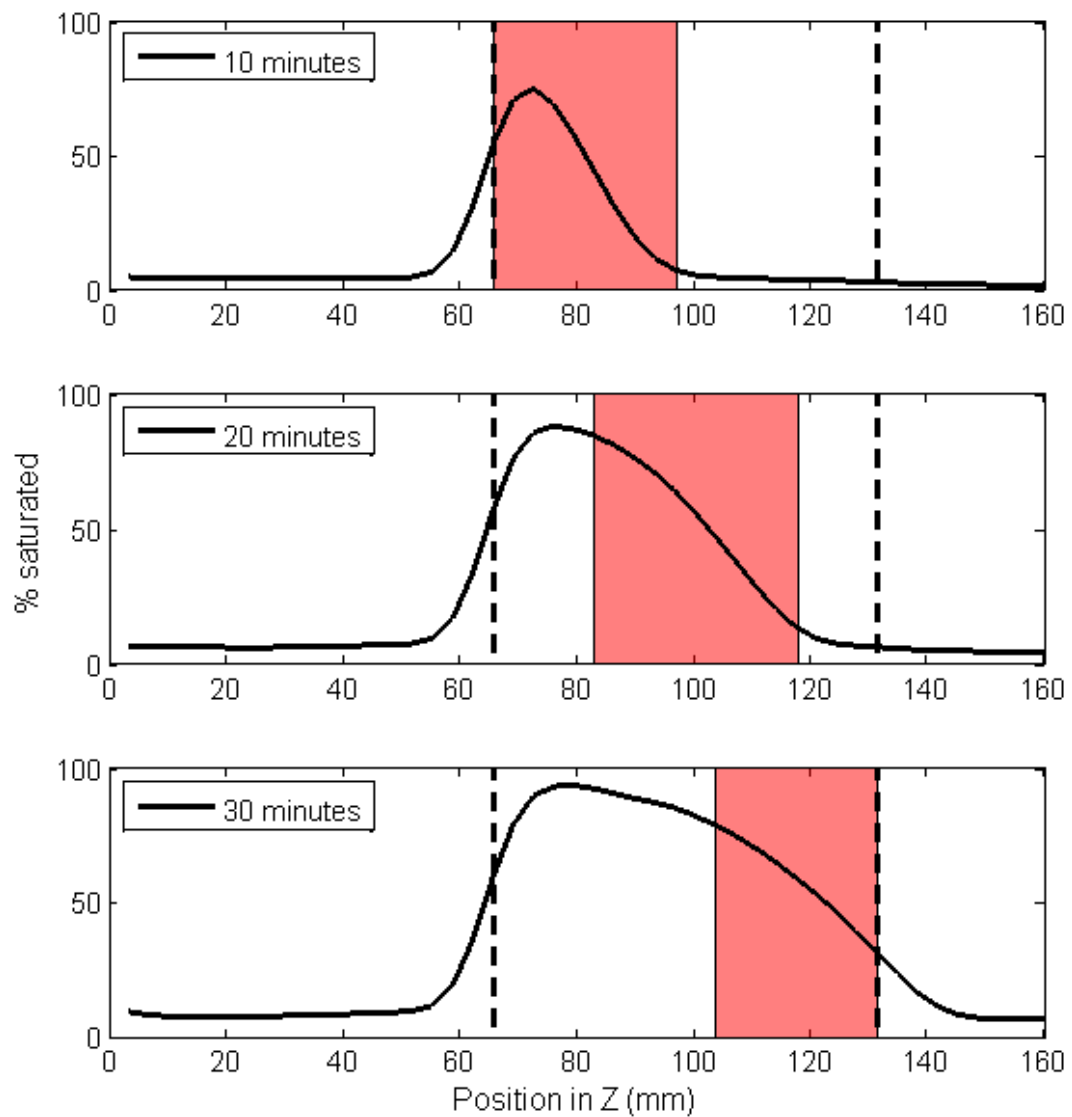


**Figure 5.84. Occupancy plots with superimposed calculated MTZ for Zeolite 13X at 1.6 MPa for 30% feed concentration. The calculated MTZ length is 35 mm (10 planes) which is half the length of the adsorbent region and the adsorption front velocity is  $2.07 \text{ mm min}^{-1}$ .**

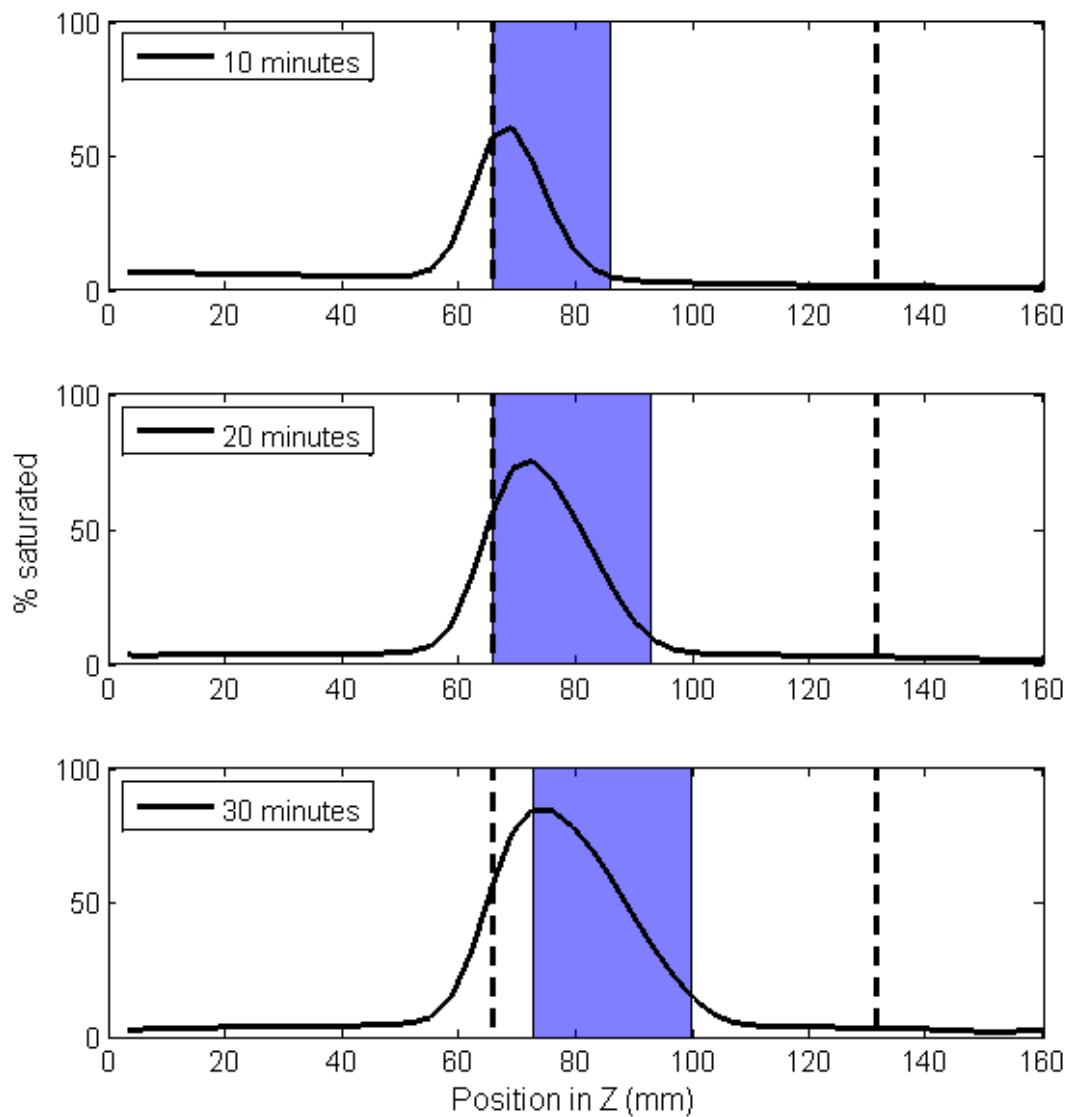


**Figure 5.85. Occupancy plots with superimposed calculated MTZ for Zeolite 13X at 1.6 MPa for 30% feed concentration. The calculated MTZ length is 27 mm (9 planes) which is about 39% of the adsorbent region and the adsorption front velocity is  $0.71 \text{ mm min}^{-1}$ .**

The figures for Activated Carbon show a common trend of indistinguishable MTZ from the occupancy plots as the amount of CO<sub>2</sub> appears to be dispersed along the column at a steady gradient from a maximum at the inlet along the length of the column. Each of the calculated MTZ lengths for Activated Carbon is greater than the length of the adsorbent region, 69 mm apart from the results for conditions 2.6 MPa and 10% CO<sub>2</sub> and 1.6 MPa and 10% CO<sub>2</sub> which were calculated to be 39 mm and 58 mm respectively. These large MTZ's imply an inefficient system as CO<sub>2</sub> is able to progress quite far down the column past a large number of empty vacancies before being adsorbed. The increase in saturation percentage at the inlet of the column for the first 30 minutes of each of the Activated Carbon runs provides insight into what is assumed to be the dominating internal uptake of CO<sub>2</sub>. The large calculated MTZ lengths appear to be reasonable as they appear to progress at a similar rate to the leading edge of the occupancy plots and they are consistent with previous conclusions which stated an expected MTZ length comparable to or larger than the length of the adsorbent region, however it is not possible at this time to state conclusively that the actual length of the MTZs are within the error bounds of the calculated values. To perform a more thorough investigation it would be desirable to use a longer column to provide more opportunity to observe the full length of the MTZ progress through the bed before reaching breakthrough.

Unlike for Activated Carbon the figures for Zeolite 13X show more clearly defined MTZ along the column at the specified time intervals with the exception of the run with conditions 1.6 MPa and 50% CO<sub>2</sub>. The plots for these conditions show behaviour similar to that seen in the Activated Carbon data. As seen in section 5.3.1 there is observable dead time correction for this set of data shown in the first two half-lives of

the  $^{11}\text{CO}_2$  (~ 40 minutes). This would affect the normalisation process in the image reconstruction protocol as the detection saturated image frames will be normalised to a limited maximum count rate that will not vary with varying concentration until the  $^{11}\text{CO}_2$  decays to an activity below the camera saturation threshold. The rest of the datasets, however, give confidence to the calculated progression of MTZs for Zeolite 13X as they are located at the point of declining occupancy at each time interval. The lengths of the MTZ also seem reasonable as they are of comparable width to the occupancy progression front.

## **5.4 DISCUSSIONS**

The results presented in this chapter have investigated the feasibility of using a radioactive gas imaging technique to study  $\text{CO}_2$  adsorption in a packed bed. The main aims of the study was to determine whether the proposed technique is capable of performing comparable measurements to a  $\text{CO}_2$  analyser and to investigate the capabilities of using the technique to non-invasively gain extra information about the kinetics inside the column.

The first stage of the results analysis was to present and discuss results obtained using a  $\text{CO}_2$  analyser to provide verification for results obtained using the imaging technique. From the comparison of calculated capacity values obtained experimentally to theoretical values produced using the Toth equation and by giving the approximate nature of these calculated capacities due consideration it may be concluded that adsorption was the process being observed in this study. The breakthrough curves for each run verify this conclusion as the time to breakthrough and the shape of the curves

can be justified by the theory of adsorption. This conclusion has allowed the image data acquired using the PET camera to be effectively analysed.

The breakthrough data obtained using the imaging technique provide reasonably accurate calculations of capacity which are comparable to the results obtained using the CO<sub>2</sub> analyser and are reasonably consistent with the expected theoretical values calculated using the Toth model. The shape of the breakthrough curves have been compared to those produced using analyser data and good similarity was generally seen for Activated Carbon, however the curves for Zeolite 13X showed unexpected inconsistencies which lead to further investigation of the image data. The calculated times to breakthrough and saturation for both measurement techniques generally showed good linear relationships once plotted against each other and showed the expected trend of increasing time with decreasing concentration.

The further image analysis shows the imaging technique to be capable of producing concentration profiles in the column. Although the results presented here are affected by axial smoothing the potential to create quantitative concentration profiles in future work is apparent. The image data was also analysed to calculate the velocity of the adsorption front along the length of the column and corresponding CO<sub>2</sub> accumulation at a specific location. A directly proportional relationship between the velocity of the MTW and the initial linear uptake of CO<sub>2</sub> onto the surface of the adsorbent was established and the regions of the accumulation curve dominated by internal adsorption were identified. By multiplying the duration of the linear uptake by the velocity of the MTW a MTZ length for each experiment was calculated and superimposed onto occupation plots at 10 minute intervals to determine the reasonability of the calculation. The occupation plots for Activated Carbon show the

shape of the MTW to be undefined and indistinguishable from the secondary internal adsorption. However, the plots for Zeolite 13X give confidence to the calculated MTZ properties as the length and progression rate are comparable to the apparent front of the occupation distribution.

## 6 CONCLUSIONS AND FUTURE WORK

This chapter summarises the overall conclusions drawn from the work performed here and possible future routes of investigation are discussed.

### 6.1 CONCLUSIONS

Preliminary studies were carried out to determine the capabilities of SPECT and PET for the study of chemical flow processes. SPECT was used to image a pseudo 2D fluidised bed where it was expected that the fluidisation regime could be characterized by calculating bubble size and velocity. However, over the course of the study it was discovered that the gas flow supplied via the  $^{81}\text{Kr}^m$  generator was not sufficiently high enough to fluidise the bed so an additional supply of compressed air was required. Although this resulted in the dispersion of  $^{81}\text{Kr}^m$  through the solid particles being imaged rather than the flow of bubbles through the bed problems with the experimental design were identified and lead to three main recommendations for any future multiphase studies: 1). The  $^{81}\text{Kr}^m$  gas should be mixed with the bulk gas phase before introduction to the multiphase system, 2). The activity of the  $^{81}\text{Kr}^m$  generator would need to be increased as the ratio of meaningful statistical data to background noise was not as high as desired, and 3). Extra shielding around the  $^{81}\text{Kr}^m$  generator as it needs to be close to the system due to the short half-life of 13.1 s and background noise needs to be reduced. For a more detailed discussion about the results of the fluidised bed preliminary study see section 3.1.1.3. The recommendations led to the successful imaging of a bubble column where the detection rate threshold of the gamma camera was tested, a relationship between bubble size and count rate was investigated and a method of measuring bubble velocity was developed. As the

residence time of the bubbles rising through the column was comparable to the half-life of  $^{81}\text{Kr}^m$  the reduction in detected events due to decay is clear. It was concluded that by measuring the  $^{81}\text{Kr}^m$  concentration in the feed gas and the initial activity then quantitative measurements could be performed using the gamma camera and a defined relationship between counts detected and bubble volume could be established, however the short half-life would make these measurements difficult. Section 3.1.2.3 provides a more detailed discussion about the conclusions drawn.

During the preliminary steady state PET study a standard imaging protocol was put in place and a data analysis technique was developed using MATLAB. This directly led to the successful imaging of  $^{11}\text{CO}_2$  flow through an adsorption column at low pressure (1MPa). A preliminary adsorption run using Zeolite 13X at 3 MPa and a  $\text{CO}_2$  feed concentration of 27% was performed and a  $\text{CO}_2$  analyser was used to monitor the  $\text{CO}_2$  concentration at the outlet allowing an optimal imaging frame acquisition rate of 1 frame per minute and a maximum total session duration of 175 minutes to be determined. Although the resulting images showed blurring this was an expected result of the spatial resolution and image reconstruction and it was concluded that with prior sensitivity and resolution testing this could be accounted for.

The conclusions drawn from the preliminary PET studies proved that it would be possible to image  $\text{CO}_2$  adsorption using the standard imaging protocol and image analysis technique developed during the feasibility studies and an experimental rig was developed to withstand high pressure. The sensitivity and resolution tests determined that the PET camera had reasonably uniform axial sensitivity and an axial spatial resolution of 10 mm and transverse resolution of 10 mm. The initial stage of the adsorption results analysis was to compare the results obtained from the imaging

system to the measurements from the CO<sub>2</sub> analyser, a commonly used breakthrough and capacity measurement technique. The equivalent of a breakthrough curve was produced from the image data by plotting the detected number of events at a specific location at the outlet of the adsorbent region and normalising this with respect to CO<sub>2</sub> feed concentration. This allowed a direct comparison between the image and analyser data and provided a means of verifying the imaging system as a measurement technique. The capacity values calculated using both techniques were very similar and well within each other's error bounds. These values were also compared to the Toth model to determine comparability with the theory and both measurement techniques proved to show good similarity. By comparing the shapes of the breakthrough curves from both techniques the results obtained for Activated Carbon showed good similarity with comparable times to breakthrough and saturation as indicated by the almost directly proportional trends displayed in Figure 5.26 and Figure 5.30. The results for Zeolite 13X, however, show inconsistencies between the image and analyser breakthrough curves, particularly observed for system pressure 1.6 MPa, despite the similar calculated capacities (Figure 5.36 and Figure 5.40). The conclusion drawn from the measurement technique comparison was that the imaging technique has been verified as a comparable measurement technique to the CO<sub>2</sub> analyser, although it would be recommended to continue using the CO<sub>2</sub> analyser simultaneously to ensure the reliability of the results.

The true extent of the capabilities of the imaging technique to observe the process within the column was discussed in section 5.3. Profiles of detected counts, referred to as intensity, were created for the length of the column for each run and were representative of the CO<sub>2</sub> concentration profile within the bed following the assumption

that the number of events detected is directly proportional to the concentration of  $^{11}\text{CO}_2$  once corrected for geometry, sensitivity, decay etc. This resulted in an investigation into the process characteristics that define the mass transfer kinetics within the bed. The velocity of the adsorption front was calculated and the variation was discussed with respect to the feed concentration of  $\text{CO}_2$  and system pressure. As expected from the Toth model it was found that pressure has very little effect on the velocity of the adsorption front but the influential factor was the feed flow rate of  $\text{CO}_2$ . With increasing  $\text{CO}_2$  feed concentration a linear increase in velocity was observed.

The net accumulation of  $\text{CO}_2$  at a specific location within the column was also analysed and an initial linear increase was observed for each run followed by a gradually decreasing rate of accumulation resulting in an exponential curve as the amount of  $^{11}\text{CO}_2$  approached saturation. This was interpreted as a linear initial instantaneous outer layer adsorption as the MTZ progressed through the bed followed by a slower rate of adsorption caused by the dispersion of molecules from the outer layer into the pores of the adsorbent, which was expected from the theory. This conclusion led to the calculation of MTZ length for each adsorption run by multiplying the duration of the linear accumulation by the velocity of the adsorption front. The calculated MTZ lengths were superimposed onto plots of  $^{11}\text{CO}_2$  concentration displayed as a percentage of the maximum concentration for specific time frames. These plots were produced for each run at 10, 20 and 30 minutes into the experiment and the displayed position of the MTZ was consistent with the calculated velocities. The concentration plots for Activated Carbon show the size of the MTZ to be indistinguishable; however, the plots for Zeolite 13X give confidence to the calculated MTZ properties as the length and progression rate are comparable to the apparent front of the concentration distribution.

This project has shown that imaging equipment typically used for medical applications can be adapted and utilised to perform chemical flow process studies. PET has proven to provide comparable adsorption breakthrough and capacity measurements to commonly used techniques with the added ability to directly observe the kinetics within the bed. This non-invasive investigation has shown the potential to develop a deeper understanding of adsorption and promises to provide a means of verifying or disproving existing kinetics models such as the Linear Driving Force (LDF) model or Lagergren first order kinetics model. It is widely reported that PET is suitable for performing quantitative measurements provided an attenuation correction of the system can be applied (Prekeges 2011b). This would provide invaluable detail about the adsorption process, which is considered a well understood process, and would open up a large number of potential avenues of research into processes that are less understood. The following section discusses possible future lines of research.

## **6.2 FUTURE WORK**

The most promising aspect of using PET to study adsorption is the direct observation of the mass transfer kinetics within the bed. In order to pursue this investigation a number of recommendations are made here to improve the experimental design for specific measurements.

For the investigation into MTZ length it would be desirable to utilise the entire axial length of the FoV to allow for larger MTZs to be defined. A possible reason that the MTZs for the Activated Carbon runs was indistinguishable is because they were of comparable length to the adsorbent region of the column or possibly longer. By filling the whole length of the column (250 mm) with adsorbent this would give a better

indication is this is actually what is being observed. Increasing the diameter of the column would also be beneficial in defining the MTZ as a larger cross sectional area will provide better insight into the dispersion of gas through the bed. The study presented here has assumed axial plug flow of the gas phase which could either be confirmed or disproved as the shape of the adsorption front progressing through the bed would be observed. A larger range of operating conditions including CO<sub>2</sub> feed concentration, mass flow rate and system pressure would allow a more definable relationship between these parameters and resulting adsorption front velocity, MTZ length and the dominance of the primary outer layer adsorption and secondary internal adsorption but this was outside the scope of this feasibility study. The imaging technique would also allow a study of the desorption of <sup>11</sup>CO<sub>2</sub> by releasing the pressure of the system after full saturation has been reached. The distribution of <sup>11</sup>CO<sub>2</sub> concentration during this process would provide valuable insight into the kinetics of desorption.

Further optimisation studies could be performed using adsorption as the subject in order to provide insight into alternative flow processes which could be investigated. It would be desirable in the future to define the optimal initial activity of the <sup>11</sup>CO<sub>2</sub> prior to introduction to the system to reduce the effects of dead time correction but to also produce adequate annihilation events for a high level of meaningful statistical data. By minimising the dead time correction and measuring the initial activity and concentration of <sup>11</sup>CO<sub>2</sub> in the bulk gas phase quantitative measurements could be made provided that a reliable attenuation correction could be performed. Optimising the initial gas activity would also allow further investigation into the temporal resolution of the camera. From the preliminary dynamic study it was confirmed that the imaging system

was capable of reducing the image frame acquisition length from one minute per frame to 45 seconds. The minimum setting of frame length for the ECART ART PET camera used is 5 s, which is a value restricted by the rotation of the detector banks. By reducing the frame length the number of coincidence events detected would be greatly reduced which would increase the statistical noise detected. Also, the maximum number of frames that can be acquired in one imaging session is 175 so for minimum frame length of 5 seconds this results in an imaging duration of 14.6 minutes. For future work the balance between sufficient meaningful data acquisition, higher temporal resolution and experiment duration must be considered, which could suggest the potential of a custom designed camera with flexible geometry being better suited to the study of gaseous flow processes.

Within the last year the University of Birmingham has acquired a MicroPET Primate P4 camera which is a full ring PET camera with increased sensitivity and improved spatial resolution. It has a 7.9 cm axial FoV and 19 cm transaxial FoV and is comprised of 32 rings of 336 Lutetium Oxyorthosilicate (LSO) crystals which are 2.2 x 2.2 x 10 mm in size. The manufacturer specifications (Concorde 2001) claim an intrinsic spatial resolution of 1.85 mm at the centre of the FoV with a reconstructed resolution of 2.25 mm in the central 80 mm of the transverse plane. The superior properties of LSO crystals provide a small decay time of ~40 ns which results in a reduced minimum timing window of 2 ns which in turn results in less random detections (Tai et al. 2001). This piece of imaging equipment would provide relatively higher temporal and spatial accuracy compared to the ECAT ART used for the studies presented in this thesis but at reduced FoV. Assuming fully functional attenuation correction and iterative

reconstruction algorithms, OSEM, it would be possible to perform a quantitative study using the MicroPET.

## 7 REFERENCES

- Abràmoff, M.D., Magalhães, P.J. & Ram, S.J., 2005. Image processing with ImageJ Part II. *Biophotonics International*, 11(7), pp.36–43.
- Akita, K. & Yoshida, F., 1974. Bubble Size, Interfacial Area, and Liquid Phase Mass Transfer Coefficient in Bubble Columns. *Industrial & Engineering Chemistry Process Design and Development* 1, 13(1), pp.84–91.
- Alessio, A. & Kinahan, P., 2006. PET image reconstruction. *Nuclear Medicine*, 1, pp.1–22. Available at: [http://www.schreisupport.com/Schreisupport/GENERAL\\_INFORMATION/PET/alessioPETRecon.pdf](http://www.schreisupport.com/Schreisupport/GENERAL_INFORMATION/PET/alessioPETRecon.pdf).
- Anger, H.O., 1958. Scintillation camera. *Review of Scientific Instruments*, 29(1), pp.27–33.
- Barigou, M., 2004. Particle Tracking in Opaque Mixing Systems: An Overview of the Capabilities of PET and PEPT. *Chemical Engineering Research and Design*, 82(9), pp.1258–1267. Available at: <http://linkinghub.elsevier.com/retrieve/pii/S0263876204726131>.
- Barth, T. et al., 2013. Study of particle deposition and resuspension in pebble beds using positron emission tomography. In *7th World Congress on Industrial Process Tomography*. pp. 2–5.
- Bell, S.D. et al., 2013. An investigation into the feasibility of radioactive gas imaging for studies in process tomography. In *7th World Congress on Industrial Process Tomography*. pp. 897–906.
- Belmabkhout, Y., Frere, M. & De Weireld, G., 2004. High-pressure adsorption measurements. A comparative study of the volumetric and gravimetric methods. *Measurement Science and Technology*, 15, pp.848–858.
- Biersack, H.-J. & Freeman, L.M., 2007. 1.3.2 Radiation Detector Performance. In *Clinical Nuclear Medicine*. Springer, pp. 8–9.
- Brits, R.J.N. & Haasbroek, F.J., 1987. The production of efficient  $^{81}\text{Rb}/^{81}\text{mKr}$  generators using zirconium phosphate. *International Journal of Radiation Applications and Instrumentation. Part A. Applied Radiation and Isotopes*, 38(8), pp.623–627.
- Brunauer, S., 1944. Chapter II: Data of Adsorption. In *Physical Adsorption of Gases and Vapours*. pp. 14–21.
- Bushberg, J.T. et al., 2012. Filtered Backprojection. In *The Essential Physics of Medical Imaging 4th Edition*. pp. 352–354.

- Caldwell, S.J., 2014. *Experimental and computational evaluation of activated carbons for carbon dioxide capture from high pressure gas mixtures*. University of Birmingham.
- Cavenati, S., Grande, C.A. & Rodrigues, A.E., 2004. Adsorption Equilibrium of Methane, Carbon Dioxide, and Nitrogen on Zeolite 13X at High Pressures. *Journal of Chemical Engineering*, 49, pp.1095–1101.
- Chahbani, M.H. & Tondeur, D., 2000. Mass transfer kinetics in pressure swing adsorption. *Separation and Purification Technology*, 20(2-3), pp.185–196.
- Cherry, S.R., Sorenson, J.A. & Phelps, M.E., 2012. B. Backprojection and Fourier Based Techniques. In *Physics in Nuclear Medicine, Fourth Edition*. pp. 256–261.
- Choi, S., Drese, J.H. & Jones, C.W., 2009. Adsorbent materials for carbon dioxide capture from large anthropogenic point sources. *ChemSusChem*, 2(9), pp.796–854. Available at: <http://www.ncbi.nlm.nih.gov/pubmed/19731282> [Accessed July 16, 2012].
- Christian, P.E. & Waterstram-Rich, K.M., 2012. 2D and 3D Scanner Configuration. In *Nuclear Medicine and PET/CT: Technology and Techniques, Seventh Edition*. pp. 330–333.
- Concorde, 2001. microPET Theory of Operation: Introduction.
- Conway-Baker, J. et al., 2002. Measurement of the motion of grinding media in a vertically stirred mill using positron emission particle tracking (PEPT) Part II. *Minerals Engineering*, 15, pp.53–59.
- Coulson, J.M. & Richardson, J.F., 1994. Chemical Kinetics of Heterogeneous Catalytic Reactions. In J. F. Richardson & D. G. Peacock, eds. *Chemical Engineering Volume 3: Chemical & Biochemical Reactors & Process Control, Third Edition*. pp. 145–146.
- Dabrowski, A. & Meurant, G., 1999. Industrial carbon adsorbents. In *Vol 1: Applications in Industry*. pp. 69–94.
- Dechsiri, C. et al., 2005. Positron Emission Tomography Applied to Fluidization Engineering. *The Canadian Journal of Chemical Engineering*, 83(1), pp.88–96. Available at: <http://doi.wiley.com/10.1002/cjce.5450830116>.
- Dry, M.E., 2002. The Fischer – Tropsch process : 1950 – 2000. *Catalysis Today*, 71, pp.227–241.
- Dwivedi, P.N. & Upadhyay, S.N., 1977. Particle-Fluid Mass Transfer in Fixed and Fluidized Beds. *Industrial & Engineering Chemistry Process Design and Development*, 16(2), pp.157–165.

- Elnashaie, S. & El-Hennawi, I., 1979. MULTIPLICITY OF THE STEADY STATE IN FLUIDIZED BED REACTORS-IV FLUID CATALYTIC. *Chemical Engineering Science*, 34(1), pp.1113–1121.
- Ergun, S., 1952. No Title. *Chemical Engineering Progress*, 48, p.89.
- Fahey, F.H., 2002. Data Acquisition in PET Imaging. *Journal of Nuclear Medicine Technology*, 30, pp.39–49.
- Fernandes, F.A.N. & Lona, L.M.F., 2001. Heterogeneous modeling for fluidized-bed polymerization reactor. *Chemical Engineering Science*, 56, pp.963–969.
- Ferno, M.A. et al., 2015. Combined PET-CT for Visualization and Quantification of Fluid Flow in Porous Rock. In pp. 1–5.
- Foo, K.Y. & Hameed, B.H., 2010. Insights into the modelling of adsorption isotherm systems. *Chemical Engineering Journal*, 156, pp.2–10.
- Geldart, D., 1973. Types of Gas Fluidization. *Powder Technology*, 7, pp.285–292.
- Godish, T., 1989. Removal of Gaseous Contaminants. In *Indoor Air Pollution Control*. pp. 282–307.
- Gomes, V.G. & Yee, K.W.K., 2002. Pressure swing adsorption for carbon dioxide sequestration from exhaust gases. *Separation and Purification Technology*, 28, pp.161–171.
- Gupta, T.K., 2013. *Radiation, Ionization, and Detection in Nuclear Medicine*, Springer.
- Hartmann, I.J. et al., 2001. Technegas Versus <sup>81</sup>mKr Ventilation-Perfusion Scintigraphy: A Comparative Study in Patients with Suspected Acute Pulmonary Embolism. *Journal of Nuclear Medicine*, 42(1), pp.393–400.
- Heijnen, J.J. et al., 1989. Review on the application of anaerobic fluidized bed reactors in waste-water treatment. *The Chemical Engineering Journal*, 41(3), pp.B37–B50.
- Himeno, S., Komatsu, T. & Fujita, S., 2005. High-Pressure Adsorption Equilibria of Methane and Carbon Dioxide on Several Activated Carbons. *Journal of Chemical Engineering*, 50, pp.369–376.
- Ho, M.T., Allinson, G.W. & Wiley, D.E., 2008. Reducing the Cost of CO<sub>2</sub> Capture from Flue Gases Using Pressure Swing Adsorption. *Industrial & Engineering Chemistry Research*, 47(14), pp.4883–4890.
- Ho, Y.S. & McKay, G., 1998. A Comparison of Chemisorption Kinetic Models Applied to Pollutant Removal on Various Sorbents. *Trans IChemE*, 76(Part B), pp.332–340.
- Jaszczak, R.J., 2006. The early years of single photon emission computed tomography

- (SPECT): an anthology of selected reminiscences. *Physics in medicine and biology*, 51, pp.R99–R115.
- Kahlil, M.M., 2011. *Basic Sciences of Nuclear Medicine*, Springer.
- Kak, A.C. & Slaney, M., 1988. 3.2 The Fourier Slice Theorem. In *Principles of Computerized Tomographic Imaging*. pp. 56–60.
- Kantarci, N., Borak, F. & Ulgen, K.O., 2005. Bubble column reactors. *Process Biochemistry*, 40(7), pp.2263–2283.
- Kirkup, L., 1994. *Experimental Methods: An Introduction to the Analysis and Presentation of Data*,
- Kuhl, D.E. & Edwards, R.Q., 1963. Image Separation Radioisotope Scanning. , 80, pp.653–662.
- Langmuir, I., 1918. The Adsorption of Gases on Plane Surfaces of Glass, Mica and Platinum. *Journal of the American Chemical Society*, 40(9), pp.1361–1403. Available at: citeulike-article-id:3880396\nhttp://dx.doi.org/10.1021/ja02242a004.
- Liaw, C.H. et al., 1979. Kinetics of Fixed-Bed Adsorption: A New Solution. *AIChE Journal*, 25, pp.376–381.
- Liu, S. & Farncombe, T.H., 2007. Collimator-Detector Response Compensation in Quantitative SPECT Reconstruction. In *IEEE Nuclear Science Symposium Conference Record*. pp. 3955–3960.
- Lyra, M., 2009. Single Photon Emission Tomography ( SPECT ) and 3D Images Evaluation in Nuclear Medicine. In Y.-S. Chen, ed. *Image Processing*. InTech, pp. 259–286.
- Lyra, M. & Ploussi, A., 2011. Filtering in SPECT image reconstruction. *International Journal of Biomedical Imaging*, 2011.
- Mazoyer, B.M., Roos, M.S. & Huesman, R.H., 1985. Dead time correction and counting statistics for positron tomography. *Physics in medicine and biology*, 30(5), pp.385–399.
- McCabe, W.L., Smith, J.C. & Harriott, P., 1993a. 7.3 Fluidization. In *Unit Operations of Chemical Engineering 5th Edition*. pp. 165–177.
- McCabe, W.L., Smith, J.C. & Harriott, P., 1993b. Chapter 25: Adsorption. In *Unit Operations of Chemical Engineering 5th Edition*. pp. 810–837.
- McCabe, W.L., Smith, J.C. & Harriott, P., 1993c. Chapter 7: Flow Past Imersed Bodies. In *Unit Operations of Chemical Engineering 5th Edition*. pp. 143–151.
- McKetta, 1993. Adsorption, General. In *Unit Operation Handbook: Volume 1*. pp. 144–

183.

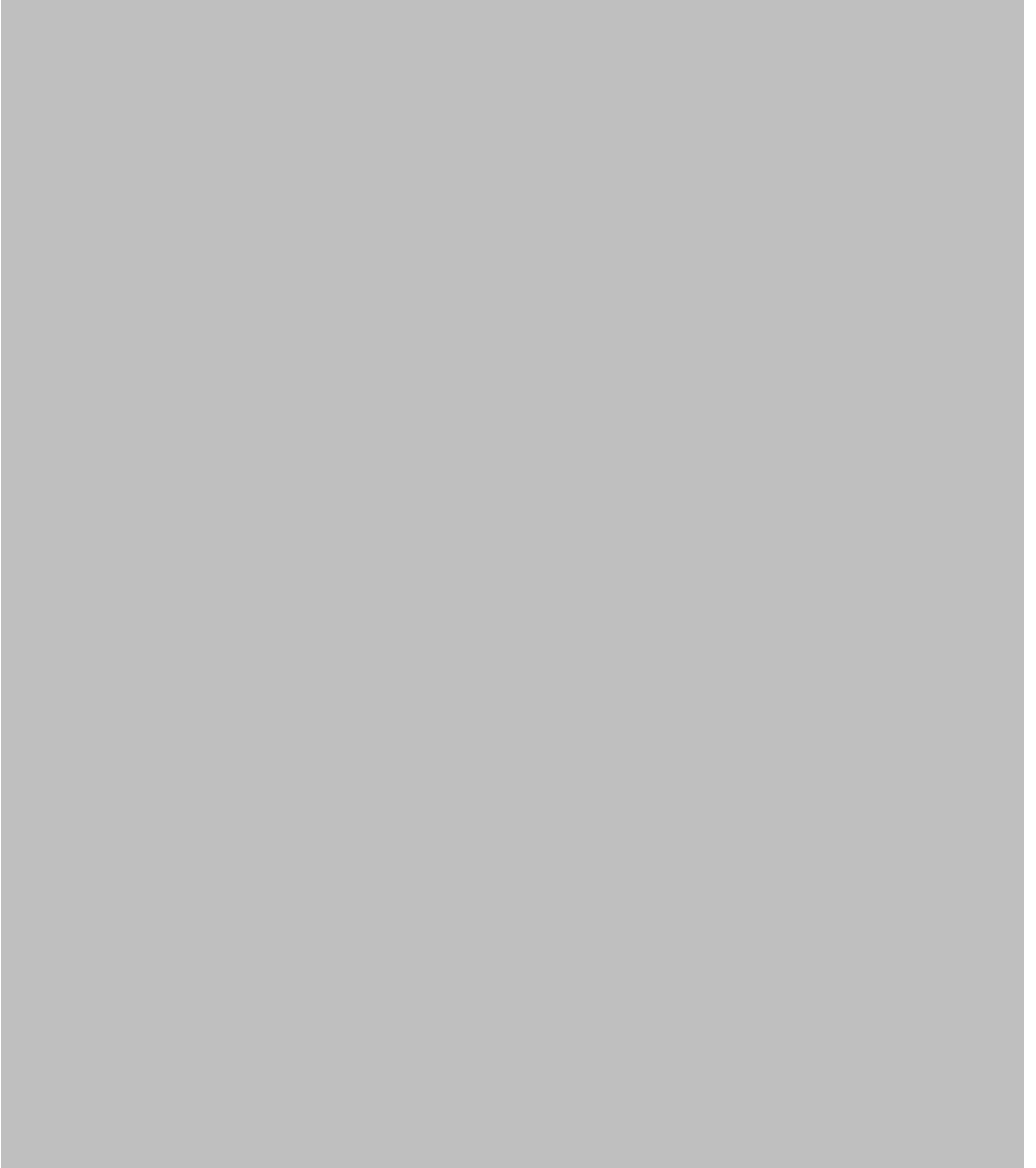
- Merel, J., Clause, M. & Meunier, F., 2008. Experimental investigation on CO<sub>2</sub> post-combustion capture by indirect thermal swing adsorption using 13X and 5A zeolites. *Industrial and Engineering Chemistry Research*, 47(1), pp.209–215.
- Mesquita, C.H. De et al., 2012. Analysis of bubble column using third-generation computed Tomography. In *6th International Symposium on Process Tomography*. pp. 1–8.
- Narayanan, M. & Perkins, A., 2013. Resolution recovery in the Ingenuity TF PET\_CT. *Philips*.
- Nutt, R., 2002. The History of Positron Emission Tomography.pdf. *Molecular Imaging and Biology*, 4(1), pp.11–26.
- Padmavathi, D.A., 2011. Potential Energy Curves & Material Properties. *Materials and Applications*, 2, pp.97–104.
- Park, J.G. et al., 2014. Performance Evaluation of Advanced Industrial SPECT System with Diverging Collimator. *Applied Radiation and Isotopes*, 94, pp.125–130.
- Parker, D.J. et al., 2002. Positron emission particle tracking using the new Birmingham positron camera. *Nuclear Instruments and Methods in Physics Research, Section A: Accelerators, Spectrometers, Detectors and Associated Equipment*, 477(1-3), pp.540–545.
- Parker, D.J. et al., 2008. Positron imaging techniques for process engineering: recent developments at Birmingham. *Measurement Science and Technology*, 19(9), pp.1–10.
- Prekeges, J., 2011a. Chapter 7: Collimators. In *Nuclear Medicine Instrumentation*. Jones and Bartlett Publishers, pp. 80–90.
- Prekeges, J., 2011b. Chapter 14: Principles of Positron Emission Tomography (PET). In *Nuclear Medicine Instrumentation*. Jones and Bartlett Publishers, pp. 189–222.
- Prekeges, J., 2011c. Chapter 2: Scintillation Detectors. In *Nuclear Medicine Instrumentation*. Jones and Bartlett Publishers, pp. 17–27.
- Prekeges, J., 2011d. Chapter 8: Imaging Characteristics and Performance Measure in Planar Imaging. In *Nuclear Medicine Instrumentation*. pp. 91–105.
- Rahmim, A. & Zaidi, H., 2008. PET versus SPECT: strengths, limitations and challenges. *Nuclear medicine communications*, 29(3), pp.193–207.
- Rashidi, N., Yusup, S. & Loong, L., 2013. Kinetic Studies on Carbon Dioxide Capture using Activated Carbon. *Chemical Engineering Transactions*, 35, pp.361–366.

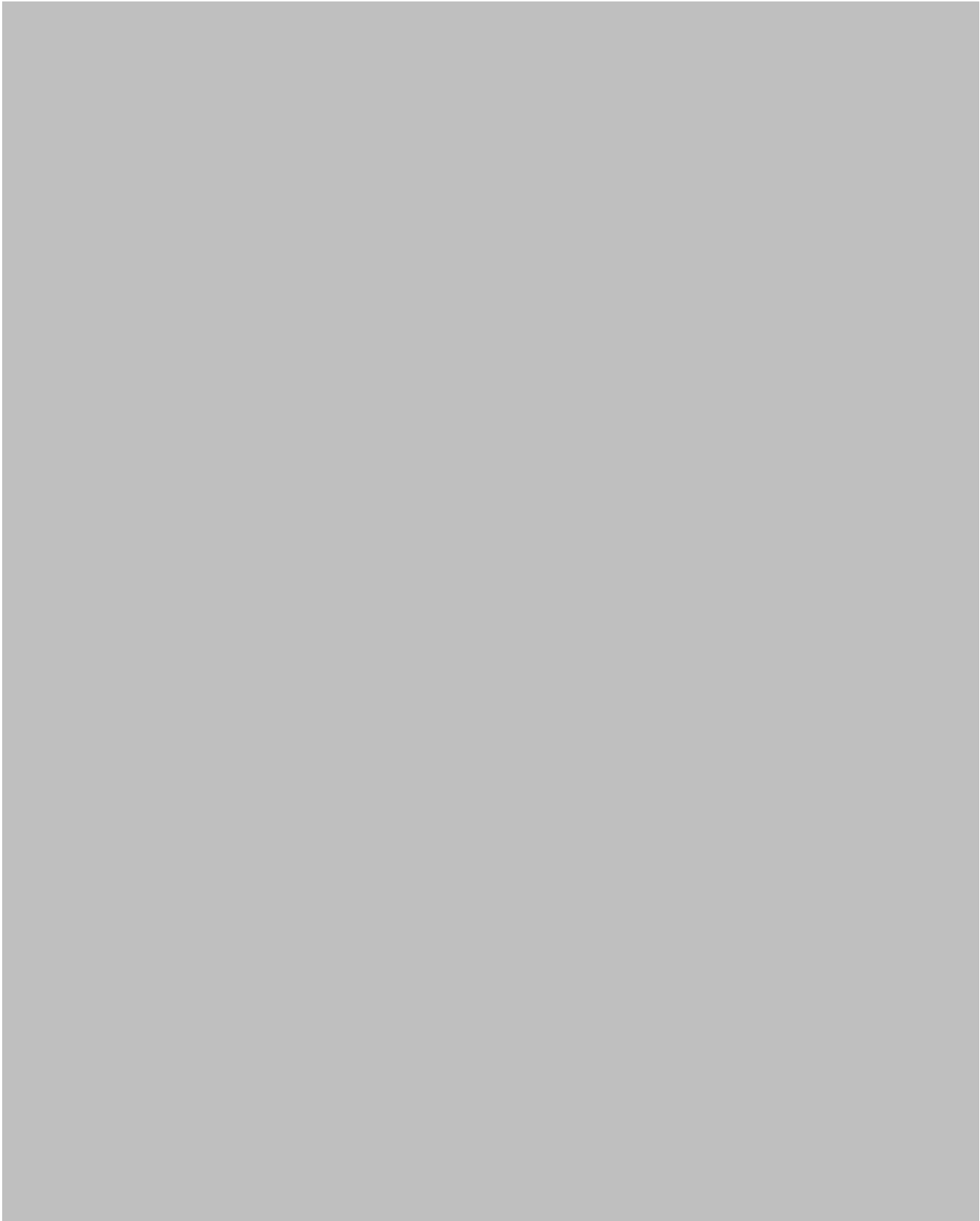
- Rory, H. et al., 1996. Exercise Myocardial Perfusion SPECT in Patients Without Known Coronary Artery Disease. *Circulation*, 93, pp.905–914.
- Saha, G.B., 2010. Chapter 6: Performance Characteristics of PET Scanners. In *Basics of PET Imaging: Physics, Chemistry, and Regulations*. pp. 97–116.
- Schlyer, D.J., 2004. PET tracers and radiochemistry. *Annals of the Academy of Medicine Singapore*, 33(2), pp.146–154.
- Servomex, SERVOFLEX MiniMP (5200 Multipurpose) Operators Manual.
- Shepp, L.A. & Vardi, Y., 1982. Maximum Likelihood Reconstruction for Emission Tomography. *IEEE Transactions on Medical Imaging*, MI-1(2), pp.113–122.
- Siemens, 1996. ECAT ART Operating Instructions. , pp.1–2 – 1–10.
- Siriwardane, R. V et al., 2001. Adsorption of CO<sub>2</sub> on molecular sieves and activated carbon. *Energy Fuels*, 15(2), pp.279–284.
- Sorenson, J.A. & Phelps, M.E., 1977. Design and Performance Characteristics of Parallel Hole Collimators. In *Physics in Nuclear Medicine*. pp. 332–345.
- Stadie, N.P., 2013. *Synthesis and Thermodynamic Studies of Physisorptive Energy Storage Materials*. California Institute of Technology.
- Tai, Y.C. et al., 2001. Performance Evaluation of the MicroPET P4: a PET System Dedicated to Animal Imaging. *Physics in medicine and biology*, 46(1), pp.1845 – 1862.
- Talaia, M. a R., 2007. Terminal Velocity of a Bubble Rise in a Liquid Column. *Internatinal Journal of Mathematical, Physical, Electrical and Computer Engineering*, 1(4), pp.11–15. Available at: <http://citeseerx.ist.psu.edu/viewdoc/download?doi=10.1.1.192.9665&rep=rep1&type=pdf>.
- Talbot, J., 1997. Analysis of Adsorption Selectivity in a One-Dimensional Model System. *AIChE Journal*, 43, pp.2471–2478.
- Turkington, T.G., 2001. Introduction to PET Instrumentation. *Journal of Nuclear Medicine Technology*, 29, pp.1–8.
- Vandewalle, T. & Vandecasteele, C., 1983. Optimisation of the Production of <sup>11</sup>C<sub>2</sub>O<sub>2</sub> by Proton Irradiation of Nitrogen Gas. *International Journal of Applied Radiation and Isotopes*, 34(10), pp.1459–1464.
- Vyas, R.K., Kumar, S. & Kumar, S., 2004. Determination of micropore volume and surface area of zeolite molecular sieves by D-R and D-A equations: A comparative study. *Indian Journal of Chemical Technology*, 11, pp.704–709.

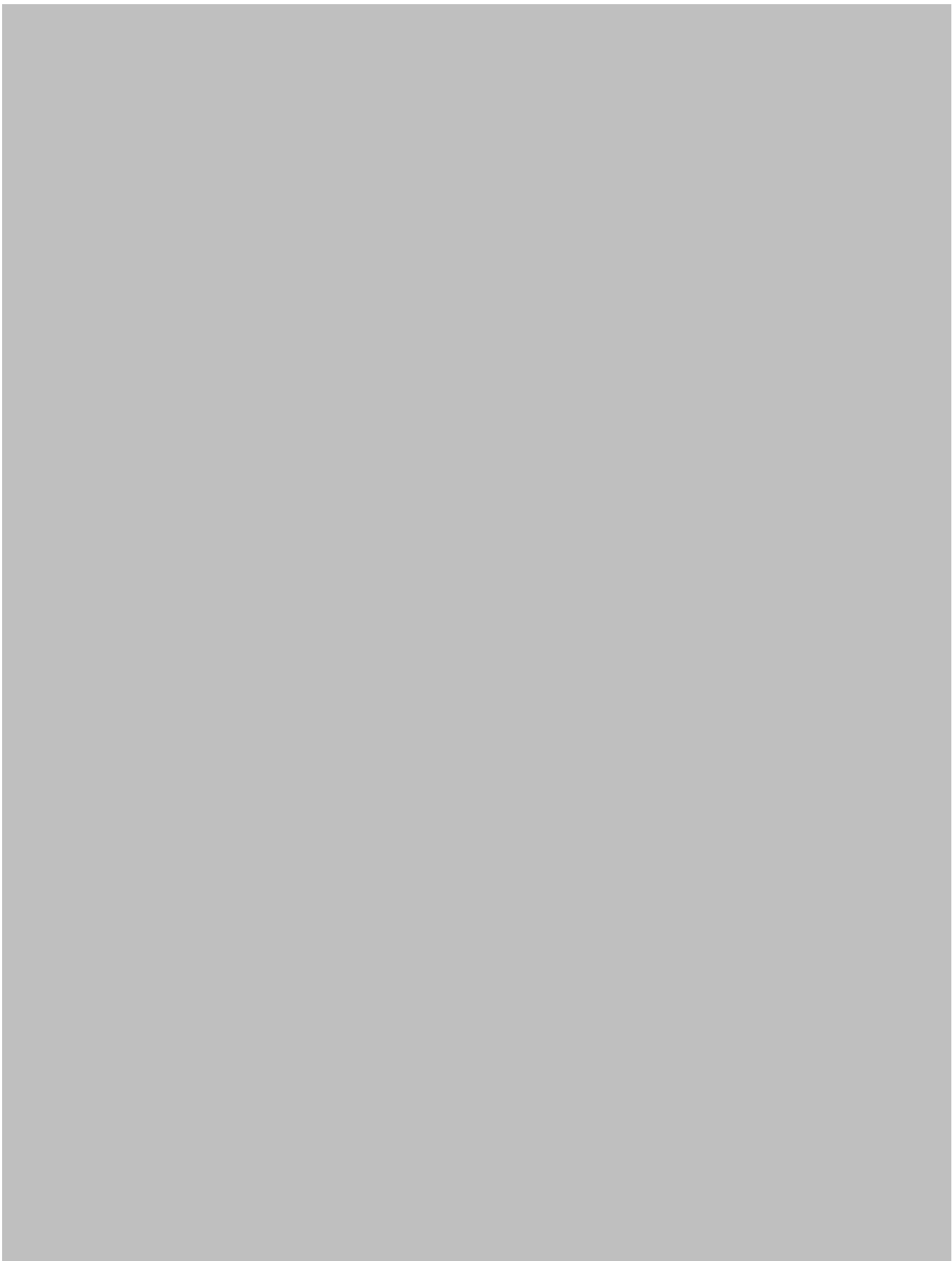
- Wang, H.G. et al., 2008. Investigation of Batch Fluidized-Bed Drying by Mathematical Modeling, CFD Simulation and ECT Measurement. *AIChE Journal*, 54(2), pp.427–444.
- Warsito, W. & Fan, L.S., 2003. ECT imaging of three-phase fluidized bed based on three-phase capacitance model. *Chemical Engineering Science*, 58(3-6), pp.823–832.
- Webb, P.A., 2003. Introduction to Chemical Adsorption Analytical Techniques and their Applications to Catalysis. *MIC Technical Publications*.
- Webb, S., 1988a. 6.4 Radionuclides for Imaging. In *The Physics of Medical Imaging*. London: IOP Publishing Ltd, pp. 181–193.
- Webb, S., 1988b. 6.9 Clinical Applications of Radioisotope Imaging. In *The Physics of Medical Imaging*. pp. 256–318.
- Wilcox, J., 2012. Adsorption Kinetics. In *Carbon Capture*. pp. 148–149.
- Wildman, R.D., Huntley, J.M. & Parker, D.J., 2001. Convection in highly fluidized three-dimensional granular beds. *Physical Review Letters*, 86(15), pp.3304–3307.
- Yang, X.H. & Zhu, W.L., 2007. Viscosity properties of sodium carboxymethylcellulose solutions. *Cellulose*, 14(5), pp.409–417.
- Yu, C., Huang, C. & Tan, C., 2012. A Review of CO<sub>2</sub> Capture by Absorption and Adsorption. *Aerosol and Air Quality Research*, 12, pp.745–769.
- Zhang, H. et al., 2015. The voidage in a CFB riser as function of solids flux and gas velocity. In *The 7th World Congress on Particle Technology (WCPT7)*. pp. 1112–1122.
- Ziegler, S.I., 2005. Positron emission tomography: Principles, technology, and recent developments. *Nuclear Physics A*, 752(1-4 SPEC. ISS.), pp.679–687.

## **8 APPENDIX**

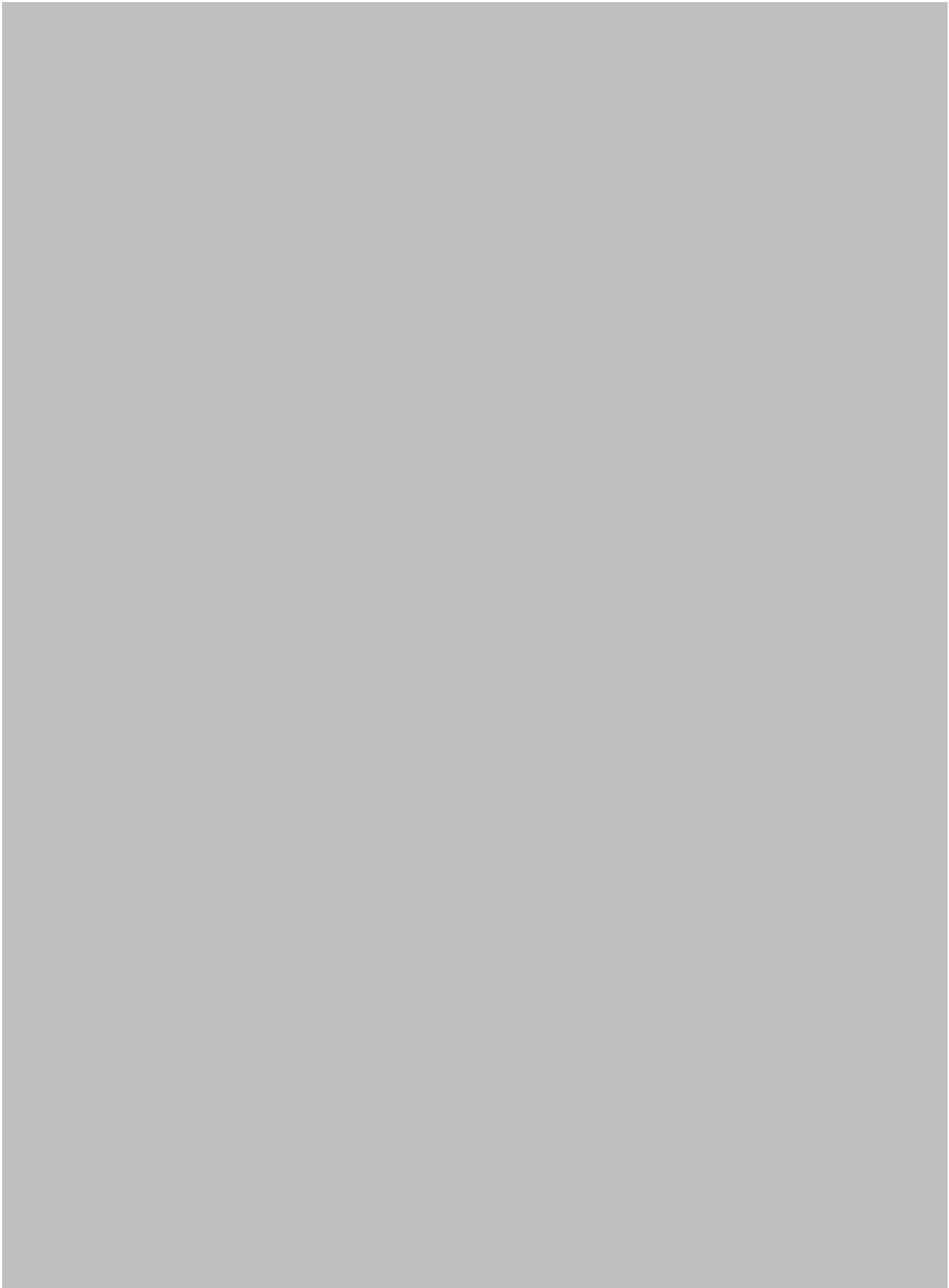
### **8.1 APPENDIX A RISK ASSESSMENT**













## 8.2 APPENDIX B CO<sub>2</sub> MASS FLOW CONTROLLER CORRECTION

The Mass Flow Controller for the CO<sub>2</sub> required a correction factor which was dependent on the pressure to the inlet of the controller. The manufacturer supplied the correction factor values at each pressure as shown in Table 19 Linear interpolation was used for intermediate pressures.

**Table 19. Correction factors for CO<sub>2</sub> Mass Flow Controller.**

<b>Inlet Pressure (bar)</b>	<b>Correction factor</b>
35	1.000
33	1.022
31	1.045
29	1.071
27	1.086
25	1.102
23	1.117
21	1.135
19	1.152
17	1.17
15	1.181
13	1.199
11	1.214
9	1.231
7	1.247
5.2	1.261

### 8.3 APPENDIX C CONCENTRATION PROFILES

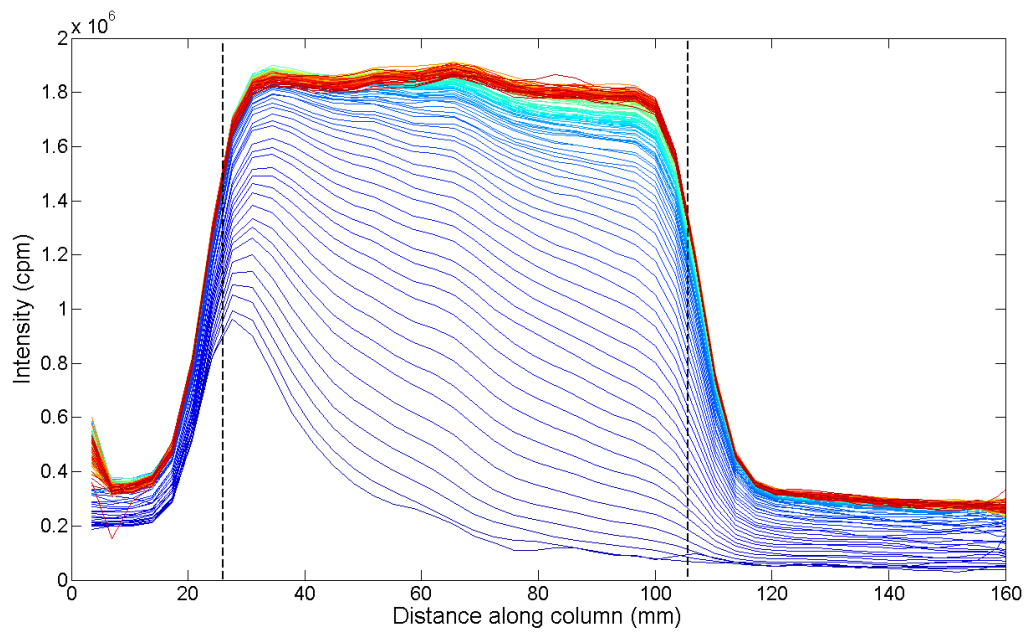


**Figure 8.1. Intensity profiles along the adsorption column for Activated Carbon at 2.6 MPa and 50% CO<sub>2</sub> feed concentration.**

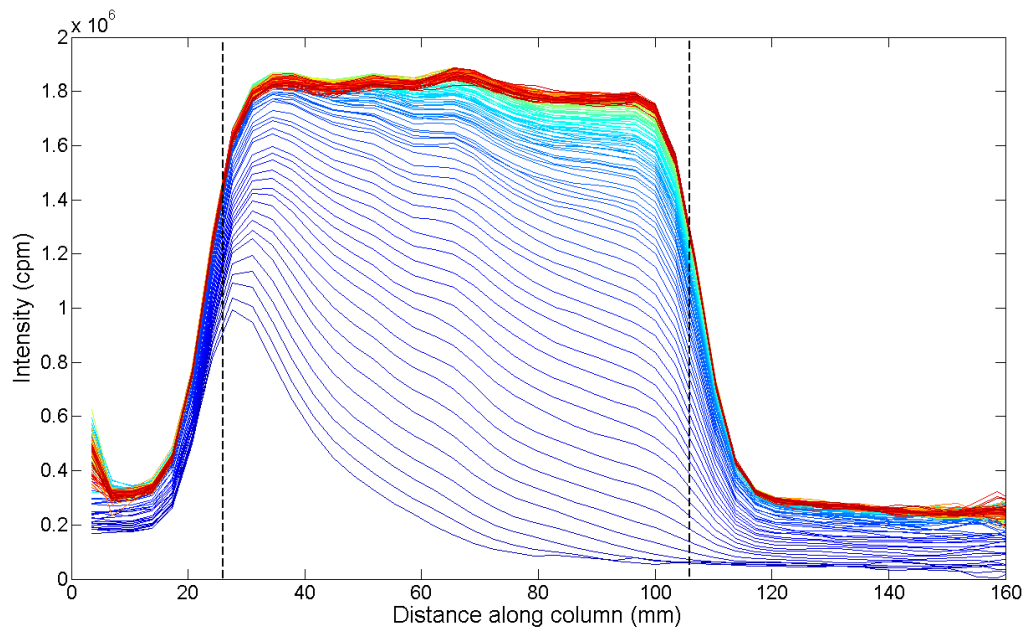


**Figure 8.2. Intensity profiles along the adsorption column for Activated Carbon at 2.6 MPa and 30% CO<sub>2</sub> feed concentration.**

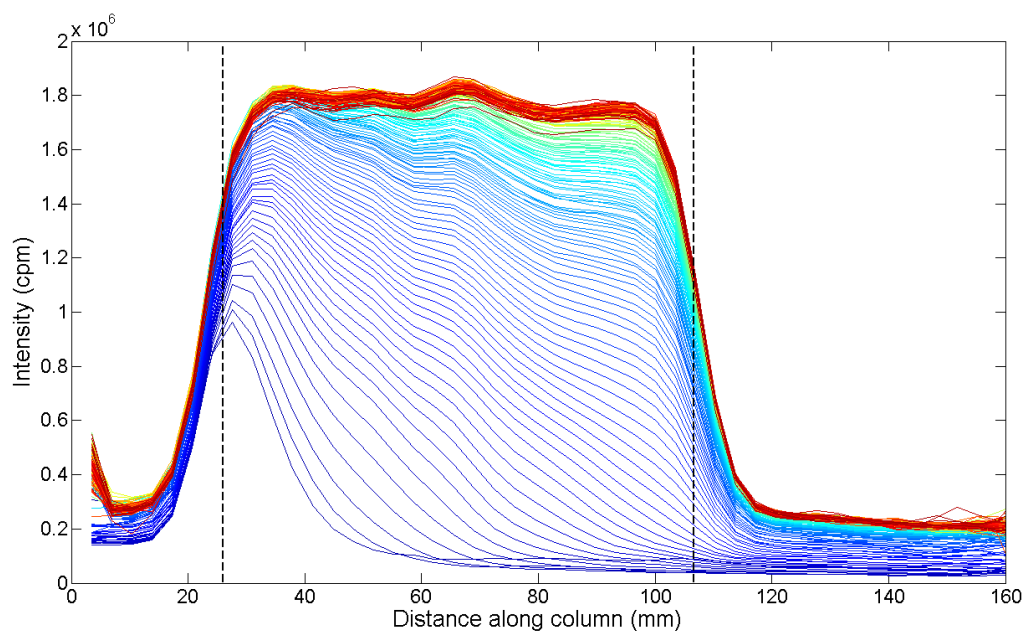


**Figure 8.3. Intensity profiles along the adsorption column for Activated Carbon at 2.6 MPa and 10% CO<sub>2</sub> feed concentration.**

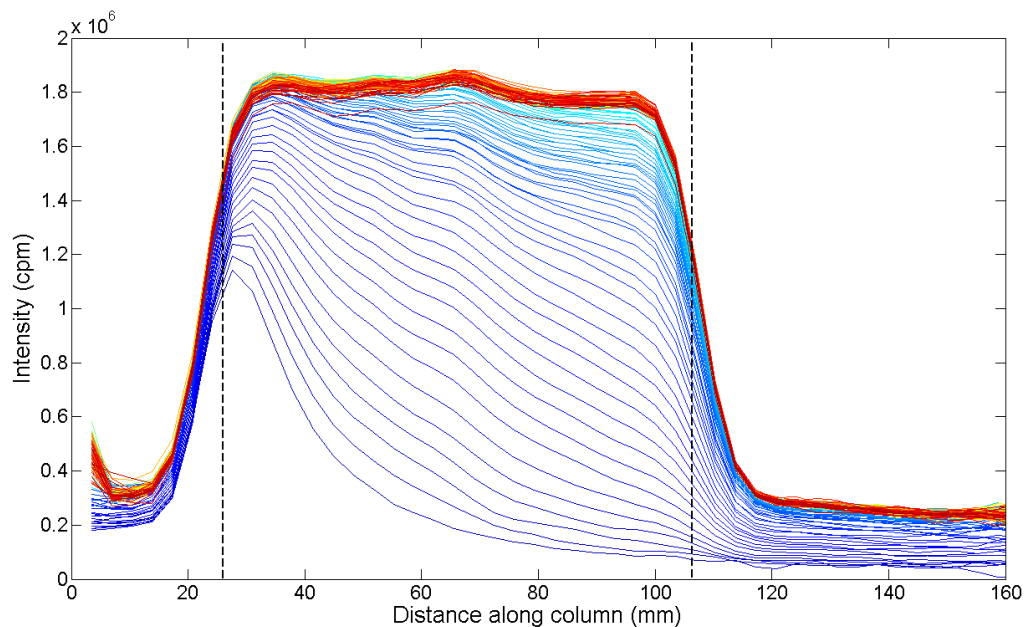


**Figure 8.4. Intensity profiles along the adsorption column for Activated Carbon at 1.6 MPa and 50% CO<sub>2</sub> feed concentration.**

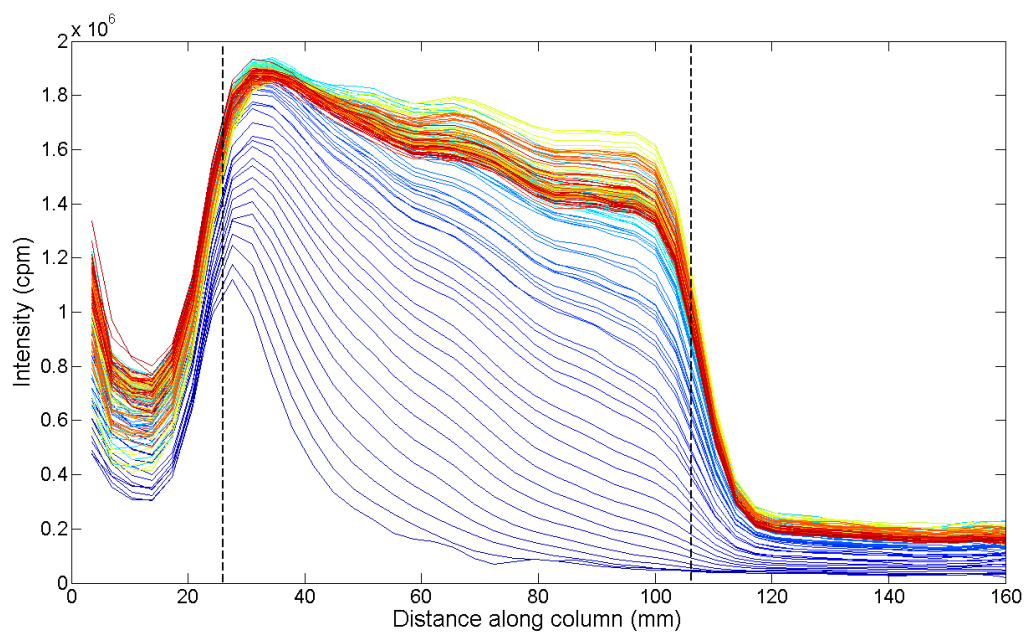


**Figure 8.5. Intensity profiles along the adsorption column for Activated Carbon at 1.6 MPa and 30% CO<sub>2</sub> feed concentration.**

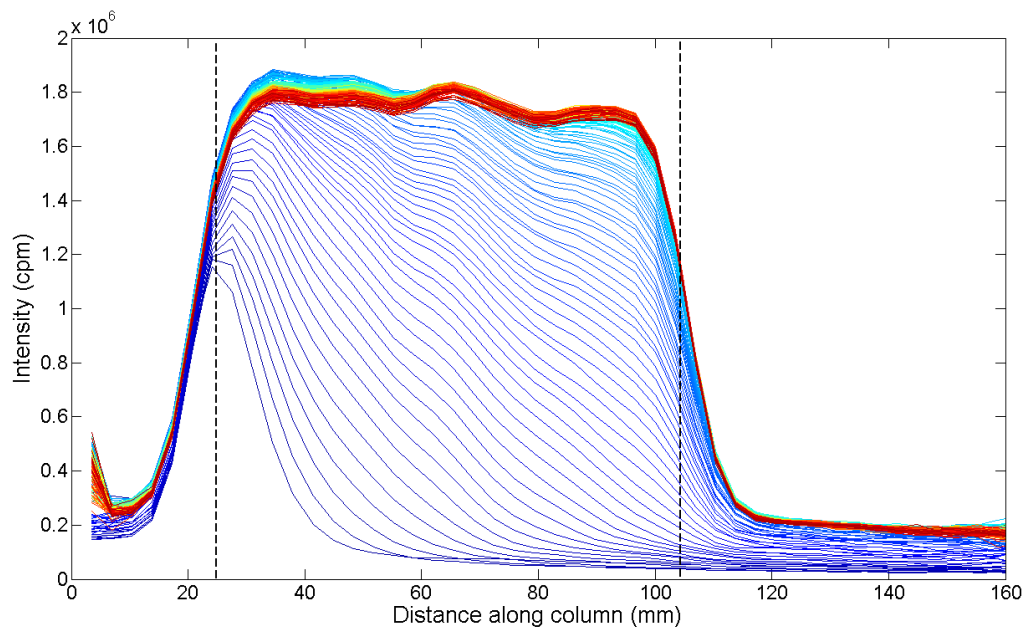


**Figure 8.6. Intensity profiles along the adsorption column for Activated Carbon at 1.6 MPa and 10% CO<sub>2</sub> feed concentration.**

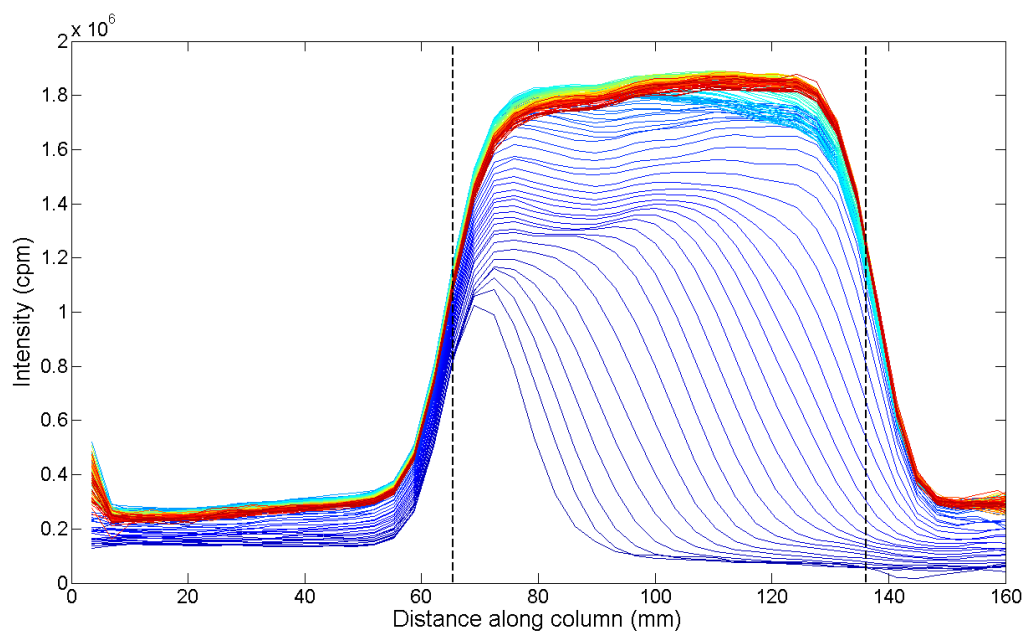


**Figure 8.7. Intensity profiles along the adsorption column for Zeolite 13X at 2.6 MPa and 50% CO<sub>2</sub> feed concentration.**

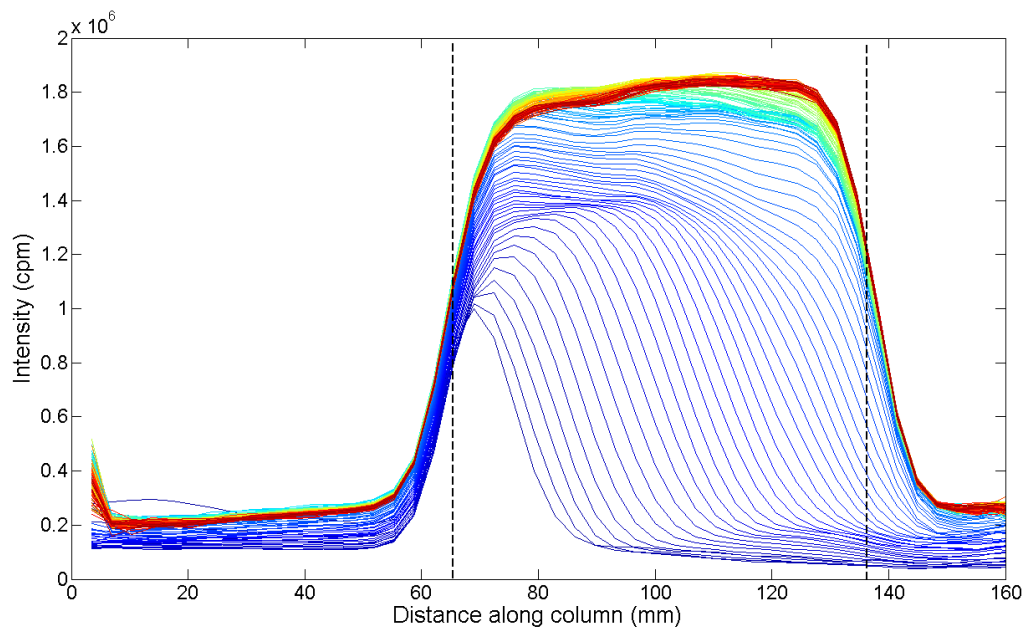


**Figure 8.8. Intensity profiles along the adsorption column for Zeolite 13X at 2.6 MPa and 30% CO<sub>2</sub> feed concentration.**

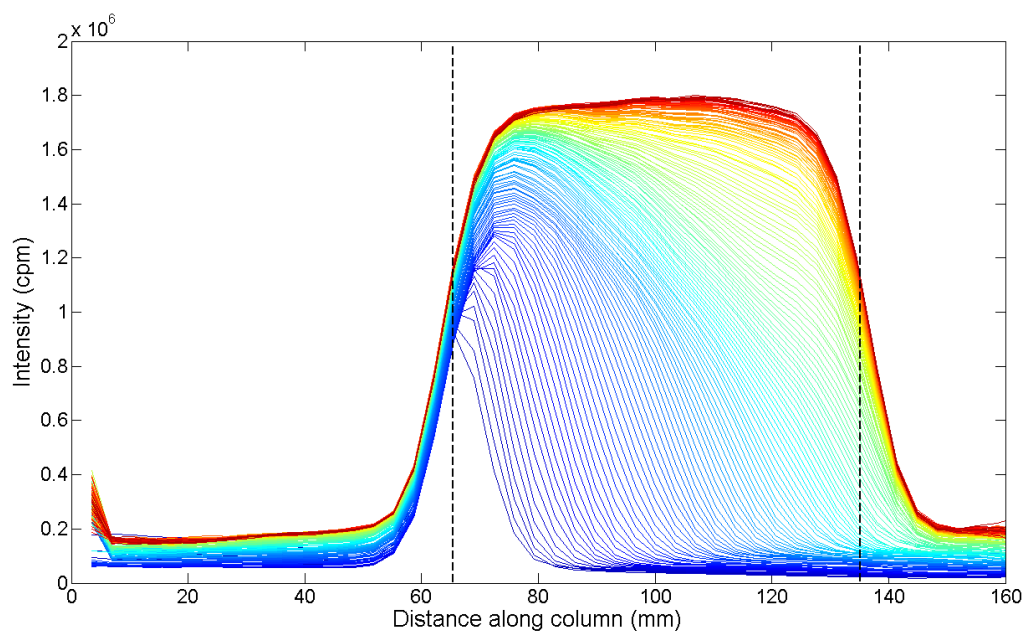


**Figure 8.9. Intensity profiles along the adsorption column for Zeolite 13X at 3.1 MPa and 10% CO<sub>2</sub> feed concentration.**

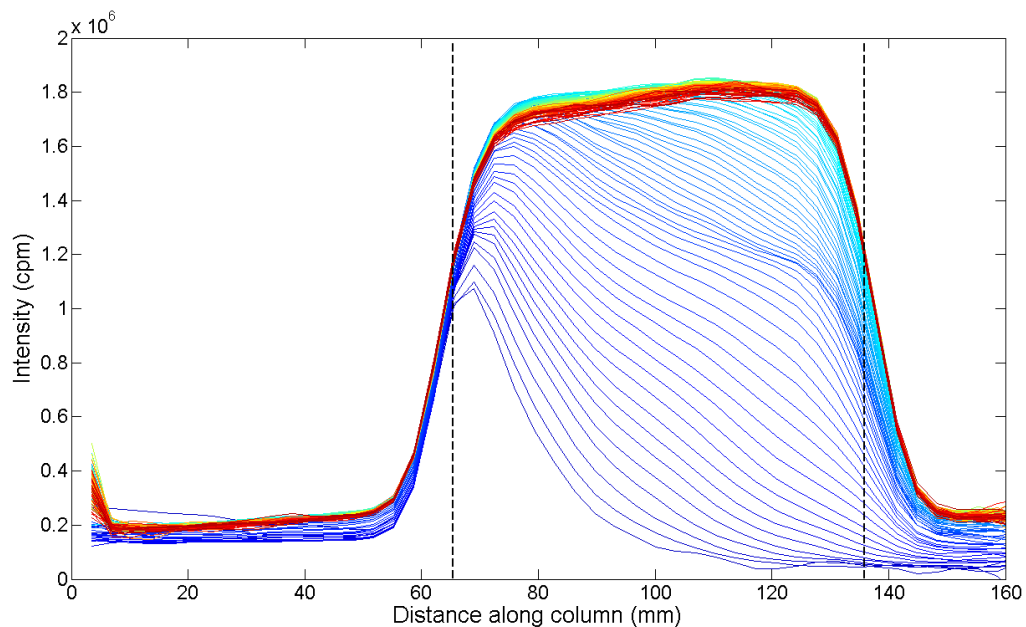


**Figure 8.10. Intensity profiles along the adsorption column for Zeolite 13X at 1.6 MPa and 50% CO<sub>2</sub> feed concentration.**

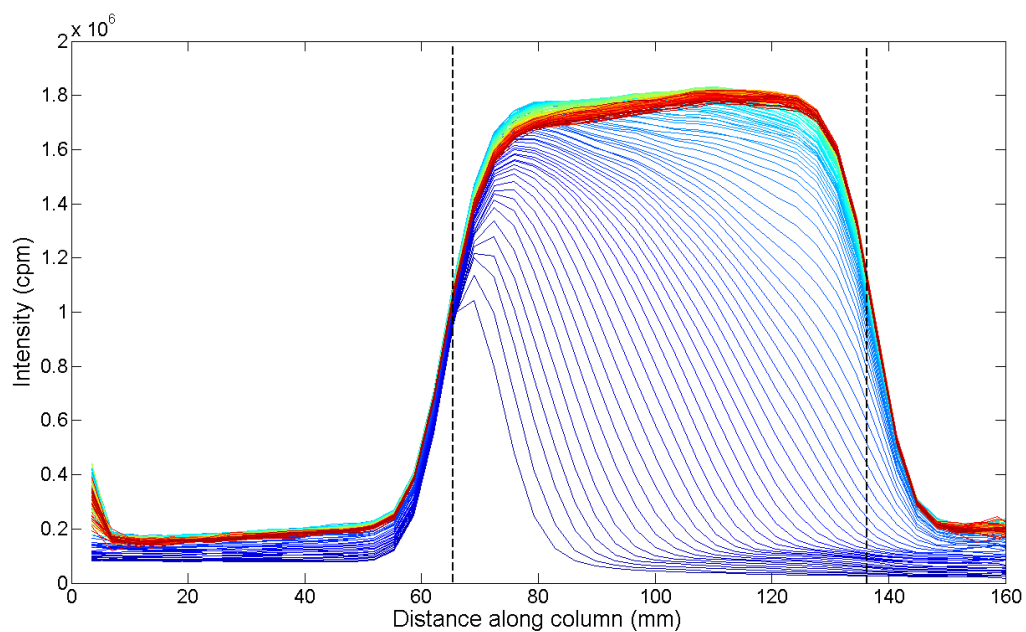


**Figure 8.11. Intensity profiles along the adsorption column for Zeolite 13X at 1.6 MPa and 30% CO<sub>2</sub> feed concentration.**

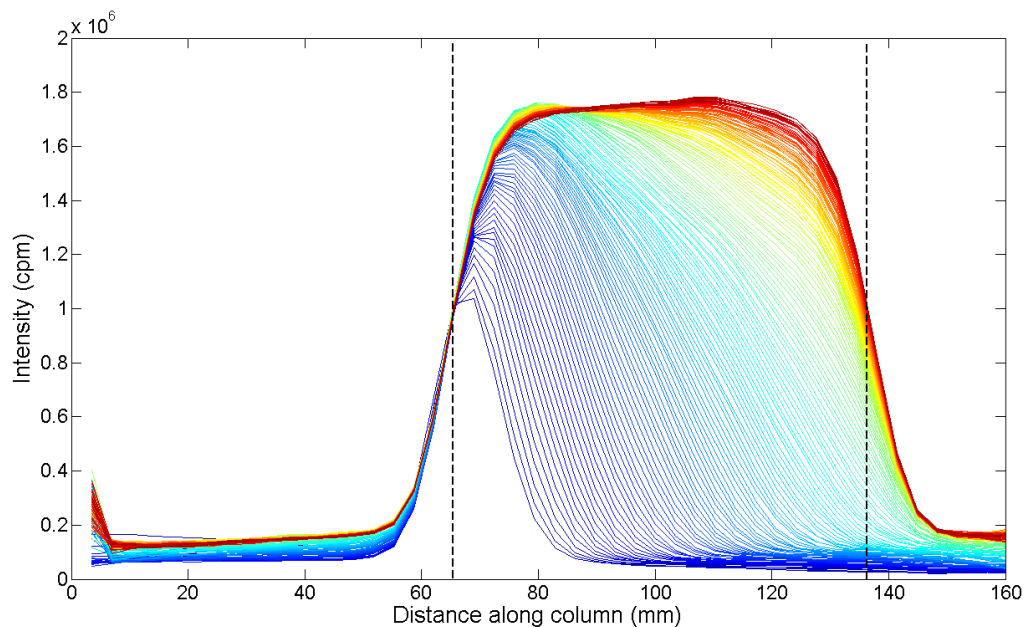


**Figure 8.12. Intensity profiles along the adsorption column for Zeolite 13X at 1.6 MPa and 10% CO<sub>2</sub> feed concentration.**

## 8.4 APPENDIX D ACCUMULATION PROFILES

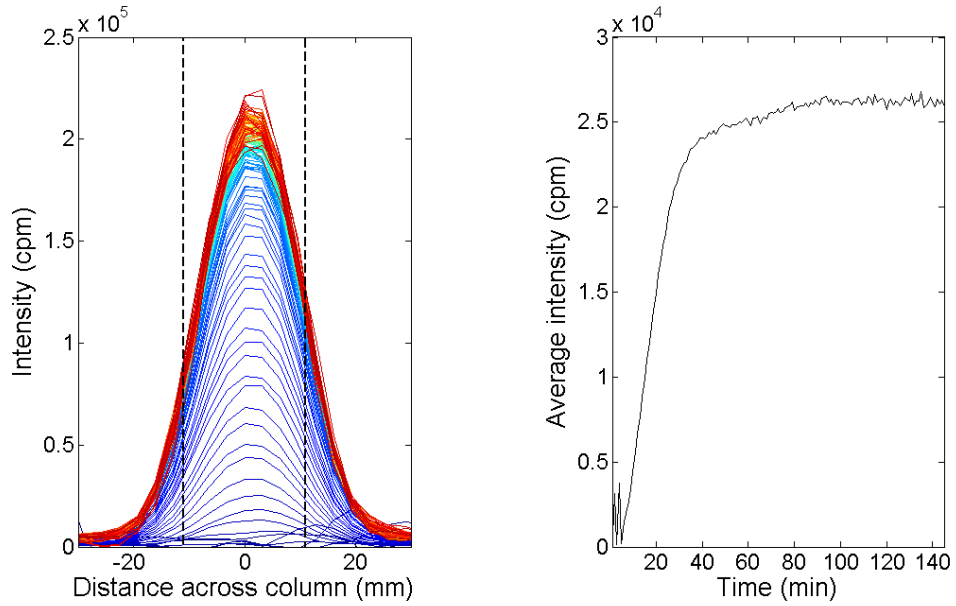


Figure 8.13. Intensity profiles across the adsorption column at plane 25 for Activated Carbon at 2.6 MPa and 50% CO<sub>2</sub> feed concentration and corresponding plot of average intensity per minute.

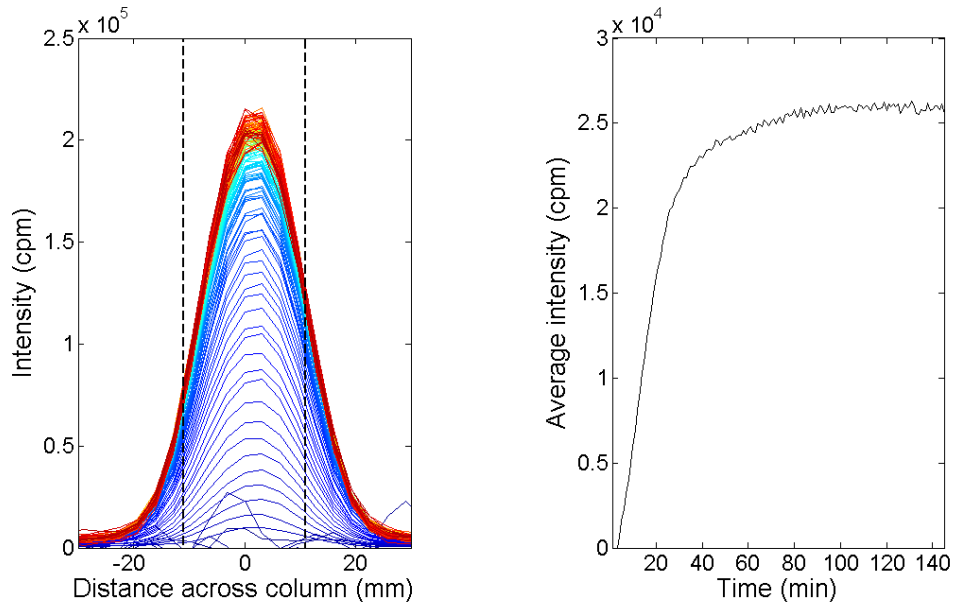
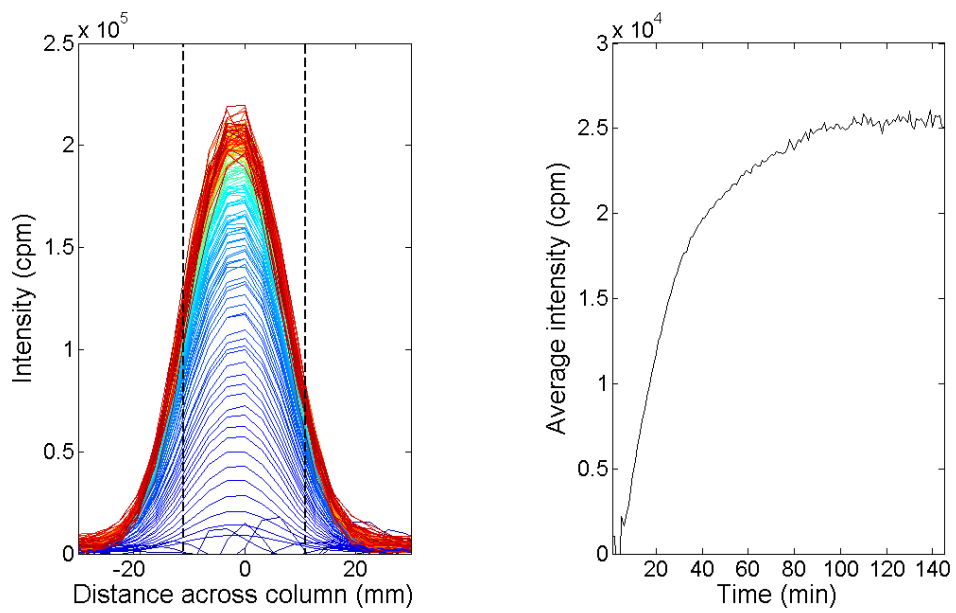
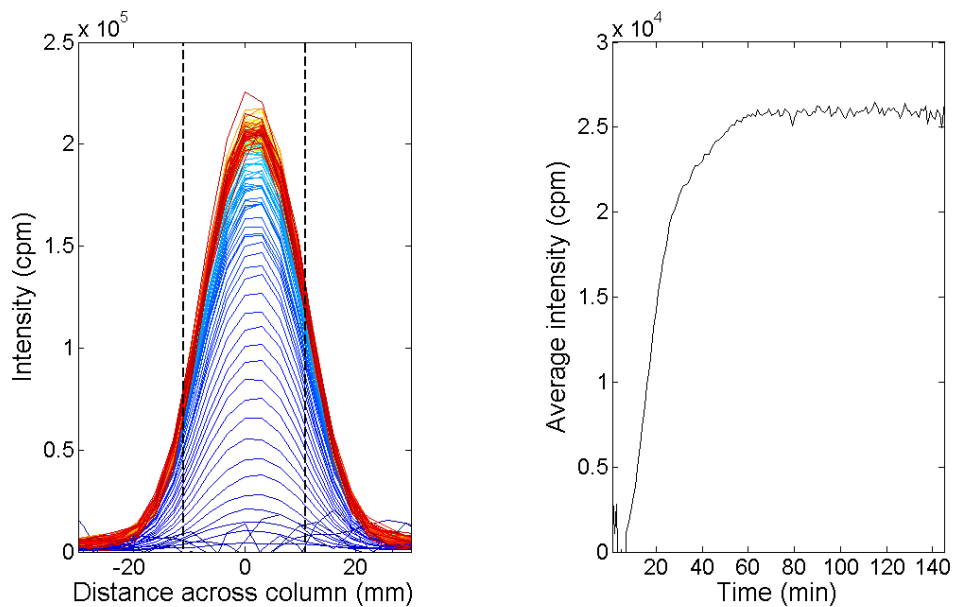


Figure 8.14. Intensity profiles across the adsorption column at plane 25 for Activated Carbon at 2.6 MPa and 30% CO<sub>2</sub> feed concentration and corresponding plot of average intensity per minute.



**Figure 8.15. Intensity profiles across the adsorption column at plane 25 for Activated Carbon at 2.6 MPa and 10% CO<sub>2</sub> feed concentration and corresponding plot of average intensity per minute.**



**Figure 8.16. Intensity profiles across the adsorption column at plane 25 for Activated Carbon at 1.6 MPa and 50% CO<sub>2</sub> feed concentration and corresponding plot of average intensity per minute.**

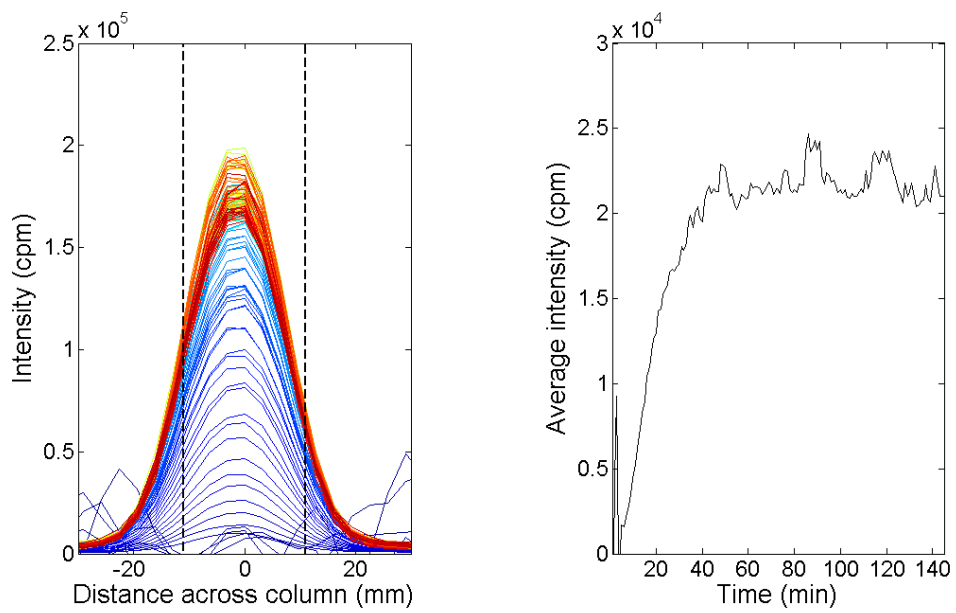


**Figure 8.17. Intensity profiles across the adsorption column at plane 25 for Activated Carbon at 1.6 MPa and 30% CO<sub>2</sub> feed concentration and corresponding plot of average intensity per minute.**

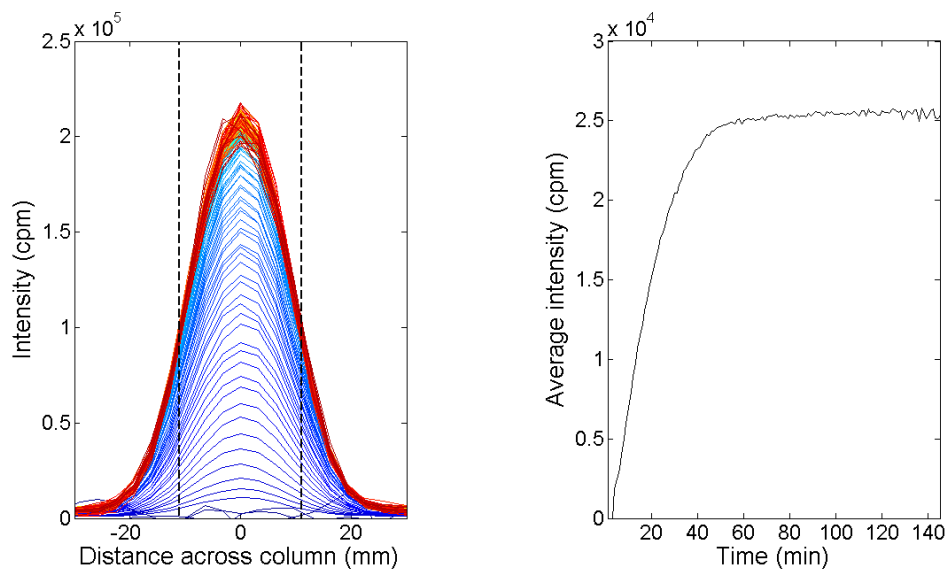


**Figure 8.18. Intensity profiles across the adsorption column at plane 25 for Activated Carbon at 1.6 MPa and 10% CO<sub>2</sub> feed concentration and corresponding plot of average intensity per minute.**

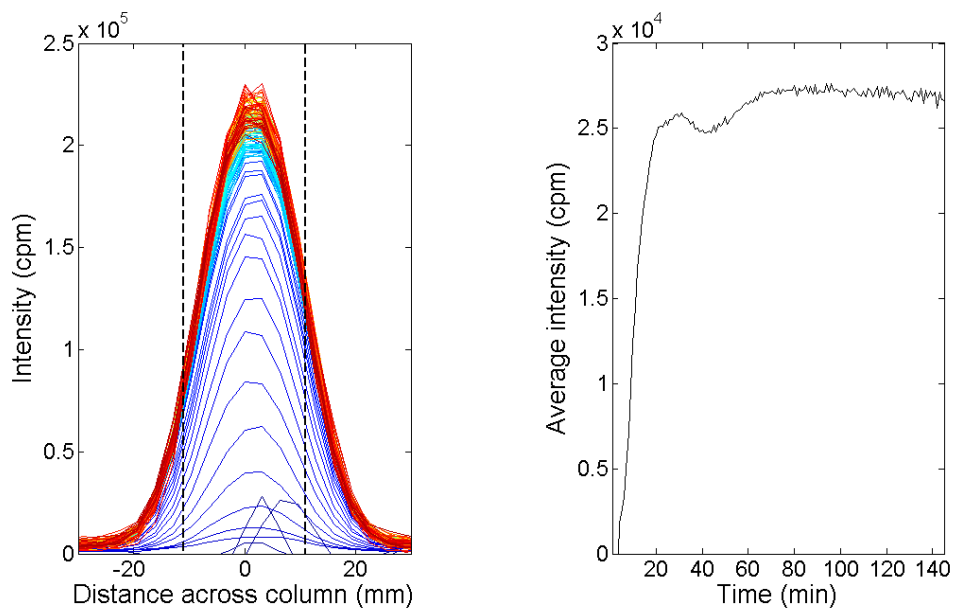


**Figure 8.19. Intensity profiles across the adsorption column at plane 35 for Zeolite 13X at 2.6 MPa and 50% CO<sub>2</sub> feed concentration and corresponding plot of average intensity per minute.**

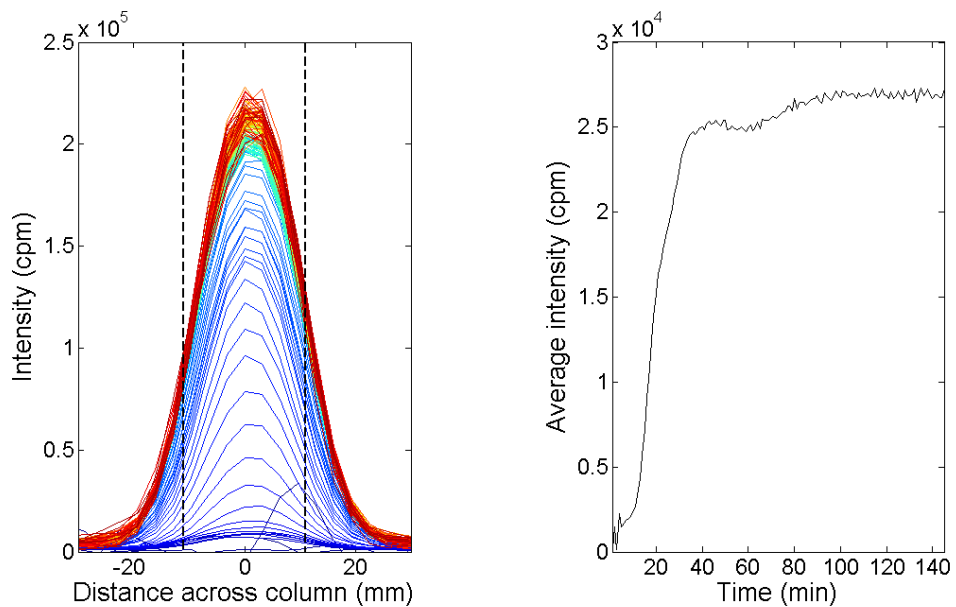


**Figure 8.20. Intensity profiles across the adsorption column at plane 35 for Zeolite 13X at 2.6 MPa and 30% CO<sub>2</sub> feed concentration and corresponding plot of average intensity per minute.**

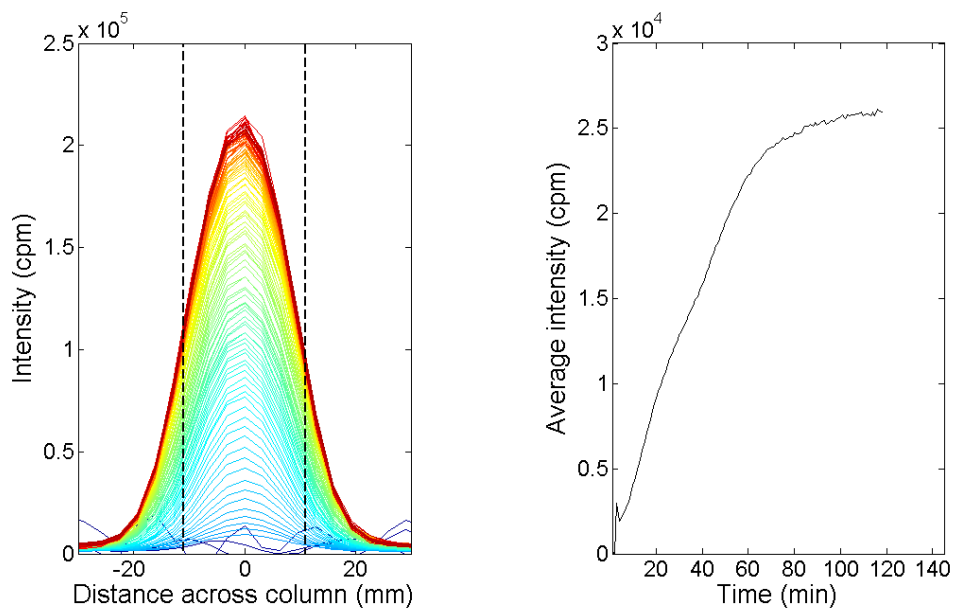


**Figure 8.21. Intensity profiles across the adsorption column at plane 35 for Zeolite 13X at 3.1 MPa and 10% CO<sub>2</sub> feed concentration and corresponding plot of average intensity per minute.**

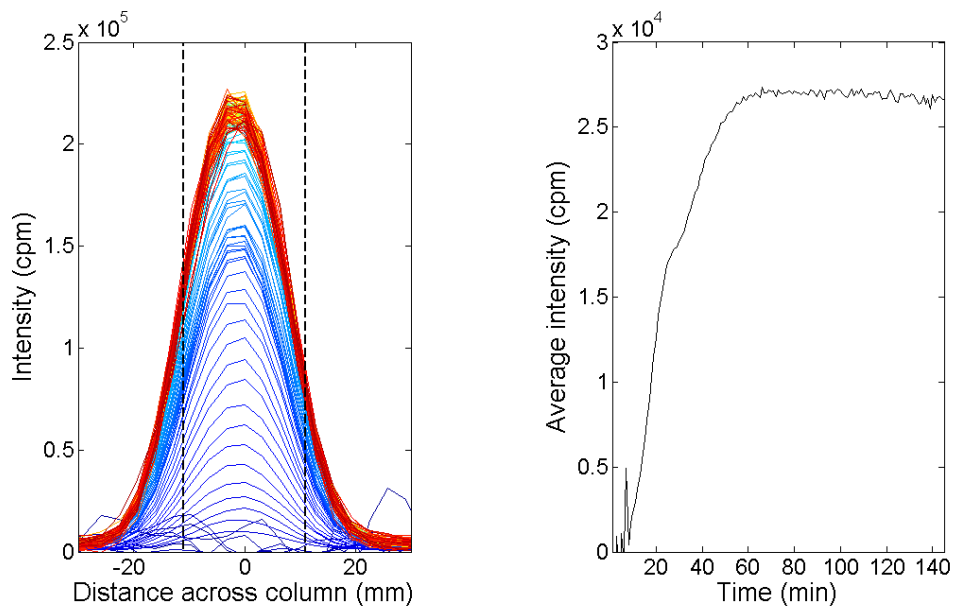


**Figure 8.22. Intensity profiles across the adsorption column at plane 35 for Zeolite 13X at 1.6 MPa and 50% CO<sub>2</sub> feed concentration and corresponding plot of average intensity per minute.**

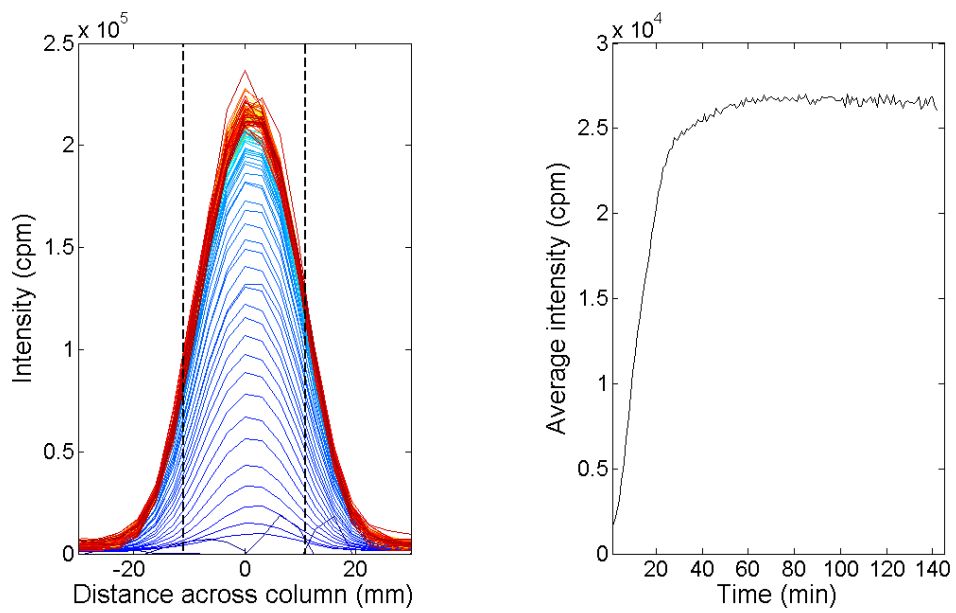


**Figure 8.23. Intensity profiles across the adsorption column at plane 35 for Zeolite 13X at 1.6 MPa and 30% CO<sub>2</sub> feed concentration and corresponding plot of average intensity per minute.**

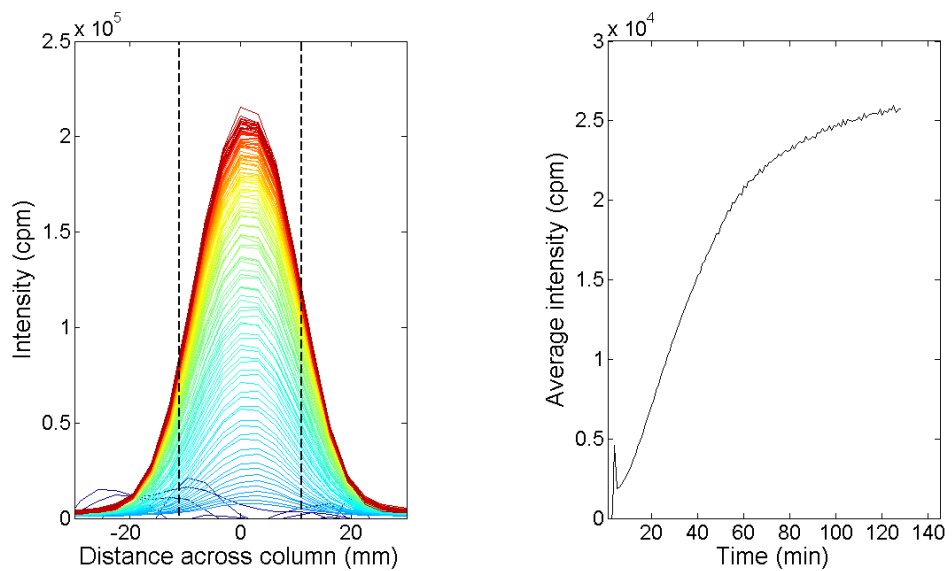


**Figure 8.24. Intensity profiles across the adsorption column at plane 35 for Zeolite 13X at 1.6 MPa and 10% CO<sub>2</sub> feed concentration and corresponding plot of average intensity per minute.**

## 9 Publications

# An investigation into the feasibility of radioactive gas imaging for studies in process tomography

S. D. Bell<sup>a,b</sup>, A. Ingram<sup>a</sup>, T. W. Leadbeater<sup>b</sup> and D. J. Parker<sup>b</sup>

<sup>a</sup>*School of Chemical Engineering, University of Birmingham, Birmingham B15 2TT, United Kingdom*

<sup>b</sup>*Positron Imaging Centre, School of Physics and Astronomy, University of Birmingham, Birmingham B15 2TT, United Kingdom*

---

## Abstract

The powerful functional medical imaging technique of Positron Emission Tomography (PET) continues to be developed and adapted as a practical means of studying engineering processes at the University of Birmingham Positron Imaging Centre. To date a considerable research effort has been made into the study of flow and mixing in solid and liquid systems and the development of Positron Emission Particle Tracking (PEPT) has made it possible to study multi-phase flow within industrial processes. However, little work has been reported on producing and imaging gases; this paper presents an initial investigation into the use of radioactive gas imaging for process systems.

Positron Emission Tomography (PET) was used to design an experimental procedure which can observe the adsorption of <sup>11</sup>CO<sub>2</sub> onto a packed bed of zeolite 13X, a mineral which can provide specific separation of CO<sub>2</sub> from other gases. A trial run was performed to determine the feasibility of imaging gases under steady state conditions and a data analysis protocol has been developed to allow the study of dynamic gaseous processes.

Keywords: Positron Emission Tomography; PET; gas imaging; Adsorption; CO<sub>2</sub>

---













